The energy spectrum and the chemical composition of primary cosmic rays with energies from 10^{14} to 10^{16} eV

Shoichi Ogio

Department of Physics
Tokyo Institute of Technology

February 2005

abstract

The energy spectrum of cosmic rays is well represented by a power law function of the primary energy. One of the significant features on the spectrum is a steepening around 10^{15} eV, which is called the knee. The knee must be deeply related to the origin of the cosmic rays and/or to the propagation mechanisms of primary cosmic rays in the Galaxy. Therefore, it is of crucial importance to obtain precise features of the primary energy spectrum as well as accurate information on the primary chemical composition. In order to obtain a reliable conclusion for the chemical composition of cosmic rays at the knee region, and to confirm our previous result, we determined EAS longitudinal developments more directly with an equi-intensity method analysis. We have measured extensive air showers with primary energies above 6 TeV at Mt. Chacaltaya in Bolivia. The data were collected by an air shower array called the Minimum Air Shower(MAS) array since March 2000. We applied the equi–intensity analysis method to the extensive air showers extended over region of their maximum developments. We varied the mixture of protons and iron nuclei in our simulations and compared the simulated equi–intensity curves with the measured ones to determine the mixing ratio of protons as a function of the primary energy. Moreover, on the basis of the obtained chemical composition, we derived the primary energy spectrum from 10^{14} to 5×10^{16} eV. Consequently, we concluded that the power law index of the spectrum is changing gradually around $10^{15.5}$ eV, and that the obtained proton ratio decreases with increasing energy. We directly measured the longitudinal development of air showers initiated by primaries with energies around the knee. We find that the average mass number of primary cosmic rays increases with increasing energy above $10^{14.5}$ eV and the dominant component around the knee is not protons.

This result suggests that the steepening of the component spectra is caused at a single rigidity of $10^{14.5}$ V. Moreover, it is consistent with our former result of the Čerenkov light observations. The measurement of Čerenkov light pulse shapes corresponded to an observation of the longitudinal developments of air showers at the earlier stages before the maximum developments. In contrast, with the equi–intensity method analysis we determined longitudinal developments around their maximum and at the later stages. Therefore, with two different observations, we measured the whole stage of EAS longitudinal developments and then we can obtain a trustworthy conclusion on the chemical composition.

On the basis of detailed simulation researches for the diffusive motions of charged particles in the galactic turbulent magnetic field, I calculated the residence times of cosmic rays in the galactic disk by solving one dimensional advective–diffusion equation. Consequently, this simple model predicts the all–particle and the component spectra, the chemical composition, and the anisotropy, with assuming the natural values of the parameters for the equations such as the magnetic field strength and the galactic wind velocity.

Contents

List of Figures

List of Tables

Chapter 1

Introduction

The study of high energy cosmic ray particles and radiations is great interest in astrophysics. Cosmic rays are believed to be concerned with the most energetic phenomena in the Galaxy and the universe. The bulk of cosmic rays are nuclei, and the primary energies of observed cosmic rays range up to $\sim 10^{20}$ eV. The origin of cosmic rays remains a mystery, however, there is general agreement that cosmic ray sources are located in our Galaxy at least for cosmic rays with energies below 10^{14} eV. Supernovae and neutron stars are eminently promising as potential cosmic ray sources. The goal of cosmic ray physics is to clarify the cosmic ray origin and the properties of the acceleration mechanisms, and those of the propagation in the Galaxy.

The origin of primary cosmic rays with energies above 10^{14} eV is still unknown. In order to solve this mystery, we must obtain at least three accurate pieces of information on primary cosmic rays, that is, pieces are the energy spectrum, the anisotropy in the distribution of arrival directions, and the primary chemical composition of cosmic rays. Many groups have reported on the isotropy in arrival directions of cosmic rays. There is not any special regions nor astronomical objects that emit cosmic rays intensely. Direct observations by balloon-borne experiments on the energy spectrum and on the chemical composition have been performed because balloon-borne experiments are efficient in the energy range below 10^{14} eV. Above 10^{14} eV, the steep falling spectrum requires large detection area or long exposure times. A large detection area can be realized with observations of extensive air showers(EASs) with ground-based detector arrays.

The energy spectrum of cosmic rays is well represented by a power law function of the primary energy, and one of the significant features on the spectrum is a steepening around 10^{15} eV, which is called the *knee*. The knee must be deeply related to the acceleration mechanisms of cosmic rays and/or to the propagation mechanisms of primary cosmic rays in the Galaxy.

In order to overcome the difficulty in the acceleration limit $E_{max} \sim 10^{14}$ eV for proton, theorists have proposed many types of models, involving such a mechanism as post–accelerations in supernova remnants [9] after the energy gain by the direct shock acceleration in supernova remnants, or introducing a new source [74], and so on. Each model predicts a somewhat different feature in the composition near the knee. For instance, Axford [9] proposed that the cosmic ray components above the knee are primarily the same as those below the knee, and the energy spectra of the latter with the cutoff at $Z \times E_{max}$ (Z is a charge of a particle) are boosted well over the knee, due to the multiple collisions with large scale shock–waves in the interstellar medium. Therefore the average mass of the primary elements does not change so drastically around the knee. Alternatively, several authors propose that some new components might give

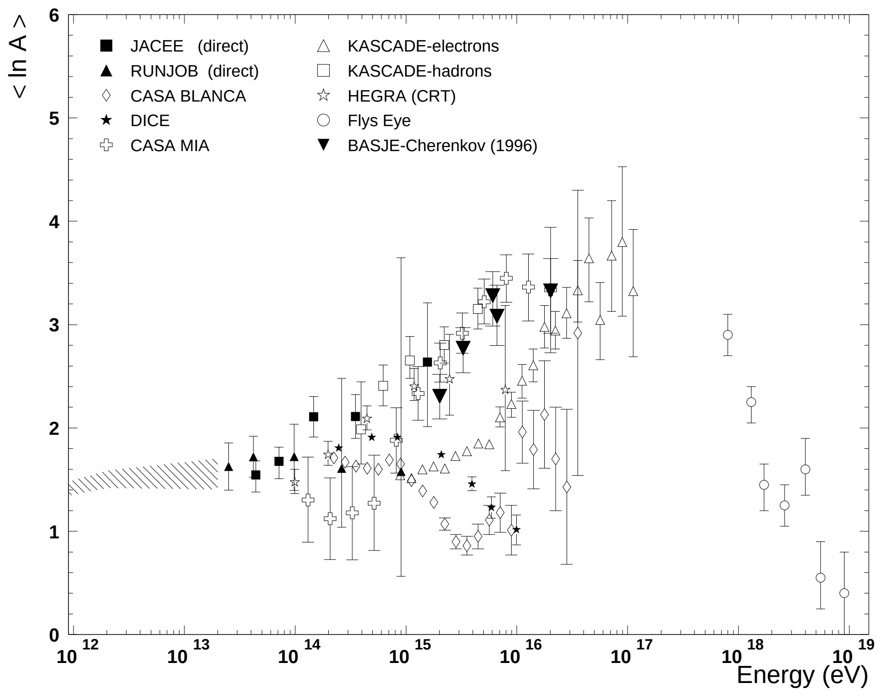

Figure 1.1: The mean logarithmic mass $\langle \ln A \rangle$ measured with balloon–borne detectors [7][8] and ground–based detectors [13][16][25][29][35][88][94], as a function of primary energy. Also the results of our former Čerenkov observations [82] are plotted. A hatched region represents the result of other direct observations, which is accumulated by Linsley [65].

rise to recovery in the energy spectrum above the knee. In this case, we expect the composition changes drastically either into heavier one or into lighter one above the knee.

Therefore, it is of crucial importance to obtain accurate information on the primary chemical composition, because the chemical composition of cosmic rays and its variation with energy reflect the acceleration mechanisms and the compositions at acceleration regions, and reflect propagation mechanisms in the Galaxy. However, although many groups have reported their results as shown in Figure 1.1, these results are contradictory each other and the chemical composition had not been determined definitely.

Unfortunately, the determinations of the energy spectrum and those of the composition from EAS experiments are interdependent and affected by an adopted model of high energy interactions. Hence, for EAS experiments, it is important to observe not only the EAS size at an array altitude, but also the EAS longitudinal development features, because longitudinal development curves reflect the composition as indicated in Figure 1.2. Since one of these methods is a measurement of Čerenkov radiation induced by EAS particles, we observed Čerenkov light pulse shapes for air showers with energies from 10^{15} to $10^{16.5}$ eV. Observations were carried out from 1995 until 1997, and we determined the cosmic ray chemical composition [82]. One of the other approaches to determine the composition is to measure the number of muons and its correlation with air shower sizes. Thus most of the composition measurements are based on the additional observables to the EAS size. Then, unfortunately, the determination of the

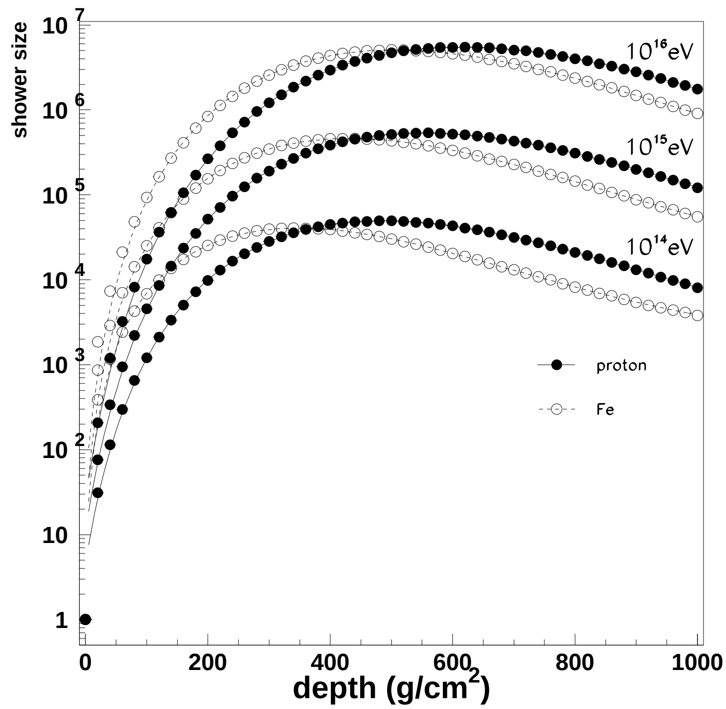

Figure 1.2: Longitudinal development curves for primary proton and iron with the energies 10^{14}, 10^{15} and 10^{16} eV. Each curve is the average of 5000 simulated showers.

chemical composition from EAS experiments is strongly affected by Monte Carlo simulation code, particularly, models of nuclear interactions. This is one of the serious problems.

In the present work, we obtained the equi-intensity curves from the observed EAS size spectra with various incident zenith angles, θ. The equi-intensity method analysis is based only on air shower size spectra. According to Monte–Carlo simulations, using the CORSIKA code [41] with the QGSJET [55] hadronic interaction model, EASs initiated by protons of $10^{15.5}$ eV reach their maximum developments around 590 g/cm^2 atmospheric depths and those initiated by iron nuclei around 450 g/cm^2 atmospheric depth [62]. According to Knapp et al. [62], there are systematic differences between interaction models on the order of 50g/cm^2 for the maximum development point(X_{max}) of protons, and the QGSJET model shows the most rapid development among the major hadronic interaction models [42].

The cosmic ray observatory at Mt. Chacaltaya in Bolivia is located at an atmospheric depth of 550 g/cm^2 so that we can observe EASs initiated by primary protons around the knee region before their maximum developments. Thus, our site is most suitable to investigate the chemical composition of cosmic rays around the knee. We installed an air shower array, which is called "Minimum Air Shower (MAS) array" in this observatory and started the observation of EASs with energies above 6 TeV in 2000 [99].

The measurement of Čerenkov light pulse shape corresponds to observation of the longitudinal developments of air showers at the earlier stages before the maximum developments. In contrast, with the equi-intensity method analysis we determine longitudinal developments around their maximum and at the later stages. Therefore, with two different observations, we can measure the whole stage of EAS longitudinal developments and then we can obtain a trustworthy conclusion on the chemical composition.

The equi–intensity method analysis is based on a single observable value: air shower sizes, and then, in comparison with the other methods for estimation of the chemical composition with the amounts of muon component or Čerenkov photons. Therefore, this method is less dependent on Monte–Carlo simulations.

In the following section I give a brief review of cosmic ray physics and unresolved problems in it. Chapter 3 is a brief review of the accelerations and the propagation of cosmic rays with energies below 10^{14} eV, and is a review of some proposed models of the accelerations of cosmic rays with energies greater than 10^{14} eV. In Chapter 4, I describe general properties of air shower phenomena produced by cosmic rays incident to the atmosphere and techniques for their detections. Before a detailed description of our air shower array, we give a brief review of the other cosmic ray instruments in Chapter 5. In Chapter 6 and 7 , I briefly describe details of the experimental apparatus, the analysis procedure and the performance of the array. In Chapter 8, with the classifications of the selected EASs into corresponding $\sec\theta$ bins, we obtain EAS size spectra for different $\sec\theta$ bins, and derive EAS longitudinal development curves with the equi–intensity method. Moreover we examine the primary chemical composition with comparing the observed EAS longitudinal development curves with those calculated, and then derive the energy spectrum of primary cosmic rays. Chapter 9 is discussions on our result about systematic uncertainty, and comparisons between our results and the expectations with acceleration and propagation models. Finally the present work is summarized in Chapter 10.

Chapter 2

Cosmic rays: overview

Cosmic ray particles hit the earth's atmosphere at a rate of about 1000 per square meter per second. They are primarily composed of ionized nuclei; about 90 % protons, 9 % alpha particles and the rest heavier nuclei. The flux of cosmic ray electrons is about 1 % of the proton flux. High energy gamma rays are also observed at the Earth, but their flux does not exceeds 10^{-3} compared to that of nuclear components. Most cosmic rays are relativistic, and a very few of them have ultra relativistic energies extending at least to 10^{20} eV.

A fundamental mystery of cosmic ray physics is their origins and acceleration mechanisms of them. The answer to the question of the origin of cosmic rays is not yet known well. However, it is clear that nearly all of them come from the outside of the solar system, but from the inside of the Galaxy, because we know an anti–correlation between the solar activity and the flux of cosmic rays at energies less than 100 GeV; they are more effectively excluded from the solar neighborhood during the periods when expanding magnetized plasma from the sun – the solar wind – is most intense. In contrast, ultra high energy cosmic rays with energies above $\sim 10^{18}$ eV may be of extra-galactic origin, because the gyro-radius of these cosmic rays in the galactic magnetic field is equivalent to the galactic disk thickness, $\simeq 300$ pc.

2.1 Energy spectrum

Figure 2.1 is the cosmic ray energy spectrum over a very wide energy range [92]. This is fitted well with an inverse power law function, and a formula of the differential flux is represented by

$$\frac{dN}{dE} \propto E^{-\gamma} \tag{2.1}$$

The spectrum continues at least up to 10^{20} eV with a roughly constant index $\gamma \simeq 2.8$. However we can see slight bends around 10^{15} eV and 10^{19} eV. These are called *knee* and *ankle*, respectively, using analogy with a human leg.

In some theories, the knee is considered to reflect propagation nature of cosmic rays in the Galaxy. The Larmor radius of a particle with an energy of 10^{16} eV and with the charge Z is $\sim 3(1/Z)$ pc in the galactic magnetic field, and this radius is equivalent to a typical size of a magnetic field turbulence in the galactic disk. Therefore, above the energy of the knee the leakage of cosmic rays from the Galaxy may become faster with increasing primary energies. In other theories, the knee is considered to reflect the size and the magnetic filed strength of sources of cosmic rays. However, we expect the maximum energy of cosmic rays accelerated

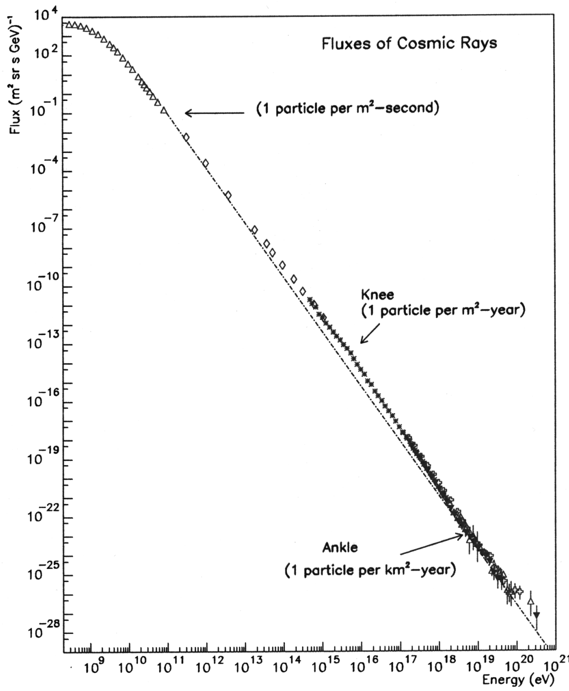

Figure 2.1: The cosmic ray energy spectrum over a very wide energy range.

with a typical supernova remnant to be $\sim 10^{14} \times Z$ eV. Although many detailed studies of the knee are carried out, there are many possible interpretations of the knee with including leakages from the galactic disk, with energy limits of the acceleration mechanism or with new additional components.

The ankle is interpreted as the point of the intersection of the galactic cosmic ray spectrum with the extra-galactic one. The Larmor radius of cosmic rays with an energy E in the Galaxy is calculated to be $\sim 3(E/10^{19}\text{eV})(1/Z)$ kpc, thus cosmic rays propagate more freely, and the deflection angle is less than one radian. Therefore, when we assume that these cosmic rays are accelerated in galactic sources, we expect a very strong cosmic ray anisotropy(the anisotropy amplitude is ~ 100 %) with a single source. However, measured anisotropy amplitudes are small above the ankle and this naturally leads that extra-galactic origins are dominant.

2.2 Chemical composition

The relative abundance of nuclear elements in cosmic rays provides important information to solve the problem of origins and the acceleration sites of cosmic rays. A comparison of the elemental abundance of the low energy cosmic rays($E \sim 10^{10}$ eV) and that of the solar system is shown in Figure 2.2 [30]. There are two striking differences between two compositions. First, nuclei with $Z > 1$ are much more abundant relative to protons in cosmic rays than those in the solar system material. This is not explained clearly, but it could reflect genuine difference in composition at the source or the fact that hydrogens are relatively hard to be ionized for injection into the acceleration process

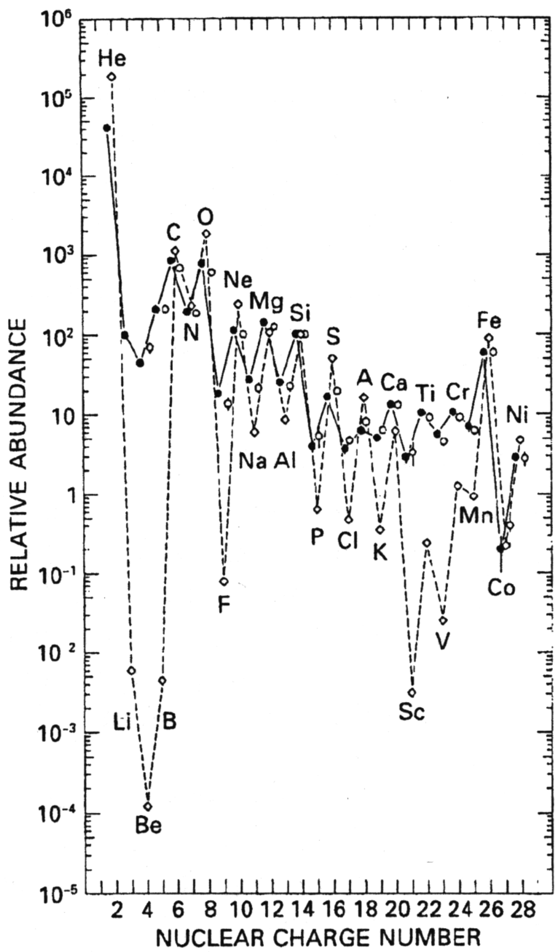

Figure 2.2: The cosmic ray elemental abundances($\sim 10^{10}$ eV) measured at the earth are compared with the solar system abundances(all is relative to silicon).

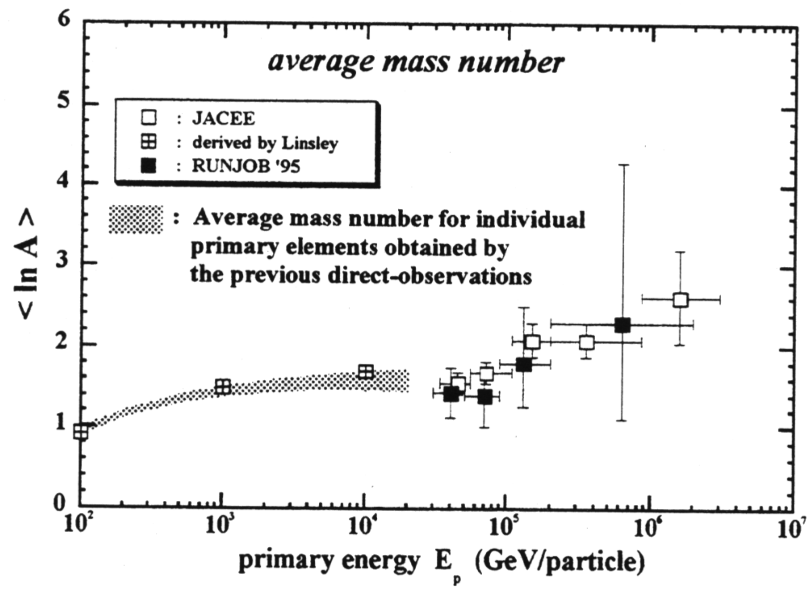

Figure 2.3: Cosmic ray chemical composition below the knee measured with the balloon–borne instruments.

Second, the two groups of elements Li, Be, B and Sc, Ti, V, Cr, Mn are many orders of magnitude abundant in cosmic rays than in the solar system material. These elements are essentially absent as the end products of stellar nucleo-synthesis. Li-, Be- and B-nuclei are nevertheless present in cosmic rays as the spallation products of the abundant nuclei: carbons and oxygens. In the same way, Sc-, Ti-, V-, Cr- and Mn-nuclei are the spallation products of irons; they are produced by collisions of cosmic rays in the interstellar medium. With the cross sections for the spallation, one can calculate total amount of matter traversed by cosmic rays between a source and the Earth. (The details are described in Chapter 3.)

The cosmic ray mass composition around the knee has special importance. Although the origin of the knee is a question in controversy, the escape probability from the Galaxy and from the acceleration region depends on the magnetic rigidity of a particle, p/Z, where p is the momentum and Z is the charge of the particle. Accordingly the abundances of cosmic ray nuclei as a function of energy reflect the properties of the cosmic ray propagation and their acceleration. Figure 2.3 [7] shows the cosmic ray composition below the knee measured by the balloon–borne instruments. We can see the average mass of the cosmic rays increases with increasing energy toward the knee. This supports the picture of the rigidity dependent propagation and the acceleration.

For ultra high energy cosmic ray measurements, a depth of a shower maximum in the atmosphere(X_{max}) which is sensitive to mass of a primary particle is one of important observables to study the chemical composition. The studies of X_{max} by Fly's Eye suggested gradual change of the chemical composition from the heavy components to light ones around $10^{18.5}$ eV. If this is true, it is a strong evidence for the cross over from galactic components to an extra-galactic ones.

Chapter 3

Propagation and acceleration of cosmic rays

Cosmic rays with energies from 1 to 10^5GeV are considered to be accelerated at supernova shocks, and to propagate diffusively in the turbulent magnetic fields in the Galaxy. Some of the main aspects of diffusive propagations and shock accelerations are summarized in section 3.1 and 3.2. The descriptions in these sections are based on text books by Gaisser [30] and by Longair [67], and on reviews by Cesarsky [20][21] and by Wefel [97]. Moreover, in the section 3.3 and 3.4, I will discuss some possible scenarios for accelerations and propagations of cosmic rays with $E > 10^{14}$ eV.

3.1 Propagation

Measurements of the chemical composition of cosmic rays below $\sim$ 1GeV/nucleon lead the fact that two groups of elements Li, Be, B and Sc, Ti, V, Cr, Mn are more abundant in the cosmic radiation by many orders of magnitude than in solar system. These nuclei are almost absent as the end products of stellar nucleo-synthesis. They are readily produced in cosmic radiation as the spallation products of the abundant "primary" nuclei such as C, O and Fe. Measurements of the "secondary" to "primary" ratios lead to following conclusions:

1. On average, cosmic rays in the GeV range traverse $5 \sim 10\text{g/cm}^2$ equivalent of hydrogen between the injection and the observation. This suggests that cosmic rays travel thousands of times as much distances as the thickness of the galactic disk during their lifetimes, because the amount of matter along a line of sight through the disk of the Galaxy is about 10^{-3}g/cm^2.

2. The effective grammage decreases with the increasing energy, at least as far as observations extend, as illustrated in Figure 3.1. This fact suggests that higher energy cosmic rays spend less times in the Galaxy, and cosmic rays are accelerated before the propagations.

The propagation of cosmic rays is described by a transport equation written by

$$\frac{\partial N}{\partial t} = \nabla\left(D_i \nabla N_i\right) - \frac{\partial}{\partial E}\left[b_i(E) N_i(E)\right] - \nabla \mathbf{u} N_i(E) + Q_i(E,t) - p_i N_i + \frac{v\rho}{m}\sum_{k\geq i}\int \frac{d\sigma_{i,k}(E,E')}{dE'} N_k(E') dE' \tag{3.1}$$

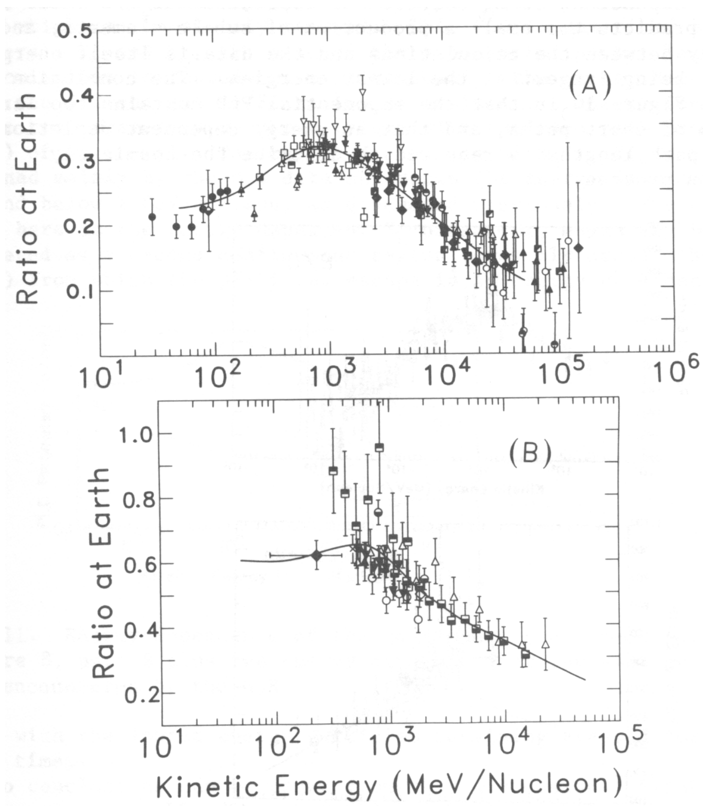

Figure 3.1: Compiled data observed at the earth for (A) the B/C ratio and (B) the sub–Fe/Fe ratio as a function of the energy(see Garcia–Munoz et al.,1984 [32] for references to the experimental data.)

where $N_i(E)dE$ is the density of particles of type i at position $\mathbf{x}$ with the energy between E and $E + dE$. The first term on the right-hand side represents the diffusion, and the diffusion coefficient can be interpreted as

$$D = \frac{1}{3}\lambda_D v \tag{3.2}$$

where v is a particle velocity and λ_D is a diffusion mean free path. With $b_i(E) \equiv dE/dt$, the second term represents energy loss. The third term represents a convection with velocity $\mathbf{u}$. The source term is $Q_i(E, \mathbf{x}, t)$ of the particle input of type i per cubic centimeter at position $\mathbf{x}$ and time t with energies E to $E + dE$. The fifth term represents losses of nuclei of type i by collisions and the decay, with

$$p_i = \frac{v\rho\sigma_i}{m} + \frac{1}{\gamma\tau_i} = \frac{v\rho}{\lambda_i} + \frac{1}{\gamma\tau_i} \tag{3.3}$$

where $\gamma\tau_i$ is a Lorentz dilated lifetime of the nucleus. Finally, the last term is a cascade term, written here to include both feed–down from higher energy as in a nuclear cascade, and nuclear fragmentation processes.

3.1.1 Leaky box model

The cosmic rays seem to propagate freely in a containment volume, with a constant probability per unit time of escape, $\tau_{esc} \ll c/h$, here h is the half thickness of the galactic disk. In this model, the diffusion term is replaced by $-N/\tau_{esc}$. With the absence of collisions and other energy changing process and without convection, the solution for a delta function source, $Q(E,t) = N_0(E)\delta(t)$, is

$$N(E,t) = N_0(E,t)\exp(-t/\tau_{esc}) \tag{3.4}$$

Thus τ_{esc} is interpreted as the mean time spent by the cosmic rays in a confinement volume and $\lambda_{esc} \equiv \rho\beta c\tau_{esc}$ is the mean amount of the matter traversed by a particle of velocity βc. In the case of neglecting energy gains and losses and convection, and in equilibrium, the function (3.1) is simplified to

$$\frac{N_i(E)}{\tau_{esc}(E)} = Q_i(E) - \left(\frac{\beta c\rho}{\lambda_i} + \frac{1}{\gamma\tau_i}\right) N_i(E) + \frac{\beta c\rho}{m}\sum_{k\geq i}\sigma_{i,k}N_k(E), \tag{3.5}$$

where $\sigma_{i,k}$ is the spallation cross section.

A great deal of data on the chemical composition of low energy galactic cosmic rays was treated within this framework, and the important result is that all the nuclei have the same propagation history, *i.e.* by (3.5) with the single parameter λ_{esc}. Within this model, the energy dependence of the secondary to primary ratios is attributed to the energy dependence of λ_{esc}. Gupta and Webber [37] obtained λ_{esc} as

$$\lambda_{esc}(\mathrm{g\,cm^{-2}}) = \beta c\rho\tau_R = \begin{cases} 10.8\beta & R < 4\mathrm{GV} \\ 10.8\beta\left(\frac{4}{R}\right)^{\delta} & R > 4\mathrm{GV} \end{cases} \tag{3.6}$$

with $\delta \simeq 0.6$, where R is a rigidity in GV. This has an important implication for the source spectrum, $Q_i(E)$. For a primary nucleus for which feed–down from fragmentation of heavier nuclei can be neglected, the solution of (3.5) has the form

$$N_P(E) = \frac{Q_P(E)\tau_{esc}(R)}{1+\lambda_{esc}(R)/\lambda_P} \tag{3.7}$$

where the suffix P represents a primary nucleus.

For protons the interaction length λ_P is $\sim 55\mathrm{g/cm^2}$ and $\lambda_{esc} \ll \lambda_P$ for all energies, so that in this case the denominator of (3.7) is approximated with unity. Thus if the observed spectrum is

$$N(E) \propto E^{-(\gamma+1)}, \tag{3.8}$$

the source spectrum must be

$$Q(E) \propto E^{-(\gamma+1-\delta)}. \tag{3.9}$$

For the observed spectral index $\gamma + 1 \simeq 2.7$, the spectral index at a source is given as ~ 2.1. This value is close to the predicted spectral index with first order Fermi acceleration at a strong shock(See next the section).

The other major constraint on models of the propagation is based on the ratios of unstable to stable isotopes of secondary nuclei. Unstable nuclei with lifetimes comparable to τ_{esc}, such as ^{10}Be and ^{26}Al, can be used as "cosmic ray clocks". For stable secondary nuclei, the solution

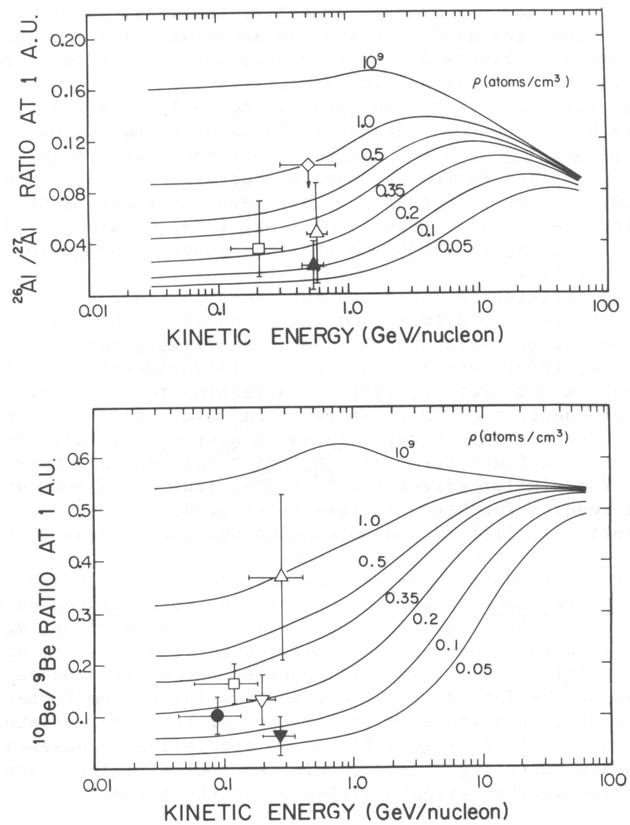

Figure 3.2: Comparison between experimental measurements of the radioactive isotopes ^{26}Al and ^{10}Be and calculated prediction [38]. (see Wefel,1988 [97] for references to the experimental data.)

of (3.5) depends only on λ_{esc} and not on τ_{esc} and ρ. A measurement of the ratio of an unstable to a stable isotope allows for as separate effects of the escape time and the density.

The most well studied example is Be. The isotope ^{10}Be is unstable with $\tau_S \sim 3.9 \times 10^6$ years. Garcia–Munoz, Mason and Simpson [31] found $\tau_{esc} \sim 2 \times 10^7$ years, with rather large uncertainties. This result implies that cosmic rays propagate in a volume of mean density ~ 0.3 protons/cm^3 (Figure 3.2), and therefore, this suggests that the containment volume in the leaky box model is considerably larger than the disk of the Galaxy, and perhaps extends into the galactic halo.

3.2 Acceleration of cosmic rays below 10^{14}eV

Supernova(SN) blast waves are considered as the major sites for accelerations of cosmic ray particles. In this picture, particles are accelerated diffusively at outer supernova remnant(SNR) shocks which convert available hydrodynamic energy of a SN explosion into ultra-relativistic particles with an overall efficiency of the order of 10%. This picture is generally accepted because: (1) the efficiency is high($\sim$10%), (2) the distribution of cosmic rays in the Galaxy is well explained with the dispersion of shocks and the distributions of SNRs, and (3) this picture leads the similarity between the observed and calculated energy spectra. In this mechanism the maximum energy to which particles can be accelerated is the order of 10^{14}eV.

3.2.1 Power

The local energy density of cosmic rays is $\rho_E \simeq 1\text{eV/cm}^3$. If this values is typical throughout the galactic disk, the power required to supply all the galactic cosmic rays is

$$L_{CR} = \frac{V_D \rho_E}{\tau_R} \sim 5 \times 10^{40} \text{ergs}\,\text{s}^{-1} \tag{3.10}$$

where the volume of the galactic disk, V_D is

$$V_D = \pi R^2 d \sim \pi (15\text{kpc})^2 (200\text{pc}) \sim 4 \times 10^{66} \text{cm}^3 \tag{3.11}$$

and where τ_R is the residence time of cosmic rays in the galactic disk. The correct estimate of the residence time is $\tau_R \sim 6 \times 10^6$ years by the leaky box model. Supernovae are the most plausible sources to supply the required power for galactic cosmic rays, because the averaged power released in the Galaxy with supernovae is

$$L_{SN} \sim 3 \times 10^{42} \text{ergs}\,\text{s}^{-1}. \tag{3.12}$$

when we assumed a type II supernova occurs in every 30 years, and it ejects 10 $M_\odot$ with a velocity $\sim 5 \times 10^8$ cm/s. There are large uncertainties in these numbers, but it is plausible that an efficiency of a few percent would be enough for SN blast waves to energize all the galactic cosmic rays.

3.2.2 First order Fermi acceleration at supernova blast waves

The Fermi mechanism was first proposed by Fermi in 1949 as a stochastic means by which particles colliding with clouds in the interstellar medium could be accelerated to high energy. Here we consider the mechanism in rather simpler fashion, that is, the particle accelerations in strong shocks. If an energy gain per encounter is proportional to the primary energy, $\Delta E = \xi E$. After n times encounters the energy $E_n = E_0(1+\xi)^n$, where E_0 is an energy at injection into the accelerator. Then, the number of encounters needed to reach energy E is,

$$n = \ln\left(\frac{E}{E_0}\right) / \ln(1+\xi)\,. \tag{3.13}$$

Thus, if the escape probability from the acceleration region per encounter is P_{esc} , the proportion of the particles accelerated to energies greater than E is

$$N(>E) \propto \sum_{m=n}^{\infty} (1-P_{esc})^m = \frac{(1-P_{esc})^n}{P_{esc}} = \frac{1}{P_{esc}} \left(\frac{E}{E_0}\right)^{-\gamma}, \tag{3.14}$$

with

$$\gamma = \ln\left(\frac{1}{1-P_{esc}}\right) / \ln(1+\xi) \simeq \frac{P_{esc}}{\xi} = \frac{1}{\xi} \times \frac{T_{cycle}}{T_{esc}} \tag{3.15}$$

where T_{cycle} and T_{esc} are the characteristic time for an acceleration cycle and that for an escape from the acceleration region, respectively. The ratio of these two times is P_{esc}. It is noticed that the Fermi mechanism leads to the desired power law spectrum.

The diffusion of charged particles in the turbulent magnetic fields physically carried along with moving plasma is a mechanism for energy gains and losses. Here we consider a physical situation illustrated in Figure 3.3. In this situation, a large plane shock front moves with velocity $-U_1$, the shocked gas flows away from the shock with a velocity U_2 relative to the shock front, and $|U_2| < |U_1|$. Thus in the laboratory frame the gas behind the shock moves to left with

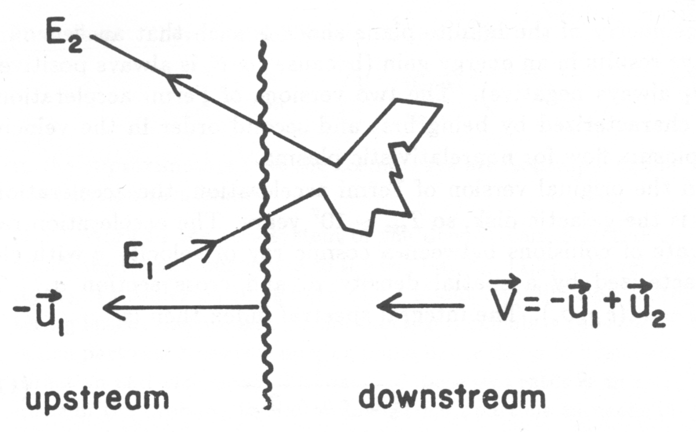

Figure 3.3: Acceleration at the plane shock front.

velocity $V = -U_1 + U_2$. Here we consider a particle with energy E_1, it goes into the shocked gas where the particle begins to diffuse by scattering on irregularities of the magnetic fields. In the rest frame of the moving gas the particle has a total energy,

$$E'_1 = \gamma E_1(1 - \beta \cos\theta_1) \tag{3.16}$$

where γ and $\beta \equiv V/c$ are the Lorentz factor and the velocity of the cloud, respectively, and the primes denote quantities measured in a frame moving with the shocked gas. All the scatterings inside the cloud are the motions of the particles in the magnetic field and are therefore elastic. Thus, the energy of the particle in the moving frame just before escapes is $E'_2 = E'_1$. Thus, the energy of the particle after its encounter is given as

$$E_2 = \gamma E'_2(1 + \beta \cos\theta'_2). \tag{3.17}$$

Substituting (3.16) into (3.17), the energy change for the particular encounter is given by

$$\frac{\Delta E}{E_1} = \frac{1 - \beta\cos\theta_1 + \beta\cos\theta'_2 - \beta^2\cos\theta\theta_1\cos\theta'_2}{1-\beta^2} - 1 \tag{3.18}$$

Averaging over $\cos\theta'_2$ and $\cos\theta_1$ gives the average fractional energy gain per encounter, ξ. An "encounter" is one pair of back and forth across the shock. The distribution of $\cos\theta'_2$ is

$$\frac{dn}{d\cos\theta'_2} = 2\cos\theta'_2, \quad 0 \leq \cos\theta'_2 \leq 1 \tag{3.19}$$

and $\langle \cos\theta_2' \rangle = 2/3$. The distribution of $\cos\theta_1$ for the plane shock is again the projection of an isotropic flux onto the plane, but this time with $-1 \le \cos\theta_2' \le 0$, so that $\langle \cos\theta_2' \rangle = -2/3$. Thus

$$\xi = \frac{1 + \frac{4}{3}\beta + \frac{4}{9}\beta^2}{1-\beta^2} - 1 \sim \frac{4}{3}\beta = \frac{4}{3}\frac{U_1 - U_2}{c} \tag{3.20}$$

For the configuration of a large and plane shock, the rate of encounters is given by the projection of an isotropic cosmic ray flux onto the plane shock front, that is

$$\int_0^1 d\cos\theta \int_0^{2\pi} d\phi \frac{c\rho_{CR}}{4\pi} = \frac{c\rho_{CR}}{4} \tag{3.21}$$

where ρ_{CR} is a number density of particles undergoing acceleration. The rate of convection downstream away from the shock front is $\rho_{CR} \times U_2$, thus the escape probability is given by

$$P_{esc} = \frac{\rho_{CR} U_2}{c\rho_{CR}/4} = \frac{4U_2}{c} \tag{3.22}$$

Thus the integral spectral index is

$$\gamma = \frac{P_{esc}}{\xi} = \frac{3}{U_1/U_2 - 1} \tag{3.23}$$

It is noteworthy that the spectral index is independent of the absolute magnitude of velocities of plasma, and that it depends only on the ratio of an upstream velocity to downstream one. The continuity of mass flow across the shock ($\rho_1 U_1 = \rho_2 U_2$) together with the kinetic theory of gases gives

$$\frac{U_1}{U_2} = \frac{\rho_2}{\rho_1} = \frac{(c_p/c_v + 1)M^2}{(c_p/c_v - 1)M^2 + 2}. \tag{3.24}$$

For a monoatomic gas the ratio of specific heats is $c_p/c_v = 5/3$, thus for a strong shock with $M \gg 1$,

$$\gamma \simeq 1 + \frac{4}{M^2}. \tag{3.25}$$

Not only the spectral index for the first order Fermi acceleration is universal, but it has a numerical value close to what is needed to describe the observed cosmic ray spectrum.

The finite lifetime of a supernova blast wave as a strong shock also limits the maximum energy per particle that can be achieved with this mechanism. The acceleration rate is

$$\frac{dE}{dt} = \frac{\xi E}{T_{cycle}} \tag{3.26}$$

with the fractional energy gain per encounter, ξ. To integrate (3.26) and to estimate E_{max}, it is necessary to know the cycle time for one back and forth across the shock. This value can be estimated with considering the number density distribution in the up and down stream regions. The particle current with convection is given by

$$\mathbf{J} = -D\nabla N + \mathbf{U}N. \tag{3.27}$$

In the upstream region, the fluid velocity $\mathbf{U_1}$ is negative relative to the shock front in equilibrium, and there is no net current, and

$$\kappa_1 \frac{dN}{dz} = -U_1 N. \tag{3.28}$$

Then in the upstream region

$$N(z) = \rho_{CR} \exp\left(-zU_1/\kappa_1\right), \tag{3.29}$$

where ρ_{CR} is the number density of cosmic rays at the shock. Therefore, the total number of particles per unit area in the upstream region is $\rho_{CR}\kappa_1/U_1$. The rate of encounter is $c\rho_{CR}/4$, thus the mean residence time of a particle in the upstream region is given by

$$\left(\frac{\rho_{CR}\kappa_1}{U_1}\right)\left(\frac{c\rho_{CR}}{4}\right)^{-1} = \frac{4\kappa_1}{cU_1} \tag{3.30}$$

In the down stream region, this form is identical to that in the upstream region. Thus

$$T_{cycle} = \frac{4}{c}\left(\frac{\kappa_1}{U_1} + \frac{\kappa_2}{U_2}\right). \tag{3.31}$$

The minimum diffusion coefficient gives a maximum possible acceleration rate and hence an upper limit to the energy accessible for an accelerator. The minimum diffusion coefficient is

$$\kappa_{min} = \frac{r_g c}{3} \sim \frac{1}{3}\frac{Ec}{ZeB}, \tag{3.32}$$

where r_g is the Larmor radius of a particle, $r_g = pc/ZeB$, so that $T_{cycle} \geq 20E/(3U_1ZeB)$ for a strong shock with $U_2 = U_1/4$. The resulting estimate of the maximum energy is

$$E_{max} \leq \frac{3}{20}\frac{U_1}{c} ZeBU_1T_{SN} \tag{3.33}$$

where T_{SN} is the lifetime of an accelerator. The value of T_{SN} is estimated as the time when a supernova has swept up its own mass, so that obtained from

$$\frac{4}{3}\pi(U_1T_{SN})^3\rho_{ISM} = M_{ejecta}. \tag{3.34}$$

For $10M_\odot$ ejected at 5×10^8 cm/s into the normal ISM with 1 proton/cm^3, $T_{SN} \sim 1000$ years. With an estimate of $B \sim 3\ \mu$G in ISM (3.33) gives

$$E_{max} \leq Z \times 3 \times 10^{13}\text{eV}. \tag{3.35}$$

Consequently, the diffusive shock acceleration by supernova shocks appears to be the mechanism for the acceleration of the bulk of cosmic rays, but seems to be limited to energies below $\sim 10^{14}$eV.

3.3 Acceleration of cosmic rays above 10^{14}eV

The simplest set of assumptions for the particle acceleration at supernova blast waves gives a very good explanation for origins of the bulk of cosmic rays. But it leaves open the origin of those with energies greater than 10^{14} eV, although cosmic rays with energies up to 10^{20} eV are observed with air shower experiments.

From (3.33) it is clear that the shock mechanism itself can achieve higher energy per particle if the magnetic field is increased or if the time–scale for acceleration is increased. In this section, we consider some of the possible scenarios for acceleration mechanisms of very high energy cosmic rays.

3.3.1 Acceleration of cosmic rays in a supernova shock which travels down a stellar wind

Biermann [14] proposed a model that energetic cosmic ray particles are accelerated up to 3×10^{18}eV in supernova shocks that travel down the density gradient of stellar winds. He assumed a stellar wind which has the standard Parker spiral magnetic–field structure,

$$(B_r, B_\phi) = B_s \left(\frac{r_s^2}{r^2}, -\frac{r_s^2}{r_W r}(1-\mu^2)^{1/2} \right). \tag{3.36}$$

Here B_s is the surface radial magnetic field of a star, r is the distance from the star, r_s is the surface radius of the star, and $r_W = v_W/\Omega_s$ where v_W and Ω_s are the wind velocity and the angular rotation rate of the star, respectively. Völk and Biermann [95] have argued that if the radial diffusion coefficient increases linearly with r, the adiabatic loss time and the acceleration time in the first order Fermi theory have the same radial dependence leading to the preservation of the highest energy reached by particles until the shocks run into the stellar wind termination shell. Biermann [14] estimated a maximum accelerated energy of

$$E_{max} = \frac{U_2}{u_1} ZerB_2 = ZerB_1. \tag{3.37}$$

Here $U_{1,2}$ and $B_{1,2}$ are the velocity and the magnetic field strength on the both sides of the shock, and Ze is the particle charge. With the assumption that the product Br has the same value on the surface as that in the wind, and is of order 3×10^{14}cm Gauss for any OB stars and any Wolf–Reyet stars, a maximum energy of particles is inferred of

$$E_{max}(protons) = 9 \times 10^{16}\text{eV} \tag{3.38}$$

and

$$E_{max}(irons) = 3 \times 10^{18}\text{eV}. \tag{3.39}$$

In this model, there are two critical postulates for radial diffusion based on the observational evidence. The first critical assumption is that the convective random walk of energetic particles perpendicular to the magnetic field can be described by a diffusive process with a downstream diffusion coefficient $\kappa_{rr,2}$ which is given by the thickness of the shocked layer and the velocity difference across the shock, and which is independent of energy:

$$\kappa_{rr,2} = \frac{1}{3}\frac{U_2}{U_1} r(U_1 - U_2). \tag{3.40}$$

The upstream diffusion coefficient can be derived in a similar way with the second assumption that the upstream length scale is just U_1/U_2 times larger, *i.e.*, r. Then the upstream diffusion coefficient is

$$\kappa_{rr,1} = \frac{1}{3} r (U_1 - U_2). \tag{3.41}$$

The energy gain due to the Lorentz transformations in one cycle of a particle remaining near the shock and cycling back and forth from the upstream to the downstream can be written by

$$\frac{\Delta E}{E} = \frac{4}{3}\frac{U_1}{c}\left(1 - \frac{U_2}{U_1}\right). \tag{3.42}$$

In addition, the energy gain associated with a drift is given by the product of the residence time, the drift velocity and the electric field is obtained as

$$\begin{aligned}
\frac{\Delta E}{E} &= \frac{4}{3}\frac{r}{c}\left(1 - \frac{U_2}{U_1}\right) \cdot V_{d,\theta} \cdot Ze\frac{U_1 B}{c} &(3.43)\\
&= \frac{4}{3}\frac{U_1}{c} f_d \left(1 + \frac{U_2}{U_1}\right)\left(1 - \frac{U_2}{U_1}\right) &(3.44)
\end{aligned}$$

where $f_d = 1/3(1 + U_1/2U_2)$, $f_d = 1$ for strong shocks, and

$$V_{d,\theta} = \frac{1}{3}\left(1 + \frac{U_1}{2U_2}\right)\frac{r_g c}{r}. \tag{3.45}$$

The first term of $V_{d,\theta}$ is due to the gradient term and the second term is due to the curvature which is increased by a lot of convective turbulences by a factor two. This additional energy gain due to a drift changes the particle spectrum by

$$\frac{3U_2}{U_1 - U_2}\left(1 - \frac{1}{x}\right) \tag{3.46}$$

where

$$x = 1 + \frac{1}{3}\left(1 + \frac{U_1}{2U_2}\right)\left(1 + \frac{U_2}{U_1}\right). \tag{3.47}$$

Moreover, the acceleration time of a particle to reach a certain energy E is represented by

$$t(E) = t_0 \left(\frac{E}{E_0}\right)^{\beta} \tag{3.48}$$

with

$$\beta = \frac{3U_2}{U_1 - U_2}\frac{2}{x}\frac{\kappa_{rr,1}}{rU_1}. \tag{3.49}$$

The particles injection rate is proportional to r^b. This leads to a correction factor for the abundance of $(E/E_0)^{-b\beta}$. However, in a d–dimensional space, particles have r^d more space available to them than when they were injected. Thus this leads another correction factor which is $(E/E_0)^{-d\beta}$. The combined effect of these two correction factors is a spectral change by

$$-\frac{3U_1}{U_1 - U_2}\frac{2}{x}(d + b)\frac{\kappa_{rr,1}}{rU_1}. \tag{3.50}$$

Hence the total spectral difference, as compared with the plane–parallel shock acceleration, is given with taking the minus sign by

$$\frac{3U_1}{U_1 - U_2}\left(\frac{U_2}{U_1}\left(\frac{1}{x} - 1\right) + \frac{2}{x}(d+b)\frac{\kappa_{rr,1}}{rU_1}\right). \tag{3.51}$$

For stellar winds we have $b = -2$ and $d = +3$, and so $b + d = 1$. Since the total spectral change is given by 1/3 for strong shock($U_1/U_2 = 4$), the source spectrum is obtained as

$$Spectrum(source) \propto E^{-7/3}. \tag{3.52}$$

After correction for the leakage from the galaxy, the spectrum at the earth is

$$Spectrum(earth) \propto E^{-8/3}, \tag{3.53}$$

, and it is very close to what is observed near the earth at particle energies below the knee.

In this model, the geometrical arguments lead to the knee energy and the spectrum of the energetic particles beyond the knee. The critical assumption is about the diffusion coefficient in the lateral direction. The characteristic velocities of particles in θ are on average the drift velocity $V_{d,\theta}$, and the characteristic distance is the distance to the symmetry axis $r\sin\theta$. Thus the diffusion coefficient is assumed to be

$$\kappa_{\theta\theta,1} = \frac{1}{3}|V_{d,\theta}|r(1-\mu^2)^{1/2} \tag{3.54}$$

where $\mu = \cos\theta$. On the other hand, an upper limit to the diffusion coefficient in the lateral directions is calculated from the residence time on any side of shock,

$$\frac{4\kappa_{rr,1}}{U_1 c} = \frac{4\kappa_{rr,2}}{U_2 c} = \frac{4}{3}\frac{r}{c}\left(1 - \frac{U_2}{U_1}\right) \tag{3.55}$$

and the maximum velocity difference $U_1 - U_2$, *i.e.*,

$$\kappa_{\theta\theta,max} = \frac{4}{9}\left(1 - \frac{U_2}{U_1}\right)^3\left(\frac{U_1}{c}\right)^2 rc. \tag{3.56}$$

There is a critical energy when $\kappa_{\theta\theta,1}$ reaches the maximum. It is another basic assumption in this model that the latitude drift is dominated by the lateral convective motions induced by the radial convection above the critical energy. Thus the drift energy gain decreases by factor 2/3. The critical energy is given by

$$E_{crit} = \left(\frac{3}{4}\frac{U_1}{c}\right)^2 E_{max}. \tag{3.57}$$

This critical energy corresponds to the knee energy E_{knee}. The reduced energy gain above the knee energy gives $x = 11/6$, and this leads to the overall spectrum at an injection,

$$Spectrum(source) = E^{-29/11} \tag{3.58}$$

and the spectrum is deformed with the diffusive transport through the Galaxy,

$$Spectrum(earth) = E^{-3} \tag{3.59}$$

as observed. The bending points of the component spectra depend on their charge; with the increasing energy the flux of protons drops off at the lowest energy, and that of heavy nuclei does at high energy. Beyond the knee, irons and other heavy nuclei dominate in the high energy galactic cosmic rays.

Stanev et al. [86] presented the all particle spectrum which is composed of following three components:

1. The explosions of normal supernovae into an approximately homogeneous interstellar medium drive blast waves which can accelerate protons to about 10^{14}eV. For these particles the spectral index is near –2.75 with taking account of the leakage from the Galaxy.

2. The explosions of Wolf–Rayet stars into their former stellar winds accelerate iron nuclei up to energies of about 3×10^{18}eV. These particles have the slightly flatter spectra with the index of $-8/3$ up to a rigidity dependent bending in the spectrum, and then beyond the bending point the spectrum has rather steeper spectra with the index of –3 up to the rigidity dependent cutoff energy.

3. The hot spots of radio galaxies produce particles with even higher energies, up to 10^{20}eV. Their spectrum is approximately proportional to E^{-2}.

Using existing data on the chemical composition of cosmic rays near TeV energies as a constraint, they showed the all particle spectrum and various contributions of the different element groups, as shown in Figure 3.4,3.5. Thus, they conclude the followings: a) For the most of energy range above 10^{14}eV the wind explosions can account for both the chemical composition and the spectrum including the knee feature, b) the highest particle energies required from the stellar wind explosions imply a magnetic field in the preexisting stellar wind of at least 3 Gauss at a distance of 10^{14}cm, and c) the chemical abundance above 10^{14}eV is dominated by heavy nuclei such as neon and higher ones.

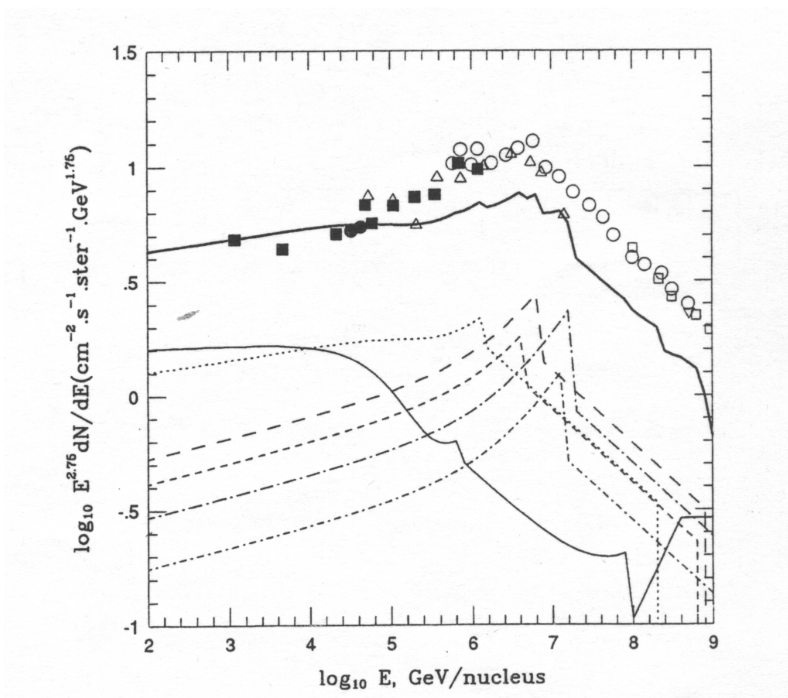

Figure 3.4: The all particle spectrum and the various contributions from the different element groups derived by Stanev et al. [86] are compared with the observational results. Here the symbols denote the following experiments: Akeno(open circles), Haverah park(open squares),Yakutsk(open triangles, pointing down),Tien Shan(open triangles, pointing up), Fly's Eye(open hexagons),Proton 4(full squares), and JACEE(full circles). The contributions of the six element groups are distinguished with the line type: H(solid), He(dots), CNO(dash), Ne–S(long dash), Cl–Mn(dash dot), and Fe(long dash dot).

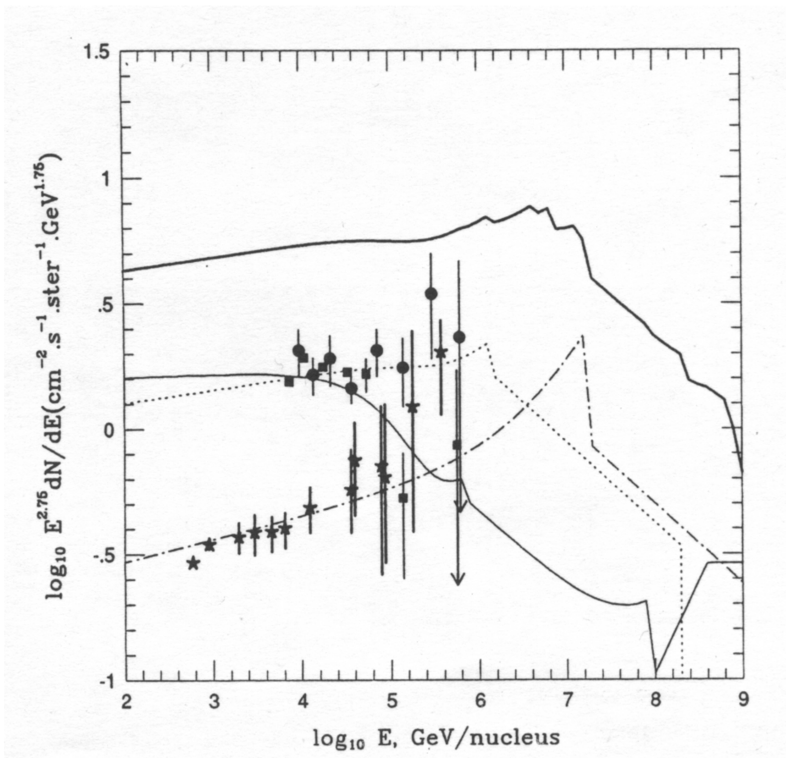

Figure 3.5: A comparison of the measured element abundances with the model calculation for H(full squares), He(full circles), and Fe(full stars).

3.3.2 Reacceleration of cosmic rays in a termination shock of the galactic wind

The observed anomalous component in the cosmic ray flux in the inner solar system with energies of the order of 1–10 MeV is explained with an acceleration model at the termination shock of the solar wind. Jokippi and Morfill [53] suggested that cosmic rays up to 10^{14}eV energy are accelerated by supernova shocks, but that particles with energies of 10^{15}eV and higher are accelerated at the termination shock of the galactic wind in analogy with the solar system. Although the existence of the galactic wind flowing outward from the Galaxy cannot be regarded as established, they estimated the properties of the galactic wind with a simple consideration. They took a supernova energy input rate into the interstellar medium of

$$\dot{E}_{SN} = 10^{42}\mathrm{erg\,s^{-1}} \tag{3.60}$$

and assumed that the energy input rate into the galactic winds is

$$\dot{E}_W = \dot{M}V_W^2/2 = 5 \times 10^{41}\mathrm{erg\,s^{-1}}. \tag{3.61}$$

Moreover, they considered the available time for accelerations at the galactic termination shock is the age of our Galaxy $T_{gal} = 1.5 \times 10^{10}$years, and assumed that the magnetic field strength at the termination shock has the Parker spiral form

$$B = B_0 \left(\frac{R_0}{R_{sh}}\right)^2 \left(1 + \frac{R_{sh}^2 \Omega_{gal}^2}{V_W^2}\right)^{1/2} \tag{3.62}$$

where R_{sh} is the shock radius, B_0 is the magnetic field at the reference radius R_0, and $\Omega_{gal} = 10^{-15}\mathrm{s}^{-1}$ is the galactic rotation rate.

The mass loss rate is estimated as the diffusive galactic matter, $5 \times 10^9 M_\odot$, divided by the life time of the Galaxy, 1.5×10^{10}years, *i.e.*, $\dot{M} = 2 \times 10^{25} \times F\,\mathrm{g\,s^{-1}}$, where F is a scaling parameter. Then, this yields a wind velocity $V_W = 500F$ $\mathrm{km\,s^{-1}}$.

They estimated the maximum rigidity of cosmic rays accelerated at the galactic wind using the time scale for the particle acceleration which is given by

$$t_{acc} = \frac{4\kappa}{V_{sh}^2} \tag{3.63}$$

where κ is the diffusion coefficient and V_{sh} is the shock velocity. If the Bohm diffusion is assumed,

$$\kappa = \frac{1}{3} r_g c \tag{3.64}$$

where r_g is a gyro radius. Thus the maximum rigidity is given by

$$R_{max}(\mathrm{volts}) = \frac{450 T_{gal}}{c} \frac{\dot{E}_W}{\dot{M}F} B_0 \eta^2 \left(1 + \frac{\Omega_{gal}^2 R_0^2 \dot{M} F}{2\dot{E}_W \eta^2}\right) \tag{3.65}$$

where $\eta = R_0/R_{sh}$. In Table 3.3.2 are displayed R_{max} for various η using $R_0 = 10$kpc, $B_0 = 3 \times 10^6$Gauss, and $F = 1$.

η	R_{sh}(kpc)	R_{max}(volts)	E_{Fe}(eV)
0.2	50	7×10^{18}	1.8×10^{20}
0.1	100	3.2×10^{18}	0.8×10^{20}
0.05	200	1.6×10^{18}	0.4×10^{20}
0.02	500	6.4×10^{17}	0.2×10^{20}

Table 3.1: The maximum rigidity and the maximum energy of iron nuclei of cosmic rays accelerated at the galactic wind termination shock.

They argued that particles accelerated at the terminus of the galactic wind will be subject to modulation by the galactic wind in analogy with the solar modulation. The models of solar problem suggest that the cosmic ray intensity behaves roughly as if the particles were decelerated in a potential field equal to the electrostatic potential difference E_{pot} between the heliospheric pole and the equator, which is

$$E_{pot} = q\frac{V_0 B_0}{c} R_0 = \frac{qB_0}{c} \frac{\dot{M}}{2\pi\rho_0 R_0} \tag{3.66}$$

Using the standard values and setting $\rho = 10^{-3} m_p$ yields a value of 10^{15}eV. Here m_p is the mass of a proton. This suggests that cosmic ray particles with energies lower than this value will be significantly modulated by the galactic wind.

They reported [54] a detailed analysis of numerical simulations of this model and represented the expected energy spectra as shown in Figure 3.6.

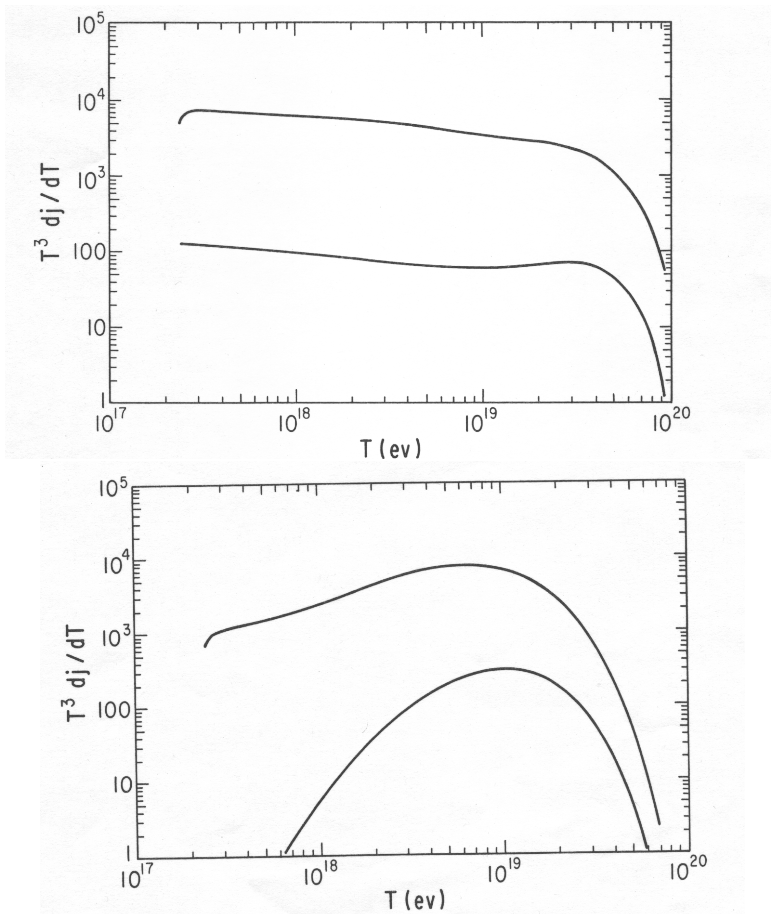

Figure 3.6: (*upper*) Computed energy spectrum of accelerated iron nuclei at the equatorial plane of the galactic wind, at radii of 10 kpc(*lower curve*) and at the shock(*upper curve*). In this case the shock is at 300 kpc, and the outer absorbing boundary is at 600 kpc. The wind velocity is 400 $\mathrm{km\,s^{-1}}$, and the diffusion coefficient is taken to be independent of energy, with a parallel diffusion mean free path of 14 times the local gyro radius of a $10^{20}eV$ particle. The magnetic field is approximated by an Archimedian spiral with a magnitude of 3×10^{-6}Gauss at a radial distance of 10 kpc, and a rotational angular velocity of $2 \times 10^{-15}\mathrm{s}^{-1}$. The particle drift velocity is set equal zero. Injection is continuous, and uniform over the shock, at the energy of 2×10^{17}eV. The spectrum is given at $\sim 7 \times 10^9$ years after the start of acceleration, when the distribution has reached a near steady state. (*lower*) The computed spectrum as in the left figure, except that the mean free path depends on both the energy and position and is 25 times the local gyro radius of the particles at any given energy.

3.3.3 Reacceleration of cosmic rays with multiple shock encounters

Axford [9] discussed about the merits and about the difficulties of different models, and drew the conclusion that accelerations of cosmic ray particles beyond 10^{14}eV might be closely related to the reacceleration of cosmic rays via multiple interactions with large scale structures in the Galaxy, *i.e.*, molecular clouds, SNRs, OB associations and rotating neutron stars, etc, and especially with the associated shock waves. Ip and Axford [51] illustrated the the quantitative aspects of this model taking into account the size frequency distribution of SNRs, the probability distributions of energy gain/loss during the SNR encounters and the compositional abundances of cosmic ray nuclei.

They considered three ways for cosmic rays to interact with SNR. First, in the case that the gyro–radius of a particle is considerably smaller than the size of a SNR and the particle enters the SNR along a magnetic filed line, the energy will be reduced as a result of the adiabatic cooling inside the expanding SNR. Second, if the initial pitch angle is large, particles are reflected at encounters with a shock front, and the energies will be increased. Since these process may be essentially considered to be of the nature of the first order Fermi acceleration, the absolute energy changes in these two types of encounters are on the order of 0.3% at the particle energy $\sim 10^{16}$eV. Finally, if particles encounter the shock with a guiding center impact parameter b within one gyro radius R_g, cosmic ray particles may be temporarily trapped and have the cycloidal motion across the shock front in the direction of the electric field $E = -V \times B$, and gain relatively large energy ($\Delta E/E$ up to 10%) at $10^{15} \sim 10^{16}$eV. This drift acceleration does not operate when R_g reaches comparable to the radius of the SNR. They found the upper energy limit $E_{max} = 3 \times 10^{17}$ eV for protons, and $E_{max} = 3 \times 10^{17} Z$ eV for heavy nuclei. In their calculations they assumed the random encounters to be entirely uncorrelated, the life time of SNR of the Sedov phase to be 2×10^5 years and the random explosion of supernovae in space and time.

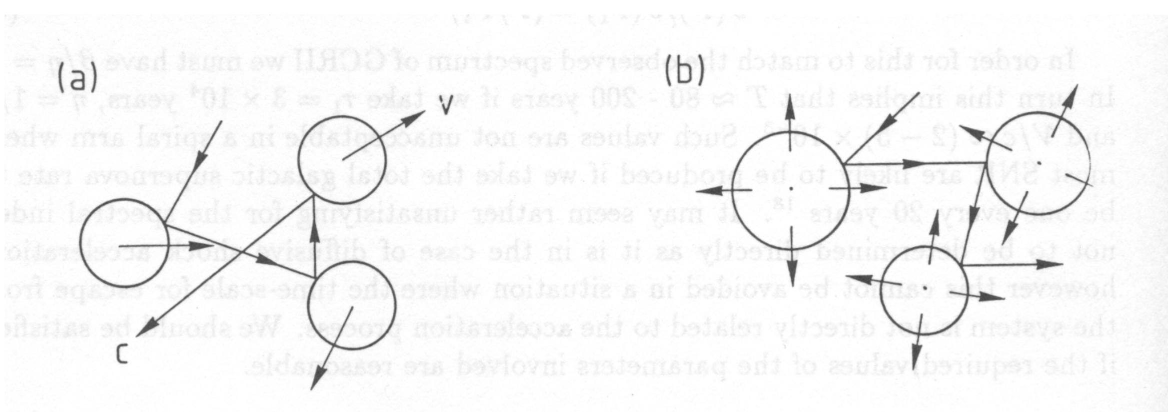

Figure 3.7: The distinction between the multiple encounter acceleration model described in the text(b), and the classical second order Fermi acceleration(a).

The simulated cumulative spectra with an assumued galactic magnetic field of 6μG are shown in Figure 3.8. With their calculations, they concluded that the power law spectral index γ is sensitive to the ratio of the dynamical escape time to the SNR encounter time, *i.e.*, $N_t = t_d/\Delta t$, and they found that a power law with $\gamma = 3$, and N_t is required to be 170 for $B_0 = 10\mu G$, and

300 for $B_0 = 3\mu G$. Although the latter value is generally accepted to be the average value of the magnetic field strength in the galactic disk, the corresponding dynamical time estimated $t_d = N_t \Delta t \simeq 3 \times 10^5$ years for $\Delta t \simeq 10^3$ years is too long. This is a matter of concern in their model.

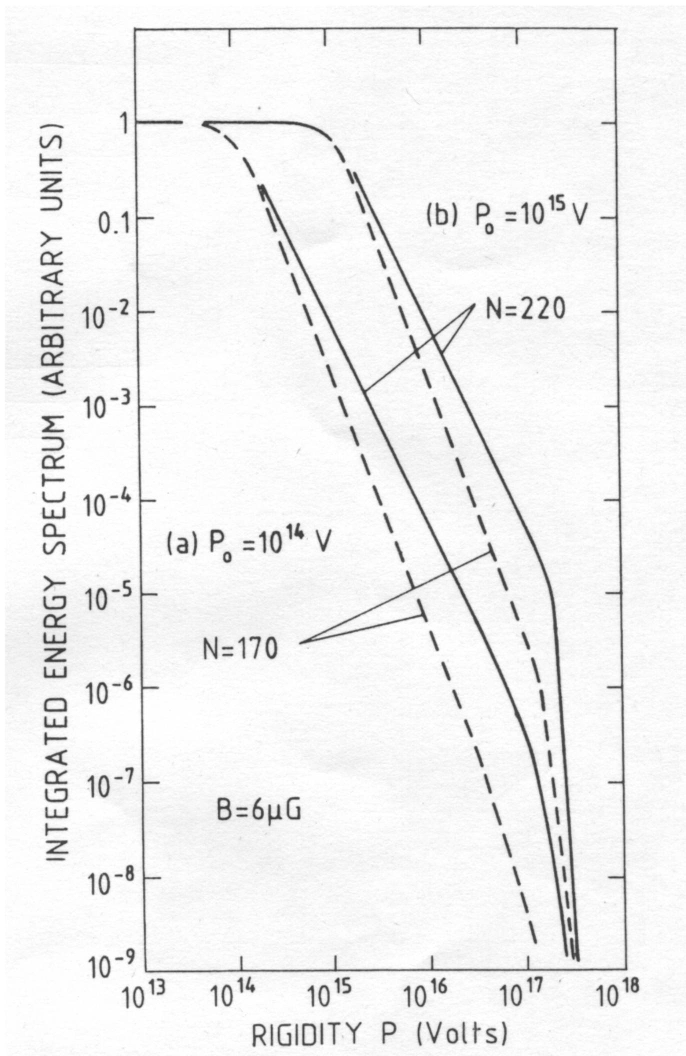

Figure 3.8: The integral energy spectra is derived by using different values of the injection rigidity(P_0) and N_t. The background magnetic field is assumed to be 6μG.

They also lead the resulting synthetic spectrum as shown in Figure 3.9 by assuming injection rigidity P_0 of 10^{14}V and $N_t = 220$. In their discussion, the discrepancy between the theoretical and the observed spectra may be partly resolved by adjusting the relative abundances of the heavy nuclei at the injection energy of 10^{14}eV.

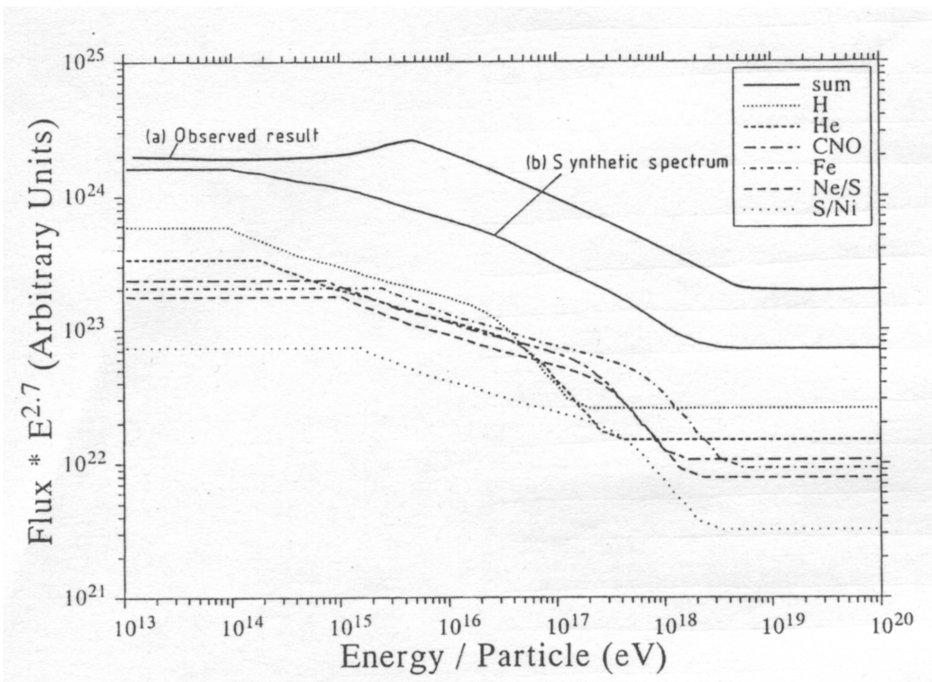

Figure 3.9: A synthetic spectrum of cosmic rays. The input parameters are $P_0 = 10^{14}$eV and $B_0 = 6\mu$G.

3.3.4 Production of cosmic rays in active galactic nuclei

Protheroe and Szabo [74] proposed that a substantial fraction of cosmic rays with energies between 10^{14} and 10^{19}eV may originate in active galactic nuclei(AGN). In this model, protons are accelerated by the first order Fermi process at a shock in an accretion flow onto a super massive black hole, and produce neutrons via the interactions with the photons at the central region of AGN. These secondary neutrons escape from the central region and decay, and thus the resulting protons are observed as cosmic rays with energies above 10^{14}eV.

In order to calculate the accelerations in an AGN central region, the authors assumed three basic properties of AGN: a) Black hole masses to be proportional to the luminosity, $M \simeq x_1(L_C/(10^{38}\mathrm{ergs\,s^{-1}}))M_\odot$, where $x_1 = R/r_S$ is the ratio of the shock radius to the Schwarzschild radius, and L_C is the luminosity for the infrared to hard x–ray continuum, b) An equi–partition between the energy density in the magnetic field and the radiation field at the shock, *i.e.*, $B^2/8\pi = U_{rad} \simeq L_C/\pi R^2 c$ to obtain the magnetic field and hence the gyro radius r_g at the shock, and c) The diffusion coefficient is larger by a factor b than the Bohm diffusion coefficient, *i.e.*,

$$D = b\frac{1}{3}r_g c \simeq 6.1 \times 10^{-21} b x_1^2 L_C^{\frac{1}{2}} E \mathrm{cm^2 s^{-1}} \tag{3.67}$$

at the shock($r = R$) where L_C is measured in $\mathrm{erg\,s^{-1}}$ and E is measured in eV.

For the shock acceleration, the acceleration rate is $dE/dt \simeq u_1^2 E/20D$ where u_1 is the upstream flow velocity. Then the free–fall velocity onto the black hole $u_1 = x_1^{1/2}c$, and this leads an acceleration rate

$$\frac{dE}{dt} \simeq 10^{-26} b^{-1} x_1 L_C^{\frac{1}{2}} U_{rad}\,\mathrm{eV\,s^{-1}} \tag{3.68}$$

where the unit of U_{rad} is $\mathrm{eV\,cm^{-3}}$. Since proton energies reach the maximum when the acceleration rate equals to the total energy loss rate with the pion photo–production and the pair production processes, they estimated the maximum energy E_{max} with a Monte Carlo simulation, $E_{max} \simeq E_0(x_1^2 L_C/b^2 L_0)^\alpha$, where $E_0 = 1.8 \times 10^{16}$eV, $L_0 = 2 \times 10^{46}\mathrm{ergs\,s^{-1}}$, and $\alpha = 0.18$(for $x_1^2 L_C/b^2 L_0 < 1$) or 0.52(for $x_1^2 L_C/b^2 L_0 > 1$).

As a result of the interactions during and after the accelerations, secondary particles which include neutrons are produced. Although the neutrons themselves are subject to the pion-photo production interactions, the some fraction will escape from the central region. The authors found that for the energy range below $\sim 5 \times 10^{16}$eV neutrons traveling radially out from the shock will escape from the intense radiation field of the central region and below 10^{15}eV all neutrons will escape from the central region.

A relativistic neutron escaped from the intense radiation field of the central region will decay on average after traveling a distance $r_0 \sim 2.8 \times 10^4 (E/\mathrm{eV})$cm. The resulting proton will diffuse in the magnetic field which is tied to the accreting plasma. The diffusion coefficient D in the accreting plasma is assumed to be

$$D(E,r) \simeq 1.3 \times 10^{61} b x_1^{-3} L_C^{-2} E r^{\frac{5}{2}} \mathrm{cm^2\,s^{-1}} \tag{3.69}$$

where E is in eV and r in cm, and protons will be trapped for a time $t_{esc} \simeq r^2/2D$. Protons traveling in the accreting plasma will be subject to the *pp* collisions and the collisions with photons. The time scale for the *pp* collisions is given by $t_{pp} \simeq (n\sigma_{pp}c)^{-1}$, where $\sigma_{pp} \simeq 30$mb is the *pp* inelastic cross section, n is the number density of the nuclei in the accretion matter, and obtained by the authors as

$$n(r) \simeq 1.3 \times 10^8 Q(x_1)^{-1} x_1^{\frac{1}{2}} L_C^{\frac{1}{2}} r^{-\frac{3}{2}} \mathrm{cm^{-3}} \tag{3.70}$$

where $Q(x_1) \simeq 1 - 0.1x_1^{0.31}$ is the conversion efficiency of the kinetic energy of in–falling matter to the relativistic particles. The time scale for $p\gamma$ collisions, $t_{p\gamma} = E/(dE/dt)_{p\gamma}$, is estimated with Monte Carlo calculations. Thus, the probability of surviving for a proton is given by

$$P_{surv} \simeq t_{esc}^{-1}/(t_{esc}^{-1} + t_{pp}^{-1} + t_{p\gamma}^{-1}). \tag{3.71}$$

Finally, with an assumption that the 2–10 keV luminosity is proportional to L_C, $L_X \simeq 0.005L_C$, they predicted the cosmic ray spectrum for the Einstein–de Sitter model with a function,

$$\frac{dI_{CR}}{dE} = \frac{1}{4\pi}\frac{c}{H_0}E^{-1}\int_0^{Z_{max}} dz\frac{g(z)}{f(z)}(1+z)^{-\frac{5}{2}}\int dL_X\rho_0\left(\frac{L_X}{f(z)}\right)\frac{dL_{CR}}{dE}((1+z)E, L_X), \tag{3.72}$$

where dL_{CR}/dE is the differential luminosity of the escaping protons, $\rho_0(L_X)\mathrm{cm}^{-3}(\mathrm{ergs\,s^{-1}})^{-1}$ is the local x–ray luminosity function of AGN, and f and g describe the evolution of luminosity and the number density in co-moving coordinate space, respectively. Using the AGN models to describe the luminosity function and its evolution, and refining the estimation of the magnetic field and photon spectrum in the central region and the treatment of the energy loss processes, the authors presented [89] the spectra of produced neutrons, that of protons escaping from an AGN(Figure 3.10), and the predicted cosmic ray spectrum due to acceleration in AGN(Figure 3.11).

With these results, they concluded that:

1. The predicted contribution from AGN to the cosmic ray spectrum is the same order of magnitude as the observed intensity in the region of the knee and the higher energies. Minor adjustment, for example, by increasing the ratio of L_C to L_X by ~ 2 in the assumed AGN continuum, could give better agreement with the observations at 10^{16}eV.

2. If this model is correct, any extra galactic component in the region of the knee will be 100% protons, and then one would expect to observe an enhancement in the relative abundance of protons in the cosmic rays at $\sim 10^{16}$eV.

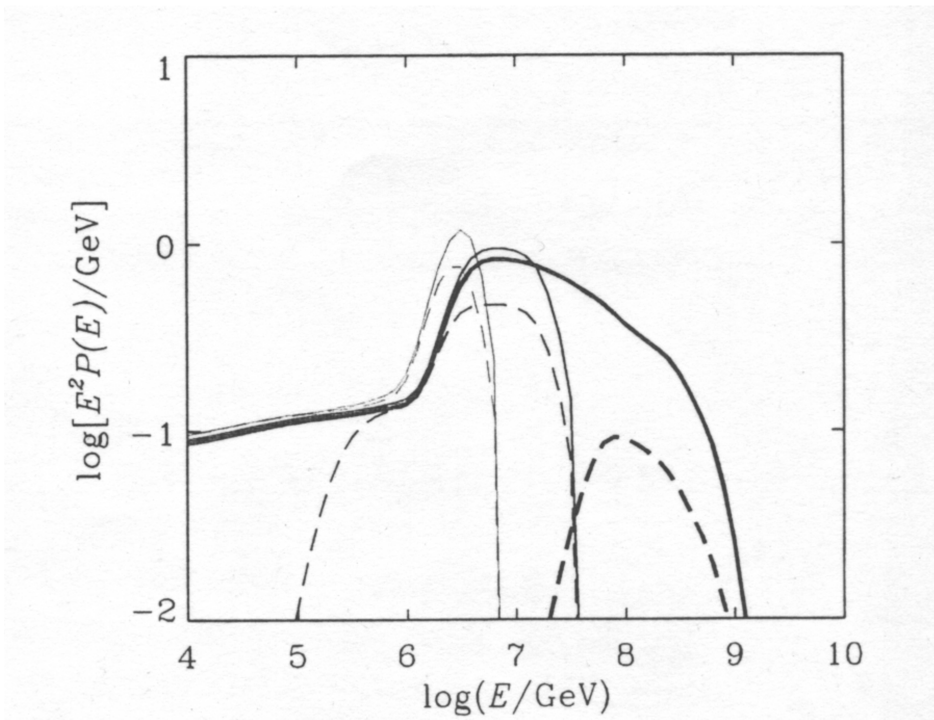

Figure 3.10: Spectra of produced neutron (full curves) and cosmic ray protons escaping from an AGN(dashed curve). Results are given for $b = 10$, $x_1 = 30$, and $L_X = 10^{42}$(left–most curves), 10^{45} and 10^{48}ergs s^{-1}. The reduction at high energies is due to interactions of neutrons with photons during the escape from the central region, while the reduction at low energies is due to interactions of decay protons with protons in the accreting plasma.

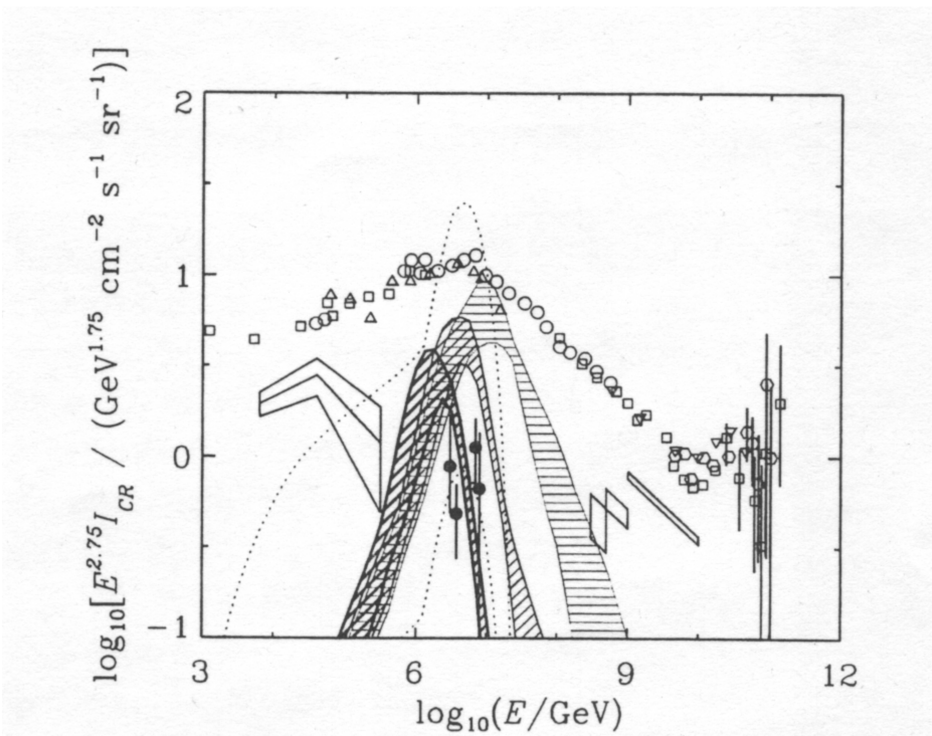

Figure 3.11: The possible contribution of cosmic rays accelerated in AGN to the observed spectrum. Results are shown for $b = 1$(horizontal hatching), $b = 10$(thin oblique hatching) and $b = 100$(thick oblique hatching). The measured total cosmic ray intensity and the proton intensity are also shown in this figure. The dotted line represents a single steady source contribution at 10 Mpc.

3.3.5 Acceleration by oblique shocks at SNRs

Kobayakawa, Sato and Samura [63] explained the knee behavior of the energy spectrum with the acceleration mechanism caused by oblique shocks. They examined that oblique shocks can accelerate particles more efficiently, because the reflections at the shock front are more important and rapid accelerations occur comparing to parallel shocks. Thus the maximum energy E_{max} is raised by a couple of orders compared to those in parallel shocks. E_{max} is mainly limited by the finite lifetime of the supernova blast wave. The effective shock acceleration can occur until the swept up mass reaches to the ejected mass $\sim 10M_{\odot}$. The lifetime of the shock t_{sh} is estimated to be some hundred years for ejecta expanding with the velocity of $\sim 10^8$ cm/s into the medium of the average density, 1 proton/cm^3. Balancing the acceleration time scale with t_{sh}, the authors lead,

$$E_{max} = \frac{R_{sh}(r-1)}{rcx} U_1 e B_1 Z \left[\cos^2\alpha_1 + \frac{\sin^2\alpha_1}{x^2} + \frac{r\left(\cos^2\alpha_1 + \frac{r^2}{x^2}\sin^2\alpha_1\right)}{\left(\cos^2\alpha_1 + r^2\sin^2\alpha_1\right)^{\frac{3}{2}}} \right]^{-1} \tag{3.73}$$

where α_1 is the angle between the shock normal and the field directions, r is the compression ratio of the shock, *i.e.*, $r = U_1/U_2$, and x is the square root of the ratio of $\kappa_{\parallel}$ to $\kappa_{\perp}$, that is $x^2 = \kappa_{\parallel}/\kappa_{\perp}$. The definitions of R_{sh}, U_1, e, B and Z were mentioned before. Substituting the various constants for plausible values, E_{max} is given as,

$$E_{max} = 2.5\times 10^{16} \left(\frac{B_1}{30\mu\mathrm{G}}\right)\left(\frac{R_{sh}}{3\mathrm{pc}}\right)\left(\frac{U_1}{10^7\mathrm{m/s}}\right) \left\{ \eta^2 + \frac{1-\eta^2}{x^2} + \frac{r\left[\eta^2 + \frac{r^2}{x^2}\left(1-\eta^2\right)\right]}{\left[\eta^2 + r^2\left(1-\eta^2\right)\right]^{\frac{3}{2}}} \right\}^{-1} \mathrm{eV} \tag{3.74}$$

where $\eta = \cos\alpha_1$. As shown in Figure 3.12, E_{max} is strongly dependent on the field inclination η. For example, E_{max} in quasi–perpendicular shocks is larger by two or three orders of magnitude for each value of x than that in parallel shocks. The maximum energy for parallel shocks($\eta = 1$), E_{crit} can be estimated in the case of strong shocks($r = 4$) with $x = 30$ and with typical values of B_1, R_{sh} and U_1,

$$E_{crit} = 1.25Z \times 10^{14}\mathrm{eV}, \tag{3.75}$$

and they defined $E_{max}(\eta = \eta_{min}) \equiv E_{cut}$.

In their model, the field inclination η is assumed to distribute uniformly, and then the probability in the width $d\eta$ can be written as

$$f(\eta)d\eta = \frac{d\eta}{1-\eta_{min}} \tag{3.76}$$

where $\eta_{min} = U_1/c \sim 1/30$. Moreover, they assumed the injection efficiency $\epsilon(\eta)$ depending on η, and took simply,

$$\epsilon(\eta) = \eta. \tag{3.77}$$

The first order Fermi acceleration mechanism gives a power–law energy spectrum, so that the differential spectrum $dJ/dE \propto E^{-q}$, with $q = (r+2)/(r-1)$. The authors considered the dependence of the spectral index on the obliquity, according to a test particle simulation work by Naito and Takahara [73], assuming that q is proportional to η such as,

$$q(\eta) = a\eta + b \tag{3.78}$$

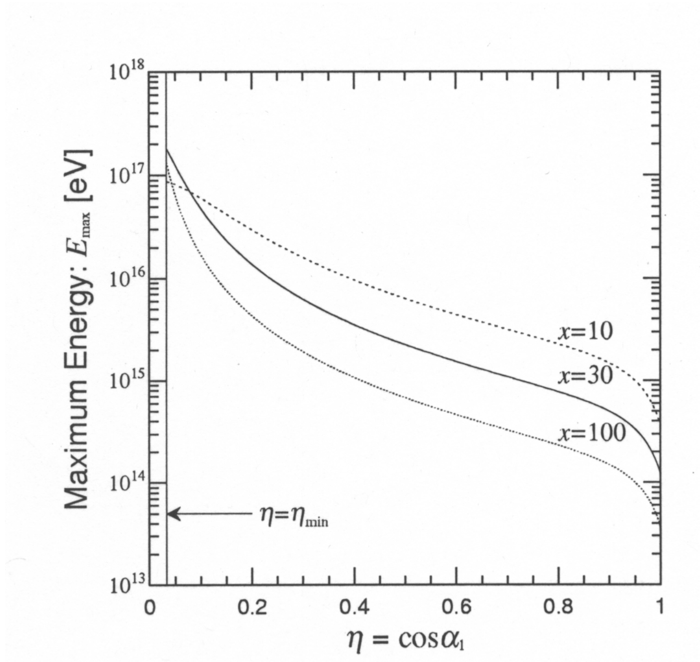

Figure 3.12: The maximum energy E_{max} for a proton with three values of x versus magnetic field inclination η.

where $a = 0.68$, $b = 1.41$ and $\eta_{min} = 1/30$. This dependence of power indices on the obliquity enhances intensities of accelerated particles by the oblique shocks. For $E_{crit} < E < E_{cut}$, taking into account the injection efficiency and the chance probability of η, a correction factor is given as,

$$g(\eta) = \frac{\eta - \eta_{min}}{1 - \eta_{min}} \frac{2}{1 - \eta_{min}^2} \int_{\eta_{min}}^{\eta} \eta' \left(\frac{E}{E_{crit}} \right)^{-q(\eta') + q(\eta_a)} d\eta' \tag{3.79}$$

Finally, the differential energy spectra can be expressed as,

$$\frac{dJ}{dE} = \begin{cases} CE^{-\gamma} & (E < E_{crit}) \\ CE^{-\gamma} g(\eta) & (E_{crit} \leq E \leq E_{cut}) \\ 0 & (E_{cut} < E) \end{cases} \tag{3.80}$$

here C and γ are fixed parameters for each chemical component and are determined with source conditions. The authors assumed two different sets of parameters, C and γ. According to the experimental results at $E = 1$TeV they predicted the energy spectra of primary cosmic ray components as shown in Figure 3.13 ,3.14 and the energy dependence of chemical composition as shown in Figure 3.15, and the parameters with subscript "HEGRA" have been taken from the analysis by the HEGRA air shower experiment, and the values with suffix "Ours" have been determined by the authors. They fixed the value $x = 30$ in their numerical calculations. The curves of the total flux in Figure 3.14 have a smooth bending around 10^{16} eV. The curve labeled "HEGRA" is consistent with DICE and CASA–MIA data, while the curve "Ours" reproduces well Tibet and Akeno data up to several times 10^{17}eV. In Figure 3.15, they showed the average value of the logarithm of mass number A as an indicator of the composition,

$$\langle \ln A \rangle \equiv \frac{\sum f_i \ln A_i}{\sum f_i}, \tag{3.81}$$

and both curves of the model predictions monotonically increase with the energy.

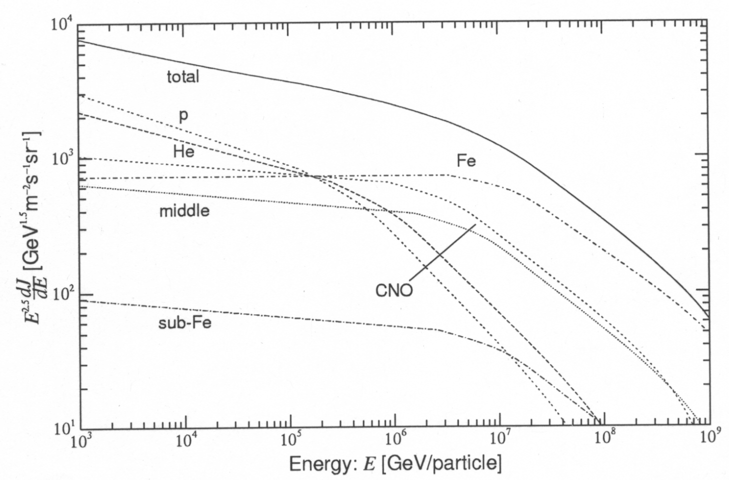

Figure 3.13: The predicted fluxes of total, proton, He, and other nuclear groups in the case of "Ours" parameter choice.

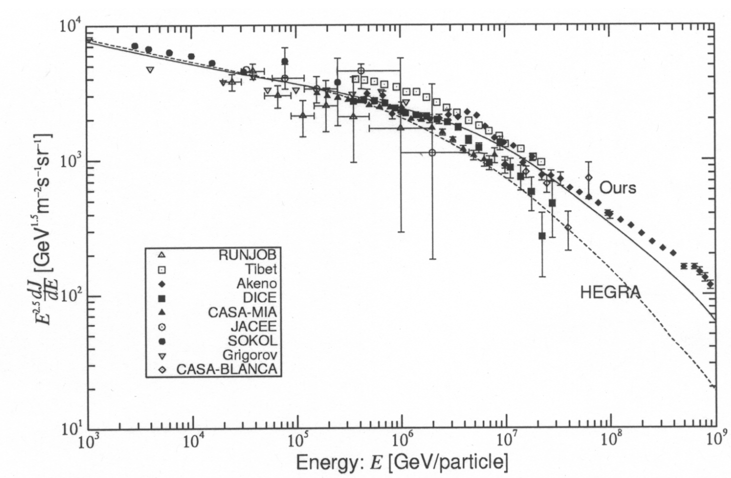

Figure 3.14: Comparison between the all–particle spectra reported by various groups and the predicted spectra with the oblique shock model.

3.3.6 Summary of acceleration models

Here I summarize the acceleration models for cosmic rays with energies $> 10^{14}$ eV. The characteristics of the model predictions are listed in Table 3.2. In the galactic wind termination

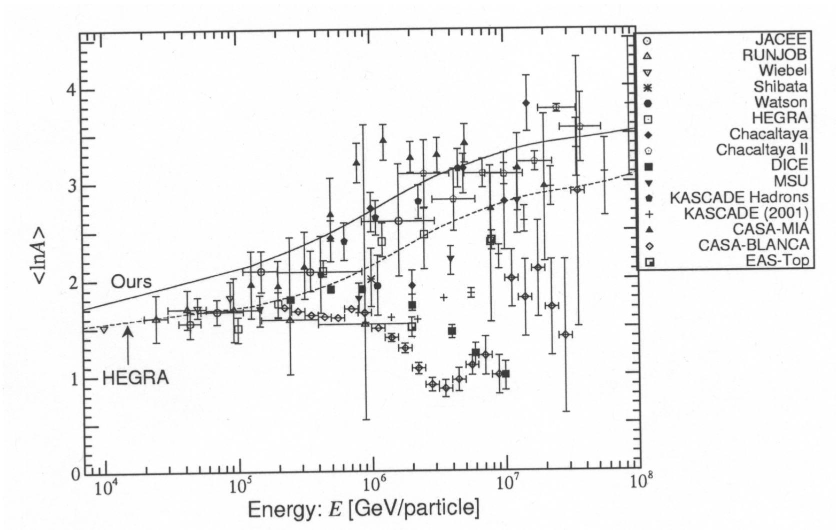

Figure 3.15: Energy dependence of chemical composition of primary cosmic rays in term of $< \ln A >$.

shock model, the chemical abundance depends on the properties of the diffusive motions of cosmic rays in the galactic disk and the galactic halo. For example, when we assume an energy independent diffusion coefficient and a leakage from the galactic disk, the chemical composition is independent of primary energies.

The predicted composition by the oblique shock model depends on the boundary condition, that is, the abundances and the spectral indices for the components around 1 TeV. However, they suggested that the predicted averaged mass number is greater than 2 when we take boundary conditions being consistent with the measured component spectra. For example, in this model, the proton dominant composition determined by KASCADE is inconsistent with the observed component spectra in TeV energy region.

model/mechanism	E_{max} (proton)	Dominant component at the knee	Energy dependence of $\langle \ln A \rangle$
SNR shock+stellar wind	9×10^{16} eV	increasing	Ne–Si
termination shock of the galactic wind	$\sim 10^{20}$ eV	–†	–†
multiple shock encounter	3×10^{17} eV	$\sim$ constant	proton
AGN origin	$\sim 10^{18}$ eV	$\sim$ constant	proton
SNR oblique shock	$\sim 10^{18}$ eV	increasing	middle*

Table 3.2: Summary of the characteristic predictions of acceleration models for cosmic rays $> 10^{14}$ eV. †: these values depend on the assumption of the diffusive motions of cosmic rays. $*$: it depends on the boundary condition, that is, the abundances and the spectral indices for the components around 1 TeV.

3.4 Advective diffusion propagation model for high energy cosmic rays above 10^{12}eV

Here I consider a cosmic ray propagation model based on the simple galactic magnetic field model and on detailed Monte Carlo simulations of charged particles in the Galaxy with assumptions of the galactic winds and the magnetic field structures.

In some models, it is explained that the knee of the energy spectrum of cosmic rays is due to the energy dependence of the acceleration processes in a source or due to differences in acceleration sites, as described in the previous section. On the other hand, some models attempt to explain the cosmic ray spectrum around the knee energy with the propagation process of cosmic ray particles in the Galaxy [75]. Many models of acceleration/propagation lead a critical energy depending on the charge of particles, so that these models predict that the mean mass number increases with the increasing energy around the knee. Moreover, the evidences to specify models and to be informative for constructions of a propagation theory, such as the primary to secondary ratio around the knee region, have not been measured because of experimental difficulties. Therefore, the detailed acceleration and propagation models are not established until now.

A propagation model must explain important facts, *i.e.*, the anisotropy of the arrival directions of cosmic rays and its energy dependence. It is known that the observed first harmonic anisotropy amplitude increases with the increasing energy above 10^{15}eV [65]. The plot reported by Hillas [45] shows that the amplitude has the same energy dependence as $E^{2.47} \times dN/dE$(Figure 3.16).

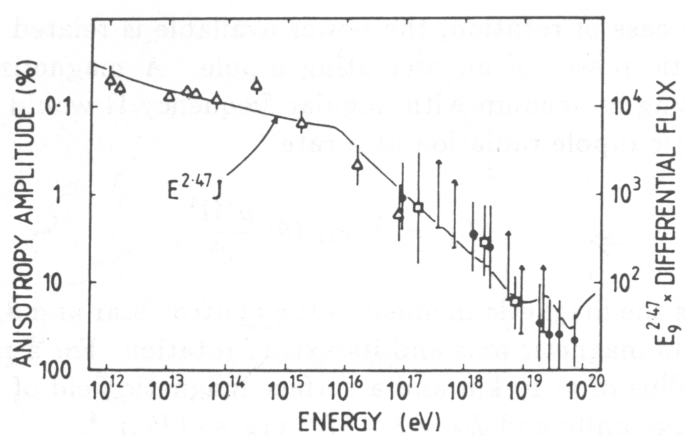

Figure 3.16: Left ordinate: the anisotropy amplitude; right ordinate: $E^{2.47} \times dN/dE$ [45]. The markers and the solid line represent the observed anisotropy and the energy spectrum, respectively.

In this section, I will briefly describe about previous researches for the diffusive motions of charged particles in the turbulent magnetic fields by Senda, Ogio and Kakimoto [79], and present a new model of propagations of cosmic ray particles energies more than 10^{12}eV. This model predicts the observed features such as the energy spectrum, the anisotropy, the mean mass number and their energy dependence.

3.4.1 Diffusive motion of charged particles in turbulent magnetic fields

The magnetic field lines in the Galaxy are nearly parallel to the spiral arms and the strength ($|B|$) is estimated to be $1-3\mu$G with the rotation measures for pulsars and galactic radio sources [22][39][50][85]. In addition to this regular component, the irregularities of the magnetic field exist, and have roughly the same strength as the regular component. The maximum scale length of the irregularities(L_{irr}) is estimated to be $10-100$pc with a large uncertainty.

We had derived the Fokker–Planck coefficients of the diffusive motion of cosmic ray particles along and perpendicular to the regular magnetic field lines with the test-particle simulations [79]. Here I briefly explain this calculation, the details are reported in reference [80]. Our calculations are based on the results by Giacalone and Jokipii [33].

The equation of the charged particle motion in a magnetic field is

$$\frac{d\mathbf{p}}{dt} = e\mathbf{v} \times \mathbf{B} \tag{3.82}$$

where the galactic magnetic field $\mathbf{B}$ is expressed by the sum of a regular component $\mathbf{B}_L$ and an irregular component $\delta\mathbf{B}$,

$$\mathbf{B} = \mathbf{B}_L + \delta\mathbf{B}. \tag{3.83}$$

The equation (3.82) is expected as the following differential equations at the position $\mathbf{x}$,

$$\frac{d\mathbf{x}}{dt} = \mathbf{v} \tag{3.84}$$

$$\frac{d\mathbf{v}}{dt} = \frac{e}{\gamma m}(\mathbf{v} \times \mathbf{B}) \tag{3.85}$$

These equations are simplified with defining a vector $\mathbf{y} = (\mathbf{x}, \mathbf{v})$ as follows

$$\frac{d\mathbf{y}}{dt} = \mathbf{F}(t, \mathbf{y}). \tag{3.86}$$

The equation (3.86) is numerically solved with the fourth order Runge–Kutta method. A position and a velocity of a test particle at a time $t + \Delta t$ is given as,

$$\mathbf{k}^{(1)} = \Delta \cdot \mathbf{F}(t, \mathbf{y}) \tag{3.87}$$

$$\mathbf{k}^{(2)} = \Delta \cdot \mathbf{F}(t + \frac{\Delta t}{2}, \mathbf{y} + \mathbf{k}^{(1)}) \tag{3.88}$$

$$\mathbf{k}^{(3)} = \Delta \cdot \mathbf{F}(t + \frac{\Delta t}{2}, \mathbf{y} + \mathbf{k}^{(2)}) \tag{3.89}$$

$$\mathbf{k}^{(4)} = \Delta \cdot \mathbf{F}(t + \Delta t, \mathbf{y} + \mathbf{k}^{(3)}) \tag{3.90}$$

$$\mathbf{y}(t + \Delta t) = \mathbf{y}(t) + \frac{1}{6}\left(\mathbf{k}^{(1)} + 2\mathbf{k}^{(2)} + 2\mathbf{k}^{(3)} + \mathbf{k}^{(4)}\right) \tag{3.91}$$

The time step is taken as

$$\Delta t = \frac{1}{50}\frac{2\pi r_g}{c} \tag{3.92}$$

here r_g is the Larmor radius of a particle and c is the light speed.

The irregular component of the magnetic field is express as a sum of the transverse waves, each of which has a wave number k_n as follows

$$\delta\mathbf{B} = \sum_{n=1}^{N_{max}} A(k_n)\left[\cos\alpha_k \mathbf{e}_{x'} \pm i \sin\alpha_k \mathbf{e}_{y'}\right] \exp\left[i\left(k_n z' + \beta\right)\right] \tag{3.93}$$

here $A(k_n)$ is the amplitude, α_k is a random angle, and β is a random phase. $\mathbf{e}_{x'}$, $\mathbf{e}_{y'}$ and $\mathbf{e}_{z'}$ are the unit vectors of the co-ordinate axis of the space of $\mathbf{r}' = (x', y', z')$. The expression (3.93)) satisfies div$\delta\mathbf{B} = 0$. The space of $\mathbf{r}'$, in which the wave number vectors point in the direction of (0,0,1), is related with the real space of $\mathbf{r}$, as follows

$$\mathbf{r}' = R_z(\phi)R_y(\theta)\mathbf{r} \tag{3.94}$$

$$R_z(\phi) = \begin{pmatrix} \cos\phi & -\sin\phi & 0 \\ \sin\phi & \cos\phi & 0 \\ 0 & 0 & 1 \end{pmatrix} \tag{3.95}$$

$$R_y(\theta) = \begin{pmatrix} \cos\theta & 0 & \sin\theta \\ 0 & 1 & 0 \\ -\sin\theta & 0 & \cos\theta \end{pmatrix} \tag{3.96}$$

Thus, in our calculations, the five values (θ_k, ϕ_k, α_k, β_k and the sign in (3.93)) are randomly defined for each space.

Many observations of the rotation measure suggest that the regular and the irregular components of the galactic magnetic field have the same order in the magnitude of their energy density, and thus we assumed

$$\frac{\mathbf{B}_L^2}{8\pi} = \frac{\delta\mathbf{B}^2}{8\pi} = \frac{1}{8\pi}\sum_{n=1}^{N_{max}} \mathbf{A}^2(k_n) \tag{3.97}$$

moreover we assumed that the energy density spectrum $P(k_n)$ has the Kolmogorov spectrum (Figure 3.17)

$$P(k_n) \propto \frac{4\pi k_n^2 \Delta k_n}{1 + (k_n L_{irr})^{11/3}}. \tag{3.98}$$

The interval of the wave number k_n is calculated with a relation $\Delta k_n/k_n = 0.05$ in our simulations. In Figure 3.18 it is shown that the examples of magnetic field lines are shown for $L_{irr} = 10$pc and 50pc, and Figure 3.19 is the track of a test particle proton with energies of 5×10^{14}eV during 5500 years in the assumed galactic magnetic field of $B_L = 3\mu$G, and $L_{irr} = 10$pc.

We calculated the diffusive motions of 1000 test particles with energies of $5 - 9 \times 10^{14}$ eV, assuming a single source of particles and $L_{irr} = 10$ pc for two cases of the magnetic field strength of 1.0 and 1.5 μG(Figure 3.20). By the calculated position $\Delta\mathbf{x}$ and the time after a explosion Δt , we obtained the Fokker–Planck coefficients,

$$D_{ij} = \frac{< \Delta x_i \Delta x_j >}{2\Delta t} \tag{3.99}$$

$$< \Delta x_i \Delta x_j > = \frac{1}{N}\sum_{k=1}^{N} \Delta x_i \Delta x_j \tag{3.100}$$

The obtained time dependences of the Fokker–Planck coefficients are shown in Figure 3.21, 3.22. As shown in these plots the Fokker-Planck coefficients become constant during several thousands years after a SN explosion. Thus, the motion of high energy particles in the galactic disk is diffusive, and the Fokker–Planck coefficients are considered to be the diffusion coefficients for the diffusive motion in the galactic magnetic field.

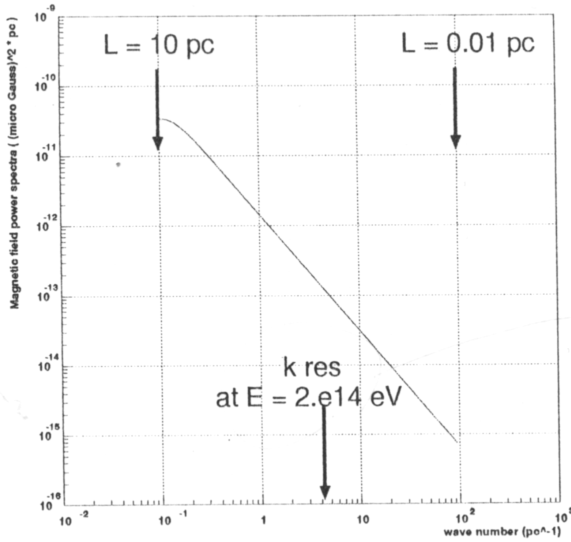

Figure 3.17: The assumed power spectrum of the magnetic field.

We plotted the diffusion coefficients versus the normalized Larmor radii r_g/L_{irr} as shown in Figure 3.23. These linear relations on logarithmic graph is expressed by [48]

$$\frac{D_{ii}}{cL_{irr}} = \left(\frac{D_{ii}}{cL_{irr}}\right)_0 \left(\frac{r_g}{L_{irr}}\right)^{\alpha} \tag{3.101}$$

The fitting parameters of equation (3.101) for the calculated diffusion coefficients are listed in Table 3.3.

parameter	parallel	perpendicular
α	0.6018 ± 0.0218	0.6627 ± 0.0142
$\log(D_{ii}/cL_{ii})_0$	0.1893 ± 0.0281	-1.481 ± 0.018

Table 3.3: The fitting parameters of equation (3.101) for the calculated diffusion coefficients.

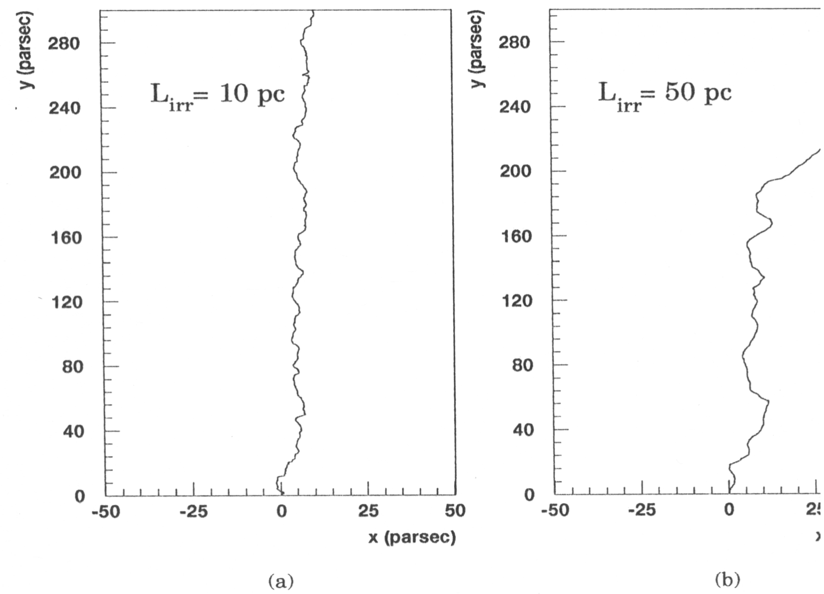

Figure 3.18: Examples of the simulated field lines, (a) for $L_{irr} = 10$pc and (b) for 50pc.

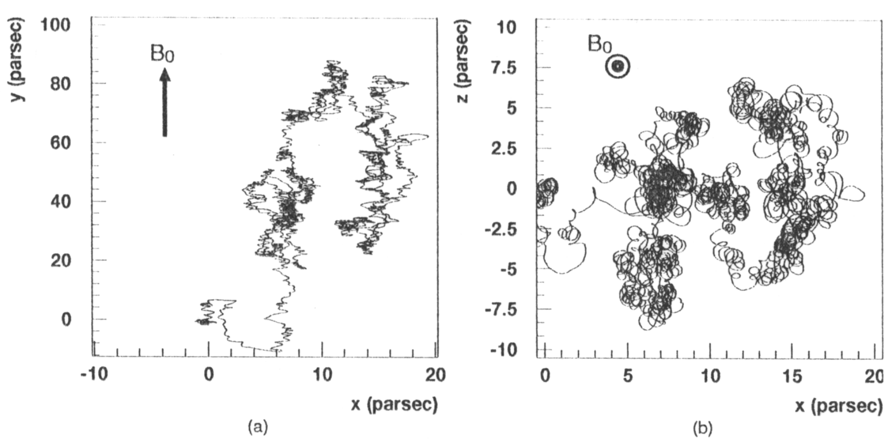

Figure 3.19: An example of a simulated track of a teat particle (proton) with energies of 5×10^{14}eV for 5500 years.

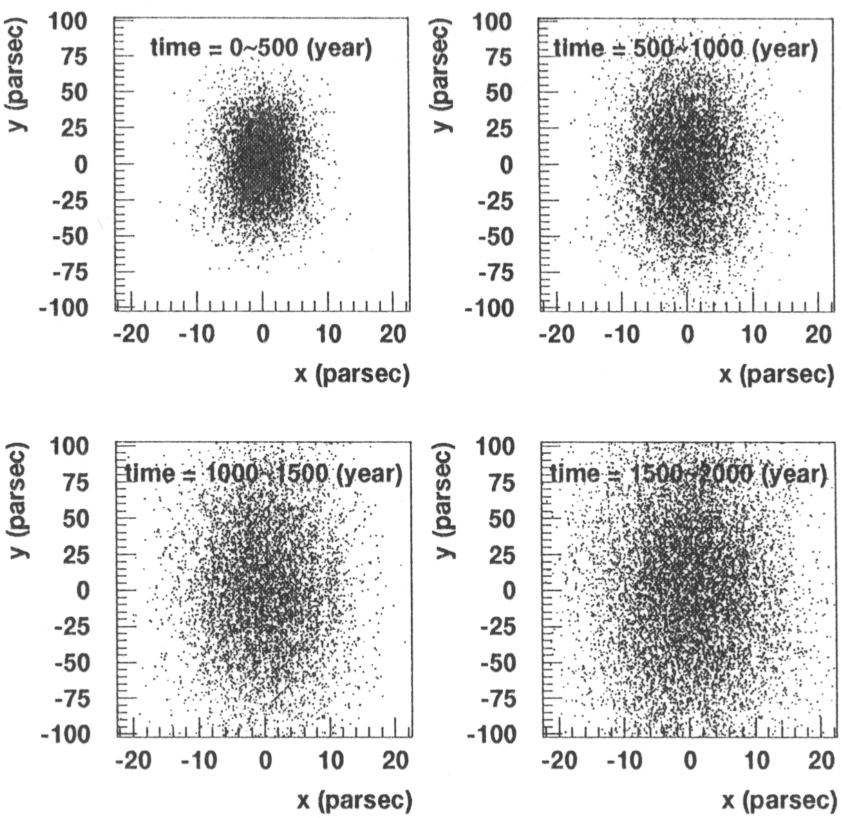

Figure 3.20: Snap shots of particle distributions after an explosion of a source(0,0) of particles with energies 5×10^{14}eV. The magnetic field strength is assumed to be $B_L = 1\mu$G and $\delta B/B = 1$. The direction of the regular magnetic field is along with y–axis.

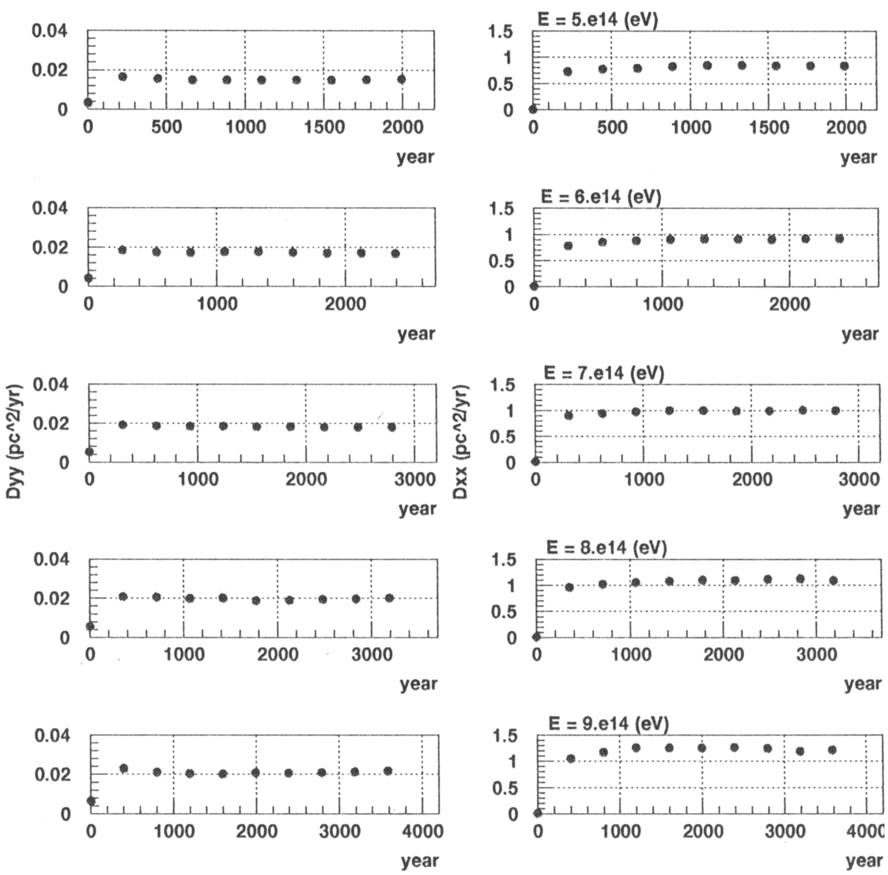

Figure 3.21: Time dependences of the Fokker–Planck coefficients for the diffusive motions of charged particles with energies $5 - 9 \times 10^{14}$eV in the assumed galactic magnetic field. D_{xx} and D_{yy} represent the coefficients for parallel and perpendicular to the regular magnetic field, respectively. We assumed $B_L = 1.0\mu$G, $\delta B/B = 1$ and $L_{irr} = 10$pc.

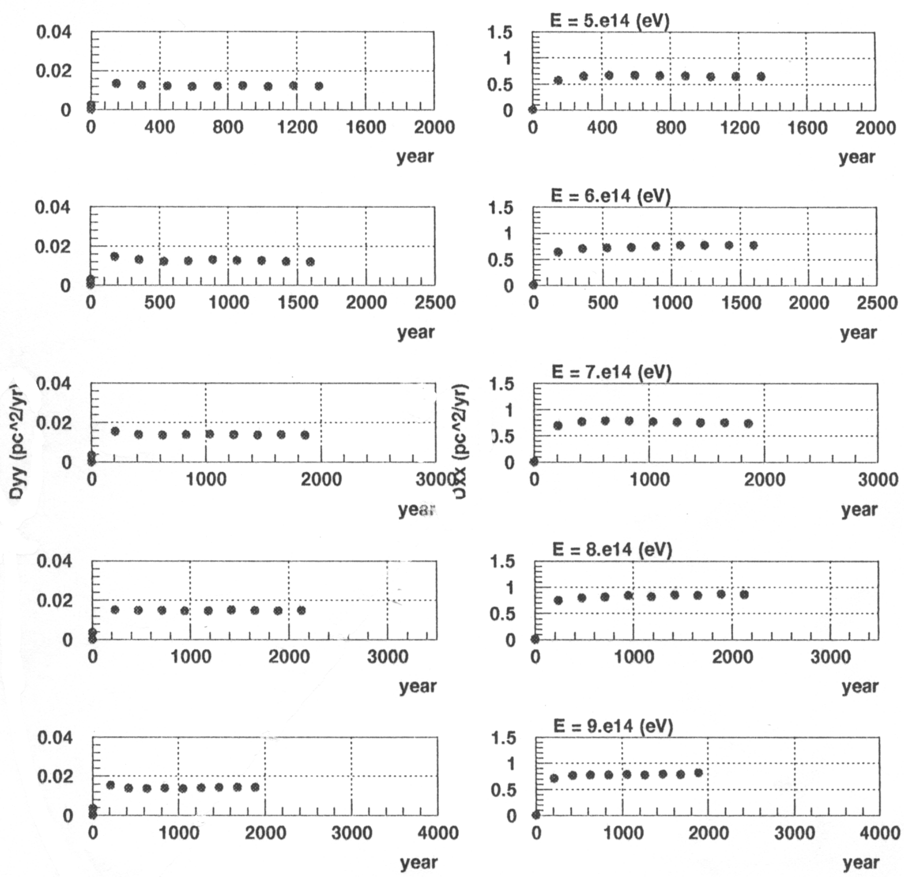

Figure 3.22: Time dependences of the Fokker–Planck coefficients for the diffusive motions of charged particles with energies $5 - 9 \times 10^{14}$eV in the assumed galactic magnetic field. D_{xx} and D_{yy} represent the coefficients for parallel and perpendicular to the regular magnetic field, respectively. We assumed $B_L = 1.5\mu$G, $\delta B/B = 1$ and $L_{irr} = 10$pc.

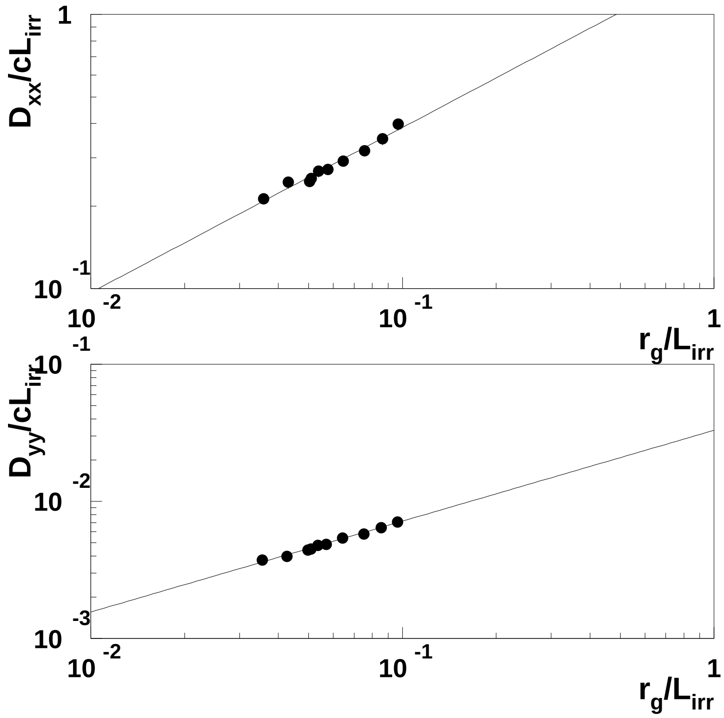

Figure 3.23: The obtained diffusion coefficients depend on the Larmor radii. The diffusion coefficients and the Larmor radii are normalized with cL_{irr} and L_{irr}, respectively and c is the light speed.

3.4.2 Advective–diffusion of cosmic ray particles

When we assume that the regular component of the galactic magnetic field is completely parallel to the spiral arms of the Galaxy, the leakage of cosmic ray particles is dominated by $D_\perp$. For example, from equation (3.101), $D_\perp$ for protons with energies 10^{14}eV is 0.005 pc^2/year for $B_L = 3\mu G$ and $L_{irr} = 100$pc. With this value, we can estimate the residence time (τ_R) in the galactic disk with the half thickness $l \sim 150$pc,

$$\tau_R = \frac{l^2}{D_\perp} \sim 5 \times 10^6 \text{years}. \tag{3.102}$$

On the other hand, an extrapolation of the leaky box model to 10^{12} eV leads a residence time of 2×10^5 years. In a different way, a residence time is estimated from the anisotropy. The observed anisotropy amplitude around 10^{12} eV is 10^{-3}. This amplitude is the order of the ratio of the diffusion velocity v_D to the particle velocity v, so that $v_D \simeq 300$ km/s. Then the averaged residence time is estimated as $l/v_D \simeq 5 \times 10^5$ years. Thus, the estimated residence time with the leaky box model and that from the observed anisotropy amplitude are small comparing with the expectation (3.102), and therefore, an idea of the diffusive leakage of cosmic ray particles perpendicular to the galactic magnetic field apparently contradicts to the observations.

With many observations for the magnetic field of the spiral galaxies, the loops and filament structures are found [69], which are considered to be due to expansions of the magnetic field via supernova explosions or the magnetic buoyancy [90](Figure 3.24). Thus in those structures we can expect the existence of the magnetic field perpendicular to the galactic disk with open field lines, in which cosmic ray particles are possible to escape more rapidly with $D_\parallel$. Moreover, the *galactic wind* which has analogy with solar wind supposed to be exist. The galactic wind is the outflow of the interstellar medium and that of the magnetic field irregularities. The existence of the galactic wind is not established, but the theoretically predicted velocity of the galactic wind depends on the assumptions of the boundary conditions between the Galaxy and the galactic halo. In a model of the galactic disk surrounded with the dark matter halo, v_g is predicted to be ~ 300 km/s [96].

Cosmic ray particles flow out along with the galactic wind because the Larmor radii of cosmic rays with energies lower than 10^{16}eV are much smaller than the scale length of the irregularities. Since, the cosmic ray particles leak out through the loops and the filament structures of the galactic magnetic field, this process is considered to be not only diffusive motions with $D_\parallel$, but also the outflows with the galactic wind of velocity v_g. Thus the cosmic ray leakage is considered to be an advective–diffusion process with $D_\parallel$ and v_g.

Here we assume that the direction of the leakages of cosmic rays is perpendicular to the galactic disk surface, and that there is leakage along neither with spiral arms nor with radial direction. Moreover, when we assume that the strength of magnetic field and the cosmic ray density n are uniform in the galactic disk, the leakage of cosmic rays is expressed with the following one dimensional advective–diffusion equation,

$$\frac{\partial n}{\partial t} + v_g \frac{\partial n}{\partial x} = \frac{\partial}{\partial x}\left(D_\parallel \frac{\partial n}{\partial x}\right) \tag{3.103}$$

where v_g is a galactic wind velocity and $D_\parallel$ is a diffusion coefficient calculated with (3.101) for a particular charge and energy. From the advective–diffusion equation(3.103), I estimated the residence time τ_R which is defined as the time, during which the number of cosmic ray particles in a confinement volume reaches $1/e$ of a initial value for cosmic ray particles with energies $10^{12} - 10^{17}$eV and for various pairs of the parameters L_{irr} and v_g.

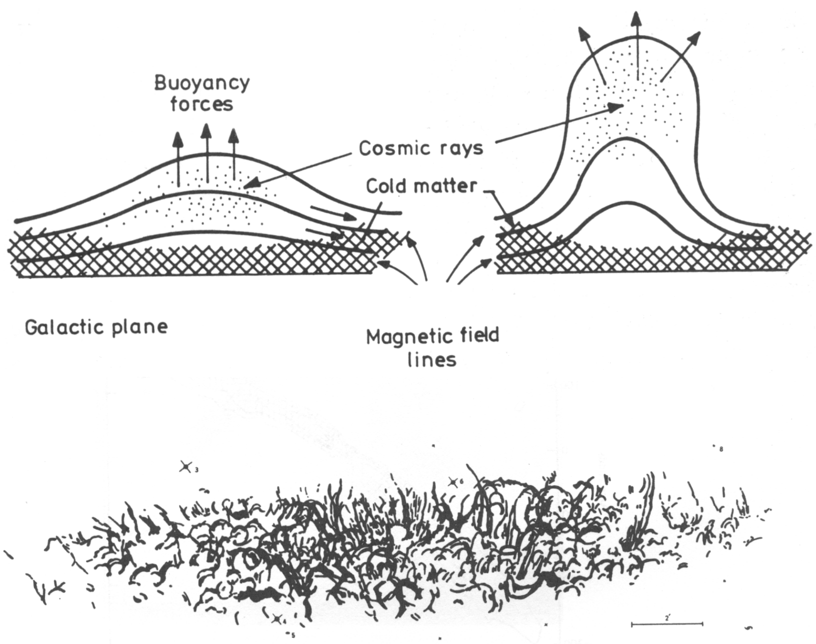

Figure 3.24: (*upper*) Illustration of the magnetic loop formation due to the instability and of relativistic gas expulsion from the galactic disk [67]. (*lower*) A sketch of dark filaments found in an optical image of spiral galaxy NGC253 [90].

3.4.3 Residence time of cosmic rays in the galactic disk

The equation (3.103) is calculated numerically with the Crank–Nicholson scheme. The equation is translated to the finite difference equations with an operator splitting method. In these calculations we took a one-dimensional confinement volume (with the length of 300 pc) where a cosmic ray source $Q = Q_0\delta(t)$ is located at the middle point. The step sizes for the calculations are 12.5 pc for distance, and 100 years for time, respectively. Here we assumed that the strength of the galactic magnetic field is $3\mu G$ for the regular and the irregular components, and decreases exponentially with a scale length of 1 kpc. The cosmic ray particles are assumed to consist of five nucleus groups as listed in Table 3.4.

ID	1	2	3	4	5
components	proton	He	CNO	Ne–Si	Fe
mass number	1	4	14	24	56
charge	1	2	7	12	26

Table 3.4: Assumed five components of cosmic ray particles.

In these calculations, all cosmic ray particles escape from the galactic disk with advective–diffusive motions with $D_{\|}$ and with v_g, *i.e.*, all the galactic magnetic field lines are assumed to be perpendicular to the galactic plane. This is a limiting case of the galactic magnetic field configuration. It is natural to consider that a proportion of magnetic field lines are perpendicular to the disk and the rest are along with the spiral arms. This proportion affects the estimated residence time of cosmic rays to extend with the same factor. However, the absolute value of τ_R shown in Figure 3.25 is not much different from the residence time estimated from the observed results, so that the proportion is not much smaller than unity.

The calculated residence times of cosmic ray protons for different advection velocities are shown in Figure 3.25. Also, the residence times for different L_{irr} and for different components of cosmic rays are shown in Figure 3.26 and 3.27, respectively.

Apparently, the energy dependence of τ_R is power law ($\propto E^{-\gamma}$) and the curves bend at $\sim 10^{14}$ eV, that is, the flat curves (index: $-\gamma_1$) are bending to the steep ones (index: $-\gamma_2$) with the increasing energy. Moreover, while γ_1 clearly depends on v_g, γ_2 is approximately independent of v_g. This result shows that the leakages of lower energy cosmic rays are dominated by the advection because the diffusion coefficient is too small to be efficient. This conclusion is supported by the result shown in Figure 3.27 in which τ_R for low energy cosmic rays and γ_1 is not strongly depend on the charge of the particles.

In contrast, it is concluded that, for high energy cosmic rays, the leakages of cosmic rays are dominated by the diffusion, and τ_R has the same power law energy dependence as the diffusion coefficient in equation (3.101). Moreover, the energies of bending points on the curves of τ_R in Figure 3.27 obviously depend on the charge of particles, and τ_R are smaller for lighter nuclei, and thus for high energy cosmic rays, the averaged mass number of cosmic ray particles is expected to increase with the increasing energy.

The power law indexes of τ_R are about -0.1 at 10^{12}eV and -0.6 at 10^{17}eV. The steepening is gradual and the bending energy is $E \sim 10^{14} - 10^{15}$eV. Since the energy spectrum $N(E) = Q(E)\tau_R(E)$, if we assume the power law index of a source spectrum $Q(E)$ is constant of -2.6, the indexes of $N(E)$ are expected to be about -2.7 at 10^{12}eV and -3.2 at 10^{17}eV, and the steepening of the spectrum at $\sim 10^{15}$eV. These expected features are remarkably consistent with those of the observed energy spectrum of cosmic rays.

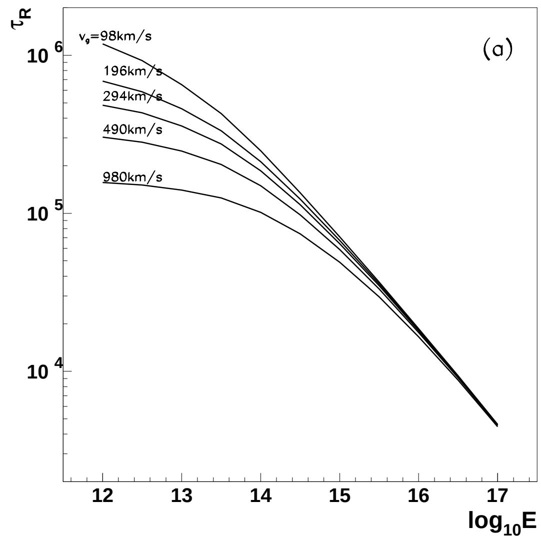

Figure 3.25: The residence time τ_R predicted with the advective diffusion model for cosmic ray protons. This figure shows τ_Rs for different advection velocities, *i.e.*, the galactic wind velocity, v_g. For all the calculations in this figure L_{irr} is fixed to be 100 pc.

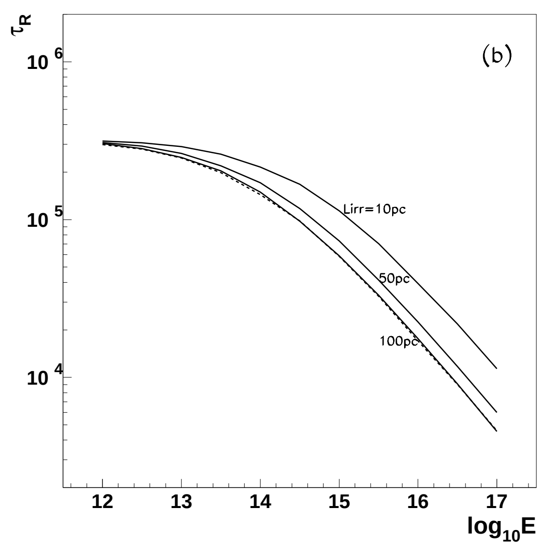

Figure 3.26: The residence time τ_R predicted with the advective diffusion model for cosmic ray protons. This figure shows τ_Rs for different maximum scale lengths of the irregularity of the galactic magnetic field, l_{irr}. For all the calculations in this figure v_g is fixed to be 5×10^{-4} pc/years = 490km/s.

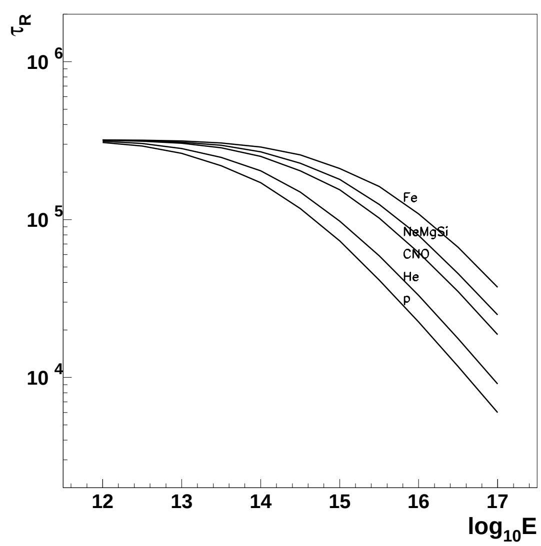

Figure 3.27: The residence time τ_R predicted with the advective diffusion model for different primary components of cosmic ray particles. For all the calculations in this figure v_g is fixed to be 5^{-4} pc/years = 490km/s and L_{irr} is fixed to be 50 pc.

Chapter 4

Extensive Air Showers

The cosmic ray spectrum is well described by a inverse power law in the energy, $\propto E^{-\gamma}$. Thus for observations of high energy cosmic rays one requires long observation times and a large effective detection area. The rate of arrivals of cosmic rays with energies above 10^{12} eV is very few, thus one cannot observe directly with a detector provided on a balloon or mounted on a satellite. Accordingly high energy cosmic rays are observed through detections of extensive air showers(EAS) developed in the atmosphere. This chapter is a description of air shower phenomena and of their properties. Detailed discussions are found in a book by Rao and Sreekantan [76].

4.1 Air showers

An extensive air shower is a swarm of particles produced by iterative interactions between the atmosphere and primary and secondary cosmic ray particles. In 1930's, Auger and his colleagues found many events of coincident signals on separated detectors. They concluded that the coincidences are due to showers of secondary particles induced by high energy primary cosmic rays at a top of the atmosphere.

The inelastic interaction cross section of cosmic ray protons with energies of a few hundred GeV on an air nucleus is about ~ 250 mb, which corresponds to the interaction length ~ 90 g/cm^2, where the mean mass number of the air is assumed ~ 14. While the total thickness of the earth's atmosphere is ~ 1000 g/cm^2, so that, a high energy primary cosmic ray interacts with the air and induces a cascade shower of secondary particles.

At the first interaction of a cosmic ray nucleus with the air, many pions and kaons are produced. These secondary particles interact further with the air, whereas some of them decay because of their finite lifetimes. A charged pion gives rise to a muon component in an air shower as

$$\begin{aligned} \text{cosmic ray} + \text{air nucleus} &\rightarrow \pi^{\pm} + \pi^{0} + K^{\pm} + \cdots \\ \pi^{\pm} &\rightarrow \mu^{\pm} + \nu(\bar{\nu}). \end{aligned}$$

A kaon also contributes to a muon component via various decay modes to pions, such as,

$$
\begin{aligned}
K^{\pm} &\rightarrow \mu^{\pm} + \nu(\bar{\nu}) \\
K^{\pm} &\rightarrow \pi^{\pm} + \pi^{0} \\
K^{\pm} &\rightarrow \pi^{\pm} + \pi^{+} + \pi^{-} \\
&\cdots .
\end{aligned}
$$

A neutral pion decays into two gamma rays practically before any other interactions because of their short lifetime, $\sim 10^{-16}$ s, in spite of the relativistic time dilation. A gamma ray initiates the iterations of the electron–positron pair production and the bremsstrahlung, which induces electromagnetic cascades,

$$
\begin{aligned}
\pi^{0} &\rightarrow \gamma + \gamma \\
\gamma &\rightarrow e^{+} + e^{-} \\
e^{\pm} &\rightarrow e^{\pm} + \gamma \\
&\cdots .
\end{aligned}
$$

Most of air showers are mixture of the nuclear and the electromagnetic cascades. Figure 4.1 shows a schematic view of an extensive air shower.

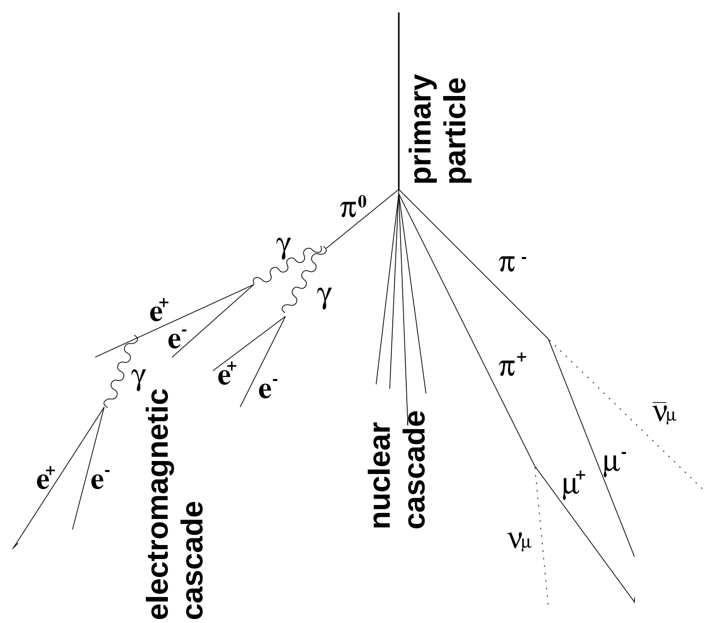

Figure 4.1: A schematic view of an extensive air shower.

As a shower travels down in the atmosphere, a number of particles, which is called a *shower size*, increases and reaches the maximum development. For example, a shower size at the maximum development amounts to $\sim 10^5$ for a shower of primary energy $E = 10^{14}$ eV. After the maximum development, a number of particles decreases with absorptions of particles by atmospheric atoms and molecules. These processes are called the longitudinal developments of extensive air showers.

4.1.1 Interaction of electrons and gamma rays

An air shower is predominantly composed of gamma-rays, electrons and positrons. Various approximate formulae to describe the electromagnetic cascade were given by many authors and here I present a brief summary. This result is also helpful to discuss the nuclear cascade.

A relativistic electron (and positron) loses its energy mainly by the bremsstrahlung. Its cross section for a relativistic electron is given by the Bethe–Heitler formulae, which is written as,

$$\sigma_{brems.}(E,v)dv = \frac{4Z^2 r_e^2}{137}\frac{dv}{v}\left[\left(1+(1-v)^2-\frac{2}{3}(1-v)\right)\ln\left(184Z^{-\frac{1}{3}}\right)+\frac{1}{9}(1-v)\right], \quad (4.1)$$

where $v = h\nu/E$, Z is the atomic number of a target nucleus, r_e is the classical electron radius. Here we define the radiation length X_0 of electrons in a medium as,

$$\frac{1}{X_0} = \frac{4Z^2 r_e^2}{137}\frac{N}{A}\ln\left(184Z^{-\frac{1}{3}}\right), \quad (4.2)$$

where N is the Avogadro's number and A is the mass number of a target nucleus. Using X_0 and integrating (4.1) by $v = 0$ to 1, the energy loss rate due to bremsstrahlung is

$$\left(\frac{dE}{dX}\right)_{brems.} \simeq -\frac{E}{X_0}. \quad (4.3)$$

The value of X_0 for the air is ~ 38 g/cm^2.

Gamma rays with energy greater than 1 MeV lose their energies mainly via electron–position pair productions. The cross section for pair production, $\sigma_{pp}(h\nu, u)$ at energy $h\nu$ is given by

$$\sigma_{pp}(h\nu,u)du = \frac{4Z^2 r_e^2}{137}du\left[\left(u^2+(1-u)^2-\frac{2}{3}(1-u)\right)\ln\left(184Z^{-\frac{1}{3}}\right)-\frac{1}{9}(1-u)\right], \quad (4.4)$$

where $u = E/h\nu$ and E is the energy of a produced electron. The interaction length of gamma rays for pair productions is obtained by integrating (4.4) by $u = 0$ to 1, and we can write the energy loss rate for gamma rays as

$$\left(\frac{dE}{dX}\right)_{pair} = -\frac{7}{9}\frac{E}{X_0}. \quad (4.5)$$

Thus the interaction length for pair production is comparable to that for bremsstrahlung.

In an extensive air shower, when the average energy of electrons is less than the critical energy E_{crit}, the ionization loss process becomes dominant and the shower size begins to decrease. The ionization energy loss rate is given by

$$\left(\frac{dE}{dX}\right)_{ion.} = -2\frac{\pi N Z r_e^2}{A}m_e\left[\ln\left(\frac{\pi^2 m_e^2}{(1-\beta^2)^{\frac{3}{2}}\,I\,(Z)^2}\right)-a\right], \quad (4.6)$$

where $I(Z)$ is the mean ionization potential: $I(Z) \sim 80$ eV, and a constant $a \sim 3$. The critical energy E_{crit} is the energy at which an electron energy loss due to ionization processes comes to comparable to that due to bremsstrahlung. If we assume the minimum ionization loss $-(dE/dX) = 2$ MeV/gcm^{-2}, we obtained the critical energy of electrons in the air; $E_{crit} \sim 80$ MeV.

For muons in an EAS, the practical energy loss process is only ionization loss, therefore, they do not suffer significant energy losses even after a maximum development. Thus, most of muons survive and reach the ground before they lose their energy entirely or decay.

4.1.2 Longitudinal development

A total number of electrons in an electromagnetic cascade N_e at an atmospheric depth t is approximately given by

$$N_e \sim \frac{0.31}{\sqrt{y}} \exp\left[t\left(1 - \frac{3}{2}\ln s\right)\right], \tag{4.7}$$

where t is in the unit of the radiation length of electrons in the atmosphere, $X_0 \simeq 38$ g/cm^2. The variable y is defined as

$$y = \ln\left(\frac{E_0}{E_{crit}}\right), \tag{4.8}$$

where E_0 is the primary energy. The age parameter s is defined as

$$s = \frac{3t}{t + 2y}. \tag{4.9}$$

From this definition, $s = 0$ at the first interaction point, and $s = 1$ at the maximum development of an EAS. The number of particles at the maximum development is obtained by substituting 1 for s in (4.7),

$$N_{max}(E_0) \simeq \frac{0.31}{[\ln(E_0/E_{crit})]^{1/2}} \frac{E_0}{E_{crit}}. \tag{4.10}$$

Fenyves et al. carried out Monte Carlo studies for air shower developments induced by protons and iron nuclei [27]. They showed that the air shower developments induced by primary nuclei are expressed by the same formula as electromagnetic cascades, (4.7), with replacing t with $t' = t + \beta(t_{max} - t)t^\gamma$, where t_{max} is the depth at the maximum development point, and $\beta(= 0.2 \sim 0.4)$ and $\gamma(\sim 0.5)$ are constants.

4.1.3 Lateral distribution of shower particles

As shower particles gain transverse momentum by the multiple scattering, the swarm of shower particles expands laterally. The root mean square of a scattering angle of electrons after traversing the amount of matter, x g/cm^2, is

$$< \theta >^2 = \left(\frac{E_s}{E}\right) x, \tag{4.11}$$

where

$$E_s = \sqrt{\frac{4\pi}{\alpha}} m_e c^2 = 21 \text{ MeV}. \tag{4.12}$$

For electrons with energy $E = E_{crit}$ at $x = X_0$, we have

$$r_m = \frac{E_s}{E_{crit}} X_0, \tag{4.13}$$

and $r_m \sim 9.5$ g/cm^2 for the air. This is called *Molière length*, which gives the characteristic length of lateral spread of electromagnetic cascades. A structure function of the lateral distribution is represented with the variable r/r_m. For an electromagnetic cascade of age s, the structure function $f(r/r_m, s)$ is well expressed with the Nishimura–Kamata–Greisen(NKG) function:

$$f(r/r_m, s) = C(s)\left(\frac{r}{r_m}\right)^{s-2}\left(1 + \frac{r}{r_m}\right)^{s-4.5}. \tag{4.14}$$

The normalization factor $C(s)$ is taken to satisfy the following relation,

$$\int_0^\infty 2\pi x f(x,s) dx = 1 \qquad (x \equiv r/r_m). \tag{4.15}$$

Thus,

$$\begin{aligned} C(s) &= \left[2\pi \int_0^\infty x^{s-1} (1+x)^{s-4.5} dx\right]^{-1} = [2\pi B(s, 4.5-2s)]^{-1} \\ &= \frac{\Gamma(4.5-s)}{2\pi\Gamma(s)\Gamma(4.5-2s)} \end{aligned} \tag{4.16}$$

where B is Beta function, and Γ is Gamma function.

Using $f(r,s)$, a local particle density $\rho(r,s)$ at a radial distance r from the shower axis is given as,

$$\rho(r,s) = \frac{N_e}{r_m^2} f(r,s) \tag{4.17}$$

where N_e is a shower size.

Fenyves et al. shows that for air showers induced by primary nuclei, the lateral distributions of shower particles can be written as the formula (4.14) with replacements of $r_m \to r_m/2$ and $t \to t'$ described in the previous section.

A shower disk has a finite thickness and a curvature, not a flat structure. Agnetta et al. reported the time structure of the air shower front, and they showed the delay time τ from a flat shower plane [2],

$$\tau = 7.7 + 9.5 \left(\frac{r}{79\text{ m}}\right)^{2.1} \text{ns}, \tag{4.18}$$

where r is the radial distance from a shower axis. Linsley gave an empirical formula of the shower disk thickness as a dispersion of arrival times of shower particles [66],

$$\sigma_\tau = 2.6 \left(\frac{r}{30\text{ m}} + 1\right)^{1.5} \text{ns}. \tag{4.19}$$

4.2 Observations of extensive air showers

One technique for detections of air showers is the coincidence method with an *air shower array*, which is a set of ground–based detectors(Figure 4.2). The total number of particles in an air shower, so called the shower size, is determined from the local particle densities sampled by detectors which are placed on the ground. The arrival direction of an air shower is determined from relative arrival times of shower particles incident on detectors. This fast–timing technique can be used because shower disks are thin enough comparing with their lateral spread as mentioned above.

4.2.1 Determination of arrival directions

Here we assume that the surface of shower disks is a plane. The equation of a shower front is expressed by

$$lx + my + nz - ct = 0 \tag{4.20}$$

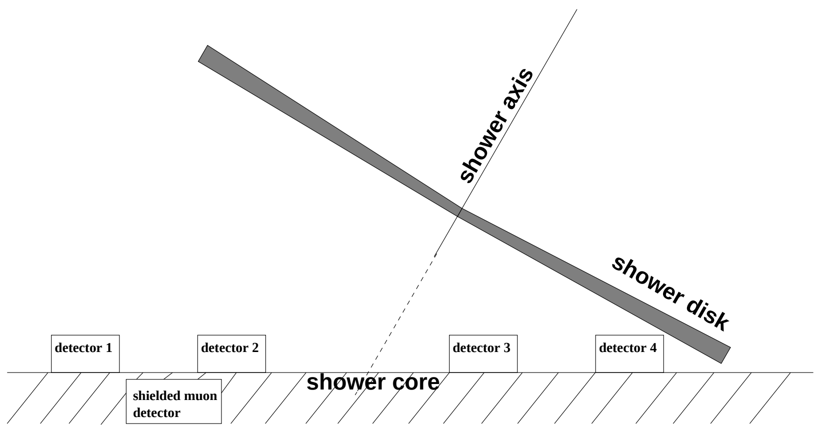

Figure 4.2: A cross–sectional view of a front plane of an air shower and detectors.

where c is the speed of light, t is an arrival time of a shower front, (x, y, z) is a position of a detector, (l, m, n) is a set of direction cosines of a shower axis with a zenith angle θ and with a azimuth angle ϕ,

$$l = \sin\theta\cos\phi \tag{4.21}$$

$$m = \sin\theta\sin\phi \tag{4.22}$$

$$n = \cos\theta \tag{4.23}$$

The vector (l, m, n) is determined by minimizing χ^2 which is defined as

$$\chi^2 = \sum_i w_i \left[lx_i + my_i + nz_i - c\,(t_i - t_0)\right]^2 \tag{4.24}$$

where (x_i, y_i, z_i) is the position of the detector i, and t_i is the arrival time of a shower front at the detector i. The weight w_i is determined from errors of timing measurements. The equation to be solved is

$$\frac{\partial\chi^2}{\partial l} = \frac{\partial\chi^2}{\partial m} = \frac{\partial\chi^2}{\partial n} = 0 \tag{4.25}$$

under the condition $l^2 + m^2 + n^2 = 1$. The plane approximation for a shower front is valid within distances less than 30 m from a shower axis.

4.2.2 Determination of shower sizes

A shower size, N_e, is determined by fitting the observed particle densities to an assumed lateral distribution function, e.g., Eq.(3.17) in the shower plane using the least square procedure. In this case χ^2 is defined as

$$\chi^2 = \sum_i w_i \left(\rho_i^{obs} - \rho_i^{exp}\right)^2, \tag{4.26}$$

where ρ_i^{obs} and ρ_i^{exp} are observed and expected local particle densities at the detector i; w_i is the weight factor for detector i. One practical method to find the core position (x_0, y_0) is obtained by calculating density–weighted means of detector coordinates, such as,

$$x_0 = \sum_i \rho_i^{obs} x_i / \sum_i \rho_i^{obs} \tag{4.27}$$

$$y_0 = \sum_i \rho_i^{obs} y_i / \sum_i \rho_i^{obs}, \tag{4.28}$$

where (x_i, y_i) is the position of the detector i. The grid–search method for searching the parameters (x_0, y_0) to minimize χ^2 is also deployed. The actual method which we used is described in Chapter 7.

The shower size is a good estimator for the primary energy. An approximated relation between shower sizes N_e and primary energies E_0 is

$$E_0 \sim 2 \times 10^9 N_e \, \text{eV}. \tag{4.29}$$

The actual energy–size relation depends on the mass composition of primary cosmic rays and on the hadronic interactions. The detailed measurement of primary composition and the assumptions for the hadronic interactions in the air are very important for the determination of the averaged relation between primary energies and shower sizes.

4.2.3 Muons and other components in air showers

Muons

Electrons are the most dominant component in air showers. However, an air shower contains also muons as decay products of charged pions and kaons. Since muons do not strongly interact, they loose their energies due to only ionizaion or decay. A total number of muons in an air shower strongly reflects the nature of particle interactions and is sensitive to primary species. The number of muons, N_μ, with energies greater than E_μ is expressed as [76],

$$N_\mu(> E_\mu) \propto N_e^\alpha, \tag{4.30}$$

where N_e is the electron size; the exponent α is ~ 0.9 for $E_\mu \sim 1$ GeV, and $\alpha \sim 0.7$ for $E_\mu \sim 200$ GeV. The lateral distribution of muons in an air shower is expressed as,

$$\rho_\mu(r) = C N_\mu r^{-0.75} \left(1 + \frac{r}{R}\right)^{-2.5}, \tag{4.31}$$

where C is a normalization constant.

Shielded detectors are used to detect muons in order to avoid background electrons. Some groups discussed cosmic ray composition through measurements of air shower muons [25]. Furthermore, the muon component in air showers is important in high energy gamma ray astronomy. Some groups measure muous in order to distinguish air showers induced by primary gamma rays from those induced by primary nuclei.

Čerenkov light

Čerenkov photons are emitted by a charged particle which has the velocity greater than the speed of light in a medium. In a medium with a refraction index n, particles with $\beta(= v/c)$

above $1/n$ only can emit Čerenkov light, thus n is setting a threshold energy. Čerenkov light is emitted the half angle θ around the direction of the particle. The angle θ is given as

$$\theta = \cos^{-1} \frac{1}{n\beta}, \tag{4.32}$$

where $\beta = v/c$. The reflectivity of the atmosphere is approximately expressed as a following function, at depth t and temperature T [44],

$$n = 1 + 0.000292 \left(\frac{t}{1030\,\mathrm{gcm}^{-2}} \right) \left(\frac{273.2\,\mathrm{K}}{T} \right). \tag{4.33}$$

The minimum energy for electrons which emit Čerenkov photons in the atmosphere is ~ 21 MeV at sea level, and the emission angle is about $1.4°$.

Fluorescence light

Charged particles in an air shower ionize and excite air molecules, and then, the molecules in particular excited states release energies as emissions of fluorescence light. Since the photon yield is very small [57], the measurements of the fluorescence light are possible for a large air shower induced by a very high energy primary. The Fly's Eye experiment [10] is the pioneer of such observations of extremely high energy cosmic rays.

4.3 Equi–intensity method analysis

The equi–intensity method is one of the techniques to measure the longitudinal development of EAS. This method is based on the measurements of air shower sizes and rate of arrivals. In the equi–intensity method it is assumed that extensive air showers induced by primary particles with a same energy develop in the same way and that rate of arrivals of cosmic rays does not vary with time and direction. We can then plot the frequency distribution of the sizes of EASs at the different slant depth, $D_1 \cdots D_n$. Since showers at large zenith angles have penetrated large slant depths to reach the detector, the size that corresponds to a given intensity(showers per $\mathrm{m}^2 \cdot \mathrm{sr} \cdot \mathrm{s}$) will be smaller for larger zenith angle. When it is assumed that showers which are observed with the same frequency of occurrence at different zenith angles are initiated by particles of the same energy, the developments of showers with depth through the atmosphere can be derived directly from the distributions observed at different zenith angles(Figure 4.3). This procedure provides an average picture of the development of EASs for a particular primary energy.

This method has a great advantage that the obtained equi-intensity curves are less independent of Monte–Carlo simulations than any other method, because the simulations depend only on the detection efficiencies of an air shower array, and because this method is not affected by the elementary processes for the detailed features of muons, hadrons, Čerenkov photons and atmospheric fluorescence photons. Moreover, observations are not restricted with weather and the phase of the moon, and there is no systematic uncertainty due to atmospheric monitoring.

The depth of shower maximum(X_{max}), which is one of the shower parameters used for inferring composition of cosmic rays, is obtained from the equi–intensity method. It is necessary to do a very high altitude experiment in order to measure the EAS development curves for primary energies of interest. An EAS initiated by a proton with an energy of 10^{15} eV reaches

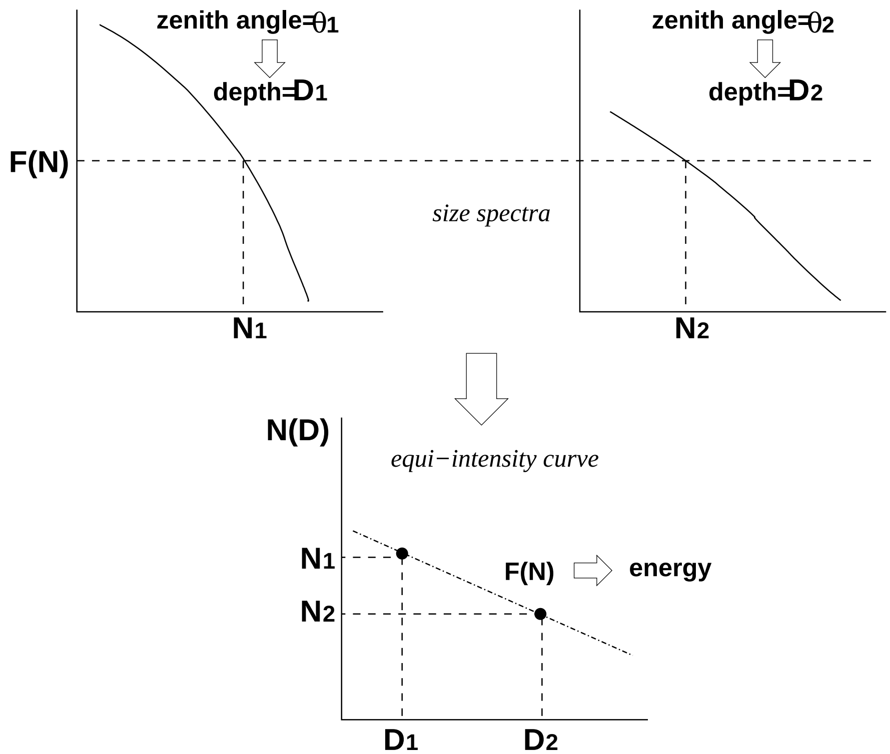

Figure 4.3: The determination of the development of EAS of different sizes through the atmosphere from observations at different zenith angles θ; $\mathbf{n(N)}$ is the rate of occurrence of shower size $\mathbf{N}$.

the maximum development at about 600 g/cm^2 and that initiated by an iron nucleus at about 470 g/cm^2. Thus the only site at such high altitude is Mt. Chacaltaya in Bolivia located at the atmospheric depth of 550 g/cm^2.

Note that one cannot compare equi-intensity curves with longitudinal development curves immediately. A measured size with air shower array does not translate directly into a number of electrons and positrons in the air shower, in part because the detected number of particles is contaminated by muons and in part because the determined size is affected by the threshold energies of the detectors. Moreover these effects have primary energy dependences, and the equi-intensity curves are affected by the energy-size relations, and energy spectra of components.

Chapter 5

Review of instruments to measure chemical composition of cosmic rays

In order to discuss the origins, the accelerations and the propagations of cosmic rays, it is the most important to measure the energy spectrum, the mass composition as a function of energy and the degree of isotropy of their arrival directions. While the arrival direction distribution can be directly measured, the other have to be deduced from measured EAS parameters. The primary energy spectrum is derived through measurements of shower size spectra, Čerenkov photon size spectra, muon size spectra, or shower development curves obtained from fluorescence light measurements, etc. The composition of the primaries is deduced through measurements of shower parameters such as the mean number as well as the fluctuations of the number of muons, the fraction of delayed hadrons, the high energy end of the hadron energy spectrum, or the depth of the shower maximum, etc., which are sensitive to mass number of a primary particle. Before we discuss the results of EAS studies with the BASJE MAS array, we shall briefly summarize the other past and present experiments on the primary energy spectrum and on the chemical composition.

5.1 CRN

The detector referred to as Cosmic Ray Nuclei(CRN) Detector on a Space Shuttle measured the nuclear composition of cosmic rays with energies well beyond TeV per amu. Figure 5.1 shows a schematic cross section of the instrument [47][87]. The instrument employed plastic scitillators(T1, T2), gas Čerenkov counters(C1, C2) and a transition radiation detector(TRD). This instrument measured nuclear charge Z, energy E over the range 40 GeV/amu to several TeV/amu and the trajectories of particles. Owing to the limitation in the dynamic range of the instrument and owing to the inherent magnitude of fluctuations in the transition radiation and the Čerenkov signals, the CRN instrument was not designed to observe protons and He nuclei.

Nuclear charges Z are measured with the scintillators utilizing the Z^2 dependence of the ionization loss. Their signals are nearly independent of the energy over the range. The scintillators also provide the coincidence triggers and the signals for the TOF measurements. The gas Čerenkov counters are filled with a N_2/CO_2 mixture at 1 atm, and provide energy measurements 40–150 GeV/amu. The TRD consists of six pairs of plastic fiber radiators and multi wire proportional chambers(MWPCs); the detection threshold for the transition radiation is reached at about 500 GeV/amu. For the energy below 500 GeV/amu, the MWPCs measure

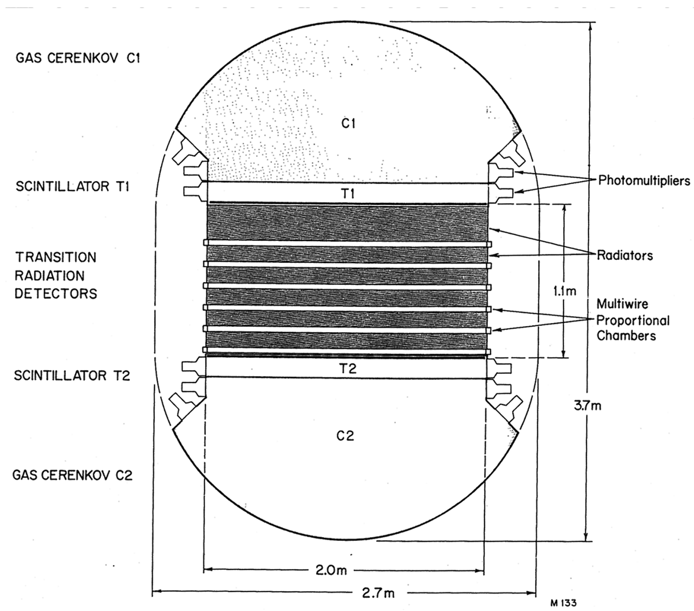

Figure 5.1: Schematic cross section of the CRN detector

the ionization losses of the particles, and is used for the coarse energy assignments. Above 500 GeV/amu, the yield of transition radiation X–rays rises rapidly with the energy up to 10 TeV/amu and provides the energy measurements. In addition to the energy measurements, the MWPCs also provide the position information to reconstruct the trajectory of a traversing particle. Consequently, the performance of the CRN instrument is characterized as; (1) the charge resolution $\delta Z = 0.2$ for oxygen($Z = 8$), $\delta Z = 0.35$ for iron($Z = 26$), (2) the energy resolutions $\delta E/E$ at 100 GeV/amu and 1TeV/amu are 35% and 11% for oxygen, respectively, and those are 13% and 8% for iron, respectively, and (3) the trajectory resolution is about $1°$.

The CRN instrument was flown in 1985 July/August in the Spacelab–2 mission of the Space Shuttle Challenger. While the total flight duration was about 8 days, the net observation time at the full aperture amounted 78 hours. Müller et al [71] reported the particle fluxes up to 2 TeV/amu for major primary nuclei as shown in Figure 5.2(left). In the same report, the authors estimated the source abundances of the element groups from their measurements with assuming a simple leaky box model of the particle propagation in the Galaxy, and then they showed the relative abundances of cosmic ray nuclei against the first ionization potentials(FIP) of the elements as shown in Figure 5.2(right). They pointed out the data which indicate the sudden suppression of particles when the FIP exceeds 10 eV. Thus, they concluded that the first stage injections of cosmic ray particles take place in stellar photo spheres at temperatures around 10^4 K [84]. Moreover they concluded that the bulk of the cosmic rays must be accelerated from material that originated in stellar eruptions or stellar winds and is enriched with ions formed in stellar photo spheres, and also they suggested that some of this material might be ejected by objects such as pre–supernova red giant stars or Wolf–Rayet stars.

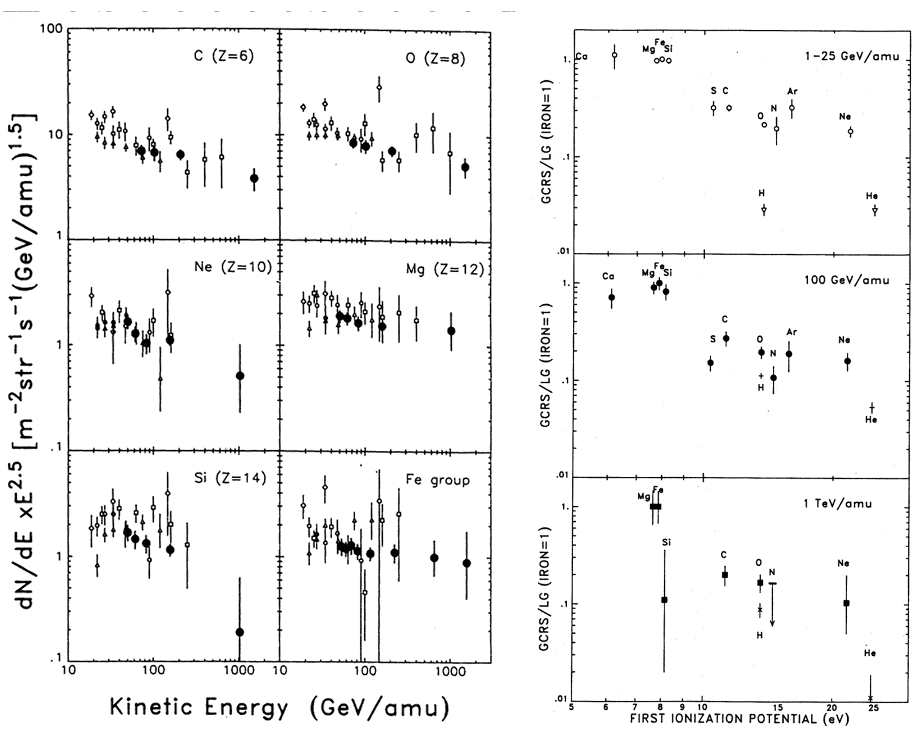

Figure 5.2: (*left*): Differential energy spectra for the cosmic ray nuclei C, O, Ne, Mg, Si and Fe measured with CRN(*solid*). Note that the fluxes multiplied with $E^{2.5}$. For other markers, see the reference [71]. (right): Abundances of the galactic cosmic ray nuclei at the source(GCRS), relative to the local abundances(LG), are plotted against the values of first ionization potentials of the elements [71]. All abundances are relative to iron.

5.2 RUNJOB

RUNJOB(RUssia–Nippon JOint Balloon–program) is a joint collaboration on the observations of primary cosmic rays with the balloon–borne emulsion chambers. They launched six long duration balloon on the trans–Siberian trajectories from 1995 until 1999. They reported experimental results of four flights in 1995 and 1996 [7]. Total exposure was 231.5m^{2}hr at the average altitude of 32 km, and the cut–off rigidity was about 3 GV along the trajectories. The detector on board had two chambers, each of which had an area of 40×50 cm^2 and the schematic illustrations are shown in Figure 5.3. The detector covered an energy range of 10–500 TeV for protons, 3–70 TeV/amu for He, and 1-5 TeV/amu for Fe–group.

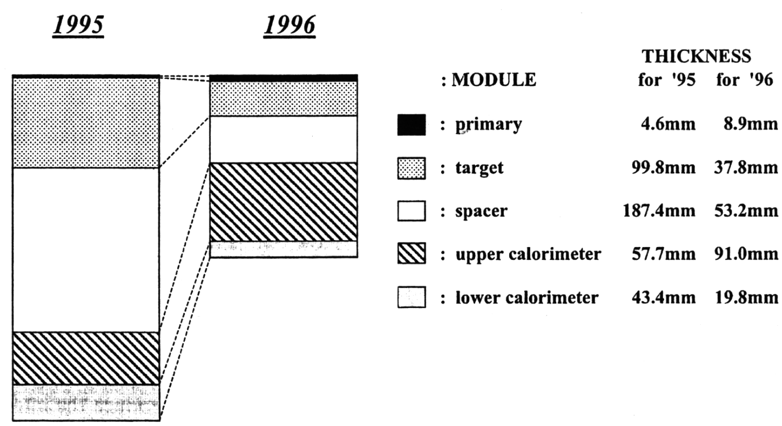

Figure 5.3: Chamber structure in 1995 and 1996 experiments.

The charge of a primary particle was determined from a darkness of a primary track on the nuclear emulsion plate of the top layer [6]. The resolution of the charge determination, which depends on the path length, was determined 0.167 for He and 1.089 for Fe in the case of 200μm path length.

The primary energy E_0 was determined from the shower energy ΣE_γ with the linear relation $E_0 = C_\gamma \Sigma E_\gamma$. The calorimetric determinations of ΣE_γ was difficult, because the thickness of the calorimeter layer was only four radiation length. Thus, for relatively low E_0 they estimated ΣE_γ from maximum darkness in the transition curves of the spot darkness on X-ray films, and for high E_0, ΣE_γ were estimated from the emission angles of γ–rays. The energy resolution, $\Delta E_\gamma / E_\gamma$, was about 15%.

Within four flights in two years, they obtained 483 tracks of primary cosmic rays, and reported the primary particle flux of five element groups as shown in Figure 5.4. The remarkable features in their results are:

- The proton spectrum is consistent with those reported by other groups but He spectrum is not consistent with JACEE and SOKOL results. The spectra of proton and He spectra have the same index ~ 2.8.
- The CNO spectrum is slightly steeper than that of other groups.
- The slopes of the energy spectra of heavy components seem to become gradually harder with the increasing mass number, *i.e.*, ~ 2.70 for CNO-group, and ~ 2.55 for Fe-group.

• Average mass is nearly constant over the wide energy range 20–100 TeV.

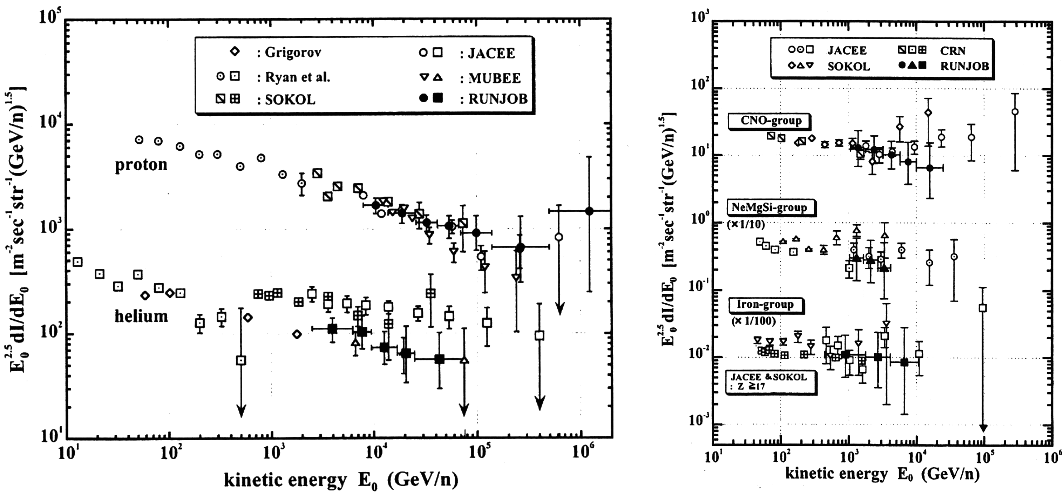

Figure 5.4: The left figure is the measured spectra of the primary protons and primary He nuclei. The right figure is the measured spectra of the heavy components.

5.3 CASA–MIA

The CASA–MIA detector [18] was the ground–based array of 1089 surface particle detector stations (Chicago Air Shower Array: CASA) and 1024 underground muon detectors (MIchigan Array: MIA) located at Dugway, Utah. The layout is shown in Figure 5.5. The mean atmo-

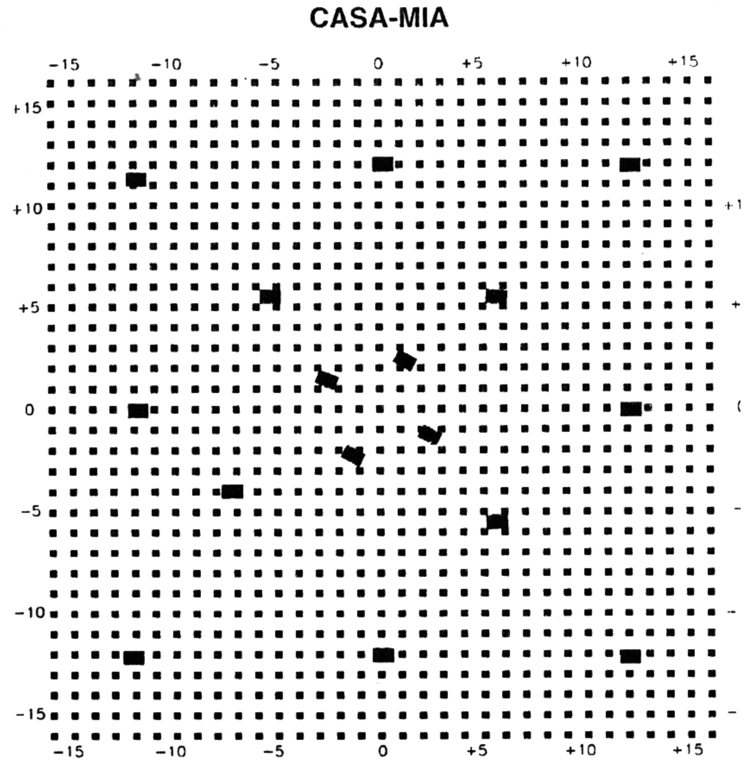

Figure 5.5: The layout of CASA–MIA array. CASA is on the surface, and MIA is buried at 3 meter underground. The CASA stations are 15 m apart from each other.

spheric overburden is 870 g/cm^2. Each station contained four counters, each of which consists of a two inches diameter PMT glued to the square sheet of an acrylic scintillator with 61 cm on a side and 1.5cm thick. Each station had 1 radiation length lead sheet on its top. The array was triggered when any three stations report at least three hit counters each.

The MIA counters were arranged in 16 patches, each of which contained 64 individual counters. Each counter was a 1.6m by 1.9m acrylic scintillator viewed by a five inches PMT. The MIA patches were buried at 3 meters underground and registered signals induced by muons with energies exceeding 750 MeV at the surface.

In order to estimate the primary energy independent of the type of primary particles they used a combination of the muon size N_μ and the electron size N_e. They reported that the empirically determined optimal value of the energy parameterization ($N_e + 60 \times N_\mu$) (Figure 5.6) has the most compositional insensitivity, and the best value of the factor of N_μ increases slightly with zenith angle reaching about 65 for the zenith angle of 45 degrees. This method of the energy determination yielded systematic differences between iron and proton energy assignments with less than 5%. The average absolute values of the energy reconstruction errors

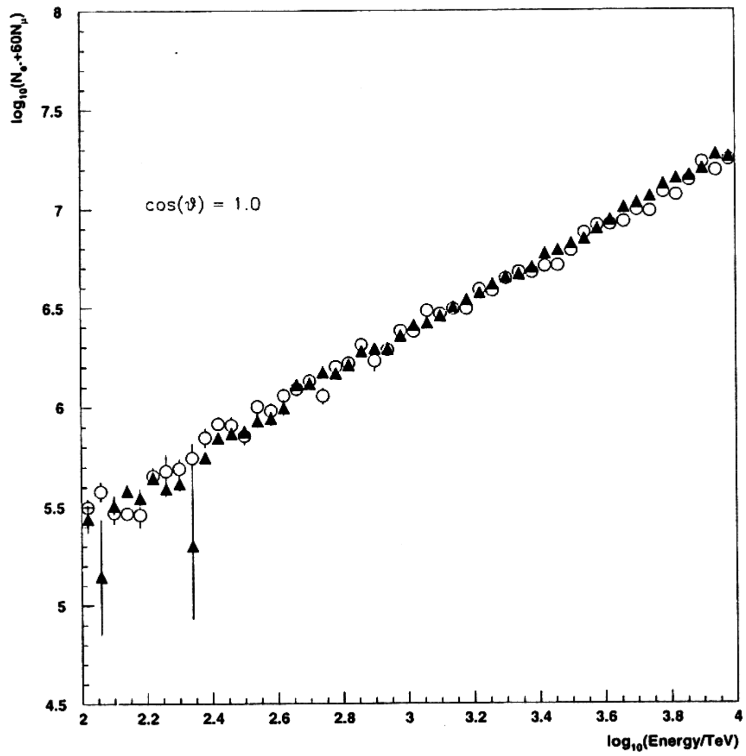

Figure 5.6: The energy parameter $\log(N_e + 60 \times N_\mu)$ as a function of the energy for simulated proton(*open circle*) and iron(*filled triangle*) vertical showers.

decreased from about 25% near 10^{14} eV to about 16% at 10^{15} eV.

The CASA–MIA group reported the all particle energy spectrum as shown in Figure 5.7 [34], and they concluded that the knee of the energy spectrum is rather a smooth transition over energies from 10^{15} eV to 3.0×10^{15} eV.

Moreover, this group studied the mass composition of cosmic rays [35]. They classified the observed events into "iron-like" group(called Heavy group) and "proton-like" group(called Light group) by parameters: ρ_e, ρ_μ, and α with "K"Nearest Neighbor (KNN) test, where ρ_e is the density of the surface particle and α is the slope of the lateral distribution near the core, and ρ_μ is the muon density at large core distance. They showed $< \ln A >$(Figure 5.8) and the energy spectra of the data groups classified according to the KNN–identified mass(Figure 5.9). In their results, the composition of cosmic rays agrees with the direct measurements near 10^{14} eV, and evenly consists of both the light elements and the heavier elements. Moreover the average mass increases with increasing energy, in the energy range from 10^{15} eV to 10^{16} eV, which coincides with the bending point of the energy spectrum.

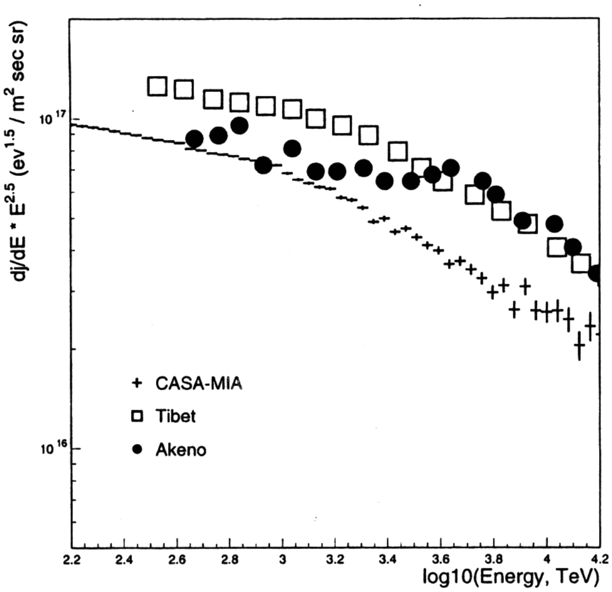

Figure 5.7: The observed energy spectrum of the CASA–MIA experiment compared with those of Tibet and of Akeno.

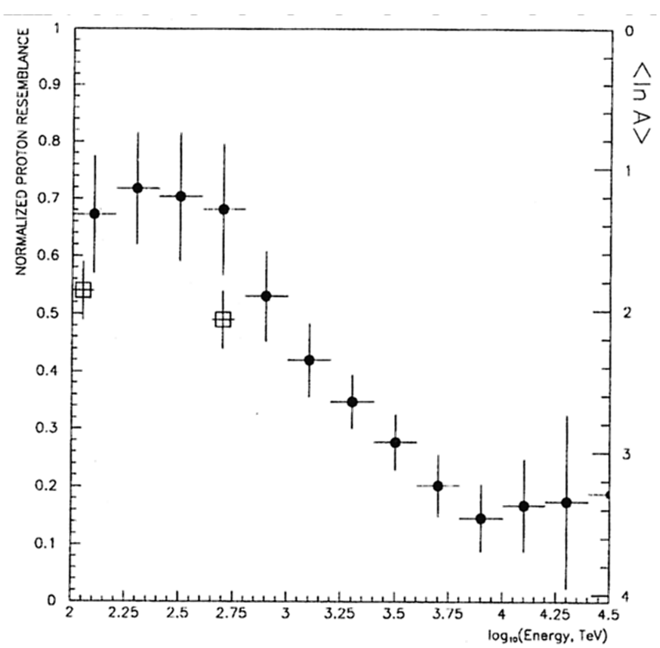

Figure 5.8: The average composition $\langle \ln A \rangle$of CASA–MIA data(*filled circle*). In the simulations for this analysis the QGSJET interaction generator were used. The open squares indicate the mean mass of the direct measurement of JACEE.

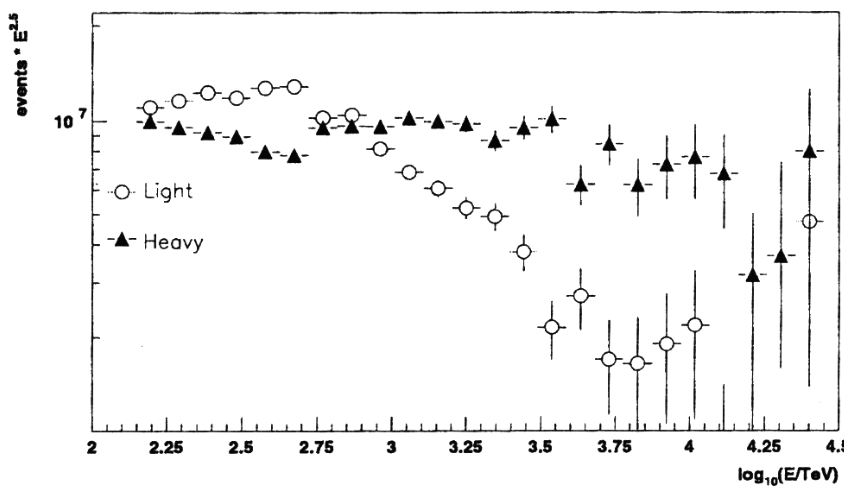

Figure 5.9: The energy spectra of each composition groups measured by the CASA–MIA experiment.

5.4 HEGRA–CRT

The HEGRA experiment is a multi component air shower installation with an air shower array; a Čerenkov light detector array and a independent Čerenkov telescope system [3] on La Palma, Canary Islands. The particle detector array consisted of 221 scintillator stations of $1m^2$ area each(Figure 5.10). The Cosmic Ray Tracking(CRT) detectors were installed and operated in the HEGRA air shower array, and had the lower threshold energy and the good angular resolution even for small air showers. One CRT detector consisted of two 2.5 m^2 circular TPC type drift chambers, and a 10 cm thick iron plate was placed as a muon filter between both chambers [12]. In total, ten CRT detectors were installed and operated in HEGRA site for about three years(1993–1996).

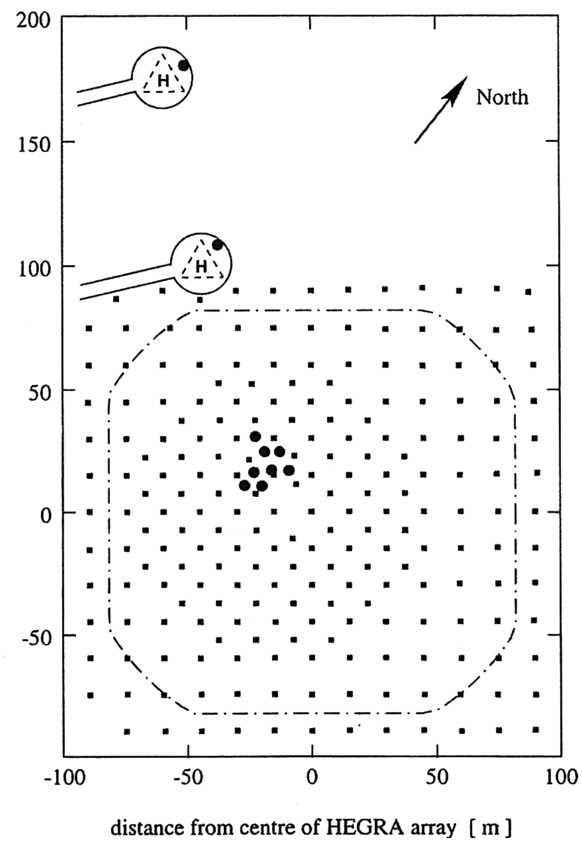

Figure 5.10: Map of the HEGRA site showing only the scintillator stations (square dots) and CRTs (circles). The dash-dotted line marks the area of shower core positions accepted in the analysis.

For studying the mass composition of cosmic rays, the analysis of CRT data were based on a statistical method using angular distributions of particles in air showers [11]. The authors reported that a measured average radial angle was closely related to an average longitudinal shower development [11]. Most muons are produced near the shower axis and rarely deflected by more than a few tenth of a degree due to multiple scattering and the geomagnetic field. Thus, muon radial angles can, in principle, be transformed into muon production heights for in a given core distance region.

Figure 5.11 shows histograms of muon radial angles for different core distance intervals [13]. Resulting measurements of median muon radial angles for 10 m core distance bins and for six different intervals of air shower sizes are shown in Figure 5.12. They estimated the cosmic ray mass composition by comparing the measured data with proton and iron nuclei simulations. The resulting average mass composition is shown in Figure 5.13. They concluded that the result shows an increase of $\langle \ln A \rangle$ in $10^{14} - 10^{15}$ eV and it agrees very well with the highest energy points of the direct measurements made by the JACEE collaboration, and an extrapolation of the directly measured spectrum with an additional constraint with a kink at a fixed rigidity of about 200 TV is consistent with the measured flux and composition.

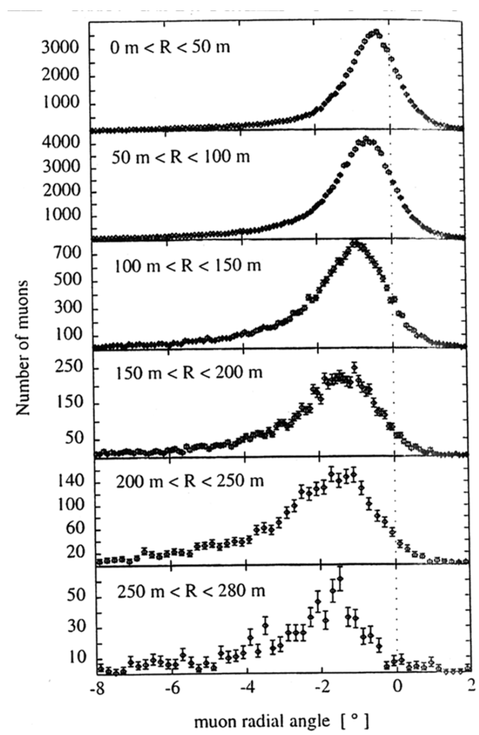

Figure 5.11: Histograms of muon radial angles observed with CRT detectors in different intervals of core distances for $15000 < N_e < 50000$. Note that particles coming from the shower axis have negative radial angles.

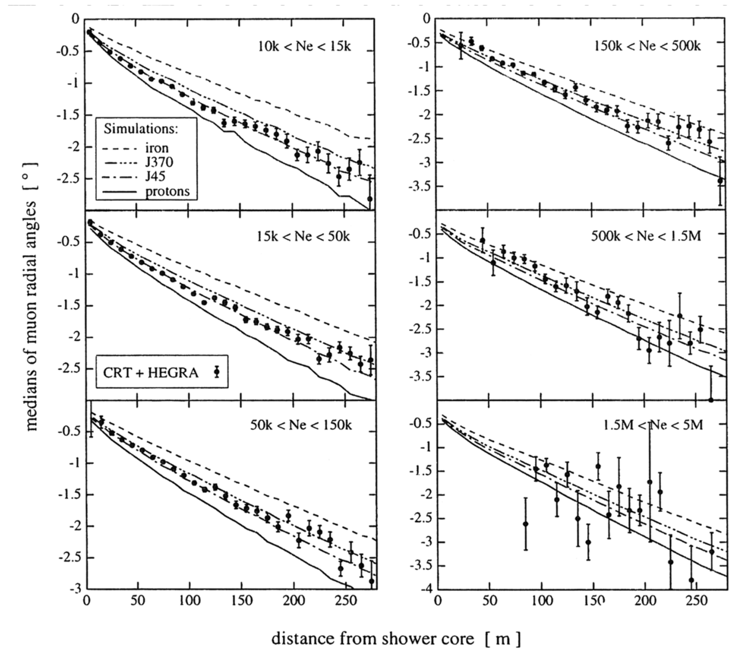

Figure 5.12: Median radial angles of muons measured with CRT detectors as functions of horizontal distance of the CRT detectors from the shower cores. Simulations are superimposed for pure protons and irons as well as the mixed compositions corresponding to direct measurements of the JACEE collaboration both above 45 TeV(J45) and above 370 TeV(J370).

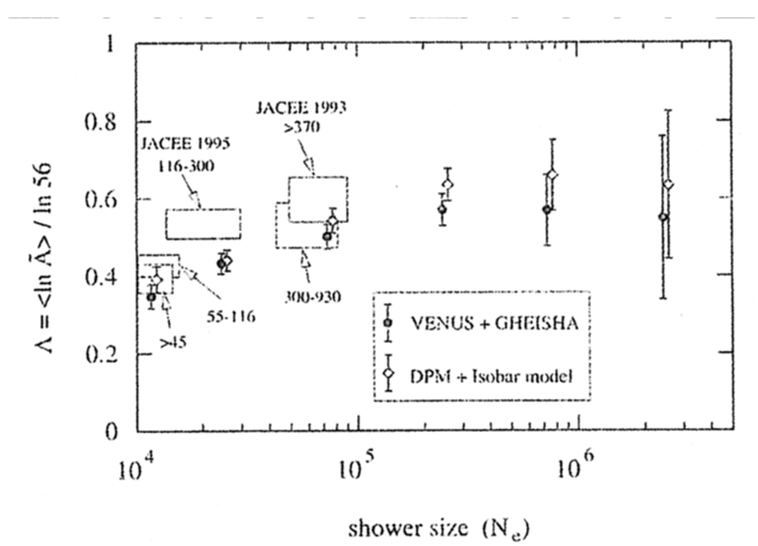

Figure 5.13: The mean mass composition obtained by comparing HEGRA–CRT data with simulations based on the VENUS/GHEISHA and DPM/Isobar interaction models.

5.5 CASA–BLANCA

Observations of atmospheric Čerenkov photons emitted by charged particles in air showers are considered as one of the integrated measurements of the longitudinal developments of air showers. For this purpose one approach is to measure lateral distributions of the Čerenkov photon densities on the ground. Slopes of the lateral distributions are related to depths of the maximum shower developments, and hence, they are related to the composition of the primary cosmic rays. However, a total number of the Čerenkov photons is a good estimator for a primary energy. Therefore, the detections of a large number of Čerenkov lateral distributions can provide information on how the composition changes with the energy.

To obtaine high quality Čerenkov lateral distribution data, the BLANCA(Broad Lateral Non–imaging Cherenkov Array) detectors were built in CASA installation. Using CASA as the cosmic ray trigger, the BLANCA detectors were operated at clear and moon less nights. In the analysis, they used the CASA data to determine the shower core positions and the arrival directions, and used the BLANCA data for the precise measurements of Čerenkov lateral distributions [28][29].

BLANCA [19] consisted of 144 angle–integrating detectors which recorded the lateral distributions of atmospheric Čerenkov photons. The BALNCA detectors were not uniformly spaced but had an averaged separation of 35–40m as shown in Figure 5.14. Each BLANCA detector contained a large Winston cone which concentrated the light striking an 880cm^2 entrance aperture onto a PMT. The effective concentration ratio is 15, the effective half–angle is about $\sim 10°$, and a typical BLANCA unit had a detection threshold of approximately one blue photon per cm^2.

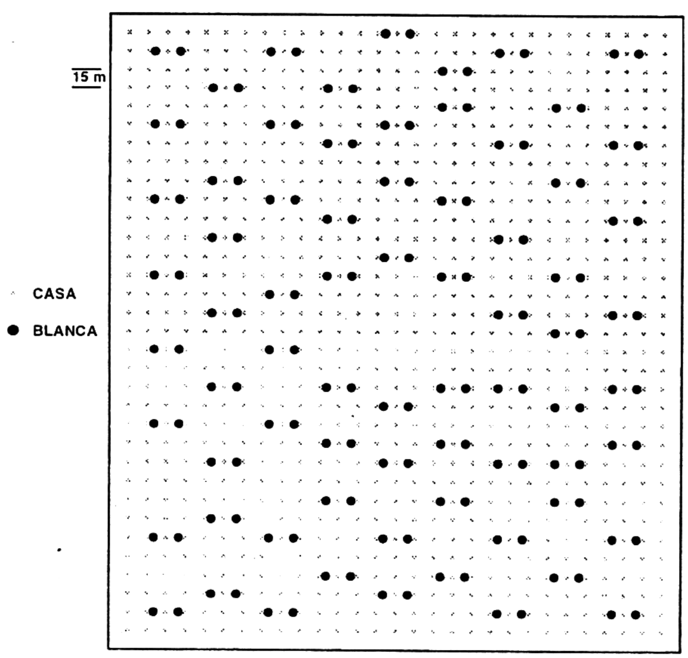

Figure 5.14: The CASA–BLANCA array.

CASA–BLANCA were operated in 90 moon less nights between January 1997 and May

1998. After removing the periods of hazy or cloudy weather, approximately 460 hours of the Čerenkov observations remained. Events were selected with the arrival directions, with the core locations and with conditions of measurements. The geometrical and temporal cuts resulted in an exposure to cosmic rays of 1.83×10^{10} m^{2}sr.

The obtained lateral distributions of photon densities were fitted to an empirical function with three fitting parameters, C_{120}, s and β:

$$C(r) = \begin{cases} C_{120} \exp\left[s(120\text{m} - r)\right] & 30\text{m} < r \leq 120\text{m} \\ C_{120}\,(r/120\text{m})^{-\beta} & 120\text{m} < r \leq 350\text{m} \end{cases} \tag{5.1}$$

The energy of each air shower was determined from C_{120} using the relation between C_{120} and primary energy obtained with the Monte Carlo simulation studies. As a result, they reported the differential all particle cosmic ray flux as shown in Figure 5.15, and concluded that the data shows a knee with one–half decade wide, and best–fit knee energy is 2.0 PeV with power law indices of -2.72 ± 0.02 for lower energies, and -2.95 ± 0.02 for higher energies above the knee.

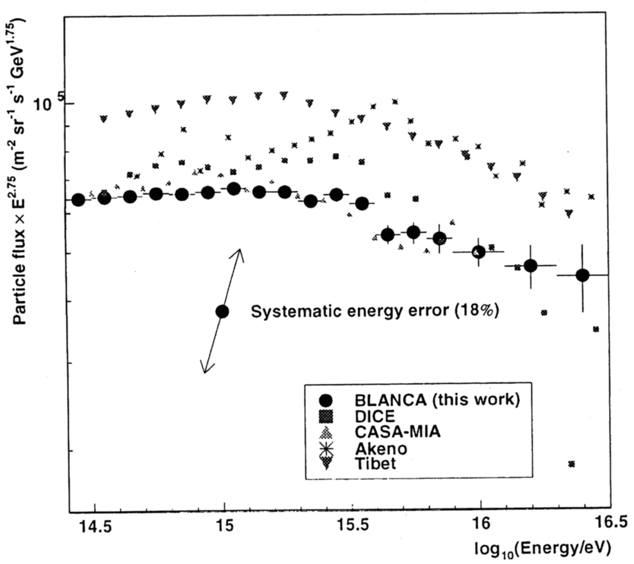

Figure 5.15: The differential all particle cosmic ray flux measured by CASA–BLANCA.

The mean primary mass was directly determined from the Čerenkov lateral distribution slope s. With their Monte Carlo studies, they insisted that, at fixed energy, s depends linearly on $\langle \ln A \rangle$, and the determined $< \ln A >$ is shown in Figure 5.16. Their result shown in the figure indicates that the cosmic ray composition is lighter near 3 PeV than that around either 300 TeV or 30 PeV, and becomes heavier with the increasing energy above 3 PeV.

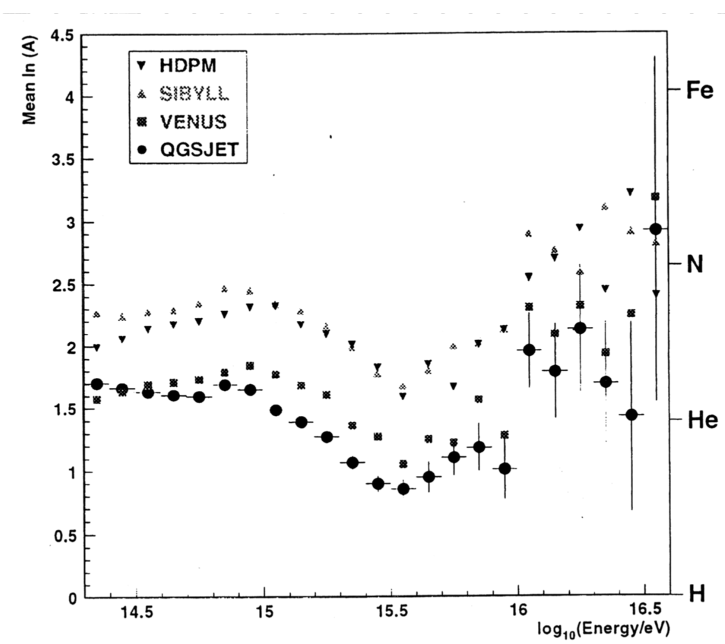

Figure 5.16: The mean logarithmic mass $< \ln A >$ measured by CASA–BLANCA as a function of the energy. The four sets of symbols show the BLANCA data interpreted using CORSIKA coupled with the indicated hadronic interaction model.

5.6 DICE

The DICE(Dual Imaging Cherenkov Experiment) project was another experiment of atmospheric Čerenkov light measurements at the CASA–MIA site. The DICE project had two telescopes and each telescope consisted of a 2m diameter f/1.16 spherical mirror with a focal plane detector of 256 close packed 40mm hexagonal PMTs which provide $\sim 1°$ pixels with an overall field of view $16° \times 13.5°$ centered about the zeith. The telescopes were on fixed mounts separated by 100 m.

A cosmic ray event in the field of view produced a focal plane image on the PMT cluster, and the shape of the image reflected the emission point distribution and the intensities of Čerenkov light. When the direction of an air shower axis and the distance of an air shower core from the telescopes were known, one can reconstruct the longitudinal development of the air shower with a simple geometry. Essentially, this procedure is geometrical and is independent of numerical simulations except for calculations which determine the angular distribution of Čerenkov photons around shower axes. This feature is an aim of this experiment, and then DICE was designed to be independent of the details of the air shower simulations.

The DICE group determined the location of shower maximum in the atmosphere(X_{max}) by fitting the shape of a shower image in each of the DICE PMT clusters. An accurate determination of energy was derived from a combination of the amount of Čerenkov photons and X_{max}. A total shower energy E and a primary particle mass A were obtained from the geometry, Čerenkov size (Ch) and X_{max}. The exact forms of these fitting functions were obtained by Monte Carlo simulations, and given as follows:

$$\begin{aligned} Ch &= C_0 E(\mathrm{PeV})^{\gamma} A^{-\epsilon} e^{-\beta r(\mathrm{m})} && (5.2) \\ X_{max} &= X_0 + X_m(\log E - \log A), && (5.3) \end{aligned}$$

where

$$\begin{aligned} C_0 &= 1.89 \times 10^6, && (5.4) \\ \gamma &= 1.144 + 0.0905 \log A, && (5.5) \\ \beta &= 0.0161(1 - 0.128 \log A) + 0.124 \log E(\mathrm{PeV})(1 + 0.322 \log A), && (5.6) \\ \epsilon &= 0.186, && (5.7) \\ X_0 &= 560\mathrm{g/cm^2}, && (5.8) \\ X_m &= 80\mathrm{g/cm^2}. && (5.9) \end{aligned}$$

The events were collected by DICE in coincidence with CASA–MIA over a period from mid 1994 to early 1996 [88]. The all particle flux by the DICE experiment is shown in Figure 5.17. They calculated the mass composition with two sets of measure values: (1) the location of X_{max} and the fitted shower energy, (2) the muon and the electron sizes in combination with the fitted energy. The results are shown in Figure 5.18. These results do not support a simple "rigidity steepening" which would lead to steady increase in the mass composition across the knee region. The dotted curve is a prediction with a model where a source spectrum is proportional to E^{-3} above the knee region and the energy dependent escape from the Galaxy was assumed to reach a plateau near the knee region. The dashed line, to which the data seem more consistent, was a model which introduces a proton source to compensate the lost flux above the SNR acceleration cutoff rigidity. This model was similar to that of Szabo and Protheroe described in Chapter

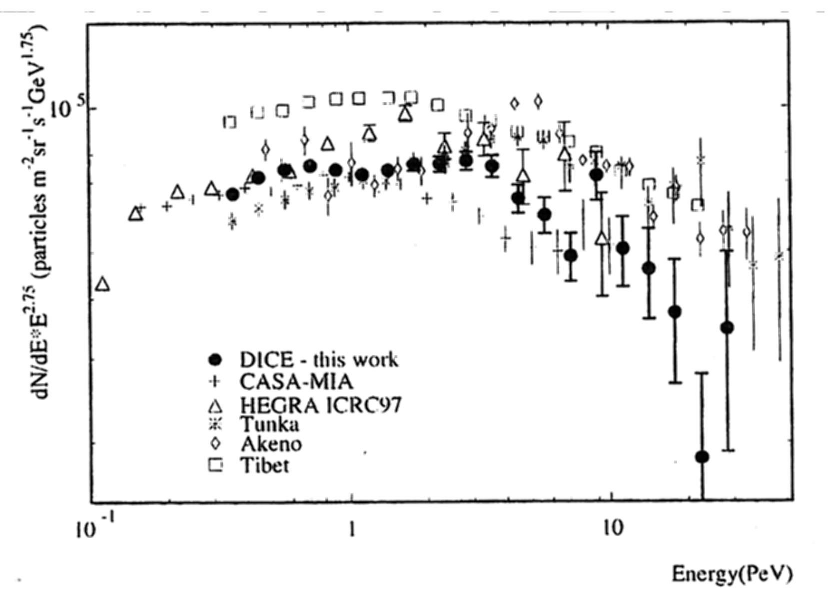

Figure 5.17: The spectra near the knee by the DICE group and by some other groups.

3 [89] where an extra-galactic component of particles produced by AGNs provides the cosmic rays at the knee region.

The DICE group made reanalysis with considering the systematic errors including the mirror spot sizes, the dead spaces between the PMTs and the electronics saturations [64]. The mass composition as the results of their reanalysis have not be published yet.

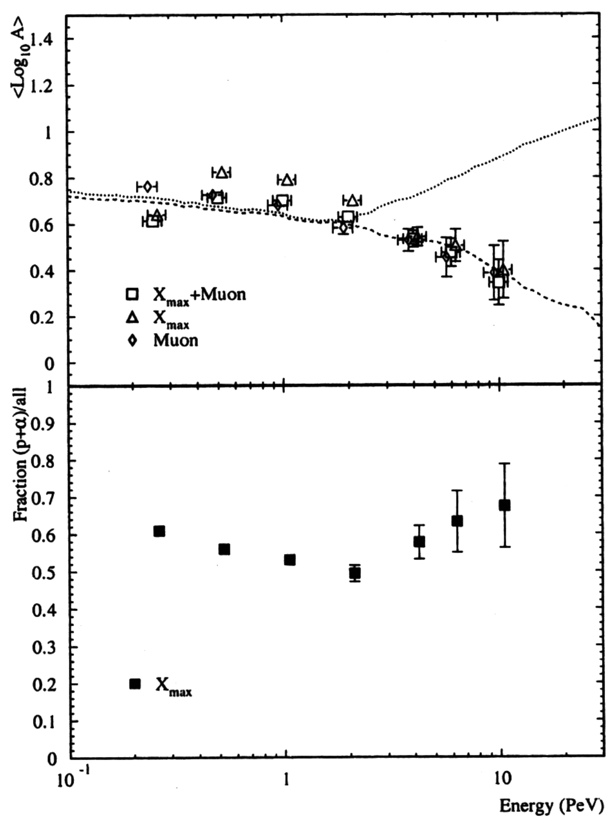

Figure 5.18: (*upper*) The result for the mean mass measurement by DICE and the model predictions. (*lower*) The result of (p+α)/all.

5.7 BASJE–Čerenkov

The BASJE experiment observed air showers at Mt. Chacaltaya (5200 m a.s.l.) in Bolivia. Shirasaki et al. [82] reported the result of their observation of atmospheric Čerenkov photons associated with air showers detected by Čerenkov detectors and the Small Air Shower(SAS) array [56](Figure 5.19). For estimation of the cosmic ray composition, they observed Čerenkov light pulse shapes which strongly reflect longitudinal developments of air showers.

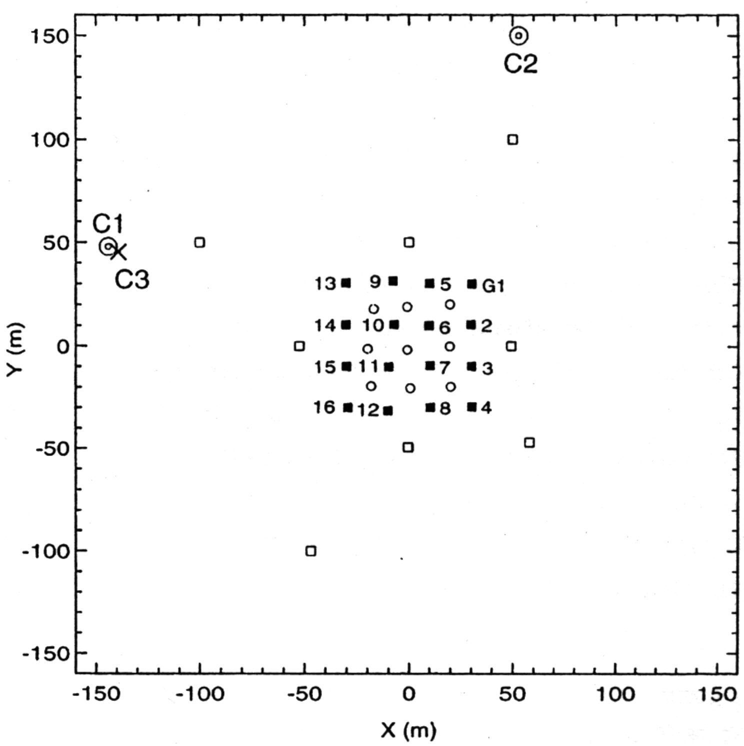

Figure 5.19: The arrangement of the scintillation detectors of the SAS array and the Čerenkov detectors.

One Čerenokov light detector consists of seven 5–inch PMTs. In 1995 and 1996, they used two Čerenkov detectors separately at 150 m from the center of the array(point C1 and C2 on Figure 5.19) to achieve wide effective detection area and enough statistics at the energy range $10^{15.8} - 10^{16.5}$ eV. In the next year, four Čerenkov detectors were install at same position(C3) and the signals of the detectors were added with fast buffer amplifiers for enhancement of signals to noise ratio and to decrease the threshold energy to 10^{15} eV.

They used the parameter T_{10-90}, which is defined as the rise time of a time–integrated Čerenkov pulse, for estimating the mass composition. Figure 5.20 shows the composition dependence of this parameter. With comparing the observed T_{10-90} distributions with the simulated ones for three different mixtures of components(ex. Figure 5.20), they estimated the mean mass number as shown in Figure 5.21.

They discussed four different source models of cosmic ray particles, and concluded that considering additional heavy matter ejected from pre–supernova, a stellar wind model proposed

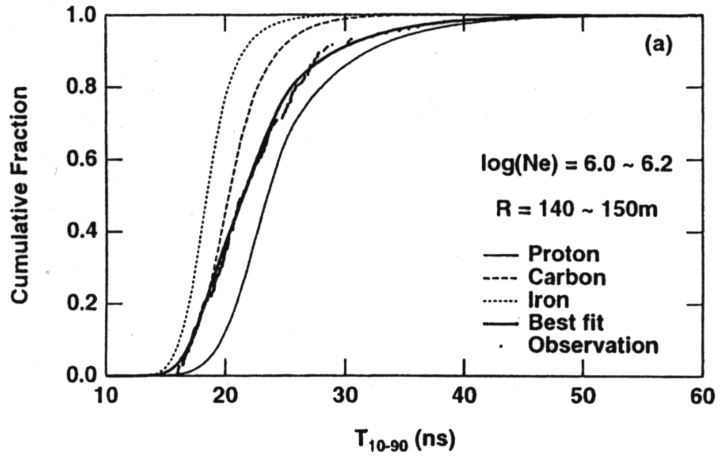

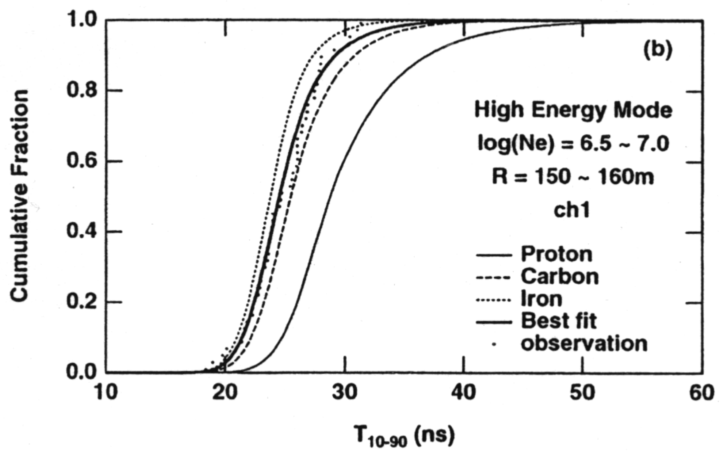

Figure 5.20: Comparison of the cumulative fraction distribution of experimentally determined $T_{10-90}(dots)$ with the distributions expected for proton, carbon and iron primaries. These are result for (a) $\log N_e = 6.0 - 6.2$, $R = 140 - 150$ m obtained in the low energy mode observations, and (b) $\log N_e = 6.5 - 7.0$, $R = 150 - 160$ m obtained in the high energy mode observations.

by Biermann [15] shows a good agreement with both the all particle flux and the mean mass number.

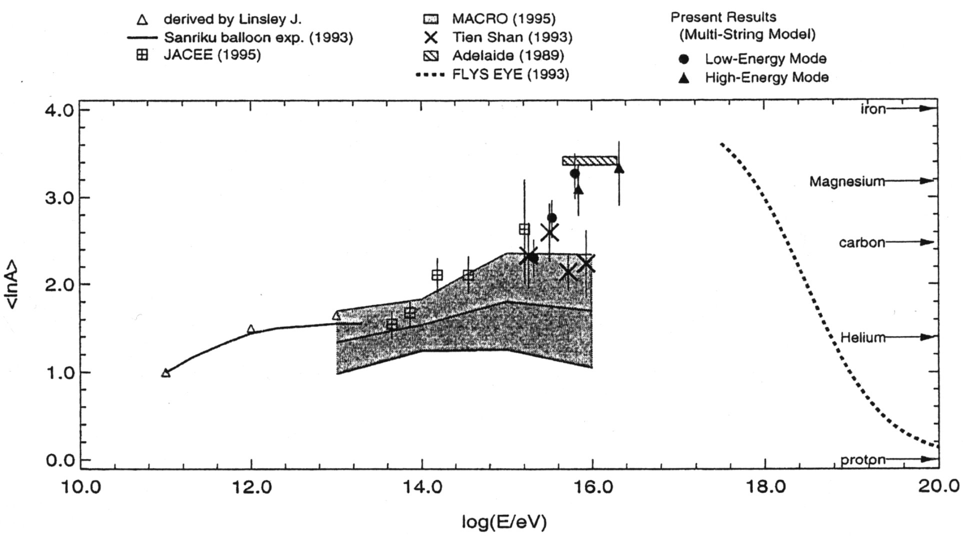

Figure 5.21: Comparison of BASJE–Čerenkov results with the other direct and indirect experimental results.

5.8 KASCADE

The KASCADE site [61] is located at the site of the Forschungszentrum Karlsruhe, Germany at an altitude of 110 m a.s.l., and they observe EASs especially in the knee region. Their air shower array consists of three major detector components(Figure 5.22): the scintillator detector surface array, the muon tracking detectors and the central detector complex.

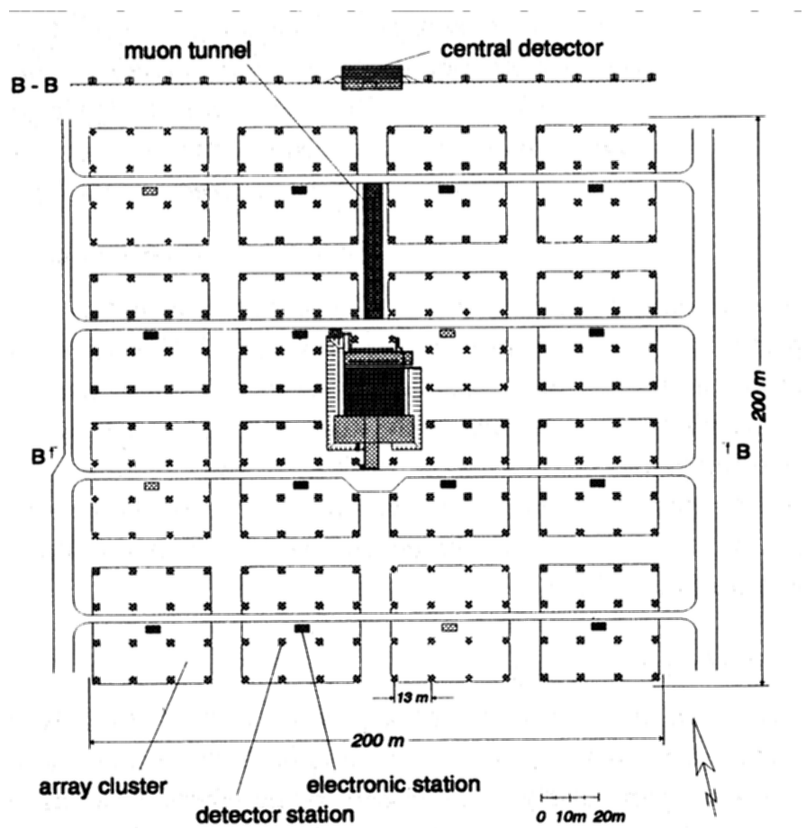

Figure 5.22: A schematic layout of the KASCADE experiment.

The surface array covers an area of $200 \times 200\mathrm{m}^2$ and consists of 252 detector stations for the detection of electron and muon components. Each station of the inner part of the array contains four liquid scintillation counters to detect electromagnetic components of an EAS. Each outer station contains only two of these detectors, but it has plastic scintillators to detect muons below an iron–lead absorber. Using the information of these detectors they reconstruct the shower core positions, the arrival directions of EASs, the total numbers of electrons, N_e, and the so called the truncated muon numbers, $N_\mu^{tr.}$. $N_\mu^{tr.}$ is the number of muons inside the concentric ring around a shower core with the inner radius of 40 m and the outer radius of 200 m. The hadronic components of an EAS is studied with a $320\mathrm{m}^2$ large iron calorimeter. The impact point, the energy, and the direction for hadrons are reconstructed above a threshold energy (= 50 GeV).

Ulrich et al. [94] determined the primary energy spectra for different mass groups by analyzing the shower size spectra of N_e and $N_\mu^{tr.}$. The data used in the analysis consist of N_e and $N_\mu^{tr.}$ spectra in three zenith angle bins; $0° < \theta < 18°$, $18° < \theta < 25.9°$ and $25.9° < \theta < 32.3°$(Figure

5.23). Their analysis was based on the relation between the measured shower size spectrum

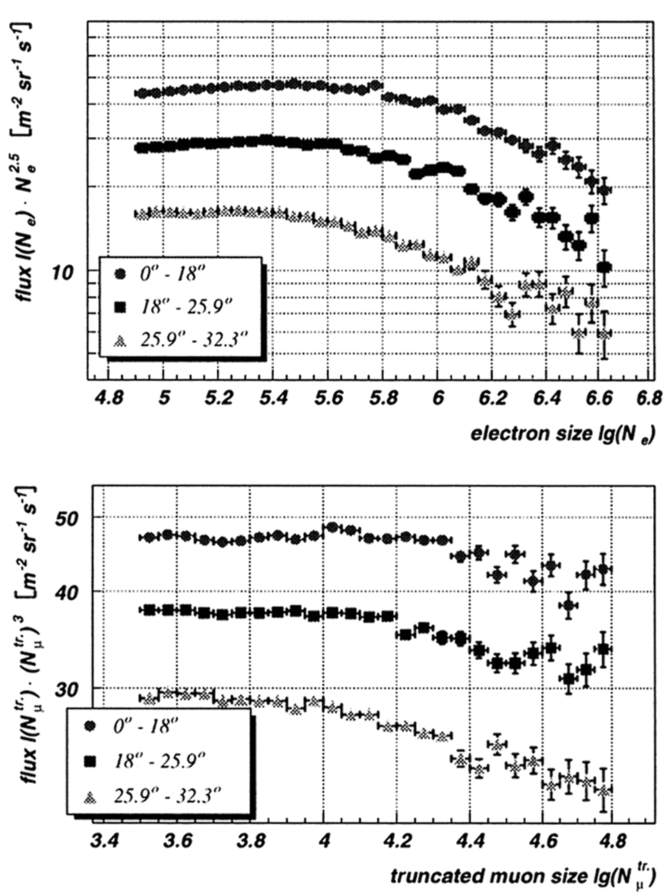

Figure 5.23: Electron size spectra (*upper*) and truncated muon size spectra(*lower*) in the intervals of zenith angle.

$dJ/d\log N$ and the primary energy flux $dJ_A(\log E)/d\log E$ for primary particles with mass number of A,

$$\frac{dJ}{d\log N} = \sum_{A=1} \int_{-\infty}^{+\infty} \frac{dJ_A(\log E)}{d\log E} p_A(d\log N|d\log E) d\log E \tag{5.10}$$

Here $p_A(d\log N|d\log E)$ is the probability for a primary particle of type A with an energy E to be reconstructed as an air shower with shower size N. The measured size spectrum transfered to a vector of numbers of events, $y_i(i = 1, \cdots, n)$, binned with EAS sizes (bin width, $\Delta \log N = 0.05$) The corresponding vector for the energy spectrum, $x^{A_j}(j = 1, \cdots, m)$, binned with the energies (bin width, $\Delta \log E = 0.1$). They obtained the vector x^{A_j} with solving the relation

$$y_i = \sum_{j=1}^{m} R_{ij}^A x_j^A. \tag{5.11}$$

Here R^A_{ij} is an element of the response matrix $\mathbf{R^A}$, which defined as,

$$R^A_{ij} = \frac{\int_i d\log N \int_j d\log E \frac{dJ_A(\log E)}{d\log E} p_A(d\log N | d\log E)}{\int_j d\log E \frac{dJ_A(\log E)}{d\log E}}. \tag{5.12}$$

In the analysis, the data vector $\mathbf{y}$ consists of 6 spectra. The mass composition of primary cosmic rays was assumed to have four components; protons, He, C and Fe. The response matrix $\mathbf{R^A}$ of the four components are arranged in one response matrix $\mathbf{R}$ consisting of 24 sub matrices, and the vector $\mathbf{x}$ represents the four unknown energy spectra.

They obtained the elements of $\mathbf{R^A}$ with the simulation calculations by CORSIKA–QGSJET model. The consequence of the analysis is shown in Figure 5.24 as the all particle spectrum and the energy spectra for four components. They summarized about their results as follows:

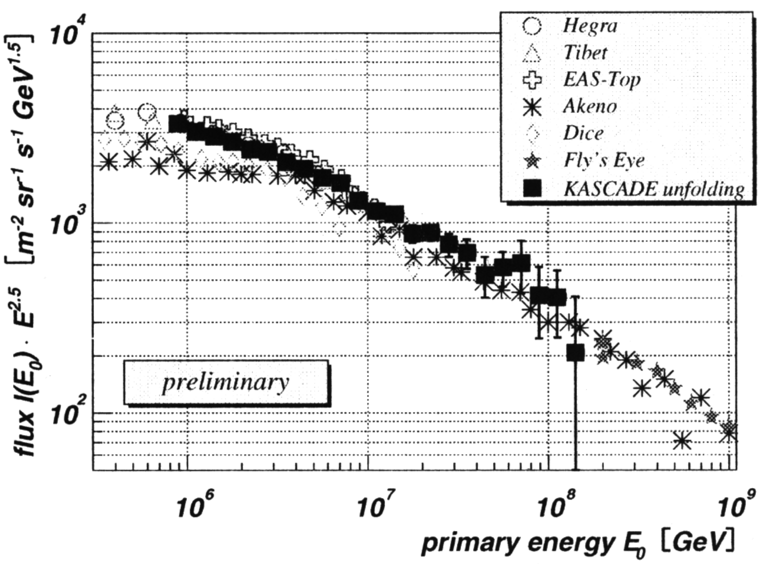

Figure 5.24: The total energy spectrum obtained with the KASCADE (N_e, $N_\mu^{tr.}$) analysis.

1. The energy of the knee on the all particle spectrum was about 5 PeV.

2. Comparing with the results of other experiments, the all particle spectrum showed a good agreement with the data of Tibet and HEGRA.

3. From the differential energy spectra multiplied by E^3 as shown in Figure 5.25, the indexes of the power law describing the individual energy spectra below the knee was steeper for proton than for He, and was flatter for C than for He.

4. From the differential spectra, the factors of the bending point energies of the individual elements relative to that of proton were 2–3 for He, 6–9 for C and $\sim$ 20 for Fe. This suggest a rigidity dependence of the individual knees.

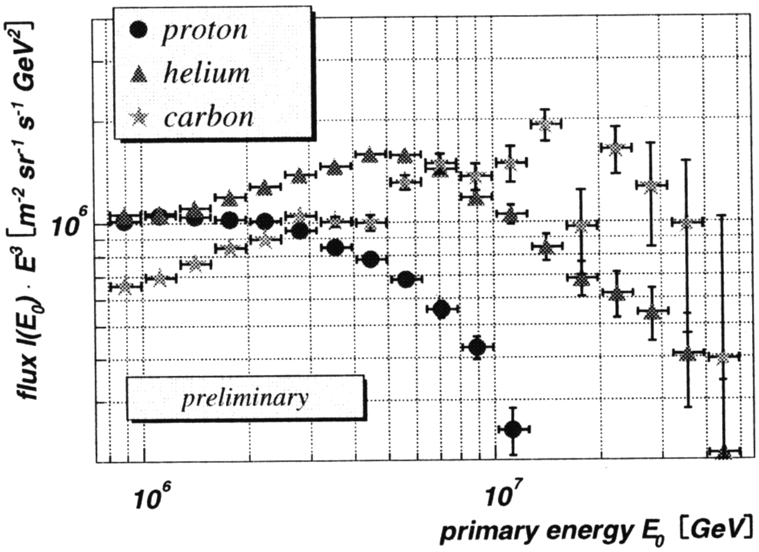

Figure 5.25: The energy spectra of proton, helium and carbon primaries between 1 PeV to 10 PeV as a result of the KASCADE (N_e, $N_\mu^{tr.}$) analysis.

5. They obtained the mean logarithmic mass $\langle \ln A \rangle$ as shown in Figure 5.26. It slowly started to increase at about 2.5 PeV with increasing energy, and $\langle \ln A \rangle$ becomes a constant above 45 PeV.

The KASCADE collaboration also reported the estimated mass composition using the hadronic component of EASs measured by the hadron calorimeter [25]. In this analysis the showers were classified according to their truncated muon size $N_\mu^{tr.}$ measured by the surface detector array. They estimated a mean mass parameter λ as a function of $N_\mu^{tr.}$ from the analysis of the six observable values, namely, the lateral hadron density distributions, the distance distributions in minimum–spanning trees, the lateral energy density distributions, the energy spectra of hadrons, the energies of the most energetic hadron, and the distributions of the fractional energy of hadrons with respect to the most energetic hadron in the showers. Figure 5.27 shows the distributions of two observables comparing with the simulations. λ is linearly related with $\langle \ln A \rangle$ as $\lambda = \langle \ln A \rangle / \langle \ln 56 \rangle$. It indicates the distance to the two extreme compositions: $\lambda = 0$ for a pure proton and $\lambda = 1$ for a pure iron composition. The result of their estimations of λ is shown in Figure 5.28. Consequently, they combined the mean values $< \lambda >$ of all the observable values and for two interaction models, and determined the corresponding $< \ln A >$ as shown in Figure 5.29.

The hadron analysis result follows the trend indicated by the RUNJOB data and by the measurement by Shirasaki et al [82]. However this result shows a too heavy composition comparing their (N_e, $N_\mu^{tr.}$) analysis result. The authors pointed out that the conflict between two results is due to the simulations, and that some investigations have revealed that the simulations generate too many hadrons at observation level [5], [77]. They mentioned that the missing hadrons are interpreted by the hadron analysis as a heavy composition, and that generating too few electrons accounts for the light composition found in the analysis using the electron

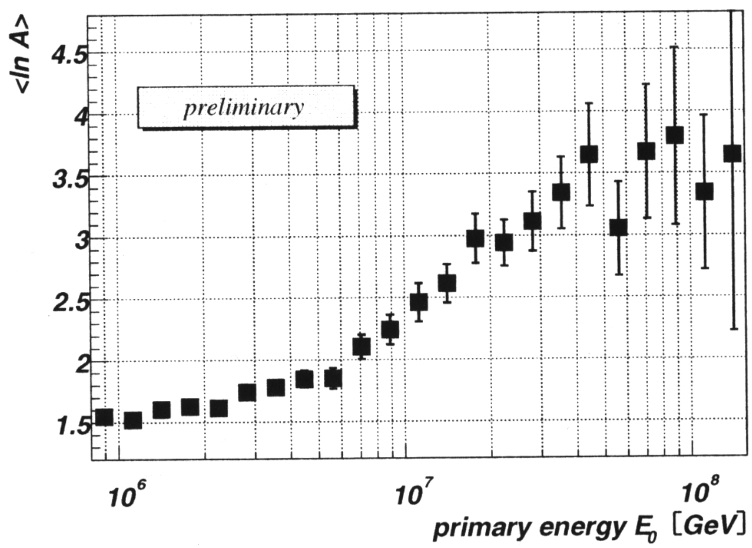

Figure 5.26: The mean logarithmic mass by the KASCADE (N_e, $N_\mu^{tr.}$) analysis.

component only.

5.9 Summary of recent measurements

Here I summarize the recent ground–based measurements of the chemical composition. All the groups detected not only the electron components of EAS particles, but also other components, namely Čerekonkov photons, muons and/or hadrons, because the angular spreads of Čerenkov photons, muons and hadrons relative to a shower axis and the pulse shapes of Čerenkov photons reflect the longitudinal developments of EASs. In addition, the multiplicity of muons and hadrons strongly depend on the mass of the primary particles. The results of the measurements can be classified into the three groups; (1) $\langle \ln A \rangle$ increases with the increasing primary energy, and the averaged mass is heavy ($\langle \ln A \rangle \simeq 2.8$) at the knee energy ($\sim 10^{15.5}$ eV), (2) $\langle \ln A \rangle$ increases with the increasing primary energy, and the averaged mass is light ($\langle \ln A \rangle \simeq 1.6$) at the knee energy, and (3) $\langle \ln A \rangle$ is almost constant up to 10^{16} eV.

From the classification of the results and of the observable values, it is concluded that:

1. In spite of using the similar observable parameters for estimations of chemical composition, the results often seem to conflict between different experiments.

2. At the same sites, the results are inconsistent when the different observable are used.

3. The results with the detections of Čerenkov lights except the BASJE group show the same tendency that $\langle \ln A \rangle$ is energy independent.

The first two conclusions reflect that simulations are imperfect as descriptions of the nature of EASs. The KASCADE group pointed out that the simulations used for their analysis seem to generate too many hadrons at the observational level. The last conclusion shows the difficulties of the corrections both of the efficiencies and the atmospheric attenuation for photons. Moreover,

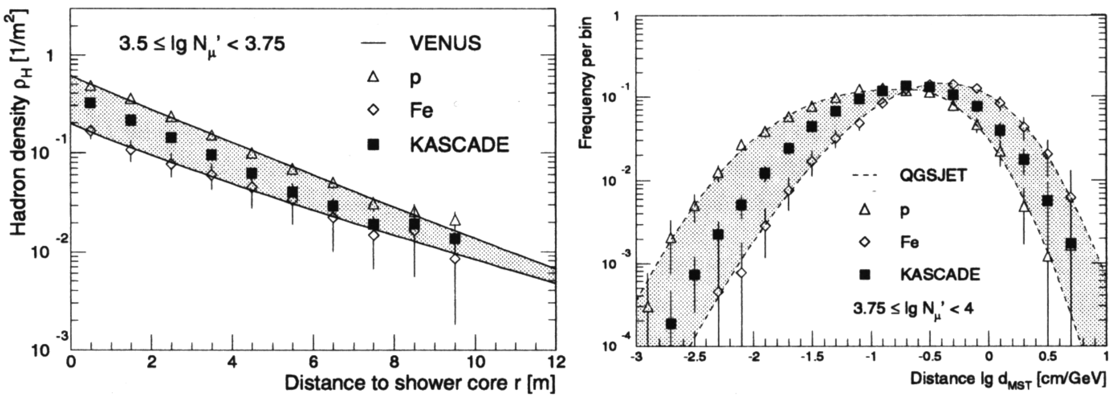

Figure 5.27: Two examples of the hadronic observables measured with the KASCADE hadron calorimeter for estimation of the primary cosmic ray mass composition.

we consider as these two effects lead to the observational biases through the parameterizations of the lateral distributions of Čerenkov photons.

Finally, we conclude that the measurement of chemical composition must be based on the observable independent on simulations and the observational conditions. Thus, I chose the equi–intensity method analysis for the observed EASs at the high altitude equivalent to the maximum development of EASs.

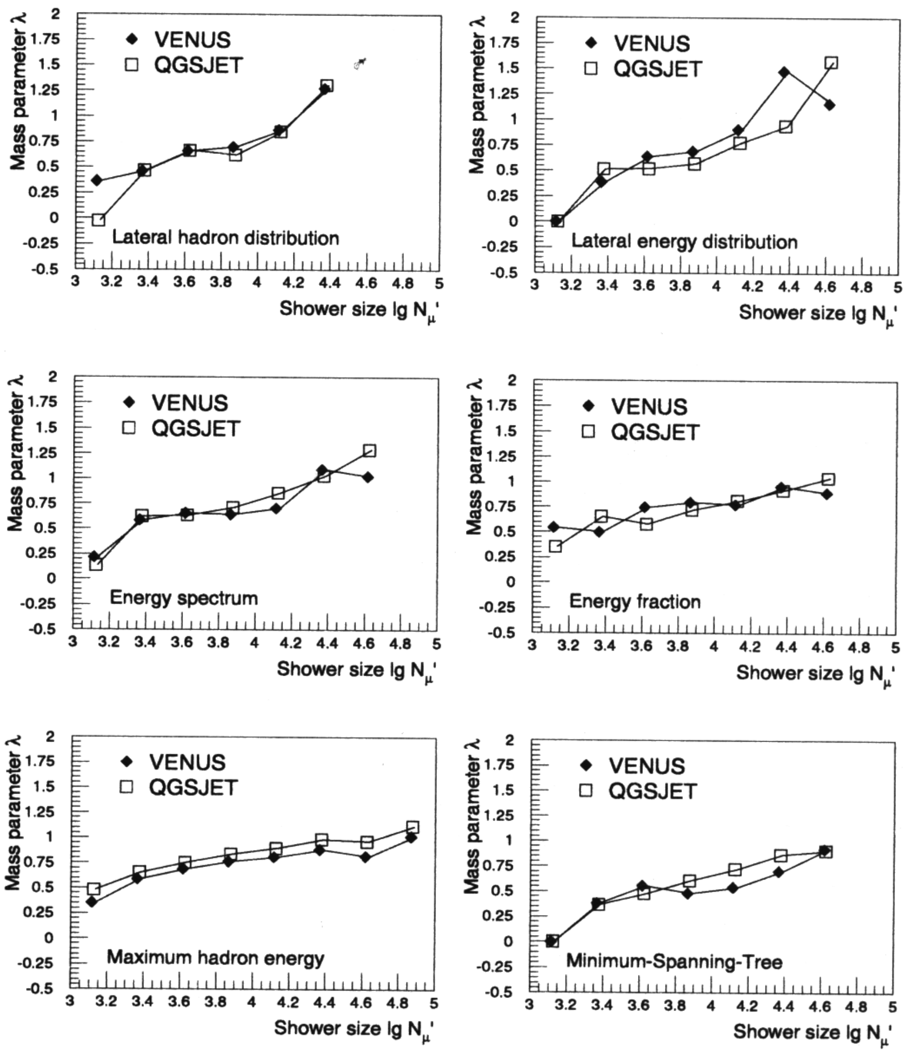

Figure 5.28: The mass parameters obtained from the six observables of the KASCADE experiment.

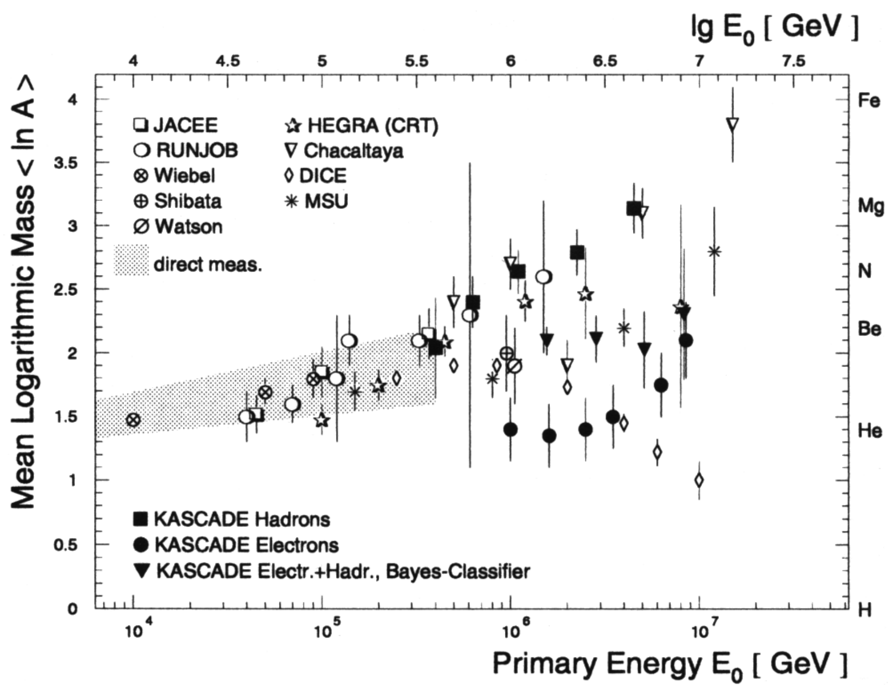

Figure 5.29: The mean logarithmic mass vs the primary energy reported by KASCADE(hadron analysis) and by other experiments.

Chapter 6

BASJE MAS array

This chapter is detailed description about BASJE[1] MAS array, including the experimental details about the site, the detectors and the electronics for the experiment.

6.1 Site

The BASJE MAS(Minimum Air Shower) array is located at Chacaltaya Cosmic Ray Observatory ($16°20'52''$S, $68°07'57''W$) in the Republic of Bolivia. This observatory was established in 1962. The altitude of the site is 5200 m above sea level, which is the highest altitude among the constantly operated observatories all over the world. The site is at about 35 km north–east of the capital city of Bolivia: La Paz.

The altitude of 5200 m a.s.l. corresponds to the atmospheric depth of 550 g/cm^2. According to many Monte Carlo simulations, EASs with primary protons of 10^{15} eV reach their maximum developments at about 600 g/cm^2 and those with primary iron nuclei at about 470 g/cm^2. Thus, we can observe EASs induced by primary protons before their maximum developments at this altitude, and this site is most suitable to investigate cosmic rays around the knee region.

The MAS array constructed as an improvement of the SAS(Small Air Shower) array [57] combined with the detectors of the LMC array [98] which were specially designed to observe the supernova SN1987A. The aim of the construction of the MAS array were, with arranging the detectors higher density than the SAS array, to achieve the lower threshold energy and

[1]The BASJE(Bolivia Air Shower Joint Experiment) collaborators:
O.Burgoa, A.Furuhata, D.Harada, F.Kakimoto, Y.Kurashina, S.Ogio, H.Tokuno and K.Yamada: *Department of Physics, Tokyo Institute of Technology, Meguro, Tokyo, 152-8551, Japan*
H.Furukawa, M.Kubo, A.Morizawa and H.Yoshii: *Department of Physics, Ehime University, Matsuyama, Ehime, 790-8577, Japan*
E.Gotoh, H.Nakatani, K.Nishi, S.Shimoda, N.Tajima and Y.Yamada: *The Institute of Physical and Chemical Research, Wako, Saitama, 351-0198, Japan*
T.Kaneko: *Department of Physics, Okayama University, Okayama, 700-8530, Japan*
Y.Matsubara: *Solar-Terrestrial Environment Laboratory, Nagoya University, Nagoya, A ichi, 464-8601, Japan*
P.Miranda and A.Velarde: *Instituto de Investigaciones Fisicas, Universidad Mayor de San Andres, La Paz, 8635, Bolivia*
Y.Mizumoto, Y.Shirasaki, and Y.Tsunesada: *National Astronomical Observatory, Mitaka, Tokyo, 181-8588, Japan*
K.Murakami: *Nagoya University of Foreign Studies, Nissin, Aichi, 470-0197, Japan*
Y.Toyoda: *Faculty of General Education, Fukui University of Technology, Fukui, 910-8505, Japan*

the higher accuracy of size determinations. At present, the MAS array consists of sixty-eight unshielded scintillation detectors and a shielded scintillation detector as shown in Figure 6.1 and 6.2. These detectors were deployed over an almost flat field of approximately 10^4 m^2. The average spacing between the detectors is about 5 m at the central area, and 30 m at the outer area. The maximum distance in the elevations among the G–detectors is 20.9 m, and among the N– and F–detectors, which are widely spread around the array, that is 59.8 m.

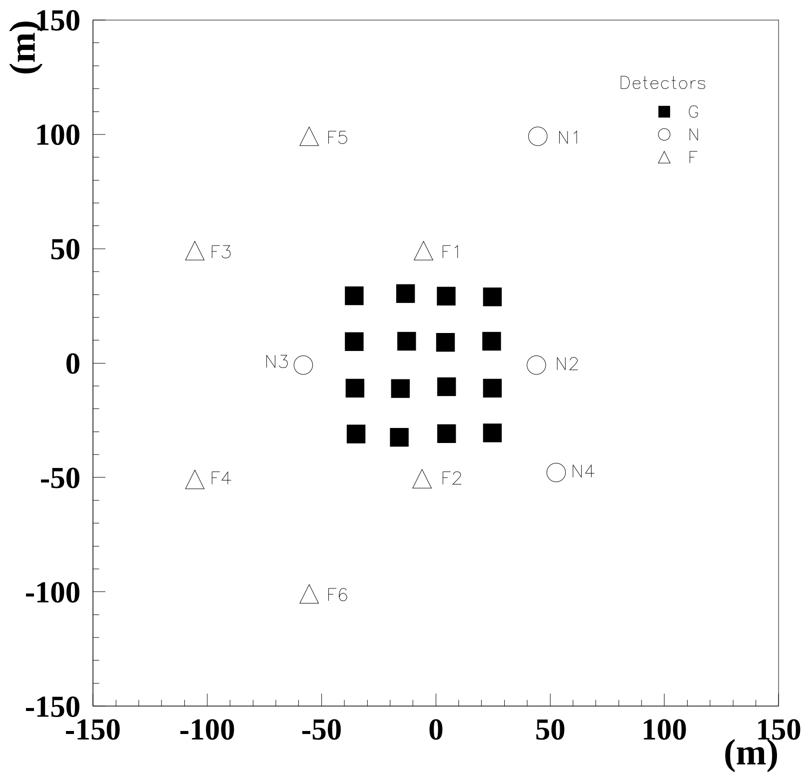

Figure 6.1: BASJE MAS array. Only N–, F– and G–detectors are shown in this figure.

The signals from all the detectors are sent to the central electronics station through coaxial cables for being processed and for being recorded. The details of the detector equipment and the electronics will be described in the following sections.

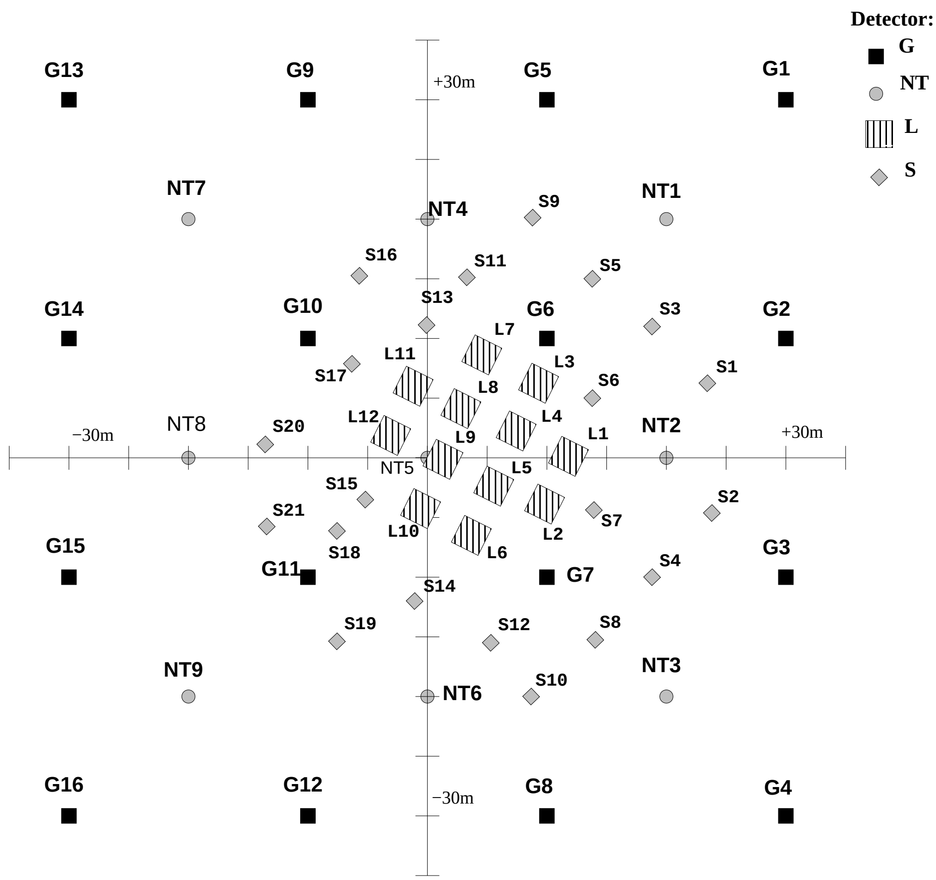

Figure 6.2: The central area of MAS array. The 60m^2 muon detector(the shielded detector) is located at the center of the array (under the L–detectors).

6.2 Detectors

As mentioned in the previous section, the MAS array consists of the sixty–eight surface detectors and one shielded muon detector, and each detector is comprised by a set of plastic scintillators and photo–multiplier tubes(PMTs). The schematic cross sectional illustrations of the surface detectors are shown in Figure 6.3, and that of the shielded muon detector is shown in Figure 6.4.

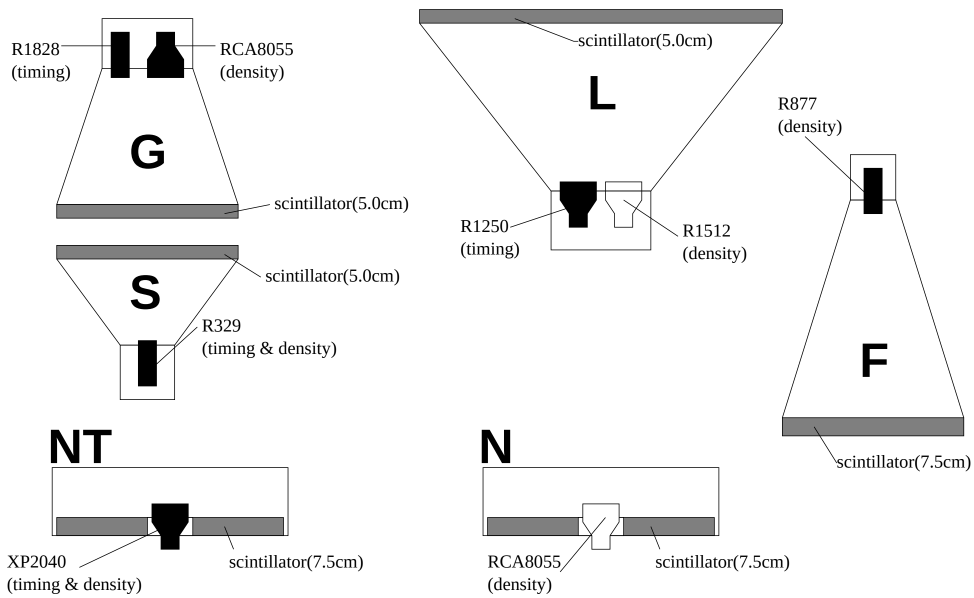

Figure 6.3: The schematic illustrations of the surface detectors of the MAS array.

The detectors are classified into G, NT, L, S, N, F and Mu detectors. The specifications of each type of the detectors are listed in Table 6.1. Each of G and L detectors has two PMTs; one PMT measures the number of particles and the other PMT is a fast-timing channel to measure arrival times of particles. Each of S and NT detectors has only one PMT, and an output signal of it is divided to the density channel and the fast-timing channel. Each of N and F detectors has only one PMT for the density channel.

We also installed a shielded muon (Mu) detector of 60 m^2 area at the center of the array to detect muons in air showers. This detector is the matrix of 3×5 scintillation detectors of 4 m^2 area each as shown in Figure 6.4. The threshold energy of this detector is 600 MeV for vertically incident muons. The characteristics of the Mu detector are reported in reference [58]. Signals of all the detectors are sent to the central station through coaxial cables. The low voltages for the pre–amplifiers and the high voltages for the detectors are supplied from the central station.

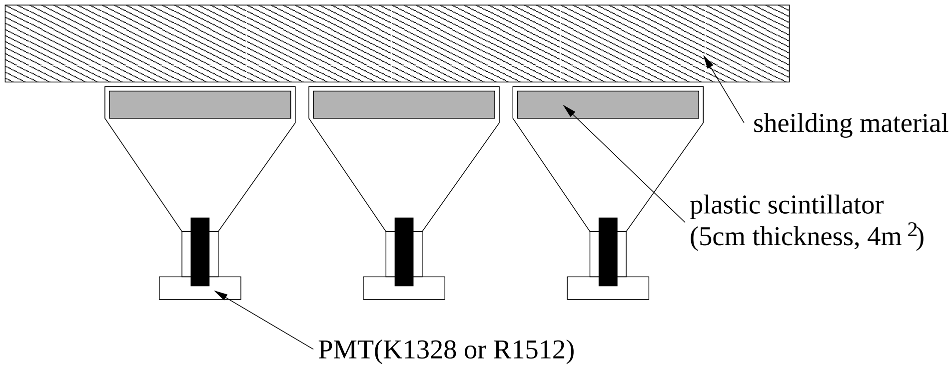

Mu3	Mu6	Mu9	Mu10	Mu13
Mu2	Mu5	Mu8	Mu11	Mu14
Mu1	Mu4	Mu7	Mu12	Mu15

Figure 6.4: The shielded muon detector has the fifteen 4 m^2 scintillation detectors.

detector	number of detectors	area(m^2)	thickness of a scintillator(cm)	PMT	
				density	timing
G	16	1.0	5	R1512	R1828
NT	9	0.87	7.5	XP2040	
L	12	4.0	5	R1512	R1250
S	21	1.0	5	R329	
N	4	0.83	7.5	RCA8055	
F	6	0.83	7.5	R877	
Mu	15	4.0	5	R1512	

Table 6.1: the characteristics of the each type of the detectors.

6.3 Electronics

The signals of the detectors are sent to the central station and processed to be recored. A block diagram of the data acquisition system of the MAS array is shown in Figure 6.5.

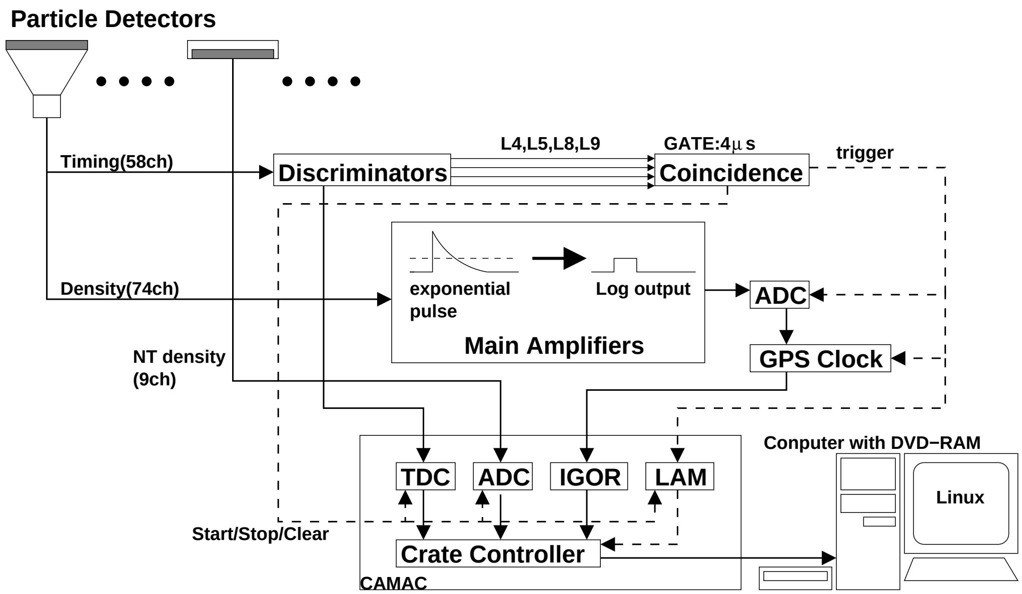

Figure 6.5: Block diagram of the MAS array electronics.

6.3.1 Local particle density measurements

Output signals of each density channel are processed by pre–amplifiers. The pre–amplifiers are installed at the vicinity of each PMT in the detector box to transmit signals with a low impedance to reduce noises and distortions of pulse profiles while signals are fed through cables.

For the measurements of air showers with very high energy cosmic rays around the energies of 10^{15} eV, the required dynamic range for local particle density measurements is four orders of magnitude. So that, a linear amplifier is not suitable to use because of saturations of signals. Therefore, in our experiment, we use following log–amplification methods to achieve the wide dynamic range. The signals of a PMT are shaped into exponential pulses by the RC circuit in the pre–amplifier, and fed into a main amplifier at the central station. After that, an amplified signal with the height V_N is discriminated at the particular level V_{th} and converted to a rectangle output pulse with the width of T_N(Figure 6.6). The pulse width T_N of the output pulse is logarithmically proportional to the pulse height V_N which corresponds to the number of particles N. The relation of T_N and V_N is written by

$$V_{th} = V_N \exp(-T_N/\tau) \quad (6.1)$$
$$= V_0 \exp(-T_0/\tau) \quad (6.2)$$

where τ is the decay constant of the exponential pulse, and depends on the constants of the RC circuit. T_0 is the pulse width of the output which corresponds to single particle signal V_0. Thus the number of shower particles N at a detector is obtained by

$$N = \frac{V_N}{V_0} = \exp\left(\frac{T_N - T_0}{\tau}\right)$$

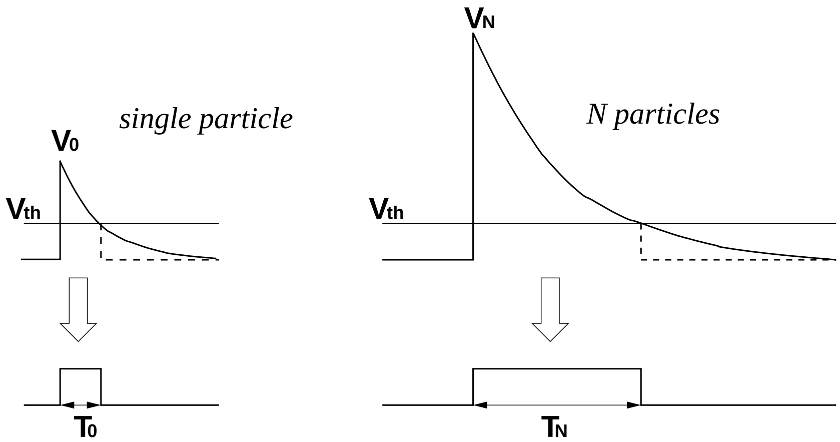

Figure 6.6: Log–amplification method.

The constants, V_0, T_0 and τ, are calibrated for all the local particle density channels. In our experiment, the pulse height of the single particle, V_0, is 2.7 Volts at the linear–output of the main amplifiers for all the density channels. V_0s for all the density channels are monitored daily with a pulse height analyzer(PHA), and adjusted with changing the applied high voltages for the PMTs(Figure 6.7). The applied high voltages range from 700 to 1200 V, and the counting

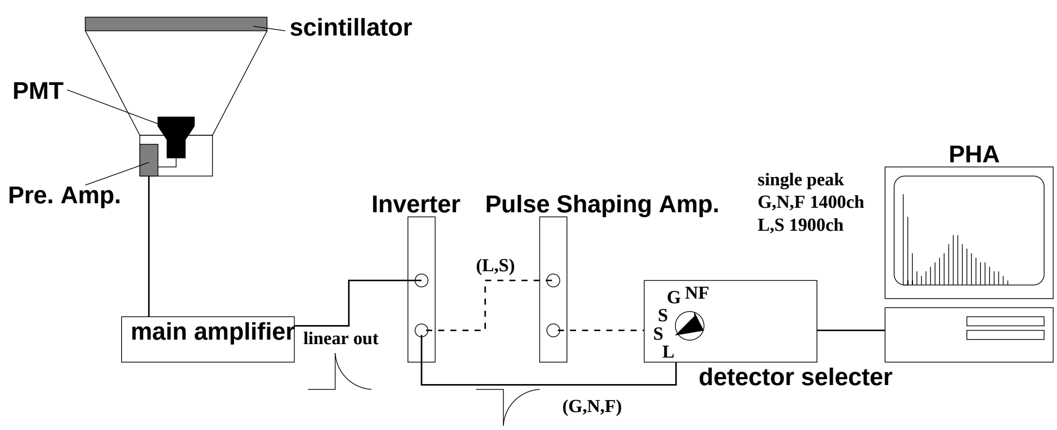

Figure 6.7: The diagram of the high voltage adjustment.

rates of the signals of greater than the single particle level are about 550 Hz/m^2.

The main amplifiers are designed for the T_0 values to be of 1 μs for L and S detectors, and to be 8 μs for G, N, F and Mu detectors. However, T_0 depends on the manufacturing tolerances and variations of the constants of the circuit, and T_0s are measured by the calibration system shown in Figure 6.8. The single particle input is generated with a set of a LED light source, the PMT and the pre–amplifier. The brightness of the LED is adjusted to a PHA peak being 2.7 V at the linear–output of the main amplifier which is calibrated. The corresponding pulse width of the log–output pulse is T_0 and it is measured with a pulse width analyzer(PWA). The error for T_0 is about 0.05 μs for L, S detectors, and is 0.1 μs for other detectors.

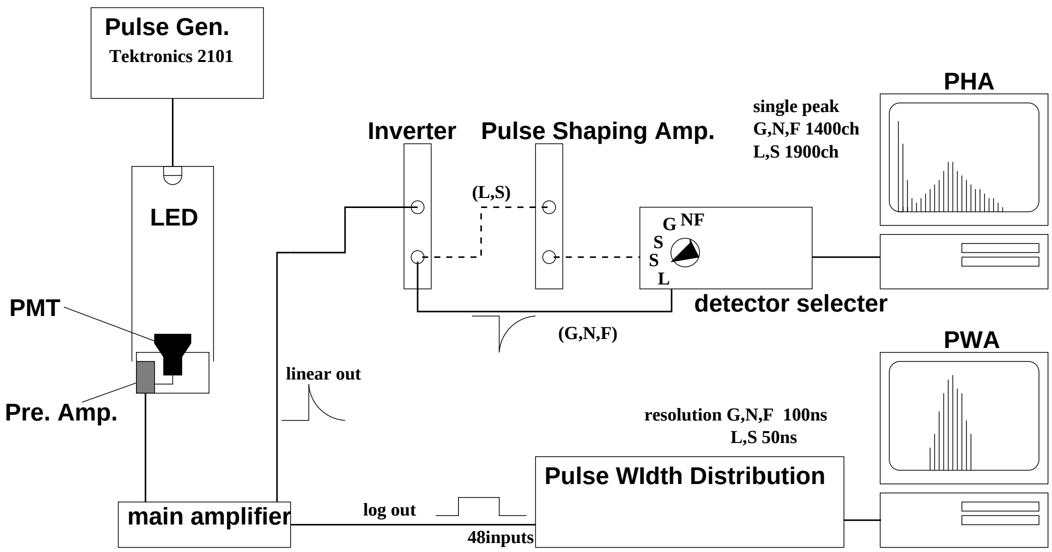

Figure 6.8: The diagram of T_0 measurement.

The time constant τ is calibrated using the relation between the input pulse height and the log–output pulse width. The block diagram of the τ measurement is shown in Figure 6.9. The input pulse is generated as same as T_0 measurements, and is variable with transmittance filters. Figure 6.10 shows an example of the measured relations between the input pulse height and the log–output width. The slope of this figure gives a τ value. The averaged τ value for L and S detectors is 1 μs, for G, N, F and Mu detectors is 10 μs, and the linearities of the relations are confirmed up to more than 10^4 particles for every density channels. The error for τ is about 0.05 μs. The log–outputs of the main amplifiers are processed to digital values with the ADC modules which were developed by the Advanced Engineering Center, RIKEN. The resolution of the ADC corresponds to 10 % for the measured number of particles. Including the errors of T_0 and that of τ and ADC resolution, the determination error for particle densities is about 3% for L detectors, 11% for S detector and 10% for other detectors.

Since we do not use the log amplification system for the measurements of the local density with NT detectors, the dynamic range of the number of particle is very narrow, and thus the data of NT density channels were not used for air shower size determinations.

6.3.2 Fast timing measurements

The accuracy in the determination of arrival directions of air showers depends on the time response of each detector. Then, for fast–timing channels, we use PMTs with fast rise times (less than 10 ns), and the fast–timing signals are fed into the central station without pre–amplifications in order to avoid the distortions of the leading edges on signals. However, we used the pre–amplified signals for S detectors' fast–timing channels because the pre–amplifiers for S detectors [93] have Burr Brown BUF600 buffer amplifiers and have a fast time response,

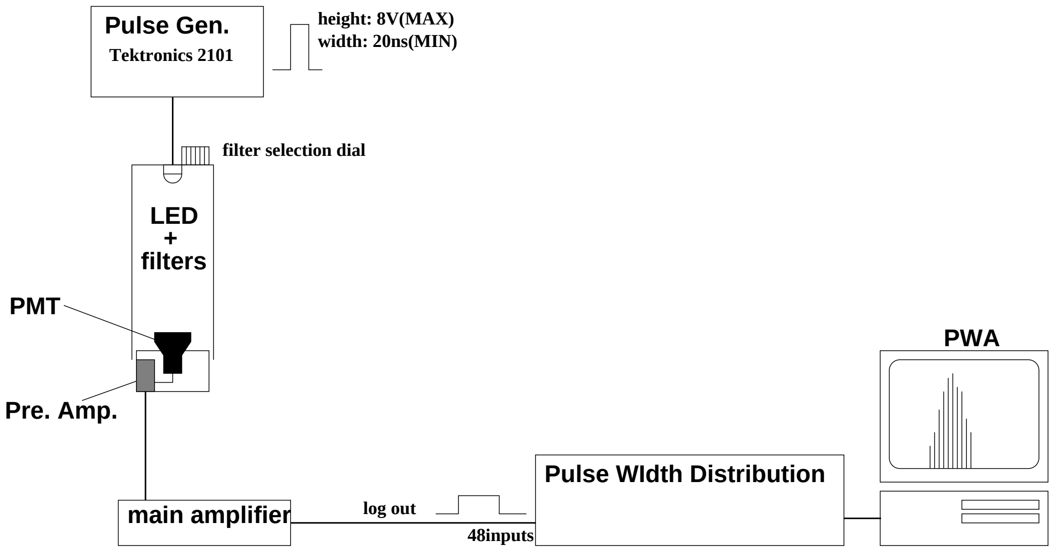

Figure 6.9: The diagram of τ measurement.

in which the typical rise time of outputs is 12 ns for the PMT(HAMAMATSU R329, typical rise time = 3.2 ns) output signals.

The fast–timing signals are discriminated and are fed through the delay cables. Finally, the relative arrival times of these signals are measured with CAMAC TDC(LeCroy 2228A). The discrimination level is set at the pulse height of 0.8 particle equivalent and the typical pulse frequency is 700 Hz/m^2. The transit times of the PMTs and the cable delays for the fast–timing channels are calibrated with a reference detector. The measured fluctuations on total delay times are about 1 ns for G, 2 ns for L and 3 ns for S and NT detectors.

The time resolutions of the TDCs are 50 ps for the L detectors, 250 ps for the S detectors and 500 ps for the other detectors. The linearities between the time difference and the TDC counts are calibrated with a CAMAC TDC tester(REPIC RPC–070). Figure 6.11 shows an example of the TDC calibration. The typical error in the linearity of the TDC is 0.001 %, and is sufficiently small for our requirement.

6.3.3 Trigger

A trigger signal of MAS array is generated with a 4–fold coincidence of the undelayed fast–timing signals of the central four detectors, *i.e.*, L4, L5, L8 and L9 within the gate time window of 4 μs. The discrimination levels for the trigger channels are set to the pulse height of 0.8 particle equivalent. The triggering rate is about 8.5 Hz.

When one of the undelayed hit signals of the trigger detectors is occurred, the coincidence module generates the common start signal for starting digitization in the CAMAC TDCs. Consecutively, if the four trigger detector signals coincide within 4 μs, a triggering signal is to ADC modules for density measurements, and to sent the GPS clock module to register the event date/time. This trigger signal is also sent to a CAMAC LAM(Look At Me) module in order to generate an interrupt signal for starting the data acquisition procedure with the CAMAC crate controller and the personal computer. If a coincidence is not occurred, the coincidence module sends a clear signal to all the modules(Figure 6.5).

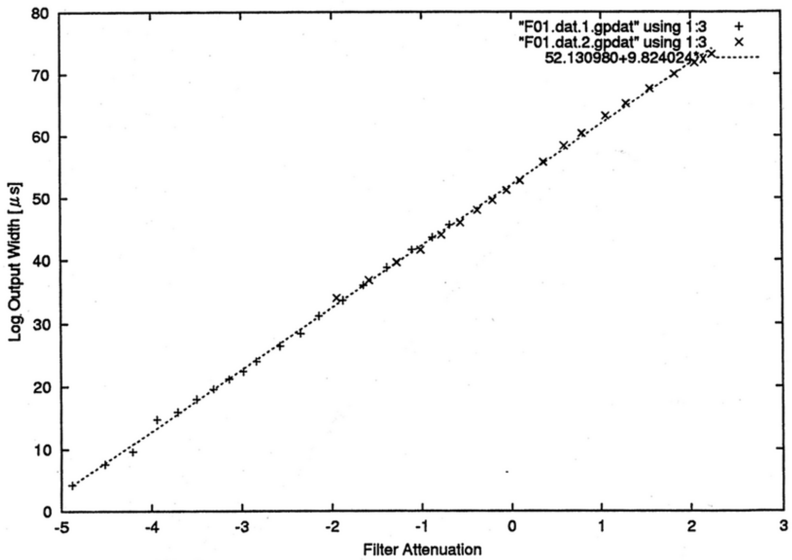

Figure 6.10: An example of τ measurement. The filter attenuation is logarithmically proportional to the pulse height. In this example, the τ value is determined 9.82 μs for the F–1 detector.

6.3.4 Data acquisition system

A local time when an air shower hits the array is measured with a digital clock calibrated with GPS. The stability of this clock is better than 10^{-7}. This clock is also developed by the Advanced Engineering Center, RIKEN. This GPS clock and the ADC modules are accessible through a CAMAC IGOR(Input Gate and Output Register, Kinetic 3063). When the data acquisition system is triggered, a set of data, *i.e.*, the output of TDC and ADC and the local time of the event, is sent to the CAMAC crate controller(TOYO CC7700) and is transfered to the DAQ computer through the PCI board(TOYO CC/PCI).

The DAQ computer is an IBM compatible PC with the cpu of MMX Pentium(166MHz) and the Linux OS(kernel version is 2.0.35). In our experiment the size of data is 348 bytes per events, and thus the total amount of data is reached 0.3 GB for a continuous operations in a day. In order to store this huge size of data, we adopted DVD–RAM drive(Panasonic LF–D102) and disks(2.6 GB) with considering its capacity, robustness, reliability and cost. The data storage has a sufficiently fast transfer speed, which is measured about 600 kB/s on the Linux OS.

A set of application programs to control the data acquisition procedures is developed. This is comprised by three programs and these processes are communicate each other through the functions on the Liunx called the shared memories and the signals(Figure 6.12).

The program named “eco” is a data acquisition program with the CAMAC functions. The CAMAC functions included in the program were developed by the KEK online group. This program reads out data from CAMAC modules and stores on a local hard disk drive(HDD). One data file contains 150,000 events(about 52.2 MB). Each data file is transfered to DVD–RAM with the program named “datast”. The forty data files are written in one DVD–RAM. These two processes are controlled by the program named “xmas”. This is X–window system application written in Tcl/Tk, and is graphical user interface to control all the process and to

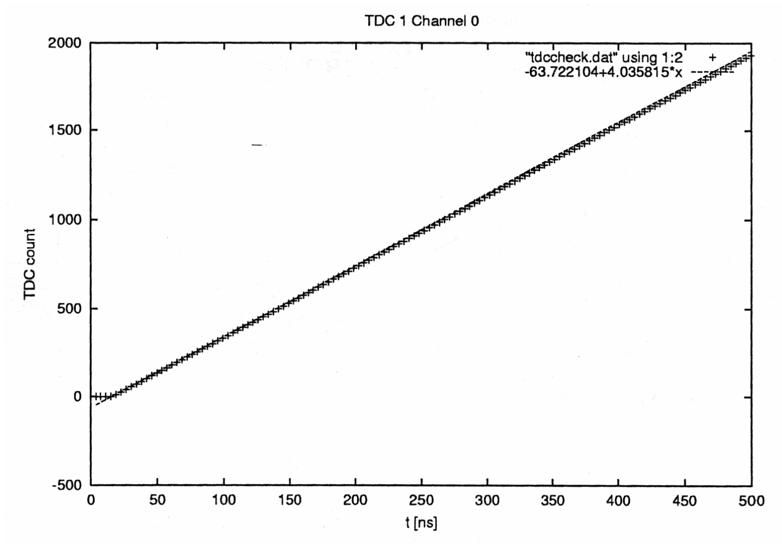

Figure 6.11: An example of the measurement for the linear relation between time differences and TDC counts.

provide the monitoring functions for the acquired data and for the acquisition processes.

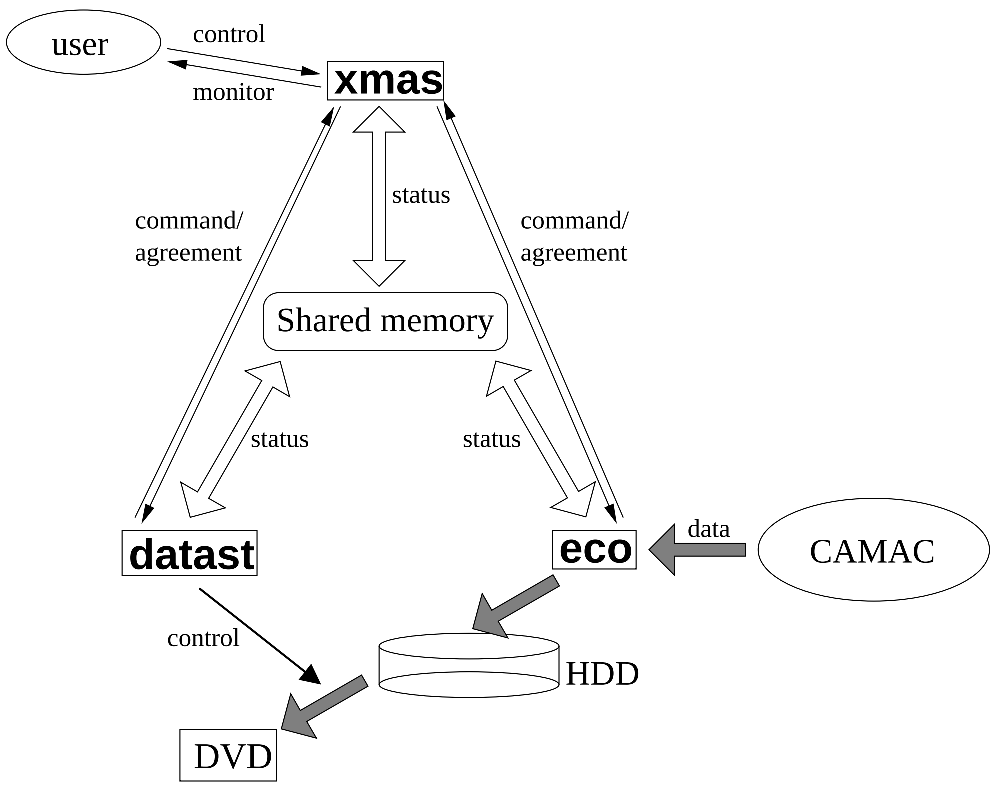

Figure 6.12: The block diagram of the data acquisition processes for the MAS array.

Chapter 7

Air shower analysis and characteristics of the array

7.1 Air shower analysis

7.1.1 Determination of arrival direction

The arrival directions of air showers are determined by the relative arrival times measured through the TDCs and with the positions of the fast-timing detectors. Each TDC value is converted to a relative time, and corrected with the calibrated delay time. When we assume that the surface of a shower disk is a plane, each set of the detector position(x, y, z) and the arrival time of a shower front(t) should satisfy the following relation,

$$lx + my + nz - ct = 0 \tag{7.1}$$

where c is the speed of light. (l, m, n) are the direction cosines of the shower axis, and have the following relations with the zenith angle θ and the azimuth angle ϕ,

$$\begin{aligned} l &= \sin\theta\cos\phi & (7.2) \\ m &= \sin\theta\sin\phi & (7.3) \\ n &= \cos\theta & (7.4) \end{aligned}$$

The vector (l, m, n) is determined by minimizing the χ^2 which is defined as

$$\chi^2 = \sum_i w_i \left[lx_i + my_i + nz_i - c\,(t_i - t_0)\right]^2 \tag{7.5}$$

where (x_i, y_i, z_i) is the position of the detector i and t_i is an arrival time of a shower front at the detector i. The weight w_i is determined from the error for the timing measurements. The equation to be solved is

$$\frac{\partial\chi^2}{\partial l} = \frac{\partial\chi^2}{\partial m} = \frac{\partial\chi^2}{\partial n} = 0 \tag{7.6}$$

under the condition $l^2 + m^2 + n^2 = 1$. In our analysis, this procedure is iterated by three times with excluding the data sets which have the relative times separated more than 15 ns from the estimated shower plane in order to avoid the determination errors based on accidental hits on the detectors by local muons.

The actual shower front has a corn–like structure, not a plane perpendicular to the shower axis. When we require an improvement of the accuracy of arrival direction determinations, the corrections of the corn structure should be applied for relative arrival times.

The corn structure of shower front is described with delay times of shower particles from the approximated shower plane as shown in Figure 7.1. The mean delay time is expressed by the empirical formula obtained through the measurements of the SAS array [57] as follows,

$$T_d = (-0.120 \pm 0.164) - (1.334 \pm 0.337) \log r + (2.125 \pm 0.156)(\log r)^2 \text{ ns} \tag{7.7}$$

with the fluctuation

$$\sigma_t = 0.777 \left(1 + \frac{r}{30\text{m}}\right), \tag{7.8}$$

where r is the distance from a shower axis.

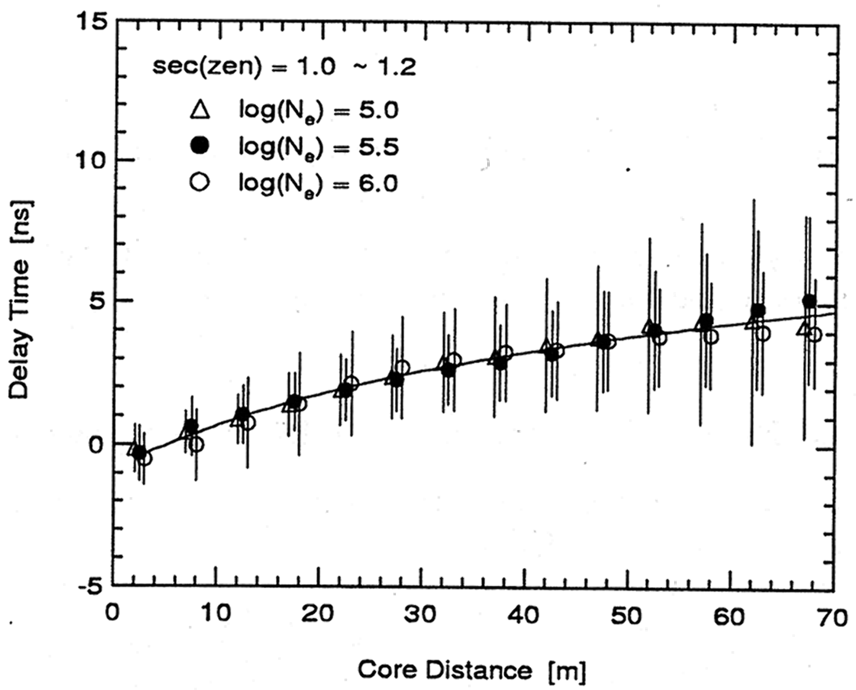

Figure 7.1: Delay time of shower particles from the shower plane measured at Mt. Chacaltaya with SAS array. The line in the figure is a calculated delay time with the formula (7.7).

The accuracy in the determination with the corn structure is 20 % better than that with the plane approximation. However, the calculation time of the cone structure fitting becomes longer that of the plane fitting, for example, by about 10 times with one present calculation code. Then we did not apply the procedure with the corn structure corrections for the following analysis.

7.1.2 Determination of shower size

The shower core position and the shower size of an air shower are determined with minimizing the following χ^2,

$$\chi^2 = \sum_i w_i \left(\rho_i^{obs} - \rho_i^{exp}\right)^2. \tag{7.9}$$

ρ_i^{exp} and ρ_i^{obs} is expected and observed particle densities at the detector i, respectively. When we measured local densities at the same core distance with more than two detectors, the densities are averaged over these detectors and the averaged density is used as ρ_i^{obs} for them. When the particles in a locally high particle density region near a shower axis hit a detector i, the weight w_i for (7.9) becomes too large, and the determined core position is drawn to the detector. Since the determined core positions are localized near the detector positions, the density averaging procedure for the equidistant detectors are performed in order to avoid this localizations. For this averaging calculation, the resolution of core distances is 1 m, because this is a typical size of the detectors. This procedure is efficient for the events with large air shower sizes.

An expected density, ρ_i^{exp} is calculated with the following functions,

$$\rho(r_i, s) = \frac{N_e}{r_m^2} f(r_i, s), \tag{7.10}$$

$$f(r_i, s) = C(s) \left(\frac{r_i}{r_m}\right)^{s-2} \left(1 + \frac{r_i}{r_m}\right)^{s-4.5}, \tag{7.11}$$

$$C(s) = \frac{\Gamma(4.5 - s)}{2\pi\Gamma(s)\Gamma(4.5 - 2s)}. \tag{7.12}$$

here r is the core distance and r_m is the half of the Molière length. In our site at 5200 m a.s.l., the length is 155m [57], and thus $r_m = 77.5$ m. N_e is a shower size, and it is estimated from the observed particle densities by

$$N_e = \frac{\sum w_i' \cdot \rho_i^{obs} \cdot r_m^2 / f(r_i)}{\sum w_i'}. \tag{7.13}$$

The weights w_i of (7.9) and w_i' are defined $w_i = 1/\sigma_i^2$ and $w_i' = f^2(r_i)/\sigma_i^2$ with the standard deviation σ_i of ρ_i^{exp}. From the detailed analysis of the observed air shower particles with the SAS array, we found that the standard deviation σ is expressed well with the following empirical formula [57],

$$\sigma = (1.25 \pm 0.68)\rho^{exp} + (7.08 \pm 0.24)(\rho^{exp})^2. \tag{7.14}$$

The observed standard deviation as a function of expected density is plotted in Figure 7.2 with the calculated curves by (7.14).

We used a simple grid–search method to find a minimum chi–square solution. This calculations are performed in orthogonal co–ordinate systems with shower axes as the z co–ordinates.

1. The density-weighted average of detector positions is chosen as a starting values of a grid–search, (x_0, y_0).

2. Place a square with sides of L meters, and the starting point(x_0, y_0) is centered in the square. The initial length of L is 120 m.

3. Search the point(x_m, y_m) minimizing χ^2 among $7 \times 7 = 49$ grid points in the square.

4. Replace L and (x_0, y_0) with $L/6$ and (x_m, y_m), respectively. Then repeat the step 2–4 until $L < 1$ m.

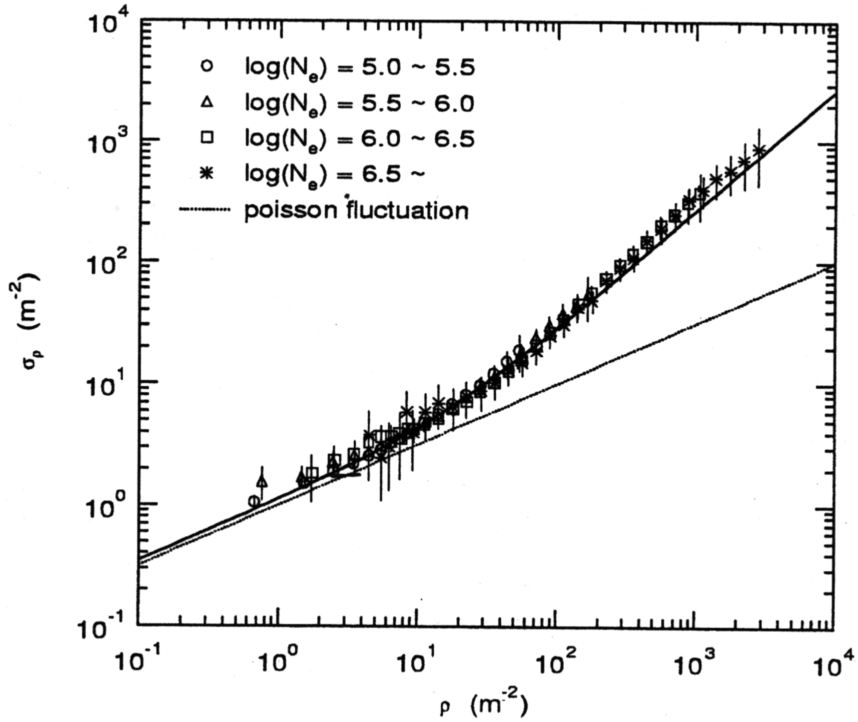

Figure 7.2: The fluctuation (σ_ρ) of shower particle density ρ. σ_ρ is independent of air shower size.

7.2 Performance of MAS array

7.2.1 Effective area

The effective area of the array is estimated with the triggering efficiency, which is defined as,

$$\eta(r, E) = \frac{\text{number of triggered events}}{\text{number of simulated events}}, \tag{7.15}$$

for air showers of a primary energy E and the core distance of $r \sim r + \mathrm{d}r$. So that, the effective area $S_{\text{eff}}(E)$ is given by,

$$S_{\text{eff}}(E) = \int_0^\infty 2\pi r \eta(r, E) \mathrm{d}r. \tag{7.16}$$

$S_{\text{eff}}(E)$ for the array shown in Figure 7.3 [99] was calculated for the events of the zenith angle $\theta < 60^\circ$ with the simulation code developed by Shirasaki [83] and Tsunesada [93].

The expected energy distribution of observed cosmic rays with the array is calculated with $S_{\text{eff}}(E)$ and primary energy spectrum. When we assume a prevalent spectrum with the index of 2.7, the expected energy distribution of cosmic rays is obtained with the following formula,

$$\left(\frac{\mathrm{d}N}{\mathrm{d}E}\right)_{triggered} \mathrm{d}E = \int_E^{E+\mathrm{d}E} S_{\text{eff}}(E) \left(\frac{\mathrm{d}N}{\mathrm{d}E}\right)_{primary} \mathrm{d}E \tag{7.17}$$

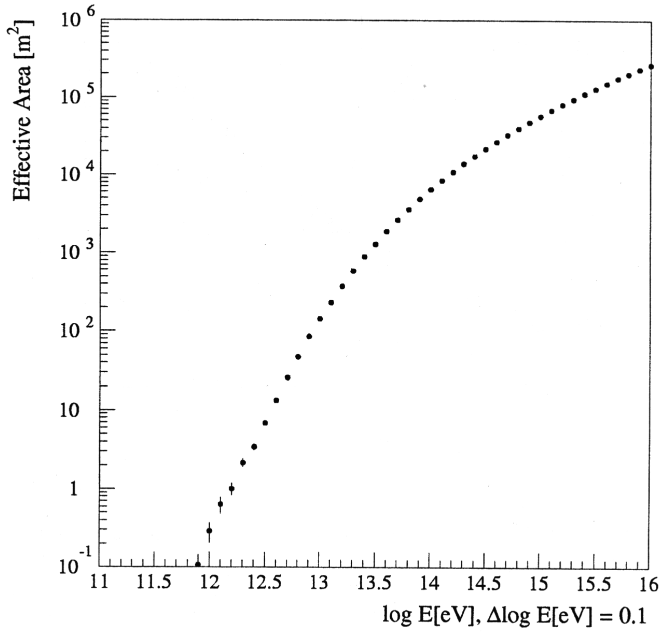

Figure 7.3: The effective area when MAS array is under the trigger condition described in the previous section.

as shown in Figure 7.4. As the result, the mode energy is found about 30 TeV. The integration of the figure over the whole energy gives the expected trigger frequency. This is about 10 Hz and is consistent with the measurements.

7.2.2 Resolutions

In order to evaluate the resolutions and the systematic errors of the shower sizes and of the arrival directions, we used an air shower simulation program, CORSIKA [41]. It is a detailed Monte Carlo simulation program to study the evolution and the properties of extensive air showers in the atmosphere. It was developed for the KASCADE experiment, and is one of the standard simulation code that is used by many experiments all over the world. We developed the program called "cor2mas " to convert the outputs of CORSIKA to simulated data which have the identical format with the measured data of the MAS array. On the translations by this program, we took account of the responses of the detectors and the electronics, the cable delays, and the fluctuations (of number of incident particles, arrival times and delays). The simulated data were processed with the completely identical analysis programs which are used for the actual observed data.

The total number of simulated events with CORSIKA no–thinning mode is 3×10^6 for primary protons and same number for primary irons. The simulation calculations covered primary energies from 10^{12} to 6×10^{15} eV, and core locations from 0 to 40 m from the center of the array. For the simulated data we applied the identical data selections with those for actual measured data, and accordingly the selected events have the reduced chi–square values for the determinations of EAS arrival directions less than 3 and the determined core position within

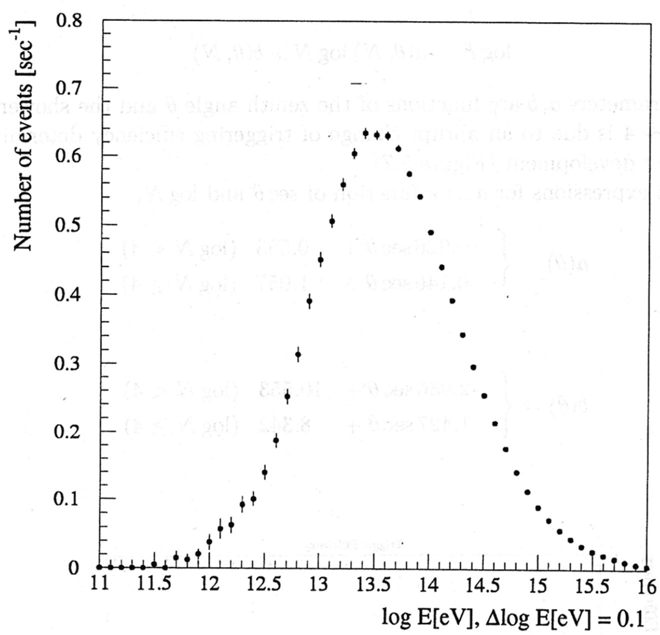

Figure 7.4: The expected energy distribution of the triggered events. The mode energy is about 30 TeV.

20 m from the center of the array.

Angular resolutions

We examine the accuracy in determination of shower arrival directions by comparing both directions of the incident particles and of the corresponding reconstructed showers. Figure 7.5 and 7.6 are the distributions of the opening angle $\Delta\theta$ for the several primary energies for the protons whose incident zenith angles are $0°$ and $44.4°$. These figures are the histograms for the simulated events which have the core positions(r) less than 20 m from the center of the array. For the events outside of this circle, the angular resolution are about 50 % large as shown in Figure 7.7. Thus in the following descriptions of the resolutions we apply the data selections with $r < 20$ m. The distribution is well expressed with the following formula;

$$\frac{\mathrm{d}N}{\mathrm{d}\Delta\theta} = \frac{1}{\sigma_\theta}\Delta\theta \exp\left(-\frac{\Delta\theta^2}{2\sigma_\theta^2}\right) \tag{7.18}$$

Figure 7.8 shows an example of the fitting of a opening angle distribution with this formula. We take the σ_θ in the formula (7.18) as the angular resolution of the array, and plot σ_θ as a function of energies in Figure 7.9. For the vertically incident primary particles, the angular resolution is $1.4°$ for EASs with primary energy of 10^{14} eV, and is $0.8°$ for those of 10^{15} eV.

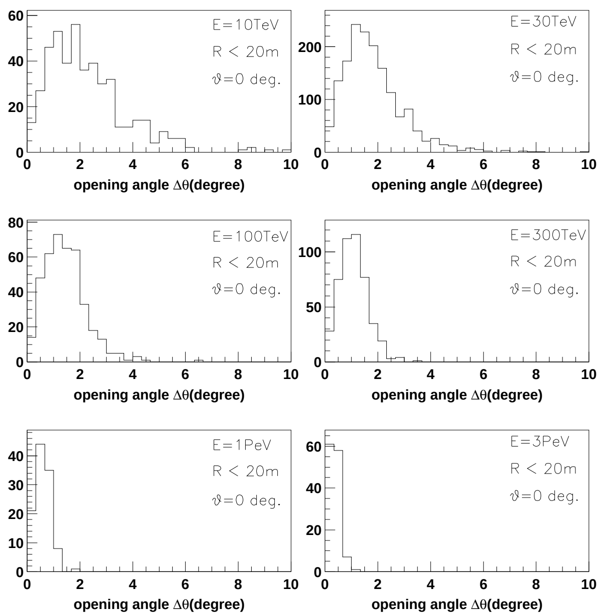

Figure 7.5: Distributions of $\Delta\theta$ of vertically incident primaries. All the events are selected with the condition $r \leq 20$ m.

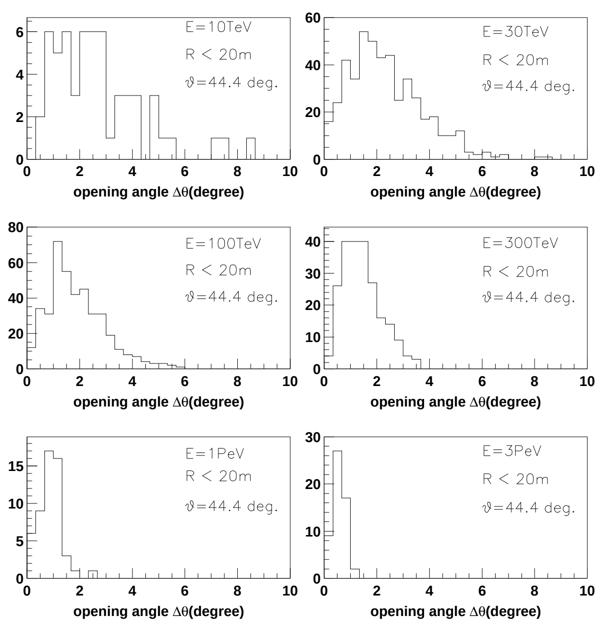

Figure 7.6: Distributions of $\Delta\theta$ of the simulated showers of $\theta = 44.4°$.

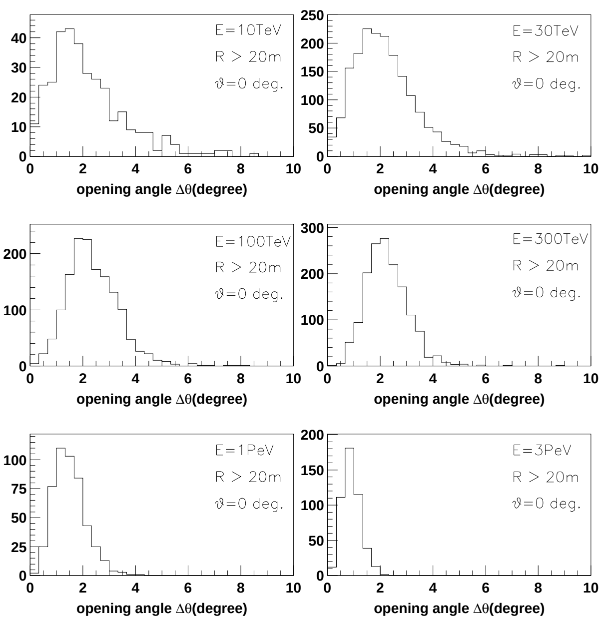

Figure 7.7: Distributions of $\Delta\theta$ for vertically incident primaries. All the events are selected with the condition $r > 20$ m. The angular determination errors of the events on the outer region of the array is large by about 50 % compared to Figure 7.5.

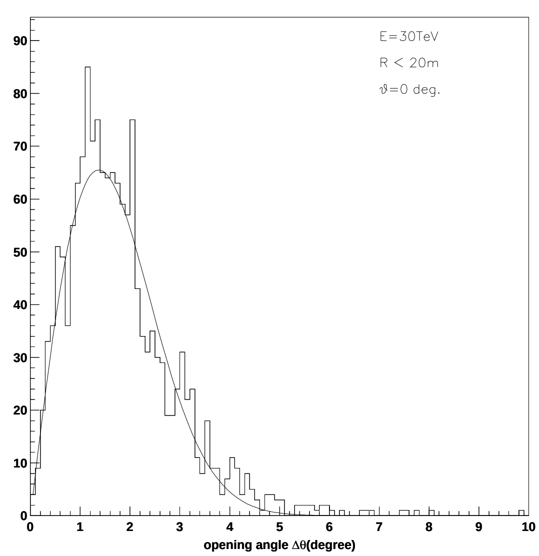

Figure 7.8: An examples of the fitting $\Delta\theta$ distribution with the formula (7.18). σ_θ is determined to be 1.94° for this distribution.

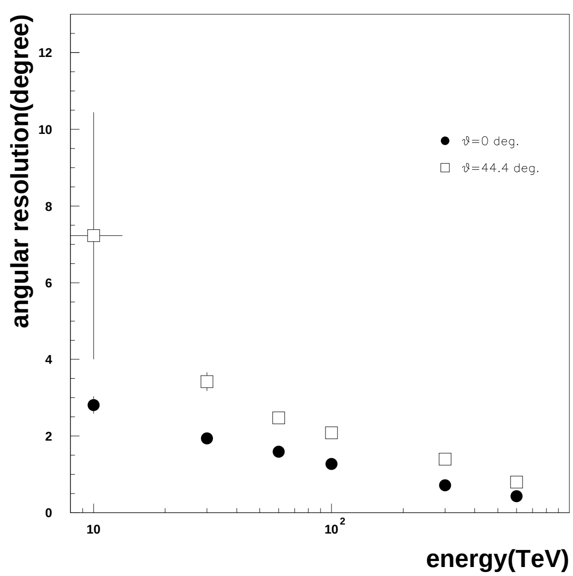

Figure 7.9: The plot of angular determination errors σ_θ as a function of primary energy.

Size determination errors

The core locations and the sizes of air showers are calculated with the grid–search procedure described in the previous section. The core position differences, the size determination error $\Delta \log(N_{rec}/N_{sim})$, the core distance resolutions are shown in Figure 7.10–7.15. Figure 7.15 shows that the EAS size resolution is 35% for vertically incident EASs with primary energy of 10^{14} eV, and is 20% for 10^{15} eV. Also, it is shown there are about 30% systematic differences between the input and the determined sizes for the primaries of E > 30 TeV.

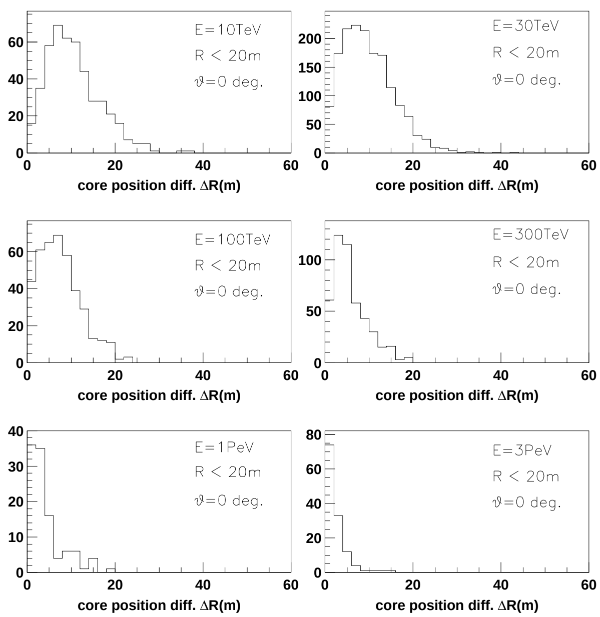

Figure 7.10: Distributions of the core position difference for the vertically incident primaries. All the events are selected with the condition $r \leq 20$ m.

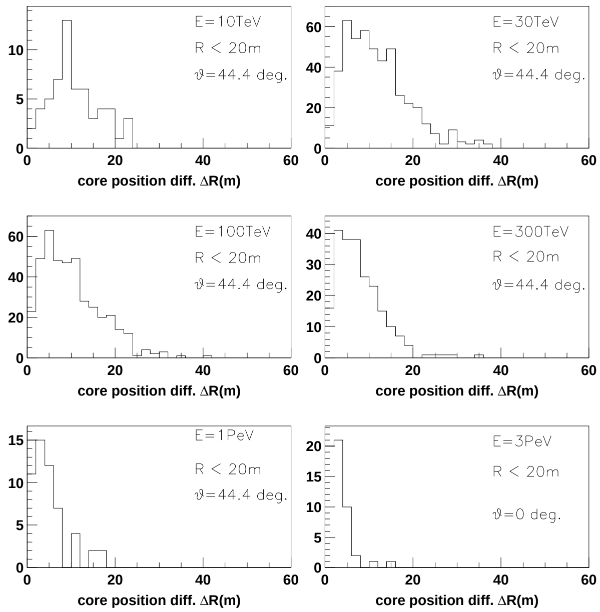

Figure 7.11: Distributions of the core position difference for the simulated showers of $\theta = 44.4°$. All the events are selected with the condition $r \leq 20$ m.

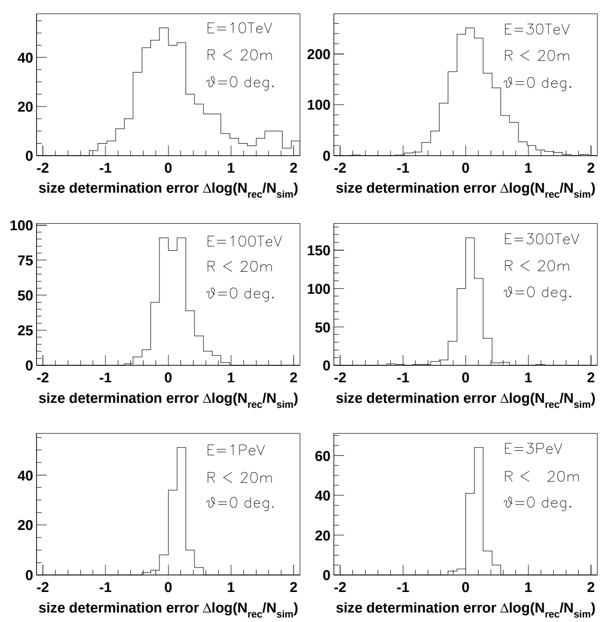

Figure 7.12: Distributions of the size determination error for the vertically incident primaries. All the events are selected with the condition $r \leq 20$ m.

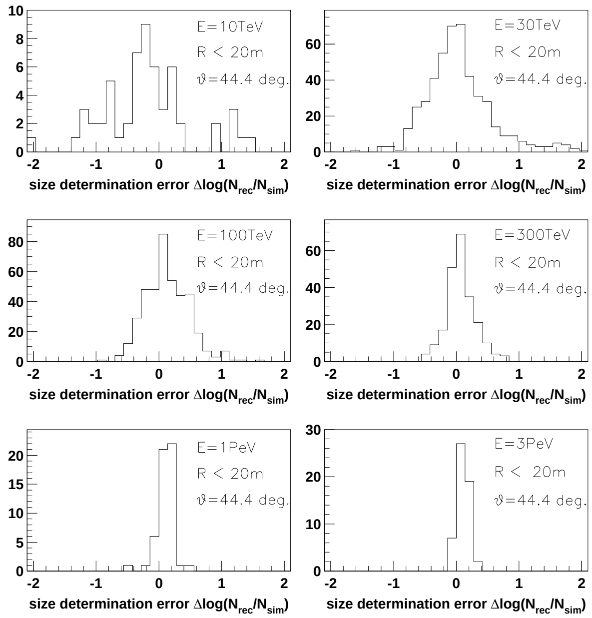

Figure 7.13: Distributions of the size determination error for the simulated showers of $\theta = 44.4°$. All the events are selected with the condition $r \leq 20$ m.

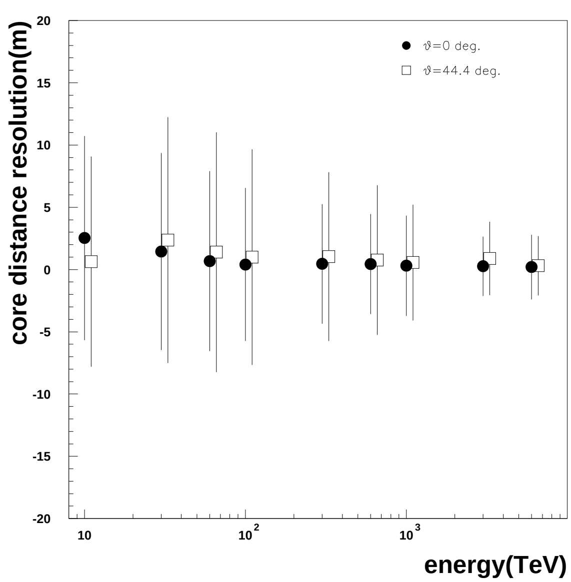

Figure 7.14: The plot of the core distance resolution as a function of primary energy. The markers indicate the systematic errors, and the error bar of each plot is the statistical error.

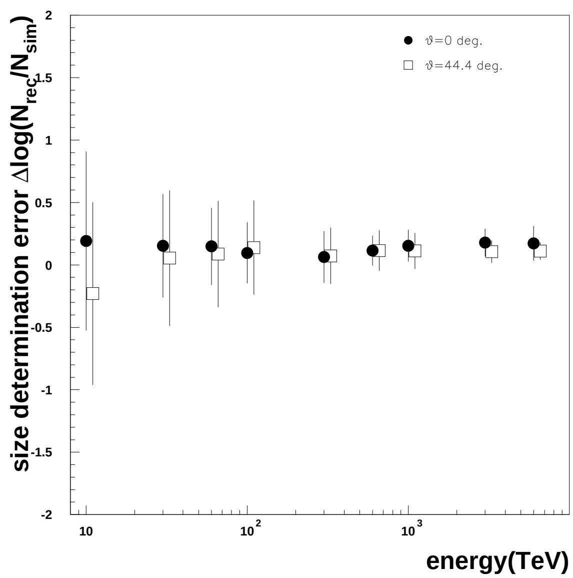

Figure 7.15: The plot of the size determination error as a function of primary energy. The markers indicate the systematic errors, and the error bar of each plot is the statistical error.

Chapter 8

Experimental Results

In order to estimate the chemical composition of cosmic rays, we measured EAS longitudinal development with the equi–intensity method analysis. In the analysis, we used the angular dependences of EAS sizes, the rate of arrivals of EASs and the resultant size distributions. Thus the equi–intensity method analysis is based only on air shower size spectra. The simulations and the results of the chemical composition and the energy spectrum are presented in this chapter.

8.1 Data selection

The details of the analysis is described in the previous chapter. The observed data were analyzed with the following procedure: (1)The arrival direction of each EAS is determined with a least square fit, assuming that the EAS front is flat, (2)The positions of the unshielded detectors are projected onto the EAS front plane, (3)The core location, the EAS size, and the age parameter are determined on this plane by minimizing the chi–square. Through this analysis, we obtained a set of the parameters characterizing each EAS event, *i.e.*, an EAS size(N_{obs}), an age parameter(s), a zenith angle(θ), an azimuthal angle(ϕ), and a core location.

The data used for the present analysis were collected between March and November of 2000. The total observation time was 8.9×10^6 s. During this period, the array was in nearly continuous operation. There were, however, short interruptions for the detector calibrations and the occasional power failures. Since these interruptions can give rise to non–uniformities on the arrival direction distributions in the observed data, we checked the continuity of the observation in each sidereal day. The data in the sidereal days which had a time gap of two consecutive events larger than 8 minutes ($2°$ in hour angle) were excluded from the analysis.

In order to choose EAS events whose arrival directions and air shower sizes are determined in good accuracy, we apply the selections of EAS events with the reduced chi–square values for the determinations of EAS arrival directions(χ^2_{dir}) and with that for determinations of EAS sizes(χ^2_{size}) to the data. Figure 8.1 and 8.2 are distributions of the reduced chi–square values, χ^2_{dir} and χ^2_{size} for a 20000 event sample. We selected the events with χ^2_{dir} less than 3. However, χ^2_{size} have a size dependence shown in Figure 8.3, and then we did not select with χ^2_{size} in order to avoid the systematic selection bias.

We selected the events of which the core positions were within distances less than 20 m from the center of the array. As shown in Figure 8.4, the events fallen outside of the region have large determination errors of arrival directions and those of core positions, and consequently, have large size determination errors.

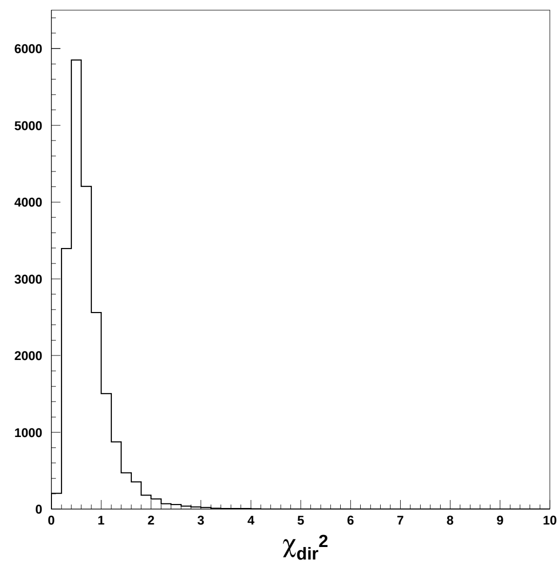

Figure 8.1: Distribution of the reduced chi–square for the determinations of the arrival directions, (7.5).

Moreover, we selected the events of which zenith angles are less than 60°. As the result, the total observation time is 8.9×10^6 s and 7.5×10^7 events are selected.

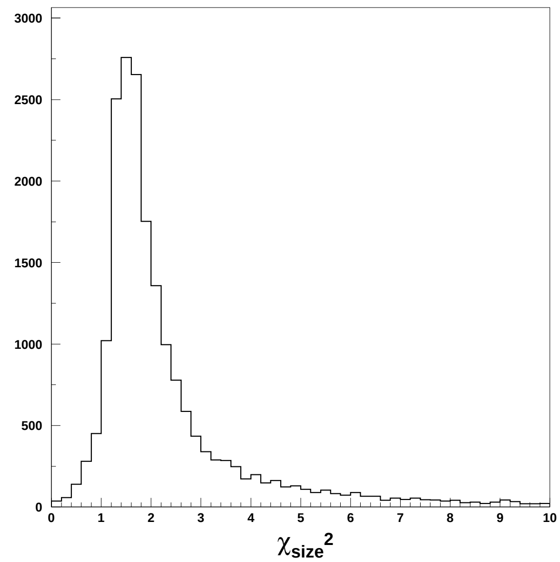

Figure 8.2: Distribution of the reduced chi–square for the determinations of the EAS sizes, (7.9).

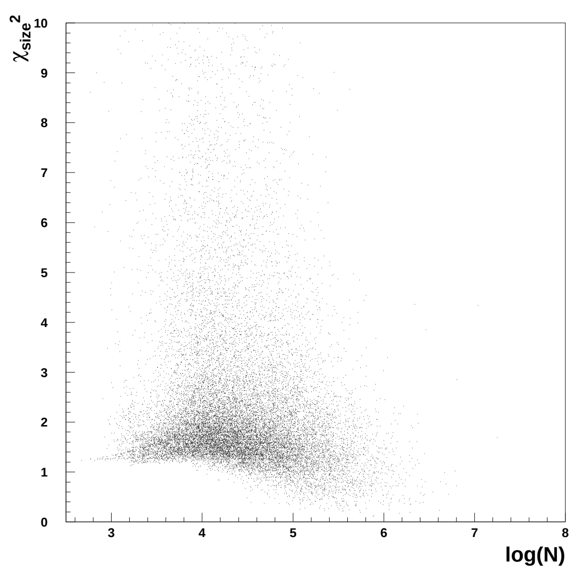

Figure 8.3: Scatter plots of χ^2_{size} vs EAS size.

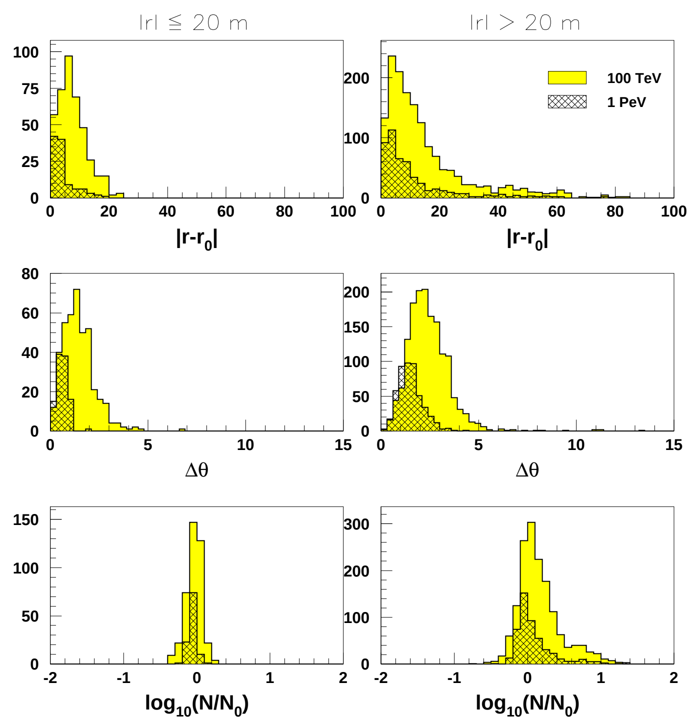

Figure 8.4: Distributions: (*first column*) of the determination errors of core positions($|r - r_0|$), (*second column*) of arrival directions($\Delta\theta$) and (*third column*) of EAS sizes($\log(N/N_0)$) for the full Monte Carlo simulated events with CORSIKA-QGSJET.

8.2 Simulations

In the analysis of the experimental data, in order to estimate the chemical composition of cosmic rays with comparing between the observed and the simulated size distributions, the number of simulated events must be at least the same as that of the collected data. However, making full Monte-Carlo simulations for such a large data set is a huge task. Therefore, we simulated events with the size–energy relations, the energy dependent size fluctuations, the angular resolutions, and the detection efficiencies. These relations were obtained with the full Monte–Carlo simulations of CORSIKA [41] of no–thinning mode with the QGSJET hadron interaction model. The Monte Carlo program CORSIKA is the most used EAS simulation program, and simulates the 4–dimensional evolution of EASs in the atmosphere initiated by photons, hadrons and nuclei. It has the full Monte Carlo simulation mode called 'no–thinning mode'. In the full Monte-Carlo simulations, we took account of the characteristics of the MAS array detectors including the pulse height distributions, the time delay and the fluctuations for the minimum ionizing particles. The simulated data were analyzed with the identical procedure with that for the real observed data.

We generated EAS events with CORSIKA for the EAS size from 10^3 to 10^7, and the events had the uniform core position distribution around the center of the array within 40 m radius. The number of simulated EAS with CORSIKA is about 6×10^6.

8.2.1 Parameterizations

The simulated data were selected with the same criteria as that for the measured data, and used to obtain (1)effective area, (2)angular resolution, (3)shower size and (4)the fluctuation of shower size for fixed primary energy as parameterized functions of the primary energy and $\sec\theta$.

effective area

The plots of the effective detection areas as a function of the primary energy for each $\sec\theta$ are shown in Figure 8.5 for primary protons and Figure 8.6 for primary irons. These plots were fitted with the following empirical formula,

$$\log S = S_1 - S_3 log\left(1.0 + \frac{10^{S_2}}{E^2}\right). \tag{8.1}$$

Here, S_1, S_2 and S_3 are the fitting parameters and E is a primary energy in TeV. The parameters are plotted in Figure 8.7 and 8.8 as functions of $\sec\theta$. These plots were fitted with polynomial functions of $\sec\theta$, and then the results for primary protons are

$$S_1 = 2.6897 + 0.64697\sec\theta - 0.25758(\sec\theta)^2 \tag{8.2}$$
$$S_2 = -0.30813 + 2.3568\sec\theta + 0.10936(\sec\theta)^2 \tag{8.3}$$
$$S_3 = 2.6021 - 0.83939\sec\theta, \tag{8.4}$$

and for primary irons are

$$S_1 = 2.8983 + 0.44159\sec\theta - 0.20076(\sec\theta)^2 \tag{8.5}$$
$$S_2 = 1.0792 + 1.5149\sec\theta + 0.18284(\sec\theta)^2 \tag{8.6}$$
$$S_3 = 7.0. \tag{8.7}$$

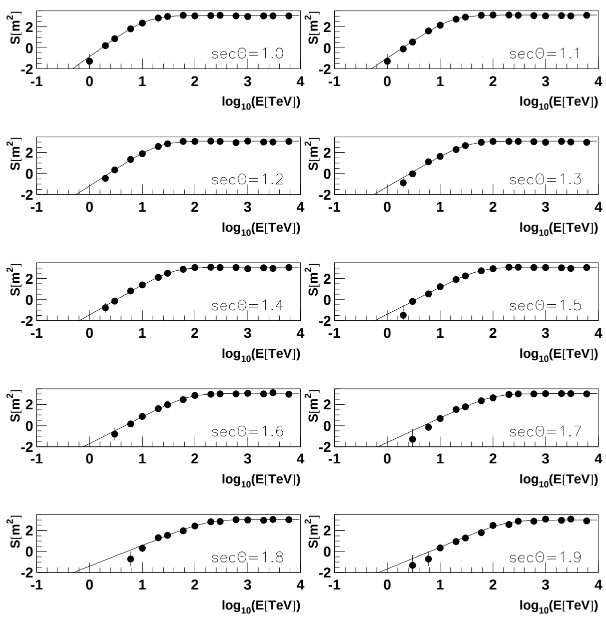

Figure 8.5: Effective detection area as a function of the primary energy for primary protons simulated with CORSIKA. The solid lines are drawn with the function (8.1).

The parameters S_1, S_2 and S_3 well represent the effective area for the possible energy and $\sec\theta$ range as shown in Figure 8.9 and 8.10.

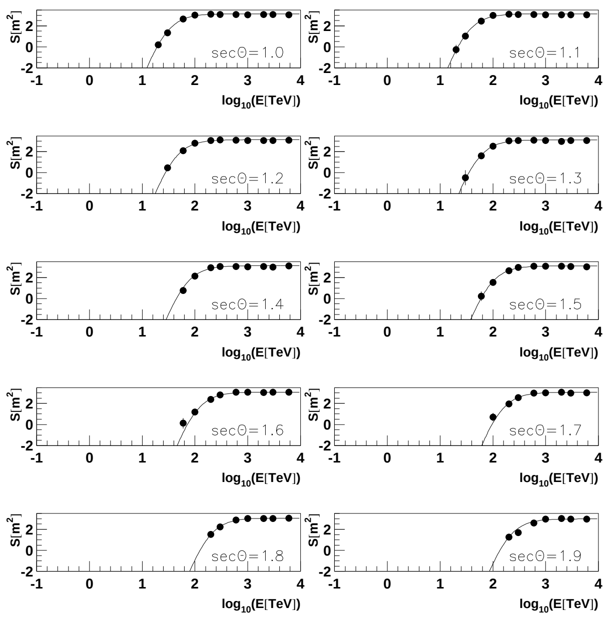

Figure 8.6: Effective detection area as a function of the primary energy for primary irons simulated with CORSIKA. The solid lines are drawn with the function (8.1).

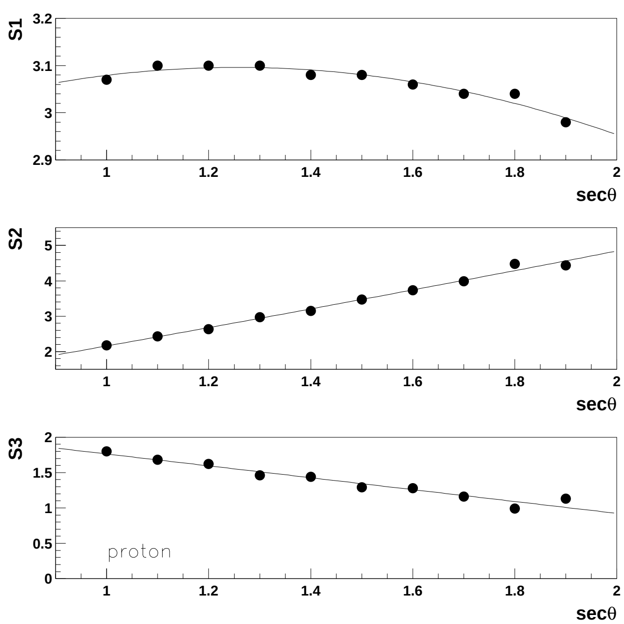

Figure 8.7: The fitting parameters of the function (8.1) for the simulated primary protons. The solid lines represent the polynomial functions of $\sec\theta$.

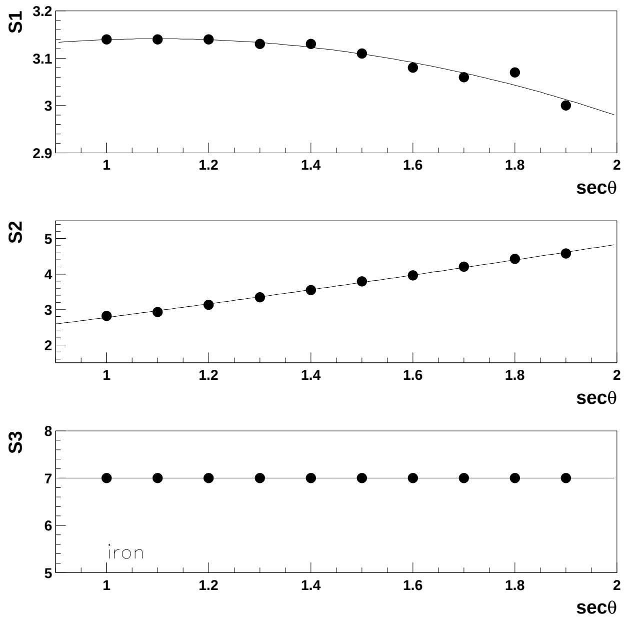

Figure 8.8: The fitting parameters of function (8.1) for the simulated primary irons. The solid lines represent the polynomial functions of $\sec\theta$.

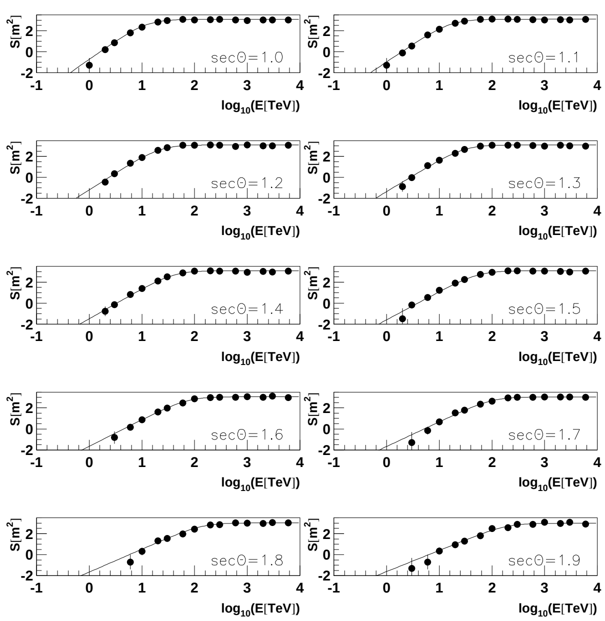

Figure 8.9: Effective detection area as a function of the primary energy for primary protons simulated with CORSIKA. The solid lines are effective area calculated with the function (8.1) and with the polynomial functions of S_1, S_2 and S_3.

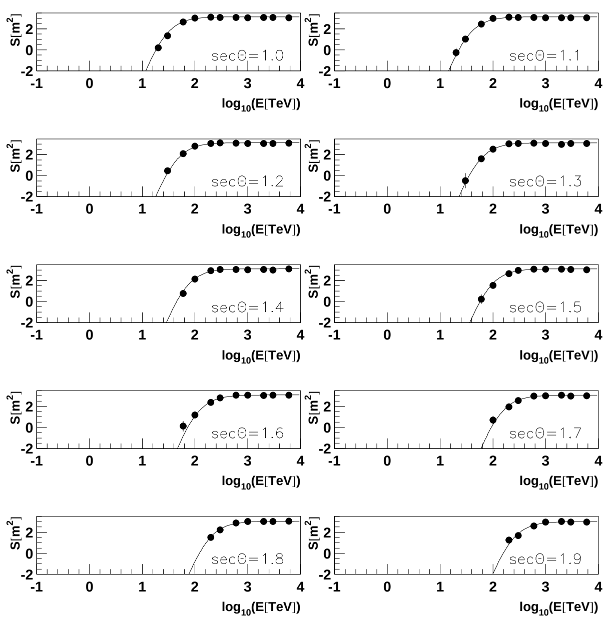

Figure 8.10: Effective detection area as a function of the primary energy for primary irons simulated with CORSIKA. The solid lines are effective area calculated with the function (8.1) and with the polynomial functions of S_1, S_2 and S_3.

angular resolution

The plots of the angular resolutions as a function of primary energy for each $\sec\theta$ are shown in Figure 8.11 for primary protons and Figure 8.12 for primary irons. These plots are fitted with a linear function of $\sec\theta$, that is $A \times \sec\theta + B$. The fitting parameters are shown in Figure 8.13. In the simulations, the angular resolutions are calculated with the natural cubic spline interpolation of these plots.

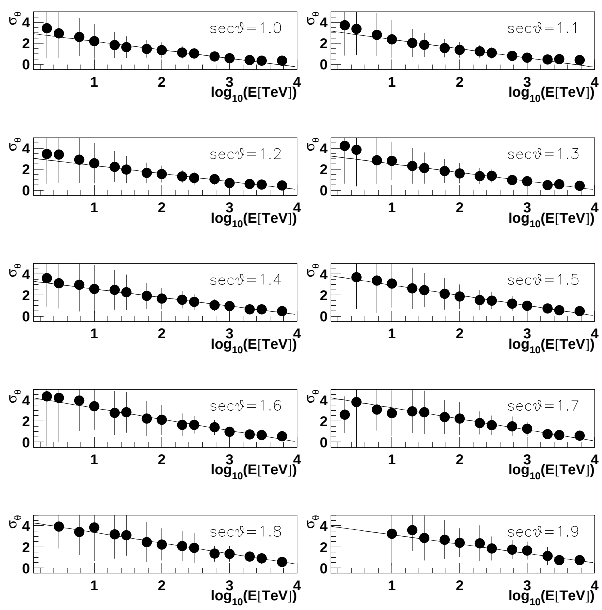

Figure 8.11: Angular resolutions as a function of the primary energy for primary protons simulated with CORSIKA are fitted with a linear function.

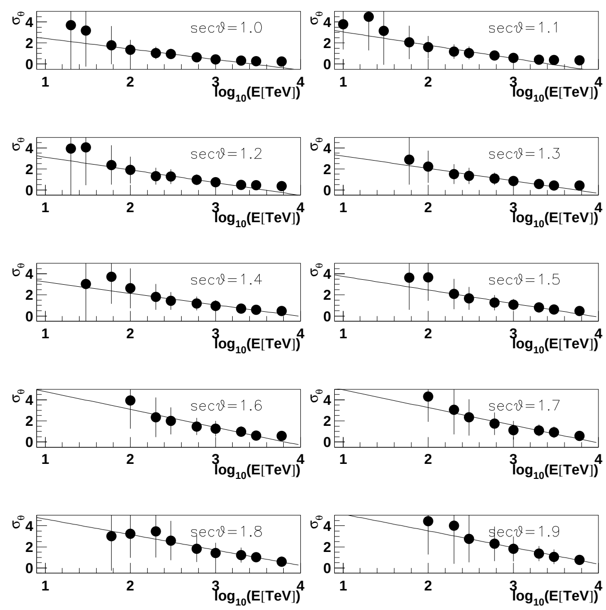

Figure 8.12: Angular resolutions as a function of the primary energy for primary irons simulated with CORSIKA are fitted with a linear function.

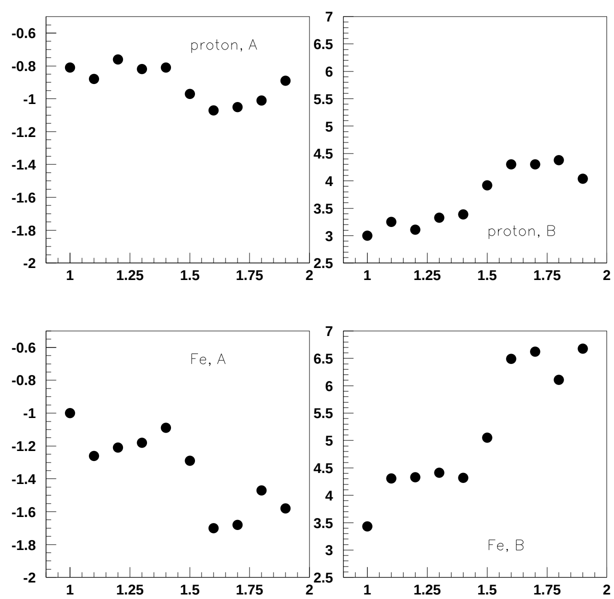

Figure 8.13: The plots of the fitting parameters for the angular resolutions.

shower size

The plots of the reconstructed shower sizes(N_{rec}) as a function of the primary energy for each $\sec\theta$ are shown in Figure 8.14 for primary protons and Figure 8.15 for primary irons. These

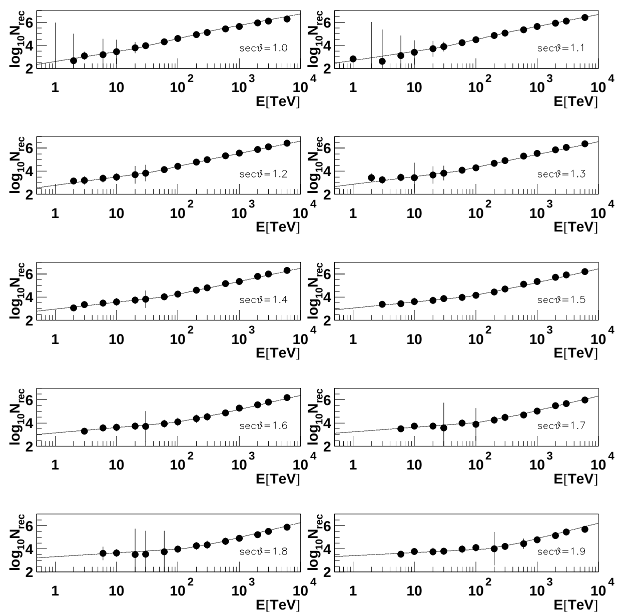

Figure 8.14: The plots of the reconstructed shower size as a function of the primary energy for each $\sec\theta$ for primary protons simulated with CORSIKA.

plots are fitted well with lines,

$$\log N_{rec} = A + B\log E \tag{8.8}$$

here E is primary energy in TeV. The parameters of these lines are shown in Figure 8.16 and Figure 8.17, as a function of $\sec\theta$. These plots are fitted with polynomial functions of $\sec\theta$, and thus the results for primary protons are

$$\begin{aligned}
A &= 1.6989 + 0.90041\sec\theta & (line1) \quad (8.9)\\
&= 2.2141 - 0.10137\sec\theta & (line2) \quad (8.10)\\
&= 5.9711 - 3.9656\sec\theta + 0.74167(\sec\theta)^2 & (line3) \quad (8.11)\\
B &= 1.5139 - 0.65675\sec\theta & (line1) \quad (8.12)\\
&= 1.5899 - 0.35788\sec\theta & (line2) \quad (8.13)\\
&= -0.31205 + 1.8017\sec\theta - 0.52547(\sec\theta)^2 & (line3) \quad (8.14)
\end{aligned}$$

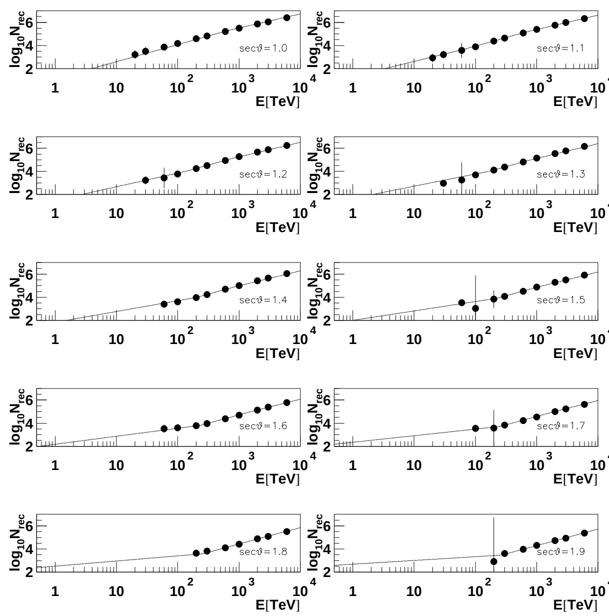

Figure 8.15: The plots of the reconstructed shower size as a function of the primary energy for each $\sec\theta$ for primary irons simulated with CORSIKA.

and for primary irons are

$$\begin{aligned}
A &= -0.56604 + 1.7134\sec\theta && (line1) && (8.15)\\
&= 2.3537 - 1.2348\sec\theta && (line2) && (8.16)\\
&= 5.8099 - 4.9532\sec\theta + 1.1001(\sec\theta)^2 && (line3) && (8.17)\\
B &= 2.6532 - 1.2265\sec\theta && (line1) && (8.18)\\
&= 1.5409 - 0.058930\sec\theta && (line2) && (8.19)\\
&= 0.19496 + 1.4247\sec\theta - 0.44074(\sec\theta)^2 && (line3) && (8.20)
\end{aligned}$$

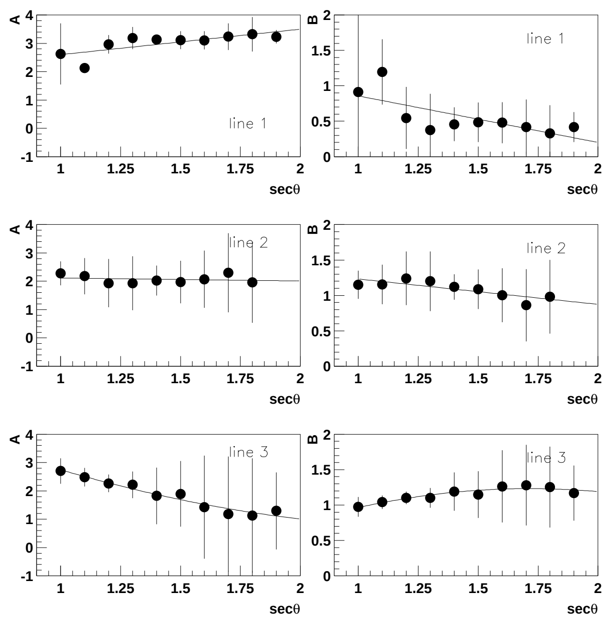

Figure 8.16: The fitting parameters of $\log_{10} N_{rec}$–$\log_{10} E$ relations for primary protons, for low energy(line 1), middle energy(line 2) and high energy region(line 3). These parameters are fitted with a polynomial function of $\sec\theta$.

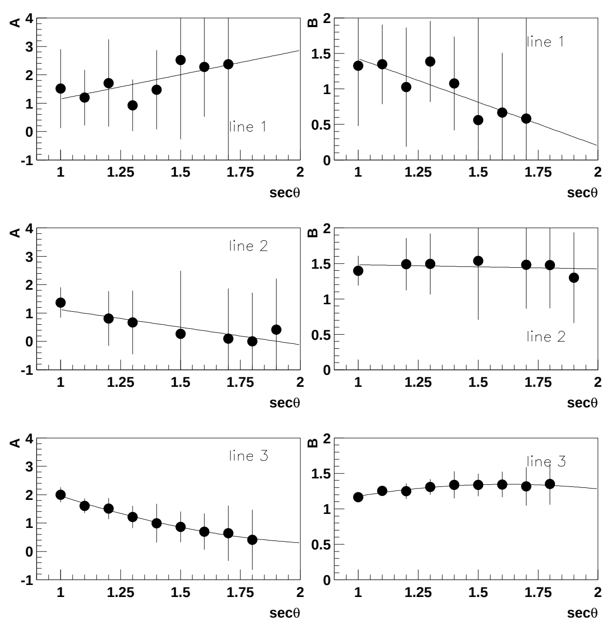

Figure 8.17: The fitting parameters of $\log_{10} N_{rec}$–$\log_{10} E$ relations for primary protons, for low energy(line 1), middle energy(line 2) and high energy region(line 3). These parameters are fitted with a polynomial function of $\sec\theta$.

The size fluctuations

The size fluctuations(σ_N) for fixed primary energies are obtained as the standard deviations of the size distributions. σ_N are plotted as a function of the primary energy for each $\sec\theta$ in Figure 8.18 and 8.19. These plots are fitted well with the following linear relation as,

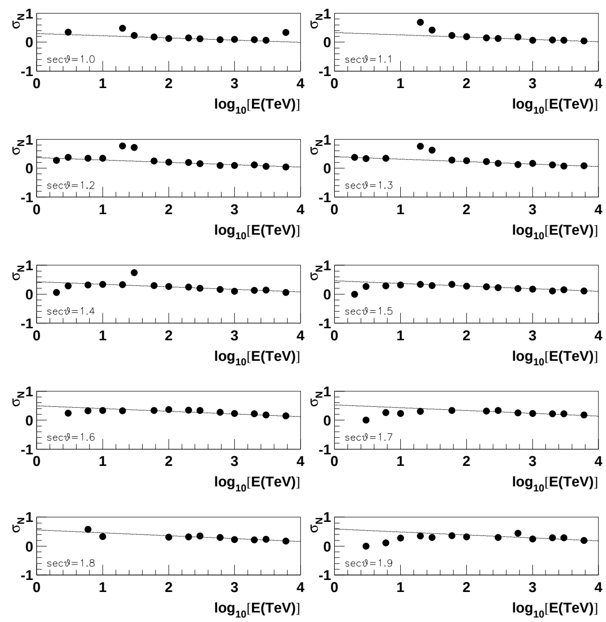

Figure 8.18: Size resolutions as a function of the primary energy for primary protons simulated with CORSIKA are fitted with a linear function.

$$\sigma_N = A + B \log E \tag{8.21}$$

here E is the primary energy in TeV. The determined values for A and B are shown in Figure 8.20, and fitted with the linear function of $\sec\theta$. The results for primary protons are

$$A = -0.023634 + 0.32377 \sec\theta \tag{8.22}$$
$$B = -0.045893 - 0.029957 \sec\theta, \tag{8.23}$$

and for primary irons,

$$A = -0.17884 + 0.42024 \sec\theta \tag{8.24}$$
$$B = 0.029940 - 0.089345 \sec\theta. \tag{8.25}$$

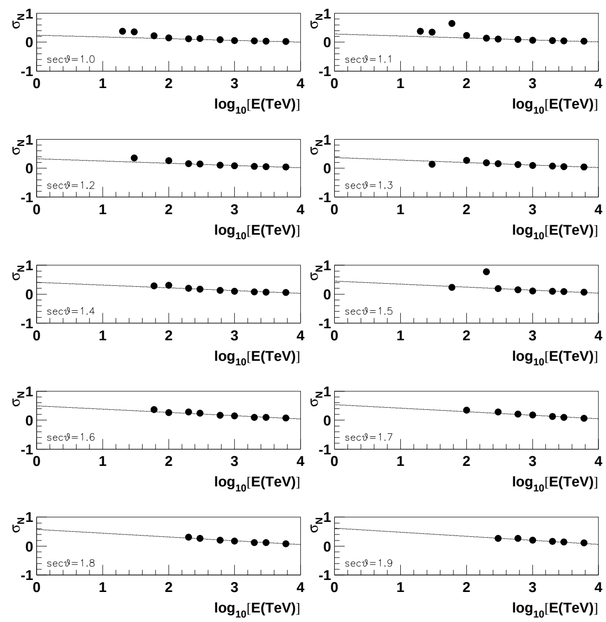

Figure 8.19: Size resolutions as a function of the primary energy for primary protons simulated with CORSIKA are fitted with a linear function.

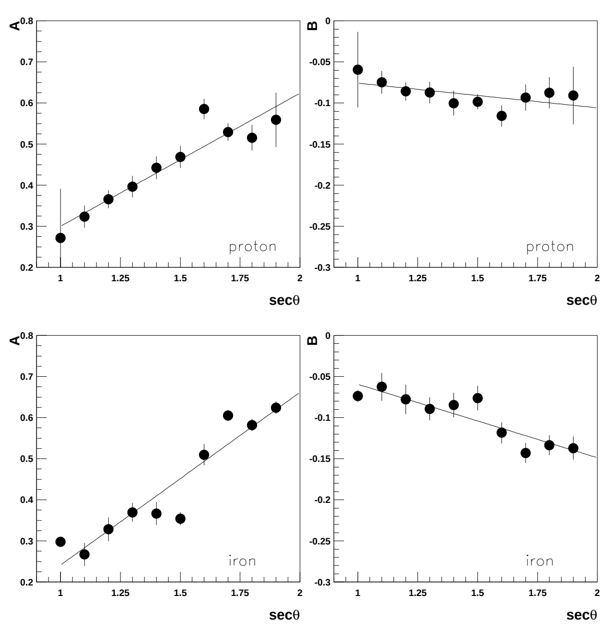

Figure 8.20: The fitting parameters of σ_N–$\log_{10} E$ relations for primary protons and irons. These values are fitted with a linear function of $\sec\theta$.

8.2.2 Simulation scheme

The simulation procedure for the EAS events observed with MAS array has a following scheme.

1. Determine the primary energy randomly. However, the frequency of the occurrence is proportional to the cosmic ray energy spectrum.

2. The primary particle type is determined. The program chooses randomly between a proton and an iron nucleus. The probability is proportional to the assumption of the averaged mass number of primary particles.

3. The incident direction of the air shower is determined randomly.

4. Calculate a detection efficiency with the primary energy and with the incident direction. The event which satisfies the event selection conditions is randomly chosen according to the calculated detection efficiency.

5. Determine the air shower size and its fluctuation with (8.8) and (8.21).

6. Output the shower parameters and go back to the top of the loop.

The data format of the output of the simulation program is identical to the output of the actual analysis program for MAS array, and then the both of observed and simulated shower parameters,*i.e.*, the air shower size, arrival directions, *etc*, are processed with the same procedures of the equi–intensity method analysis described in the next section.

In Figure 8.21 and 8.22, I show the simulated EAS sizes for primary protons compared with those simulated with CORSIKA no–thinning mode for several primary energies and incident zenith angles. The calculations with the fitted parameters well reproduce the size distributions with the full Monte Carlo simulations.

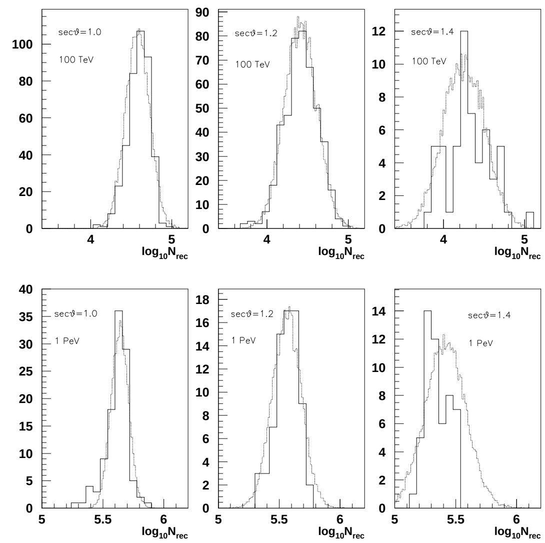

Figure 8.21: The distributions of the simulated sizes for primary protons with the fixed several primary energies and incident zenith angles. The solid lines are those simulated with CORSIKA–QGSJET no–thinning mode, and the dotted lines are those simulated with the parameterized functions derived in the text.

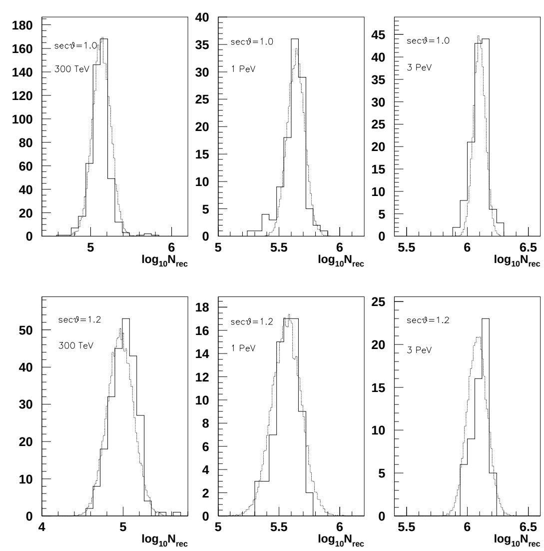

Figure 8.22: The distributions of the simulated sizes for primary protons with the fixed several primary energies and incident zenith angles. The solid lines are those simulated with CORSIKA–QGSJET no–thinning mode, and the dotted lines are those simulated with the parameterized functions derived in the text.

8.3 Size Spectra and Equi–Intensity Curves

The observed EASs were classified into two dimensional bins of EAS size(N^{obs}) and $\sec\theta$ (θ: zenith angle of arrival direction). The size of each bin is 0.2 in logarithm of N^{obs}, and 0.1 in $\sec\theta$. We then obtained the size distributions for each $\sec\theta$ interval. It it possible that there is some deformation in these distributions from the true distributions due to the uncertainties in size and in θ. Therefore, the correction factors for the number of events in each bin were obtained with the EAS simulations.

Moreover the non–uniformity of azimuth angle distributions must be taken into consideration. Since the array is located on the side of the mountain, the array slopes slightly down to the valley. Thus the detection efficiency of the array is not uniform in azimuth directions. The azimuth angle distributions of each $\sec\theta$ bin is shown in Figure 8.23. These non–uniformities are due to the geometry of the array and are confirmed to be independent of EAS sizes. Thus, the correction factors were calculated from the observed azimuth angle distributions partly shown in Figure 8.23 which bin sizes are 0.1 in $\sec\theta$ and 3° in azimuth angle, and the number of events were normalized to that in a maximum efficient direction.

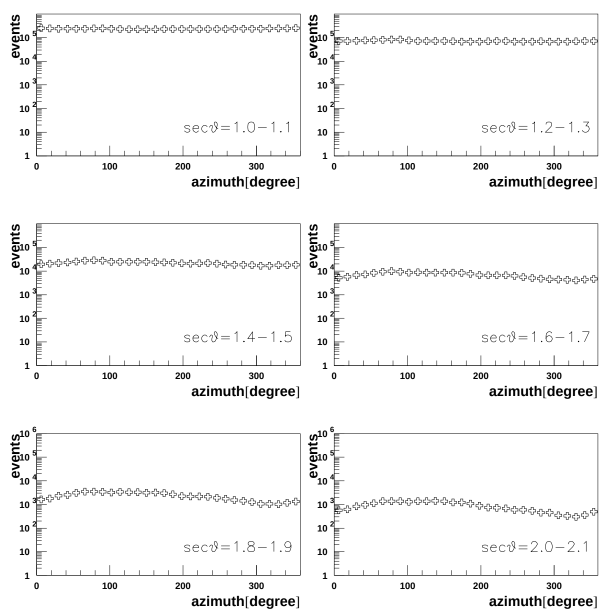

Figure 8.23: The azimuth angle distributions of particular $\sec\theta$ bins.

After the corrections for measured size distributions, finally, we obtained the integral N^{obs} spectra for each $\sec\theta$ bin, as shown in Figure 8.24. We selected EAS with $N^{obs} > 10^{4.5}$ for further analysis, because our simulation shows that the detection efficiencies for $N^{obs} > 10^{4.5}$ are approximately 100% and independent of an adopted primary component.

A differential size spectra $dF/d\log N^{obs}$ for $\sec\theta = 1.0-1.1$ is shown in Figure 8.25, in which the intensity have been multiplied by $N^{1.5}$ to flatten the spectrum and enhance its steepening. The size spectrum is well represented by the power–law, and steepens at around $N^{obs} = 10^{6.0}$, and there is not any other bending points. Thus the measured size spectrum is fitted with the

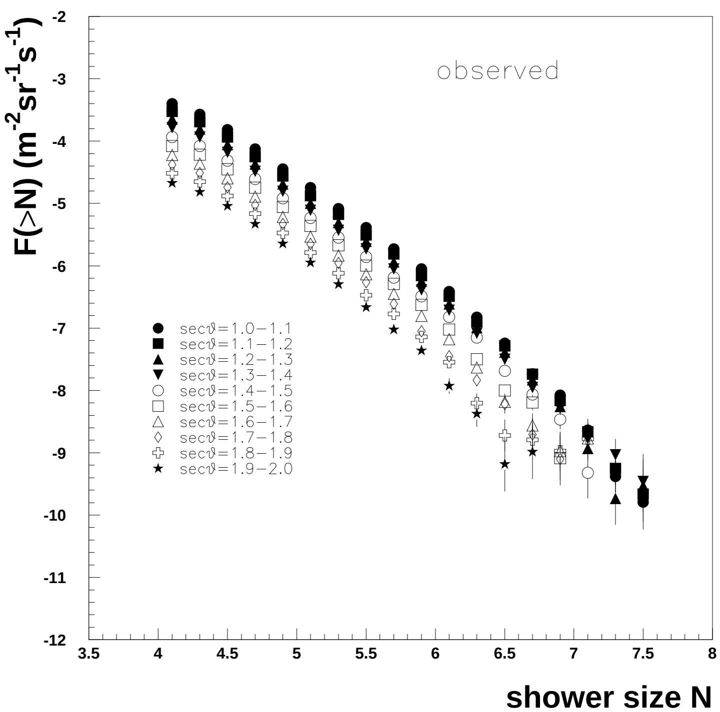

Figure 8.24: The observed integral EAS size spectra for each $\sec\theta$ bin.

following relation,

$$\log(\frac{dF}{d\log N}[\mathrm{m}^{-2}\mathrm{s}^{-1}\mathrm{sr}^{-1}]) = \begin{cases} (3.85 \pm 0.03) - (1.57 \pm 0.01) \times \log N & (\log N < 5.9) \\ (6.80 \pm 0.87) - (2.07 \pm 0.14) \times \log N & (\log N \geq 5.9) \end{cases} \tag{8.26}$$

where N is equal to N^{obs}.

If it is assumed that air showers initiated by primary cosmic rays with a certain energy arrive at the earth isotropically with a constant rate, the air shower size plots with the same flux as a function of θ, i.e., the atmospheric depth represents the corresponding longitudinal development curve. For this equi–intensity method analysis, we classified again the observed data into the bins of $\sec\theta$ of which bin size = 0.05 in order to draw the details of longitudinal development. We used the events only with $\sec\theta < 1.5$ because the angular determination errors become larger than the bin size$\Delta\sec\theta = 0.5$ for $\sec\theta \geq 1.5$. After correcting the size distributions again with same procedures as described before, we derived the equi–intensity curves for air showers with the integral of rate $F(> N^{obs})$ from $10^{-5.2}$ to $10^{-8.2}$ $\mathrm{m}^{-2}\mathrm{sr}^{-1}\mathrm{s}^{-1}$ for $10^{-0.25}$ steps. The results are shown in Figure 8.26.

Please note that one cannot compare the curves in Figure 8.26(a) with the longitudinal development curves immediately. The measured EAS size with the air shower array is not translated directly into the number of electrons and positrons in the air shower, in part because the detected number of particles is contaminated by muons and in part because the determined size is affected by the threshold energy of the detectors. Moreover the equi–intensity curves are affected by the energy-size relations, and by the energy spectra of components, as described

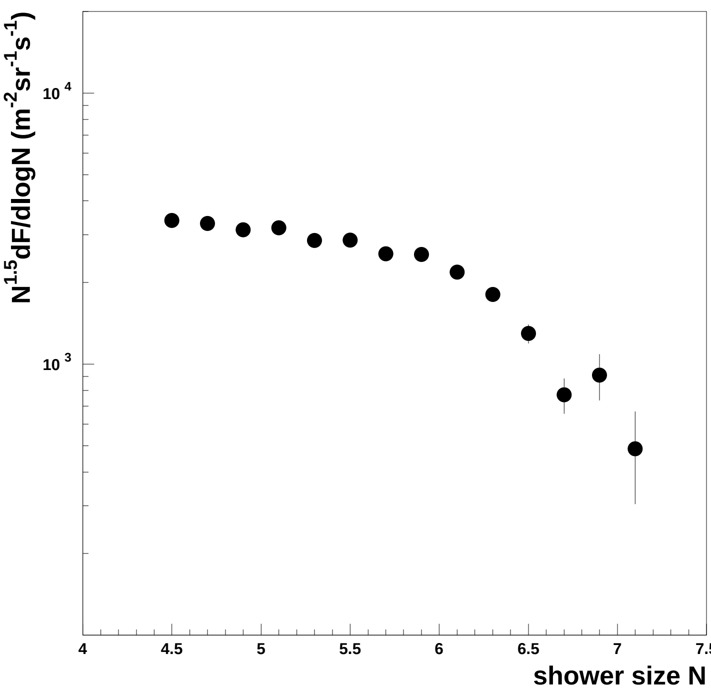

Figure 8.25: The differential size spectrum for $\sec\theta = 1.0 - 1.1$ measured by BASJE–MAS array. The intensity has been multiplied by $N^{1.5}$ to flatten the spectrum.

above. The maximum development points show disagreement with the X_{max} of the longitudinal development curves simulated with CORSIKA/QGSJET [62]. For example, for 4 PeV one obtains $X_{max}\sim$ 590g/cm^2 for primary protons with CORSIKA/QGSJET, but at corresponding flux, $10^{-7.2}$m^{-2}sr^{-1}s^{-1}, the maximum point of the equi–intensity curve is $\sim$ 660g/cm^2 for primary protons as shown in Figure 8.26(a).

In Figure 8.26(a), we show equi–intensity curves obtained with the same analysis procedures for the simulated data as were applied to the real observed events. The simulation was performed with four different models in which the composition of the primaries was varied: pure protons, pure iron nuclei, and two different mixtures of protons and iron nuclei. The air shower sizes at certain fluxes depend on the adopted all particle spectrum and on the adopted mixing ratio of protons and iron nuclei. Only when we simulate air showers with the actual all particle energy spectrum and with the real mixing ratio, the equi–intensity curves will coincide with the measured ones. Otherwise, a measured curve will not agree with a simulated one for a same rate of arrival.

The knowledge of the cosmic ray chemical composition is essential to the determination of the energy spectrum from a measured air shower size spectrum as in the case of our analysis. On the other hand, unless an adopted energy spectrum for the simulations is totally different from the actual one, the correlations between a mixing ratio and the shape of an equi–intensity curve are less dependent on an adopted energy spectrum. Therefore, as the first step of determination of the mixing ratios, we compared shapes of the observed and the corresponding simulated equi–

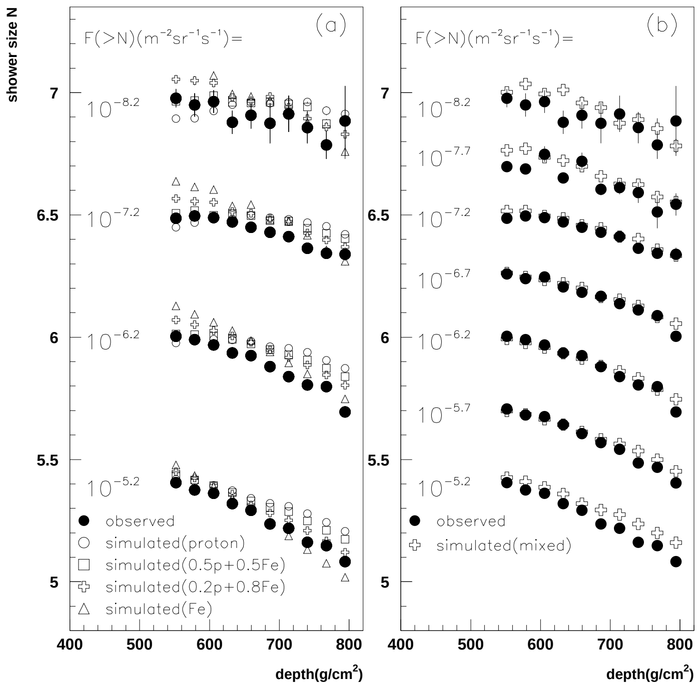

Figure 8.26: (a)The observed equi–intensity curves are compared with simulated ones for primary protons, iron nuclei and (50% protons + 50% irons), without any normalization. The attached value for each curve is the integral flux. In the analysis, we derived the curves for $F(> N)$ from $10^{-5.2}$ to $10^{-8.2}$ $\mathrm{m^{-2}sr^{-1}s^{-1}}$ with $10^{-0.25}$ step, but in this figure we show a part of these curves to avoid confusions. (b)Simulated equi–intensity curves with the measured ones without any normalization. In the simulation, we took consideration of not only the obtained mixing ratios of protons and irons, but also obtained all particle energy spectrum.

intensity curves. Next, we calculated the relation between primary energies and air shower sizes with the Monte Carlo simulations under the requirement of the obtained mixing ratios. The observed size spectrum is then converted to the all particle energy spectrum. Using the resultant energy spectrum, we examined the mixing ratios and the energy spectrum again, iteratively. In total, we repeated this process four times to converge with the final results shown below.

The slope of equi–intensity curves becomes flatter with increasing proton ratio. However, as shown in Figure 8.27, the flattening is not linearly proportional to proton ratio. So that, in order to determine a mixing ratio, the measured equi–intensity curves are compared with mixed composition simulated ones. This is described in more detail in the next section.

The simulated curves of primary protons with an integral rate less than $10^{-6.2}\mathrm{m^{-2}sr^{-1}s^{-1}}$ definitely show that the depths of shower maximum points should be deeper than the atmospheric depth of our observation site. However, in our results, these maximum points are not seen. Therefore, the major component of primary cosmic rays is considered to be heavier than proton even in this energy range.

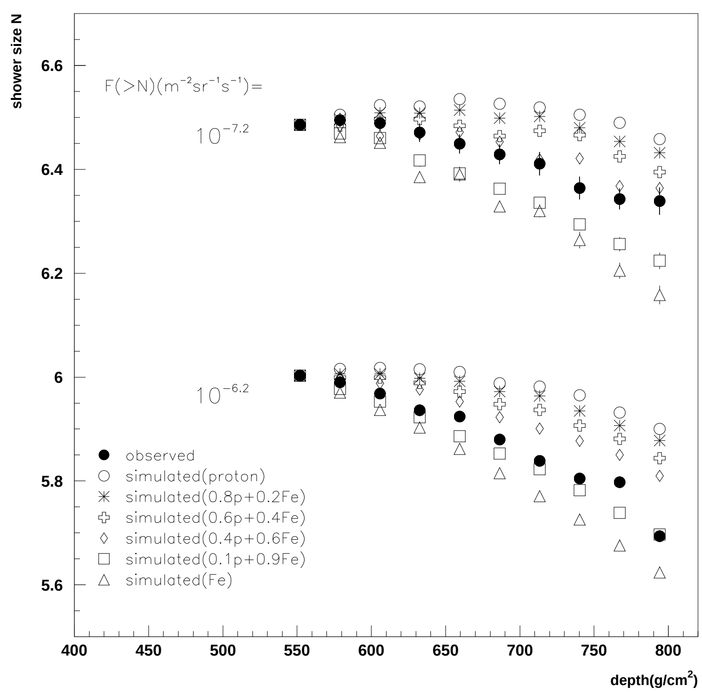

Figure 8.27: The observed equi–intensity curves are compared with simulated ones. The attached value for each curve is the integral flux. The simulated curves are normalized at 578 g/cm^2 with the measured curves.

8.4 Chemical Composition and Energy Spectrum of Primary Cosmic Rays

8.4.1 Chemical Composition

We determined the primary chemical composition by comparing the observed equi–intesity curves with the calculated ones. In our calculation, we assumed that the primary chemical composition is a mixture of protons and iron nuclei, and that both the energy spectra of primary protons and those of iron nuclei are proportional to $E^{-\gamma}$ with $\gamma = 2.67$ up to $E = 3.9 \times 10^{15}$ eV and with $\gamma = 3.41$ above this energy [59][98]. We examined not only the primary composition but also all particle energy spectrum. We simulated EASs with varying the proportion of protons to the total (sum of protons and iron nuclei, $(\mathrm{n_p}/(\mathrm{n_p} + \mathrm{n_{Fe}}))$. The proportion was varied from 0.0 to 1.0 with steps of 0.1.

The longitudinal development curves with the simulated data sets are obtained for each proton mixing ratio. Comparing the observed curves with the simulated ones, we estimated the mixing ratios by the least squares method with the following observation equation,

$$v_i = l(z_i, x_0) - l^{obs}(z_i) + \frac{\partial l(z_i, x_0)}{\partial x}\Delta x \tag{8.27}$$

Here $l^{obs}(z_i)$ is an observed equi–intensity curve and $l(z_i, x_0)$ is a calculated equi–intensity curve for the mixture x_0, z_i is the atmospheric depth for i-th $\sec\theta$ bin. The best estimated x_0 is determined with a minimum chi–squares method and the correction value of Δx is determined with the least squares method. Notice that each primary energy listed in Table 8.4.1 is determined from the integral flux, and not from the EAS size, because the size–energy relations are strongly depend on the chemical composition of primary cosmic rays.

Here we used the following energy spectrum measured with SAS array [81],

$$(dF/dE)_{SAS} = \begin{cases} 6.44 \cdot 10^{18} \times E^{-2.62} & (14.1 < \log E < 14.6) \\ 6.91 \cdot 10^{20} \times E^{-2.76} & (14.6 < \log E < 15.7) \\ 2.31 \cdot 10^{29} \times E^{-3.30} & (15.7 < \log E) \end{cases} \tag{8.28}$$

Moreover, for primary protons and iron nuclei, the primary energies and the energy bin widths corresponding to an identical EAS size and a identical size bin width are different. So that, the mixing ratios as a function of primary energy were corrected by considering the energy spectrum, and the energy–size relations of primary protons and iron nuclei. Finally, the results of the estimation of the mixing ratios $x_0 + \Delta x$ are listed in Table 8.1.

The errors in the table are the fitting errors of 68% confidence level and the statistical errors. The systematic and statistical errors for the the values of $\mathrm{n_p}/(\mathrm{n_p} + \mathrm{n_{Fe}})$ are estimated as the result of the identical analysis of simulated data. For the estimation, we simulated 50 independent data sets, each of which has the identical number of events to the observed data. The differential flux of the simulated data has the identical energy dependences to the measured all–particle spectrum described below, and the proton mixing ratios of the simulated data were equal to those of the measured ones. The systematic and the statistical errors for the equi–intensity curves with the several different fluxes and their mixing ratio dependences are shown in Figure 8.28.

The systematic errors were estimated from the primary energies of protons and of iron nuclei to contribute to each flux. A difference between the estimated energy of protons and that of iron nuclei gives a systematic error of an estimated energy. We obtained the systematic and

$\log F(>N)$	$\log E$[eV]	$\log N$	$n_p/(n_p+n_{Fe})$	$\log F(>N)$	$\log E$[eV]	$\log N$	$n_p/(n_p+n_{Fe})$
−5.20	14.55 ± 0.10	5.41	0.444 ± 0.029	−6.95	15.54 ± 0.01	6.38	0.284 ± 0.039
−5.45	14.70 ± 0.09	5.56	0.369 ± 0.021	−7.20	15.65 ± 0.00	6.49	0.312 ± 0.034
−5.70	14.85 ± 0.07	5.71	0.334 ± 0.023	−7.45	15.76 ± 0.01	6.59	0.220 ± 0.080
−5.95	15.00 ± 0.06	5.86	0.260 ± 0.026	−7.70	15.87 ± 0.02	6.70	0.148 ± 0.080
−6.20	15.15 ± 0.05	6.00	0.291 ± 0.024	−7.95	15.98 ± 0.05	6.87	0.077 ± 0.110
−6.45	15.29 ± 0.04	6.13	0.286 ± 0.085	−8.20	16.08 ± 0.04	6.98	0.095 ± 0.101
−6.70	15.42 ± 0.02	6.26	0.259 ± 0.027				

Table 8.1: The integral fluxes, corresponding primary energies, the average EAS sizes for $\sec\theta = 1.0-1.05$ and estimated values of $n_p/(n_p+n_{Fe})$ for each energy. The unit of integral flux $F(>N)$ is $m^{-2}sr^{-1}s^{-1}$.

$\log F(>N)$	systematic bias	statistical error	$\log F(>N)$	systematic error	statistical error
−5.20	+0.0233	±0.0102	−6.95	+0.0028	±0.0339
−5.45	+0.0011	±0.0128	−7.20	-0.0048	±0.0206
−5.70	-0.0019	±0.0172	−7.45	-0.0186	±0.0702
−5.95	-0.0121	±0.0094	−7.70	-0.0502	±0.0652
−6.20	-0.0100	±0.0115	−7.95	+0.0473	±0.1052
−6.45	+0.0066	±0.0158	−8.20	+0.1451	±0.0971
−6.70	+0.0231	±0.0200			

Table 8.2: The systematic errors of $n_p/(n_p+n_{Fe})$.

statistical errors with the simulations for the mixing ratios as listed in Table 8.2. We calculated the systematic errors in primary energy and the values appear in Table 8.1.

By using these result, the mean logarithmic mass number $\langle \ln A \rangle$ (where A is atomic number) is calculated and is compared with those of other measurements as shown in Figure 8.29. Our result shows good agreement with the results of the direct measurements by JACEE [8] and by RUNJOB [7] at primary energies from 10^{14} to 10^{15} eV. Moreover, $\langle \ln A \rangle$ obtained with our result is increasing with the primary energy above the knee up to 10^{16} eV.

Our result also agrees well with the results of our Čerenkov radiation observations [82], of CASA–MIA [35], of KASCADE with the analysis using hadrons and muons [25], and of HEGRA–CRT [13]. Clearly, the observed $\langle \ln A \rangle$ increases with the primary energy around the knee. This feature is apparently inconsistent with the preliminary results of KASCADE with unfolding analysis using electrons and muons [94], and of CASA–BLANCA [29].

Our result combined with the direct measurement of $\langle \ln A \rangle$ shown in Figure 8.29 indicates that $\langle \ln A \rangle$ is constant up to about $10^{14.5}$ eV. Above this energy, $\langle \ln A \rangle$ increases with the energy up to 10^{16} eV. The factor between these two characteristic energies is about 30, and this is equal to the charge of iron, *i.e.*, $Z = 26$. Thus one possible explanation of this feature of the measured $\langle \ln A \rangle$ is that the energy spectrum of each cosmic ray component is steepen at a fixed rigidity.

As mentioned in the previous section, the present result shows that the dominant component in the energy region around the knee becomes heavy such as iron nuclei. In our previous observations of Čerenkov radiation induced by EASs, we observed EAS longitudinal development at the stages before shower maxima. With the present analysis, we determined the longitudinal

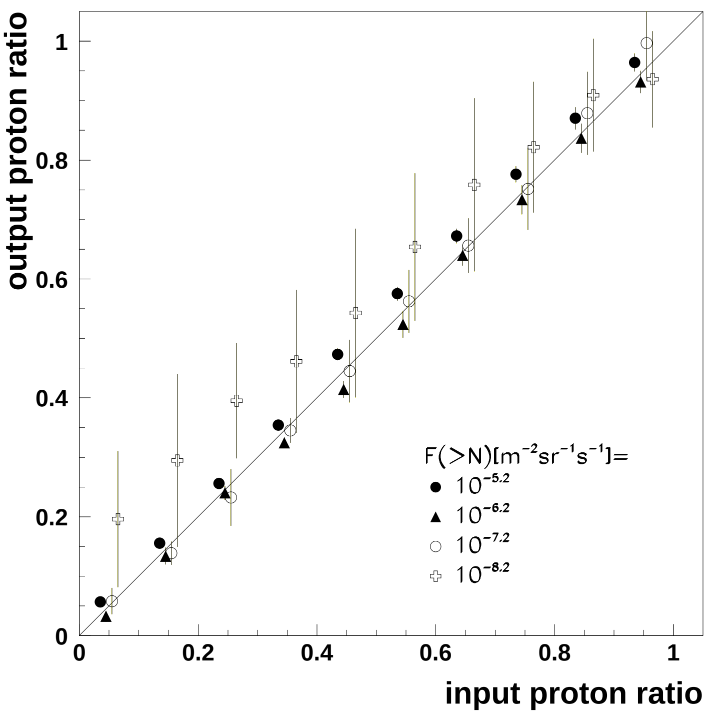

Figure 8.28: The systematic and the statistical errors of $n_p/(n_p + n_{Fe})$. The errors are estimated for simulated data with equivalent number of events as observed.

developments at the later stages. Nonetheless, both measurements of the chemical composition with two different and the independent observations are consistent each other. Thus, we successfully measured whole longitudinal development of EASs with the two observations and thereby reach an estimation of the chemical composition.

The present result is consistent with the results both CASA–MIA and KASCADE(hadrons), but inconsistent with those of KASCADE(electrons) and CASA–BLANCA. The validity of our result is shown in the observed longitudinal development curves by comparisons with the simulated curves of the primary protons. While the calculated EAS longitudinal development curves are dependent on the hadron interaction model, our adopted QGSJET model shows the most rapid developments among the major models. Therefore, it is not possible to explain our observed development curves with any hadronic interaction models with proton dominant compositions.

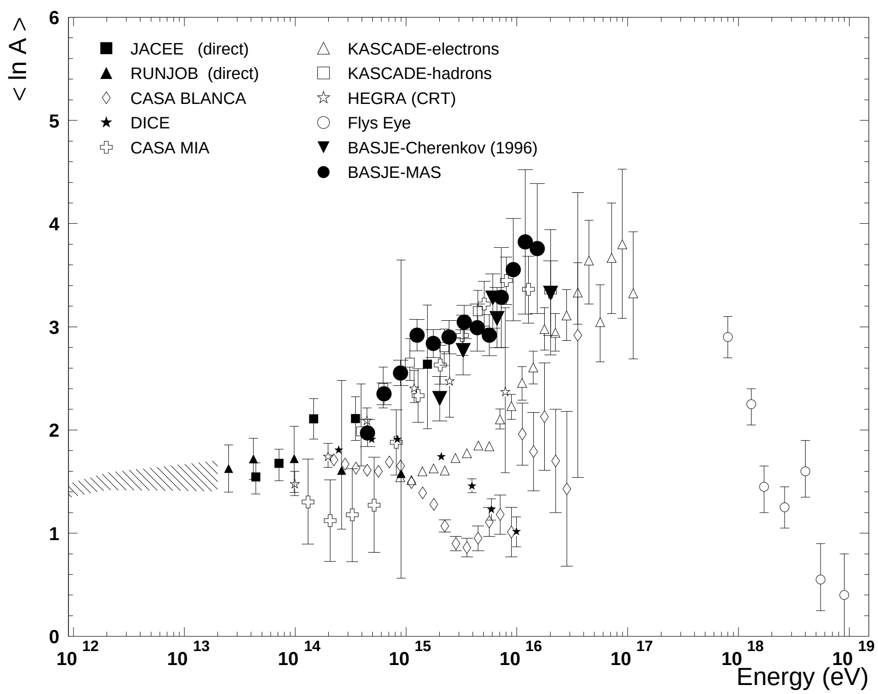

Figure 8.29: The mean logarithmic mass $\langle \ln A \rangle$ measured by BASJE–MAS array as a function of the primary energy, are compared with the results of other experiments with balloon–borne detectors(JACEE [8], RUNJOB [7]) and ground–based detectors(CASA–MIA [35], KASCADE(hadrons) [25], HEGRA–CRT [13], KASCADE(electrons) [94], CASA–BLANCA [29], DICE [88], Fly's Eye [16]). Also the results of our former Čerenkov observations [82] are plotted. A hatched region represents the result of other direct observations, which are accumulated by Linsley [65].

8.4.2 Energy spectrum

Taking into account the determined proton mixing ratio, the average relation between the primary energies and the observed EAS sizes for EASs with $1.0 \leq \sec\theta < 1.1$ was calculated with the simulations. The results are plotted in Figure 8.30.

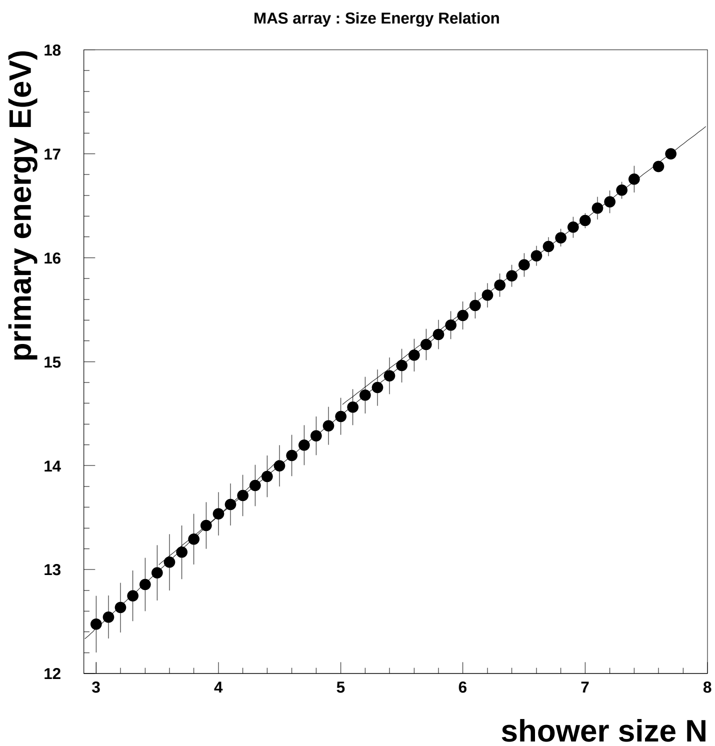

Figure 8.30: The relation between the primary energies and the reconstructed EAS sizes with our array with $1.0 \leq \sec\theta < 1.1$

The size–energy relation was obtained with fitting of the plots, and is derived as follows,

$$\log E = \begin{cases} 0.95 \times \log N_{rec} + 9.65 & (\log E < 15.7) \\ 0.85 \times \log N_{rec} + 10.36 & (\log E \geq 15.7) \end{cases} \tag{8.29}$$

Finally, using this relation, we derived the primary energy spectrum.

The resultant differential energy spectrum, dF/dE is shown in Figure 8.31 and is well expressed by the following,

$$\log(\frac{dF}{dE}[\mathrm{m}^{-2}\mathrm{s}^{-1}\mathrm{sr}^{-1}\mathrm{eV}^{-1}]) = \begin{cases} (19.26 \pm 0.07) - (2.66 \pm 0.01) \times \log E[eV] & (\log E < 15.4) \\ (27.44 \pm 1.77) - (3.19 \pm 0.11) \times \log E[eV] & (\log E \geq 15.4) \end{cases} \tag{8.30}$$

In Figure 8.31, we also plot the results reported by other groups. At energies around 10^{14} eV the present result is consistent within uncertainty with the direct measurements and with CASA-MIA [34] and DICE [88] measurements. Comparing our result with those by Tibet and by KASCADE, both of the absolute intensity and the energy of the knee in our spectrum are low. These differences could be due to the systematic difference of energy estimation procedures

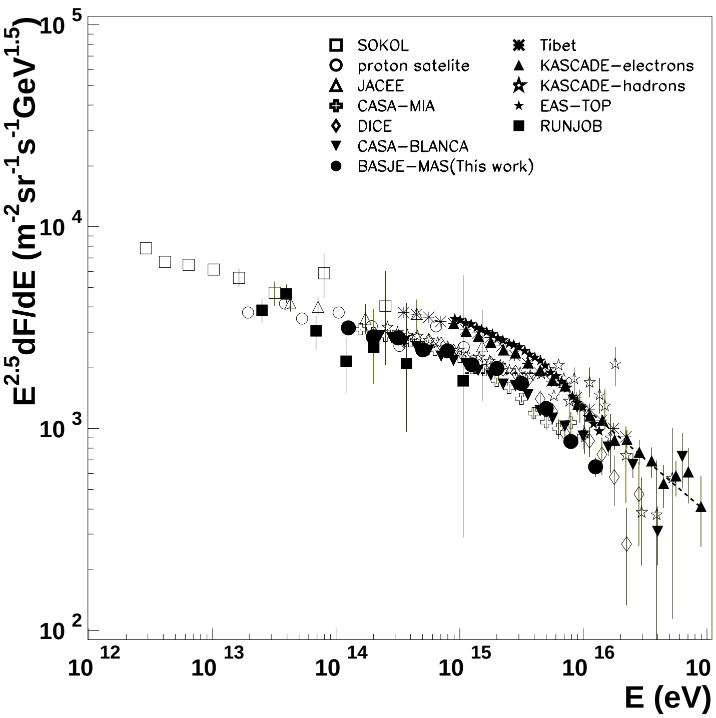

Figure 8.31: The differential all–particle cosmic ray flux measured by BASJE–MAS array. Also plotted are the cosmic ray fluxes reported by JACEE [8], RUNJOB [7], SOKOL [52], proton satellite [36], KASCADE(hadrons) [25], KASCADE(electrons) [94], CASA–BLANCA [29], CASA–MIA [34], DICE [88], Tibet [4], EAS–TOP [1], and the dashed line represents the flux measured by Akeno group [72].

as mentioned by the CASA–MIA group [35]. According to their discussion, the required energy shift is small. Lowering the Tibet energy scale by 20% would reduce the discrepancy between the experiments.

We show simulated equi–intensity curves with the measured ones without any normalization in Figure 8.26(b). In the simulation, we took into consideration not only the obtained mixing ratios of protons and iron nuclei, but also the all particle energy spectrum(8.30). In this plot we show only the statistical uncertainties. When we consider the uncertainties in the energy spectrum determination, which strongly affect the uncertainties in the rate of arrival, we concluded that the simulation gives good agreement with the experimental results.

Chapter 9

Discussion

9.1 The systematic errors in the determination of chemical composition and primary energy

In the present analysis, we assumed the primary cosmic ray component is a mixture of two nuclei, *i.e.*, protons and iron nuclei. To see how the longitudinal developments reflect the composition, here we consider (4.8) and (4.9) in the superposition approximation for incident nuclei. The superposition model leads the mean depth of maximum development, X_{max}, for a primary energy E_0 as follows,

$$X_{max} = X_0 \sum_i w_i \ln \left(\frac{E_0}{A_i E_{crit}} \right) \tag{9.1}$$

$$= X_0 \left(\ln \frac{E_0}{E_{crit}} - \langle \ln A \rangle \right), \tag{9.2}$$

where X_0 is the radiation length for the air, A_i is the mass number, w_i is the relative abundance of the component i, and E_{crit} is the critical energy for the air. In the relation (9.2), it is shown that the longitudinal development curves depend only on $\langle \ln A \rangle$. That is to say, in the superposition approximation, through the measurement of the averaged properties of the longitudinal development curves, we can determined a correct $\langle \ln A \rangle$ for any mixture of components in the superposition approximation.

With the detailed Monte–Carlo studies, we can estimate the tolerance of the superposition approximation. For example, the mixture of 50% proton + 50 % iron nuclei and the mixture of 10% protons + 90% carbon nuclei show the equivalent X_{max}, 655 g/cm^2 and 653 g/cm^2 by the simulations with CORSIKA and QGSJET model($\log E = 16.8 - 17.0$). On the other hand, each $\langle \ln A \rangle$ for the different mixtures considered above is 2.01 and 2.24, respectively. The difference of $\langle \ln A \rangle$ for these mixture is about 0.2, and this value is a systematic error based on the choice of the components for the analysis.

One can estimate primary energy from the two different observable values, *i.e.*, the rates of arrivals and the EAS sizes. The primary energies estimated from the rates of arrivals (8.30), E_{rate} and the energies determined from the EAS sizes with the size–energy relation (8.29), are listed in Table 9.1. From this table, the averaged difference $\log E_{size} - \log E_{rate}$ is about 0.2. This is the systematic energy determination errors for the present result totally including the effects of the equipments, the composition uncertainty, the analysis and the simulations.

$\log F(>N)$	$\log E_{rate}$[eV]	$\log N$	$\log E_{size}$[eV]	$\log F(>N)$	$\log E_{rate}$[eV]	$\log N$	$\log E_{size}$[eV]
−5.20	14.61	5.41	14.79	−6.95	15.55	6.38	15.78
−5.45	14.76	5.56	14.93	−7.20	15.66	6.49	15.88
−5.70	14.91	5.71	15.07	−7.45	15.78	6.59	15.96
−5.95	15.05	5.86	15.22	−7.70	15.89	6.70	16.06
−6.20	15.19	6.00	15.35	−7.95	16.00	6.87	16.20
−6.45	15.32	6.13	15.47	−8.20	16.12	6.98	16.30
−6.70	15.44	6.26	15.60				

Table 9.1: The table of the integral fluxes, corresponding primary energies E_{rate}, the average EAS sizes and corresponding energy E_{size}The unit of integral flux $F(>N)$ is $\mathrm{m^{-2}sr^{-1}s^{-1}}$.

In the equi–intensity method analysis it is postulated that showers which are observed with the same frequency of occurrence at different zenith angles are initiated by particles of the same energy. Here the validity of this assumption is checked with Monte Carlo simulations. Figure 9.1 shows the relation between the mean energies and the atmospheric depths on the equi–intensity curve corresponding to a certain rate of arrival. In the Monte Carlo simulation I used the mixing ratios shown in Table 8.1. The averaged energies over all the components are practically constant as shown in Figure 9.1. However, the mean energies of each component vary with the atmospheric depths because of the difference of the longitudinal developments between air showers induced by protons and those induced by iron nuclei. Therefore, the mixing ratios on the equi–intensity curve also vary with the atmospheric depths as shown in Figure 9.2. Practically, the fact that the mean energies and the mixing ratios are not constant on an equi–intensity curve does not causes the systematic errors on the determinations of the mixing ratios. Because the measured equi–intensity curves are compared with the calculated ones with the air shower simulations including the assumptions of the all–particle energy spectrum and the chemical composition.

The difference of the indexes of component spectra between protons and iron nuclei is a possible cause of a systematic error, because in equi–intensity method analysis we supposed that all the spectral indexes are identical in a range of the energies of cosmic rays contributing to a equi–intensity curve. However, the indexes are not identical as shown in Figure 9.18. In order to estimate the systematic error, I simulated the equi–intensity curves for two cases. In *case 1*, the indexes of the component spectra are not identical in a range of the energies of the contributing cosmic rays, *i.e.*, $\langle \ln A \rangle$ is increase with the energy in the range. In *case 2*, the indexes are identical, *i.e.*, $\langle \ln A \rangle$ is constant in the energy range. The comparisons between case 1 and case 2 are shown in Figure 9.1 and 9.2. The differences between the two cases are very small, and less than the measurement errors, and then the systematic errors based on the different indexes are negligible.

9.2 Comparisons the results with the source models

We compare the results of our all–particle flux and $\langle \ln A \rangle$ to those of a composition model with five cosmic ray components (protons, He, CNO, Ne–Si, Fe). In this model, it is assumed that each component spectrum has the index that measured by the RUNJOB collaboration and the component spectra are steepened at the fixed rigidity $10^{14.5}$ V. The calculated flux of each

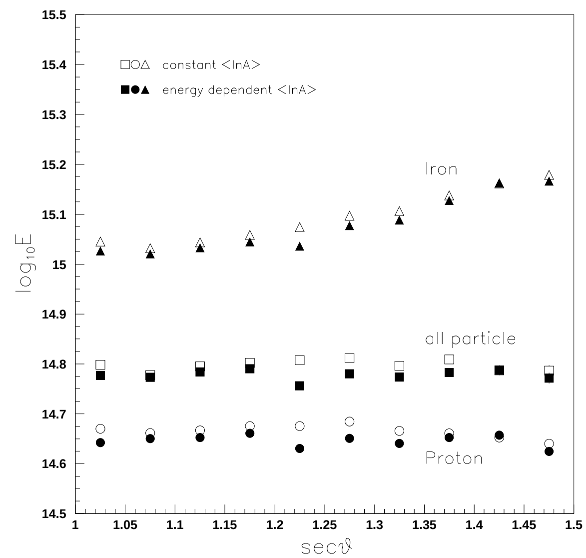

Figure 9.1: These plots are simulated results of the relation between the mean energies and the atmospheric depths on the equi–intensity curve corresponding to a certain rate of arrival.

component is summed each other according to the relative abundances measured by SOKOL [52] at 10^{12} eV and the total flux is normalized to the all–particle spectrum obtained also by SOKOL at the same energy. Moreover, we examined two different cases for the model. In the first case (a), each spectral index is steepened by 0.6, corresponding to the rigidity. This is expected in the case that the energy dependence of the diffusion coefficient dominates the cosmic ray propagation processes changes at a fixed rigidity. In the second case (b), the spectral index changes, irrespectively of A, to -3.2 in the energy corresponding to the same rigidity. This is expected in the case that the dominant acceleration process of cosmic rays is changed above the rigidity. The values of 0.6 in model (a) and -3.2 in model (b) are assumed with our measured all–particle spectrum. The calculated spectra and the resultant $\langle \ln A \rangle$ are shown in Figures 9.3 and 9.4, respectively. Although both the calculated fluxes in Figures 9.3(a) and 9.3(b) are slightly less than the measured one at $10^{14.7} - 10^{15.7}$ eV, the all–particle fluxes at the other energy range and the predicted $\langle \ln A \rangle$ of models (a) and (b) are consistent with present results. This suggests that iron nuclei are the dominant component at the primary energies greater than 10^{15} eV. The model predictions do not fit the measured spectrum between $10^{14.7}$ and $10^{15.7}$ eV and result in two knees at $10^{14.7}$ eV and at $10^{15.7}$ eV. Therefore, the simple models described here are not sufficient to produce the measured spectrum and composition.

In the report of HEGRA–CRT group [13], they suggested that the each spectrum of the primary components is steepened at a fixed rigidity and that the dominant component at the knee energy is CNO. They also showed an increase in $\langle \ln A \rangle$ with the energy. Their simple model is consistent with our present result up to 10^{15} eV. However, the $\langle \ln A \rangle$ in their model saturates around this energy and does not fit to our result at the higher energies. Hörandel [49] proposed the model with introducing the charge dependent cut–off energies and the ultra–heavy nuclei(Z=30–92) components, this is inconsistent with our result because the model predicts protons are dominant at the knee.

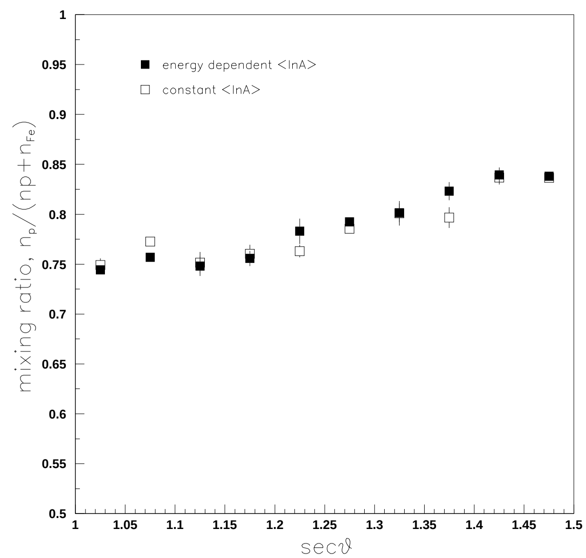

Figure 9.2: These plots are simulated results of the relation between the mixing ratio and the atmospheric depths on the equi–intensity curve corresponding to a certain rate of arrival.

The model of the particle acceleration by oblique shocks proposed by Kobayakawa, et al. [63] predicts the knee and the gradual increase of $\langle \ln A \rangle$ with the increasing energy from 10^{14} to 10^{16} eV without any assumption of a rigidity dependent cut–off. Their prediction on $\langle \ln A \rangle$ is consistent with our result, but the predicted absolute value of $\langle \ln A \rangle$ is smaller than our result.

In the model of Völk and Biermann [95], cosmic rays from 10^{13} eV to the knee are mainly accelerated during explosions of massive stars. Biermann [14] developed this model further and examines explosions of Wolf–Rayet stars. He concluded that at the knee, the particles segregate with particle energy according to their charge, that protons drop off first, then the C–N–O elements, next Mg, Si, etc., and finally iron nuclei. At the surfaces of Wolf–Rayet stars helium and heavier elements are enhanced rather than protons. This can be reflected effectively to the chemical composition of primary cosmic rays. As discussed in our previous paper by Shirasaki et al. [82], the measured $\langle \ln A \rangle$ suggests that the accelerated particle abundance must be heavier than the stellar winds of Wolf–Rayet stars. Since the accelerated particles are a mixture of the stellar wind particles and ejected matters, Biermann's model seems to be very promising favourable to our former and present results.

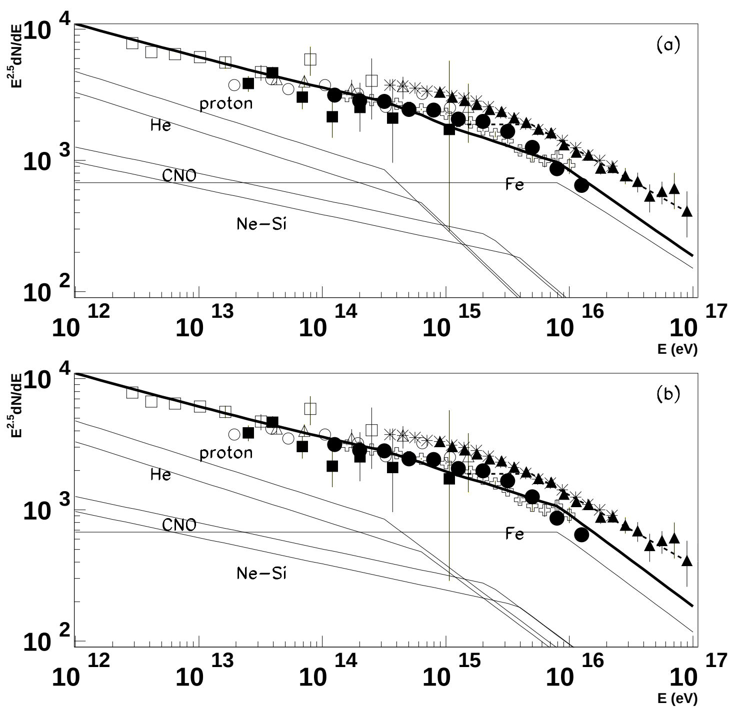

Figure 9.3: All–particle spectrum and the contributions of five components calculated with model (a)(upper panel) and with model (b)(lower panel) are compared with the measured spectra.

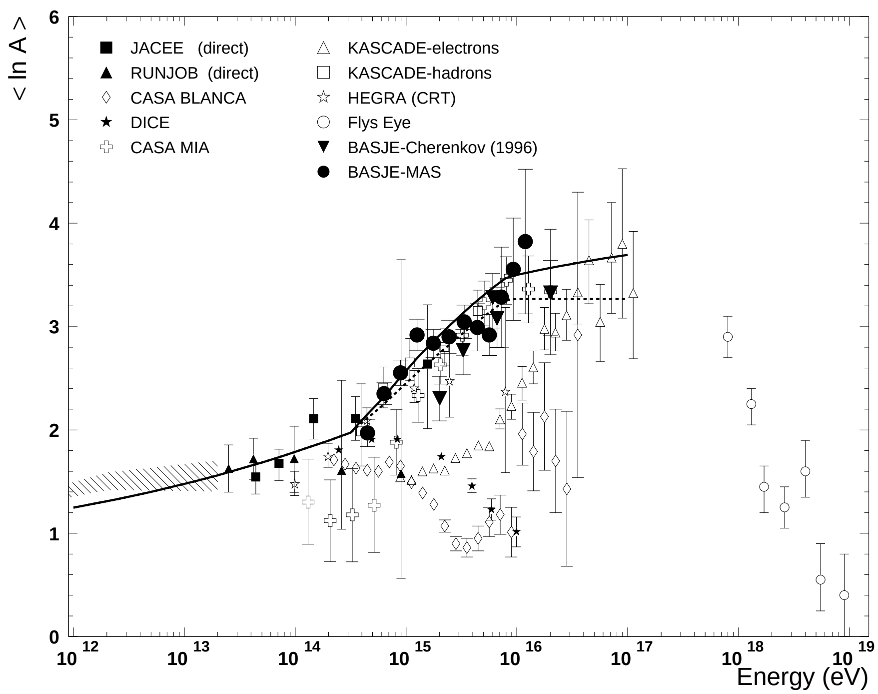

Figure 9.4: The predicted mean logarithmic mass $\langle \ln A \rangle$ with the model (a)(*solid line*), and (b)(*dashed line*).

9.3 Comparisons the results with the advective diffusion propagation model

In the previous section, I presented a very simple models to explain the chemical composition and the energy spectrum. In that model the fixed rigidity at the bending points of the spectra and the index jump of the steepening are determined empirically. The advective diffusion model described in section 3.4 for the calculations of the residence time in the galactic disk with the advective–diffusion function naturally predicted the observed features such as the energy spectrum, the anisotropy, the mean mass number and its energy dependence.

Using the calculated residence times τ_R in section 3.4.3, the component spectra, the all particle spectrum, the chemical composition and the anisotropy amplitude are estimated with a simple assumed relation $N(E) = Q(E)\tau_R(E)$. The expected flux of i–th component N_i and all particle flux, N_{all}, were given by

$$N_i = \tau_{Ri} \times c_i \mathcal{A} E^{-\gamma_i} \quad (9.3)$$

$$N_{all} = \sum_i N_i \quad (9.4)$$

where c_i is relative abundance of i–th component at a source, $\mathcal{A}$ is a normalization factor and γ_i is the spectral index of i–th component. For this calculation, c_i were determined from the consequences of the direct observations for primary cosmic rays of less than 10^{12}eV, because the observed spectra for low energies are expected to be equal to source spectra in the advective diffusion model. Here c_i are calculated from the measured relative abundance by SOKOL on COSMOS satellite above 2.5 TeV [52], and these are listed in Table 9.2, and consistent with the reported values by CRN for more lower energy cosmic rays [71].

component	abundance	spectral index		
	($E > 10^{12}$eV)	model J	model $\mathrm{R_C}$	model $\mathrm{R_F}$
proton	0.39	2.7	2.6	2.7
He	0.27	2.5	2.7	2.7
CNO	0.13	2.4	2.4	2.6
Ne–Si	0.10	2.6	2.6	2.6
Fe	0.11	2.5	2.5	2.4

Table 9.2: Assumed relative abundance and three models of the spectral indices for five component of cosmic ray particles.

The spectral index γ_i for i-th component is estimated from the direct measurements of SOKOL, Ryan et al. [78], Sanriku [60], JACEE [8] and RUNJOB [7]. Since the measured spectra by SOKOL, JACEE and RUNJOB are different each other, I took the three different sets of γ_i listed in Table 9.2. Model J is chosen to fit the results of JACEE, and this has rather flatter spectra for He and CNO compared with the proton spectrum. Model $\mathrm{R_C}$ is chosen to fit the He spectrum by RUNJOB and the spectra of other component are consistent with the result of JACEE and with that of SOKOL. This model predict a flat CNO spectrum. Model $\mathrm{R_F}$ is chosen to fit the spectra by RUNJOB, except the Fe spectrum. This model has a slightly flat Fe spectrum.

The calculated all particle spectrum was normalized to that of observed at 10^{12}eV with the factor $\mathcal{A}$. The other parameters in this model are v_g and L_{irr}. These parameters are not determined with the current observations as mentioned in section 3.4. Thus, I used the six pair of these parameters as listed in Table 9.3 to calculate the energy spectrum, the composition and its energy dependences.

Model ID	1	2	3	4	5	6
L_{irr}(pc)	10	50	100	10	50	100
v_g(km/s)	490			196		
(pc/yrs)	0.0005			0.0002		

Table 9.3: The model ID and the corresponding sets of the parameters pairs, L_{irr} and v_g.

9.3.1 All particle spectrum

The all particle spectra calculated with the models $\mathrm{J}-1$(spectral index model J + model ID=1), $\mathrm{J}-2$ and $\mathrm{J}-3$ are shown in Figure 9.5, and those with the models $\mathrm{J}-4$, $\mathrm{J}-5$ and $\mathrm{J}-6$ are shown in Figure 9.6. The spectrum of $\mathrm{J}-1$ is too flat and too large flux at energies less than 10^{14}eV, but this curve fits well with the Tibet and KASCADE–electron results. The curve with the model $\mathrm{J}-2$ is gradually steepening around 10^{15}eV and the spectral index is changed from -2.7 to -3.1. These features of the spectral shape and the flux which are predicted with the model $\mathrm{J}-2$ are consistent with the direct measurements below 10^{14}eV and our results of BASJE–MAS, CASA–MIA and the other measurements up to 10^{17}eV. The predicted flux with the model $\mathrm{J}-3$ is slightly less than the observed results in the energies greater than 10^{15}eV.

The curves of $\mathrm{J}-5$ and $\mathrm{J}-6$ are too steep to fit the measured spectrum, because the advection velocity $v_g = 0.0002$pc/years is too slow, so that the diffusion process is dominated for the whole energies regions $10^{12}-10^{17}$eV. Moreover, the curve of model $\mathrm{J}-4$ resembles that of $\mathrm{J}-2$, thus only the models of 1, 2 and 3($v_g = 0.0005$pc/years) are considered for further discussions.

The spectra predicted by the model $\mathrm{R_C}$ and $\mathrm{R_F}$which are shown in Figure 9.7 and 9.8. These curves are not much different from that of the model J. From Figure 9.8, the spectra of the model $\mathrm{R_F}$ have the bends with index of -2.7 to -3.0 at the knee, because the dominant component above the knee is iron nuclei, which has rather flatter spectrum of the index -2.4 than the other models. The curves of $\mathrm{R_F}-1$ and $\mathrm{R_F}-2$ are not inconsistent with the measurements, but the flux predicted by $\mathrm{R_F}-2$ at $10^{15}-10^{16.5}$eV is less than the observed one.

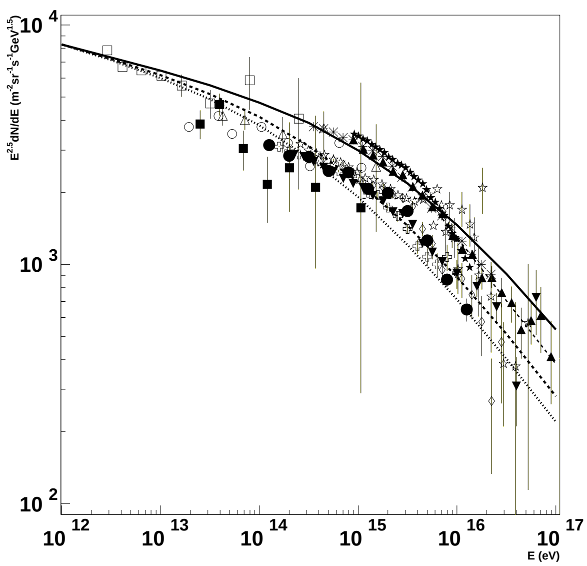

Figure 9.5: Calculated all particle spectra with the advective–diffusion models of $J-1$(solid line), $J-2$(thick dashed line) and $J-3$(dotted line). The markers represent the observed energy spectra, by SOKOL [52](□), proton–satellite [36](◯), RUNJOB [7](■), JACEE [8](△), CASA–MIA [34](+), KASCADE–hadron [25](⋆), Tibet [4](∗), CASA–BLANCA [29](▼), DICE [88](◊), EAS–TOP [1](★), KASCADE–electron [94](▲) and this work(BASJE-MAS)(•). Thin dashed line represents the flux measured by Akeno group [72].

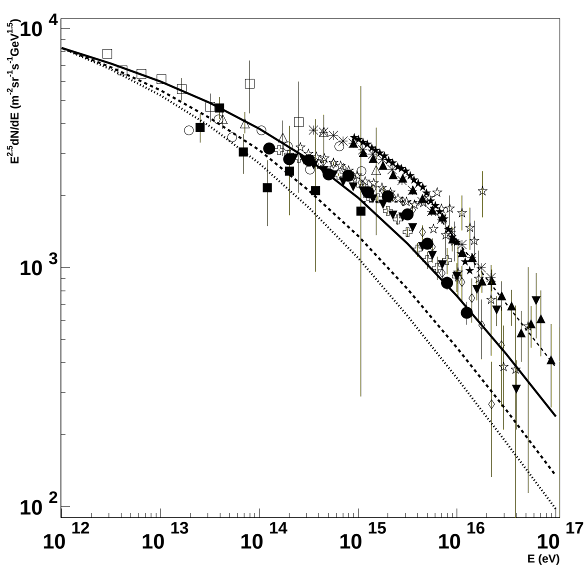

Figure 9.6: Calculated all particle spectra with the models of $J-4$(solid), $J-5$(thick dashed) and $J-6$(dotted).

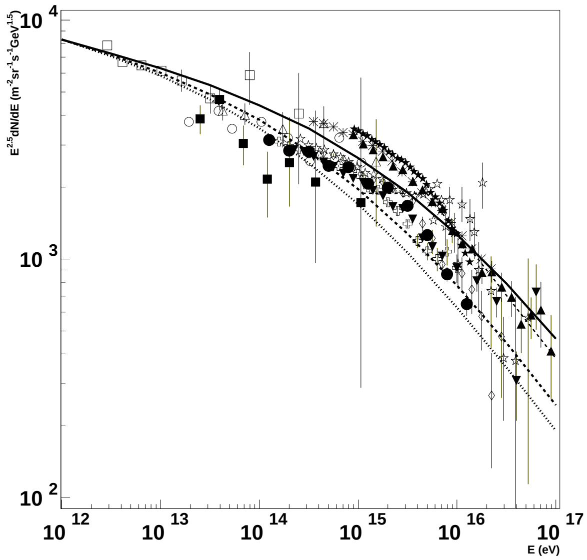

Figure 9.7: Calculated all particle spectra with the models of $R_C - 1$(solid), $R_C - 2$(thick dashed) and $R_C - 3$(dotted).

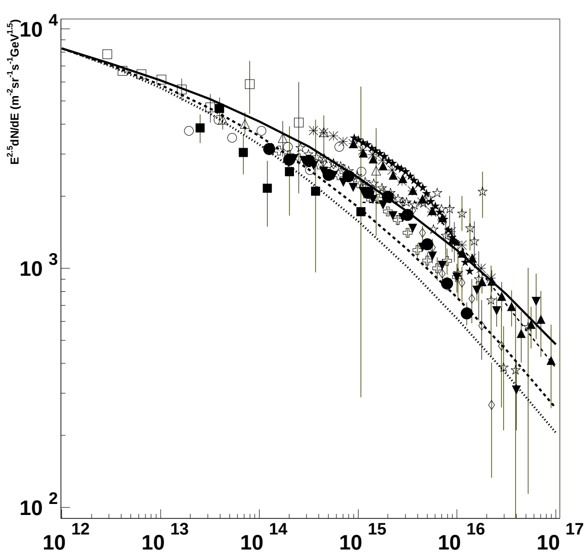

Figure 9.8: Calculated all particle spectra with the models of $R_F - 1$(solid), $R_F - 2$(thick dashed) and $R_F - 3$(dotted).

9.3.2 Spectra for the element groups

The most significant differences of the observed spectra by JACEE and RUNJOB are appeared in the He and CNO flux. The spectra for the element groups are shown in Figure 9.9 which are calculated with the model J, 9.10 with R_C and

9.11 with R_F. The spectra of model J fits well with the JACEE data within the error as shown in Figure 9.9. The He spectrum of the model R_C, and the He and CNO spectra of the model R_F are based on the RUNJOB data. For every models, the calculated spectra are well consistent with the observed spectra assumed in whole energy range in which the direct measurement data exist.

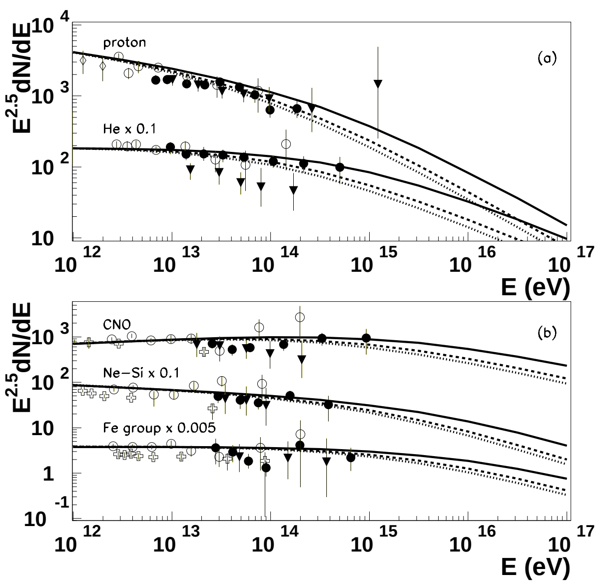

Figure 9.9: The lines are the calculated energy spectra for the assumed five components with the advective–diffusion models of $J-1$(solid), $J-2$(dashed), $J-3$(dotted). The marker plots represent the observed energy spectra of five groups of cosmic ray species by the direct measurements of Ryan et al. [78]($\Diamond$), SOKOL [52]($\bigcirc$), JACEE [8]($\bullet$), CRN [71](+) and RUNJOB [7]($\blacktriangledown$).

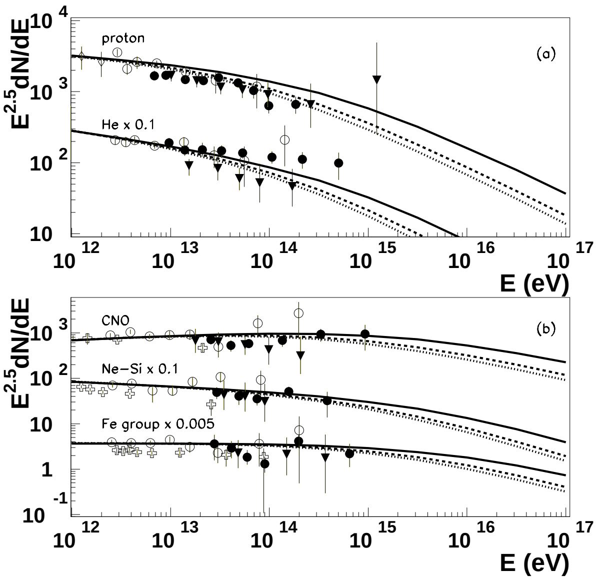

Figure 9.10: The lines are the calculated energy spectrum for each component with the models of $\mathrm{R_C}-1$(solid), $\mathrm{R_C}-2$(dashed), $\mathrm{R_C}-3$(dotted).

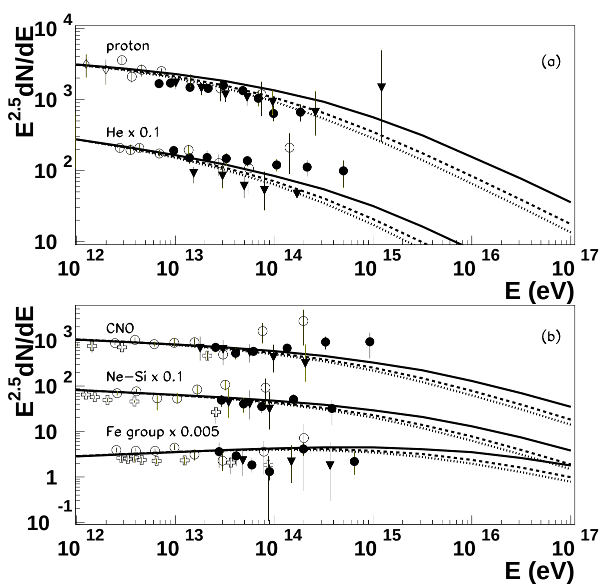

Figure 9.11: The lines are the calculated energy spectrum for each component with the models of $\mathrm{R_F}-1$(solid), $\mathrm{R_F}-2$(dashed), $\mathrm{R_F}-3$(dotted).

9.3.3 Average mass number

As an indicator of the composition, here we calculate the average value of the logarithm of mass number A given by

$$< \ln \mathrm{A} > \equiv \frac{\sum(N_i \times \ln \mathrm{A}_i)}{\sum N_i} \tag{9.5}$$

where N_i is obtained with equation (9.3). The results of the model calculations are shown in Figure 9.12, 9.13 and 9.14 with the observed results. The difference among the models of 1, 2 and 3 is not significant, and every model has the same tendency, that is, $\langle \ln \mathrm{A} \rangle$ increases with the increasing energy up to 10^{17}eV. This feature is consistent with many experimental results including the BASJE–MAS result, but not consistent with some measurements. In the model J and the model $\mathrm{R_C}$, which show the same tendency, $\langle \ln \mathrm{A} \rangle$ are saturated below 3, so that these model are inconsistent with our results. On the other hand, the curve of the model $\mathrm{R_F}$ shows a good agreement with the direct measurements by JACEE, BASJE–MAS and some observations in the energy range $10^{12}\mathrm{eV} - 10^{17}\mathrm{eV}$.

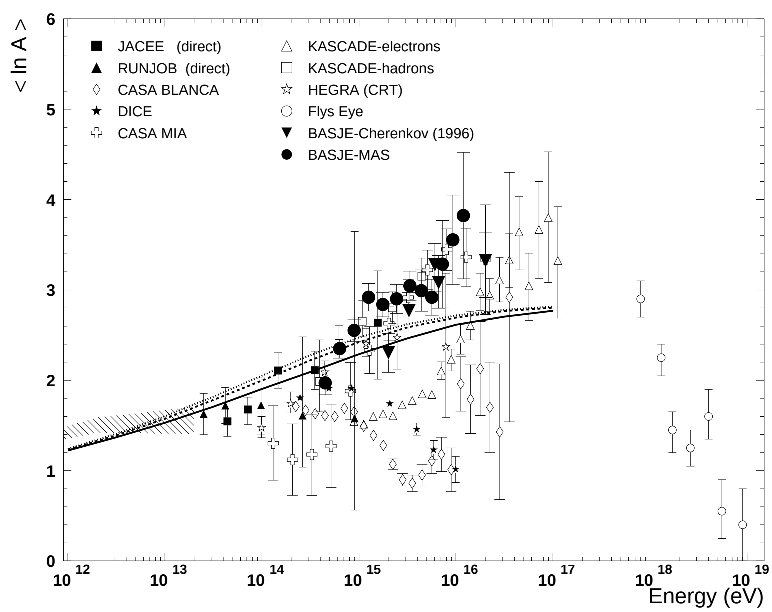

Figure 9.12: The averaged mass number, $< \ln A >$, calculated with the models of $\mathrm{J}-1$(solid), $\mathrm{J}-2$(dashed) and $\mathrm{J}-3$(dotted). The estimated values with various different types of measurements [82]–[16] are also plotted in this figure. A hatched region represents the result of other direct observations, which are accumulated by Linsley [65].

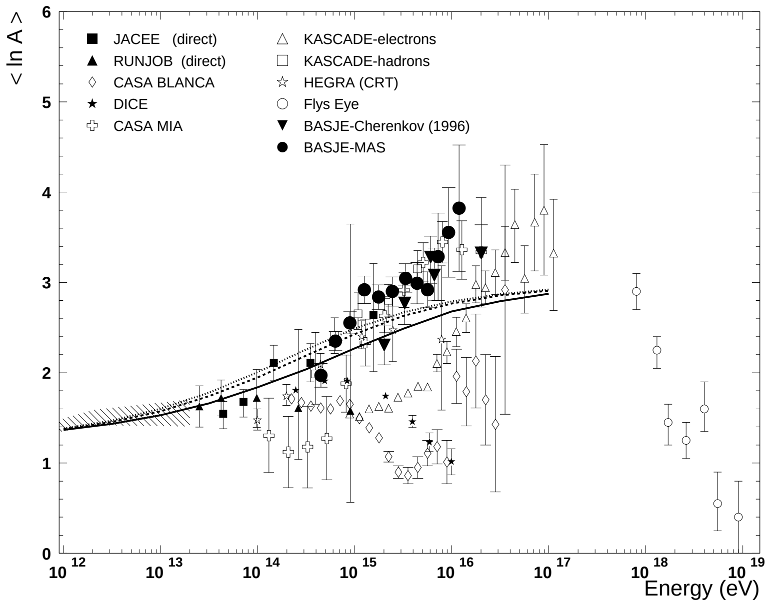

Figure 9.13: The averaged mass number, $< \ln A >$, calculated with the models of $\mathrm{R_C}-1$(solid), $\mathrm{R_C}-2$(dashed) and $\mathrm{R_C}-3$(dotted).

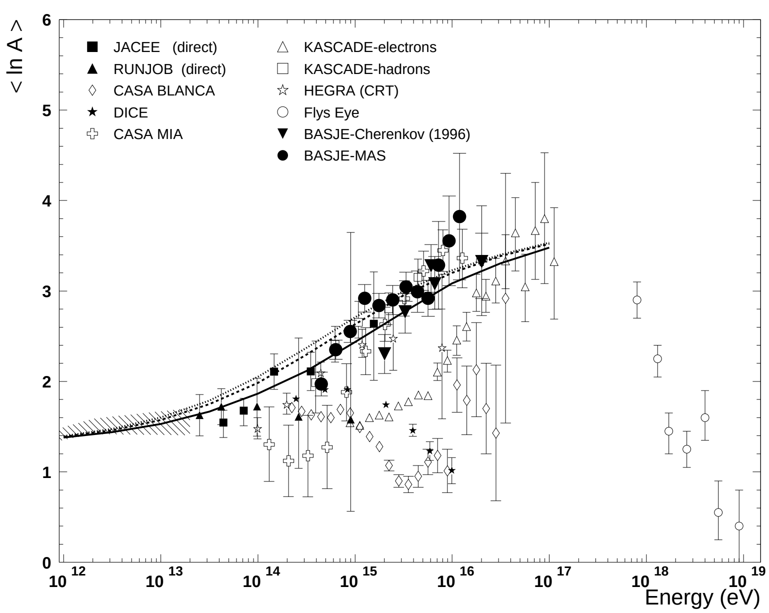

Figure 9.14: The averaged mass number, $< \ln A >$, calculated with the models of $\mathrm{R_F}-1$(solid), $\mathrm{R_F}-2$(dashed) and $\mathrm{R_F}-3$(dotted).

9.3.4 Residence time and anisotropy

The calculated residence times with the model J, R_C and R_F are shown in Figure 9.15(a), 9.16(a), 9.17(a). The differences of the residence times between the models are not significant, $\tau_R \sim 10^5$ years at 10^{12}eV and $\sim$ several $\times\, 10^4$ years at 10^{17}eV. The calculated τ_R at 10^{12}eV is of the same order of magnitude as the estimated value, 5×10^5 years, from the anisotropy amplitude described in Section 3.4.

The predicted anisotropy amplitudes estimated with the relation of $A \propto 1/\tau_R$ are shown in Figure 9.15(b), 9.16(b), 9.17(b). The normalization factors were chosen to fit with the measurements at 10^{12}eV. The model estimations have the tendency for the anisotropy amplitude to be almost constant up to $\sim 10^{14}$eV , and to increase with the increasing energy above $\sim 10^{14}$eV. This feature and the estimated values are consistent with the measured amplitudes.

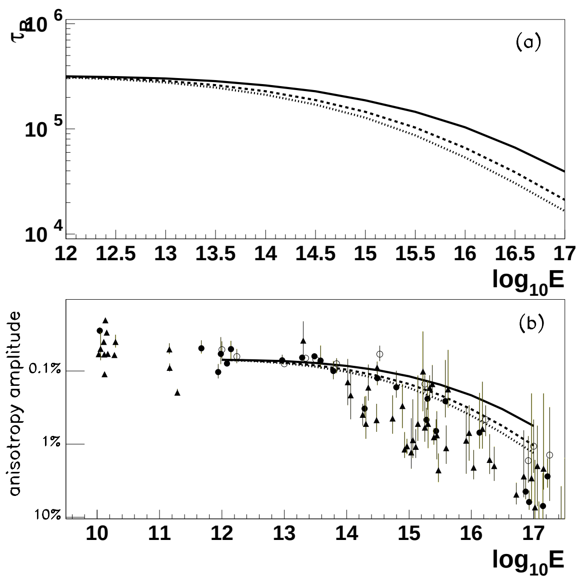

Figure 9.15: (a)The residence times calculated with the models of $J-1$(solid), $J-2$(dashed line) and $J-3$(dotted). (b)The measured anisotropy amplitude compared with the estimated values from τ_R on (a). The estimated anisotropies are calculated with a relation $A \propto 1/\tau_R$ and a normalization factor obtained at 10^{12}eV. The measured anisotropies are accumulated by Hillas [45](◯), Linsley [65](●) and Hayakawa [40](▲).

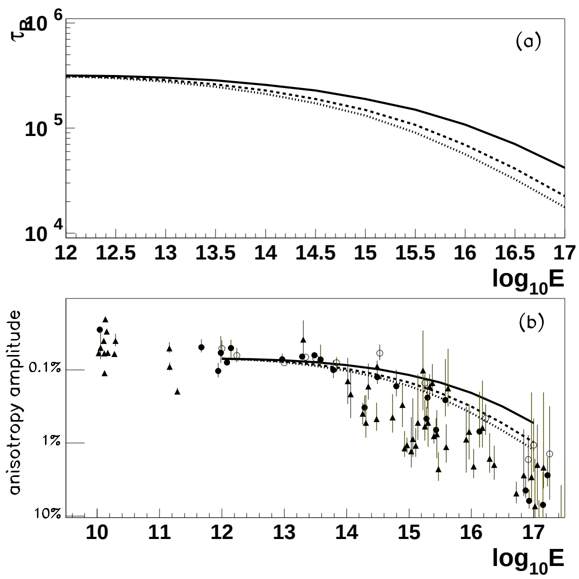

Figure 9.16: (a)The residence times calculated with the models of $\mathrm{R_C}-$(solid), $\mathrm{R_C}-2$(dashed line) and $\mathrm{R_C}-3$(dotted). (b)The measured anisotropy amplitude compared with the estimated values from τ_R in (a). The estimated anisotropies are calculated with a relation $A \propto 1/\tau_R$ and a normalization factor obtained at 10^{12}eV.

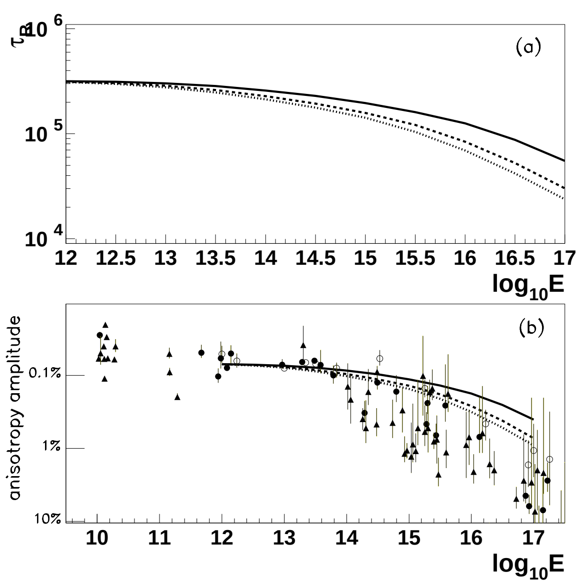

Figure 9.17: (a)The residence times calculated with the models of $\mathrm{R_F}-1$(solid), $\mathrm{R_F}-2$(dashed line) and $\mathrm{R_F}-3$(dotted). (b)The measured anisotropy amplitude compared with the estimated values from τ_R in (a). The estimated anisotropies are calculated with a relation $A \propto 1/\tau_R$ and a normalization factor obtained at 10^{12}eV.

9.3.5 Summary of the advective diffusion model

Here we summarize the advective–diffusion model. The comparisons of the measured all particle spectrum with the model calculated ones showed that the most optimum pair of the parameters is $v_g = 0.0005$ pc/years and $L_{irr} = 50$ pc. These values agree with the observations of the galactic magnetic fields and a model of the galactic wind.

In Figure 9.18, 9.19 and 9.20, we show the all particle spectrum and the contributions of the element groups with the model 2 with the spectral index model J, $\mathrm{R_C}$ and $\mathrm{R_F}$. The model $\mathrm{R_F} - 2$ is only model of which $\langle \ln \mathrm{A} \rangle$ fit the satellite–, the balloon borne– and our measurements. In $\mathrm{R_F}$ model the He and CNO spectral indices are assumed to be same as the RUNJOB data. When the flatter spectra for these species as measured by JACEE will be established, it is necessary to exist an extra contribution of heavy nuclei in cosmic rays with energies greater than 10^{15}eV to fit with the observed results.

The advective–diffusion model predicts the energy independent escape time for cosmic rays with energies below about 10^{13} eV. This is inconsistent with the prediction of the leaky box model, $\tau_{esc} \propto R^{-0.6}$, where R is a rigidity. But this contradiction can be solved by considering the nested leaky box model [23]. In this model, it is assumed that small confinement regions are surrounding the sources with relatively high density in which particles diffuse for a short time. The energy dependence of the secondary to the primary nuclei ratio is attributed to an energy dependent leakage from the source regions, and is characterized by the energy dependent escape length, $\lambda_1(E)$. The Galaxy is considered as an outer volume in which the nuclei from shrouded sources may traverse a further small amount of matter with the energy independent escape length, λ_2(Figure 9.21). In this model, the earth is not inside the inner volume, so that, we observe the source spectrum. Thus cosmic ray accelerators will need to have a differential spectrum with $\gamma \simeq 2.7$. This prediction agrees with the assumption for the advective diffusion model. Therefore, we can draw a following scenario: the low energy cosmic rays propagate in the galactic halo with a process of the nested leaky box model, and for the higher energy cosmic rays, the confinement volume is the disk and such cosmic rays are leaking with the advective diffusion process, as shown in Figure 9.21.

The escape times predicted with the nested leaky box model and with the advective diffusion model are not depend on the particle energies, so that the spectral index is not changed up to the knee. However, the outer confinement volume of the nested leaky box will have to be larger than that in the simple leaky box model to allow the ^{10}Be/Be ratio to fall to its observed value with keeping small λ_2. Since the outer confinement volume is not the galactic disk as the advective diffusion model, the size of confinement volume should change at the intermediate energy, which may be less than 10^{12} eV, and this evidence would appear in an observed primary energy spectrum. Thus, we need more detailed investigations of the properties of the galactic halo and the energy spectrum above 10^{12} eV.

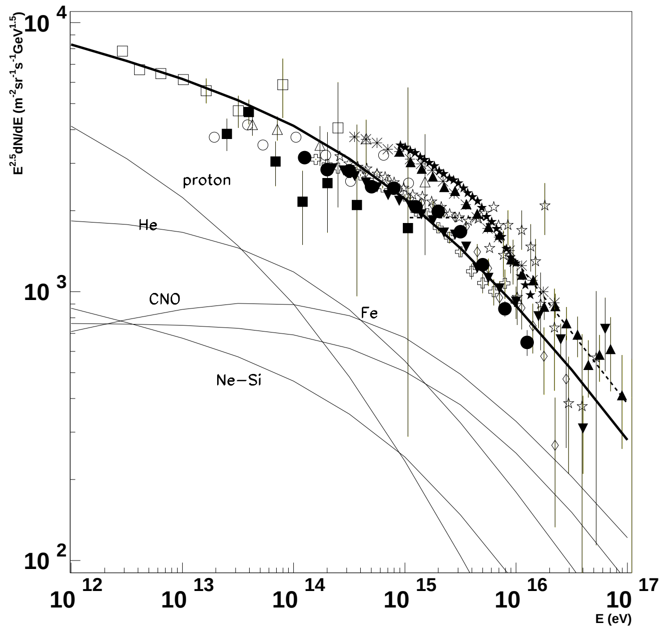

Figure 9.18: Calculated all particle spectrum and the contributions of five components with the model $\mathrm{J}-2$.

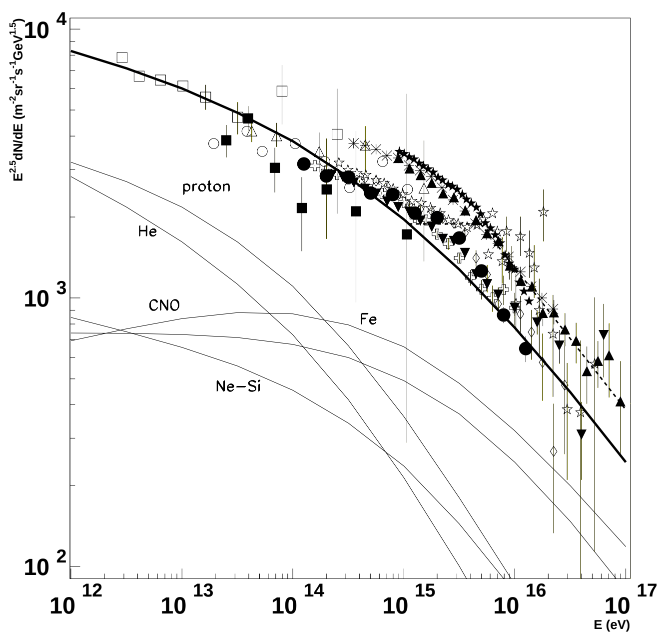

Figure 9.19: Calculated all particle spectrum and the contributions of five components with the model $\mathrm{R_C}-2$.

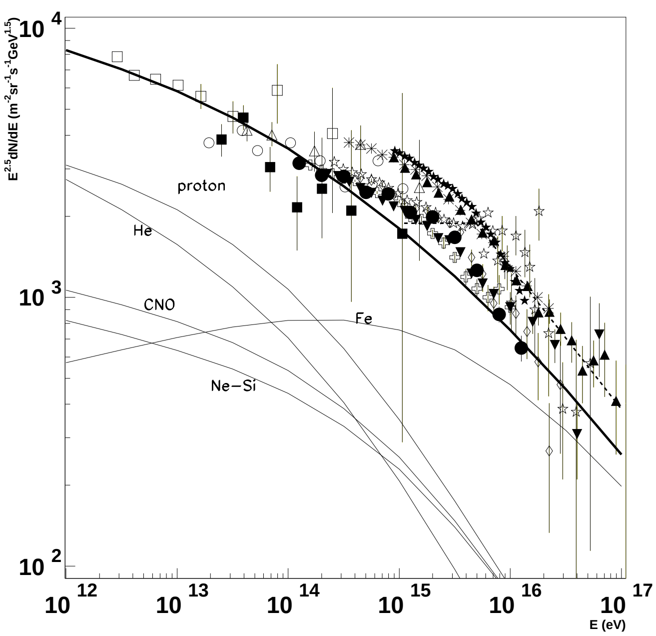

Figure 9.20: Calculated all particle spectrum and the contributions of five components with the model $\mathrm{R_F} - 2$.

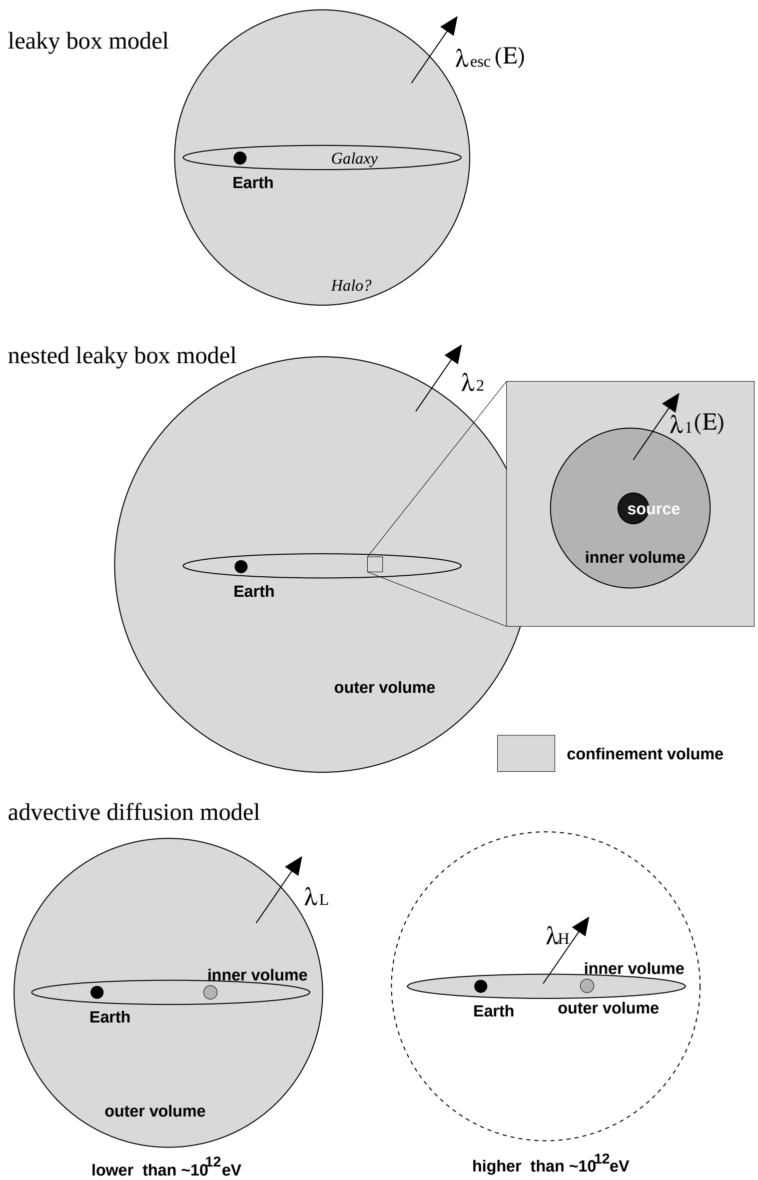

Figure 9.21: The schematic view of three cosmic propagation models.

Chapter 10

Conclusions

10.1 Summary of observational results

Using the equi–intensity method we obtained the mean equi-intensity curves of EASs with the primary energies from 10^{14} to 10^{16} eV observed with the MAS array at Mt. Chacaltaya, 5200 m a.s.l.(550 g/cm^2). The data used in the analysis consists of 7.5×10^7 selected EAS events.

The apparent maximum development points which are expected to be found with a proton dominant composition model are not found in the measured equi-intensity curves around the knee energy. By comparing the measured curves with those calculated with the Monte–Carlo simulation, the mean logarithmic mass $\langle \ln A \rangle$ was obtained as a function of the primary energy. The measured $\langle \ln A \rangle$ increases with the increasing energy in the range of $10^{14.5} - 10^{16}$ eV, and this is consistent with our former Čerenkov light observations and with the measurements of some other groups. The observed $\langle \ln A \rangle$ suggests that the steepening of the component spectra is caused at a single rigidity of $10^{14.5}$ V.

The measurement of Čerenkov light pulse shapes corresponds to an observation of the longitudinal developments of air showers at the earlier stages before the maximum developments. In contrast, with the equi-intensity method analysis we determined the longitudinal developments around their maximum and at the later stages. Therefore, with two different observations, we measured the whole stages of EAS longitudinal developments and then we could make the trustworthy conclusion on the chemical composition based.

From the observational results, we obtained a power–law form EAS size spectrum for the measured EAS events with the zenith angle range of $\sec\theta = 1.0 - 1.1$,

$$\log(\frac{dF}{d\log N}[\mathrm{m}^{-2}\mathrm{s}^{-1}\mathrm{sr}^{-1}]) = \begin{cases} (3.85 \pm 0.03) - (1.57 \pm 0.01) \times \log N & (\log N < 5.9) \\ (6.80 \pm 0.87) - (2.07 \pm 0.14) \times \log N & (\log N \geq 5.9) \end{cases} \tag{10.1}$$

where N is the measured size.

With the investigated chemical composition we obtained the energy spectrum of primary cosmic rays in the energy range of $10^{14.5} - 10^{16}$ eV,

$$\log(\frac{dF}{dE}[\mathrm{m}^{-2}\mathrm{s}^{-1}\mathrm{sr}^{-1}\mathrm{eV}^{-1}]) = \begin{cases} (19.26 \pm 0.07) - (2.66 \pm 0.01) \times \log E[eV] & (\log E < 15.4) \\ (27.44 \pm 1.77) - (3.19 \pm 0.11) \times \log E[eV] & (\log E \geq 15.4) \end{cases} \tag{10.2}$$

The present result of cosmic ray flux is consistent with other experiments, and the obtained all–particle spectrum has a gradual steepening around $10^{15.5}$ eV with the spectral index jump from -2.66 to -3.19. Around the energies of 10^{14} eV the present result is consistent with those of the direct measurements within uncertainties and consistent with those reported by CASA-MIA and by DICE. Comparing our result with those by Tibet and by KASCADE, both of the absolute intensity and the knee energy in our spectrum are inconsistent. These differences could be due to the systematic difference of energy estimation procedures.

10.2 Cosmic ray source models and propagation models

The supernova acceleration model with the stellar winds and with ejected matters of Wolf–Rayet stars is one of the plausible models to explain our results. We conclude that the actual model should predict that the dominant component above 10^{15} eV is iron nuclei, and that the $\langle \ln A \rangle$ increases with the increasing energy and it becomes about 3.5 at 10^{16} eV.

With the detailed research for the diffusive motions of charged particles in the galactic turbulent magnetic fields, I calculated the residence times of cosmic rays in the galactic disk with solving an one dimensional advective–diffusion equation. Consequently, this simple model predicts all the observed features, *i.e.*, the energy dependences of the flux for the all–particle and the components, the chemical composition and the anisotropy with assuming the natural values of the parameters for the equation, such as the magnetic field strength and the galactic wind velocity. However, in this model we assumed that the regular magnetic fields are open toward the galactic halo, that the maximum energy of cosmic ray accelerations is at least 10^{16} eV and that the source spectrum index $\gamma \simeq 2.7$. Thus, we need more detailed investigations for the galactic magnetic fields and the galactic winds and new discoveries and investigations for cosmic ray accelerators with observations of cosmic ray anisotropies [93] and very high energy gamma rays [26].

10.3 Future Prospects

The results of our measurement and other observations suggest that cosmic rays with energies less than 10^{16} eV originate in this galaxy. Up to the present date cosmic rays with energies greater than 10^{20} eV are observed with air shower experiments. Ultra high energy cosmic rays ($> 10^{19}$ eV) may be of extra galactic origin because the arrival direction distribution of ultra high energy cosmic rays does not show any enhancement of cosmic rays from the galactic plain. Therefore, the maximum accelerated energy for galactic cosmic ray sources is expected to be less than 10^{20} eV, and the slight bend in the energy spectrum at $10^{18.5}$ eV (called *ankle*) is believed to show the transition from galactic sources to extra galactic ones with the increasing energy. The difference between origins of cosmic rays will be observed as the variation of the chemical composition with th primary energy, so that, the study of the chemical composition of cosmic rays with energies greater than the knee gives some crucial information on possible galactic and extra galactic sources and acceleration sites of cosmic rays. The BASJE collaboration is preparing the observations of air showers with primary energies from 10^{15} to 10^{17} eV. The particle detectors of the MAS array will be re–deployed in an array with the area of 400 m $\times$ 700 m. The rearrangement will be finished in 2005, and the observations will be continued for 3 years.

For air showers with primary energies greater than 10^{17} eV, the measurement of X_{max} by the Fly's Eye group showed that the averaged mass number is decreasing with the increasing primary energy. On the other hand, the Akeno group reported that they cannot observe any evidence of the variation of the chemical composition, so that, both of the results are contradictory to each other. The chemical composition of this energy region will be stringently verified by the proposed TALE (Telescope Array Low energy Extension) project using the hybrid detection method with fluoresces light telescopes and surface particle detectors [46].

When an air shower is detected with a surface detector array, the primary energy and the species are not determined independently each other. This is the main drawback to measuring cosmic rays with air shower arrays. If we determine a primary energy of a measured air shower, we need information of the stage of the longitudinal development of the shower. However, the longitudinal developments depend on primary species. Therefore, the size–energy relation id determined with Monte Carlo simulations taking a assumed chemical composition into consideration. For estimations of the chemical composition, muons or Čerenkov photons are measured simultaneously with air shower sizes, or we use the equi–intensity method. However, primary species are not determined on event by event in any methods, only the averaged mixing ratio of species can be estimated. In order to obtain the energy spectra of each component group with air shower observations, we need a new method for the determinations of primary species independently with primary energies. The most promising method is the hybrid observations of air shower, *i.e.*, the simultaneous detections with air fluorescence telescopes and with surface detector arrays. The arrival directions and the core positions of air showers are determined by the surface array. On the other hand, the fluorescence telescopes are analogous with hadron calorimeters. The primary energies are determined from atmospheric fluorescence photon yields, and we can separately obtain longitudinal development curves. Therefore, in the hybrid observations, the estimations of species are independent with the determinations of primary energies, and then it is possible to estimate the primary species on event by event. With simple Monte Carlo simulations of air shower developments, it is demonstrated that we can classified the primary particles according to the longitudinal developments into three different types of species, *i.e.*, light, middle and heavy nuclei, and can obtain the energy spectra of each component with hybrid measurements [70].

Since accelerated high energy particles interact with magnetic fields and the ambient matters of sources, sources or their environments radiate high energy gamma rays. So that, we believe that the astronomical objects which accelerate cosmic rays are observed as high energy gamma ray sources. Many sources of gamma rays with energies less than 10^{13} eV have been discovered with satellites and ground–based Čerenkov telescopes. However, for all the very high energy gamma ray sources, the process are explained with the synchrotron radiations and subsequent inverse Compton scattering, *i.e.*, the emissions of high energy electrons. SN1006 is only instance of the source which radiate π^0 decay gamma rays induced by high energy nuclei [91]. However the emissions from this object also can be explained with the radiations from electrons. Up to now, acceleration sites of cosmic rays with energies greater than 10^{14} eV have not been discovered yet. Even for lower energy cosmic rays which are accelerated in supernova remnants, source objects are not identified. We hope discoveries of the sources by observations with the next generation Čerenkov telescopes, such as HESS [43], MAGIC [68], etc.

Since cosmic charged particles move on complex trajectories in galactic magnetic field, we cannot trace back to their sources directly from their arrival directions. However, if there are nearby cosmic ray sources or a gradient in the source distribution, we expect a small anisotropy oriented to their directions. We found a significant anisotropy in the galactic longitude region $l = 220 \sim 260^\circ$ from the observations with the BASJE MAS array, and we concluded that this anisotropy is due to the nuclear component of cosmic rays [93]. The calculations of cosmic ray propagations in the galaxy clarify the contributions of the local sources to the cosmic ray flux at the earth as well as the resultant anisotropies. It is shown that the Vela SNR and Monogem can give rise to the anisotropy found in our observations. In order to identify the contributing source to the anisotropy we need detailed measurements of the anisotropy and its energy dependence and need to reveal the structures of the galactic magnetic field.

Cosmic rays with energies less than 10^{14} eV are accelerated in supernova remnants and propagate in the galactic halo. This model had been confirmed by observations of the flux ratio between the primary nuclei and the secondary nuclei which are fragmentation of the primary nuclei, and by measurements of the abundance ratios of radio isotopes. We need to measure the amount of matter traversed and the escape time of cosmic rays with energies greater than 10^{14} eV in order to definitively identify the acceleration and propagation mechanisms. For these measurements we have to directly detect primary cosmic rays with satellites or balloon–borne equipment. The CREAM experiment [24] using the transition radiation detectors challenges to direct measurements of knee region cosmic rays, but we need improved detectors having more larger effective area and the higher charge resolution.

Acknowledgments

The authors would like to thank to Prof. Fumio Kakimoto for his support to over all my cosmic ray researches. I also acknowledge Prof. Hisashi Yoshii(Ehime University), Prof. Yutaka Matsubara(Solar–Terrestrial Environment Laboratory, Nagoya University), Prof. Kazuaki Murakami(Nagoya University), Prof. Tatsunosuke Kaneko(Okayama University), Dr. Yuji Shirasaki(National Astronomical Observatory of Japan), Dr. Yoshiki Tsunesada(National Astronomical Observatory of Japan), Prof. Yoshihiko Mizumoto(National Astronomical Observatory of Japan) and Prof. Yoshio Toyoda(Fukui Institute of Technology) for their useful comments and discussions. I acknowledge to Mr. Katsuo Nishi, Mr. Susumu Shimoda, Mr. Norio Tajima and Mr. Yutaka Yamada for their support for the observations. I am grateful to all other colleagues in the BASJE Collaboration. I would like to appreciate helpful support by all the staff of Instituto de Investigaciones Fisicas, Universidad Mayor de San Andres, La Paz, Bolivia. Especially I wish to acknowledge Ing. Pedro Miranda and Prof. Alfonso Veralde.

I express thanks to Dr. Kenichi Kadota(Musashi Institute of Technology), Mr. Daijiro Senda(Tokyo Institute of Technology), Mr. Yutaka Kurashina(Tokyo Institute of Technology), Dr. Hisao Tokuno(University of Tokyo) and Mr. Dai Harada(Tokyo Institute of Technology) for useful discussion.

My thanks are due to all the colleagues in the Kakimoto Laboratory for their encouragement. The author also would like to appreciate for the continued support of our experiment at Mt. Chacaltaya by the staff of Institute for Cosmic Ray Research, University of Tokyo.

This work is supported in part by a Grant–in–aid for Scientific Research from the Ministry of Education, Culture, Sports, Science and Technology of Japan.

Bibliography

[1] Aglietta, M., et al., *Astropart. Phys.*,**10**, 1(1999)

[2] Agnetta, G., et al., *Astropart. Phys.*, **6**, 301(1997)

[3] Aharonian, F.A., and Heizelmann, G., *Nucl. Phys.(Proc. Suppl.)*, **60B**, 193(1998)

[4] Amenomori, M., et al., *Ap. J.*,**461**, 408(1996)

[5] Antoni, T., et al., *Proc. 26th ICRC(Salt Lake City)*, **1**, 131(1999)

[6] Apanasenko, A.V., et al., *Proc. 25th ICRC, Durban*, **5**, 13(1997)

[7] Apanasenko, A.V., et al., *Astorpart. Phys.*, **16**, 13(2001)

[8] Asakimori, K., et al. *Proc. 24th ICRC(Roma)*,**2**, 707(1995); *Astrophys. J.*,**502**,278(1998)

[9] Axford, W.I., *Proc. ICRR int'l symp., Astrophysical Aspects of the Most Energetic Cosmic Rays, Eds., M.Nagano and F.Takahara*(World Scientific), 134 (1991)

[10] Baltrusaitis, R.M., et al., *Nucl. Inst. Meth.*, **A240**, 246(1985)

[11] Bernlöhr, K., et al., *Astropart. Phys.*, **5**, 139(1996)

[12] Bernlöhr, K., et al., *Nucl. Inst. Meth.*, **A369**, 284(1996)

[13] Bernlöhr, K., et al., *Astropart. Phys.*, **8**, 253(1998)

[14] Biermann, P.L., *Astron. & Astrophys.*,**271**,649 (1993)

[15] Bierman, P.L., *Astron. Astrophys.*, **271**, 649(1993)

[16] Bird, J.D. *Phys. Rev. Lett.*, **71**, 3401(1993)

[17] Boothby, K., et al., *Proc. 24th ICRC(Roma)*, **2**, 697(1995)

[18] Borione, A., et al., *Nucl. Inst. Meth.*, **A346**, 329(1994)

[19] Cassidy, M., et al., *Proc. 25th ICRC(Durban)*, **5**, 189(1997)

[20] Cesarsky, C.J., *Ann. Rev. Astron. Astrophys.*,**18**,289 (1980)

[21] Cesarsky, C.J., *Proc. 20th ICRC, Moscow*,**8**,87 (1987)

[22] Chi, X. and Wolfendare, A.W., *J. Phys. G*, **16**, 1409 (1990)

[23] Cowsik, R. and Wilson, L., *Proc. 13th ICRC(Denver)*, **1**, 500 (1973); Meneguzzi, M., *Nature Physical Science*, **241**, 100(1973)

[24] CREAM collaboration, *http://cosmicray.umd.edu/cream/cream.html*

[25] Engler, J, et al., *Proc. 26th ICRC(Salt Lake City)*, **1**, 349(1999); Kampert, K.–H., et al., *Proc. 26th ICRC(Salt Lake City)*, **3**, 159(1999)

[26] *for exmaple,* Enomoto, R., et al., *Nature*, **416**, 823(2002)

[27] Fenyves, E.J., et al., *Phys. Rev. D*, **22**, 1839(1996)

[28] Fortson, L.F., et al., *Proc. 26th ICRC(Salt Lake City)*, **3**, 125(1999)

[29] Fowler, J.W., et al., *Astropart. Phys.*, **15**, 49(2001)

[30] Gaisser, T.K., *Csomic Rays and Particle Physics* (Cambridge University Press) (1990)

[31] Garcia–Munoz, M., Mason, G.M. and Simpson, J.A., *Ap.J.*,**217**, 859 (1977)

[32] Garcia–Munoz, M., et al., *Ap.J.*,**280**, L13 (1984)

[33] Giacalone, J. and Jokipii, J.R., *Ap. J.*, **430**, L137 (1994), *J. Geo. Res.*, **101**, 11095 (1996)

[34] Glasmacher, M.A.K., et al., *Astropart. Phys.*, **10**, 291(1999)

[35] Glasmacher, M.A.K., et al., *Proc. 26th ICRC(Salt Lake City)*, **3**, 129(1999)

[36] Grigorov, N.L., et al., *Proc. 12th ICRC(Hobart)*,**5**,1760(1971)

[37] Gupta, M. and Webber, W.R., *Ap.J.*,**340**, 1124 (1989)

[38] Guzik,, T.G., et al., *Proc. 19th ICRC(La Jolla)*,**2**,76 (1985)

[39] Han, J.L. and Qiao, G.J., *Astron. & Astrophys.*, **288**, 759 (1994)

[40] Hayakawa, S., *Cosmic Ray Physics*(John Wiley & Sons)(1969)

[41] Heck, D., et al., *Report FZKA*(Forschungszentrum Karlsruhe), 6019(1998)

[42] Heck, D., et al.,*Proc. 27th ICRC(Hamburg)*,**1**,233(2001)

[43] HESS collaboration, *http://www.mpi-hd.mpg.de/hfm/HESS/HESS.html*

[44] Hillas, A.M., *J. Phys. G.*, **8**, 1475(1982)

[45] Hillas, A.M., *Ann. Rev. Astron. Astrophys.*, **22**, 425 (1984)

[46] HiRes collaboration, *http://www.hires.physics.utah.edu*

[47] L'Heureux, J., et al., *Nucl. Inst. Meth.*, **A295**, 246(1990)

[48] Honda, M., *Ap. J.*, **319**, 836 (1987)

[49] Hörandel, *Proc. 27th ICRC(Hamburg)*,**1**,71(2001)

[50] Inoue, M. and Tabara, H., *Pub. Astron. Soc. Japan*, **33**, 603 (1981)

[51] Ip, W.H., and Axford, W.I., *Particle Acceleration in Cosmic Plasmas, Eds., G.P.Zank and T.K.Gaisser*(A.I.P. NewYork), 400 (1992)

[52] Ivanenko, I.P., et al., *Proc. 23th ICRC(Calgary)*,**2**,17(1993)

[53] Jokipii, J.R., and Morfill, G.E., *Ap.J.*,**290**, L1 (1985)

[54] Jokipii, J.R., and Morfill, G.E., *Ap.J.*,**312**, 170 (1987)

[55] Kalmykov, N.N. and Ostapchenko, S.S., *Yad. Fiz.*,**56**, 105 (1993)

[56] Kakimoto, F., et al., *Nucl. Inst. Meth.*, **A373**, 282(1996)

[57] Kakimoto, F., et al., *Nucl. Inst. Meth.*, **A372**, 527(1996)

[58] Kakimoto, F., et al., *J. Phys. G.*, **9**, 339(1983)

[59] Kakimoto, F., et al. *Proc. 23th ICRC(Calgary)*,**2**,103(1993)

[60] Kamioka, E., *Astropart. Phys.*, **6**, 155(1997)

[61] Klages, H.O., et al., *Nucl. Phys. B(Proc. Suppl.)*, **52B**, 92(1997)

[62] Knapp, J., et al., *Astropart. Phys.*, **19**, 77 (2003)

[63] Kobayakawa, K., Sato, Y. and Samura, T., *Proc. 26th ICRC(Salt Lake City)*,**4**,467(1999); *Astropart. Phys.*, submitted; private comunication

[64] Larsen, C.G., Kieda, D.B., and Swordy, S.P.,*Proc. 27th ICRC(Hamburg)*, **1**, 134(2001)

[65] Linsley, J., *Proc. 18th ICRC, Bangalore*, **12**, 135 (1983)

[66] Linsley, J., *Proc. 19th ICRC(La Jolla)*, **3**, 461(1985)

[67] Longair, M.S., *High Energy Astrophysics* (Cambridge University Press) (1994)

[68] MAGIC collaboration, *http://magic.mppmu.mpg.de*

[69] Mathewson, D.S. and Ford, V.L., *Mon. Not. R. Astron. Soc.*, **74**, 139 (1970)

[70] Matsuzaki, E., *Master thesis*(Tokyo Tech.), (2004)

[71] Müller, D., et al., *Ap. J.*, **374**, 356(1991)

[72] Nagano, M., et al., *J. Phys. G*,**10**, 1295(1984)

[73] Naito, T., and Takahara, F., *Prog. Theor. Phys.*,**93**, 287 (1995), *Mon. Not. R. Astron. Soc.*,**275**, 1077 (1995)

[74] Protheroe, R.J., and Szabo, A.P., *Phys. Rev. Lett.*,**69**, 2885 (1992)

[75] Ptuskin, V.S., et al., *Astron. & Astrophys.*, **268**, 726 (1990)

[76] Rao, M.V.S., and Sreekantan, B.V, *Extensive Air Showers* (World Scientific), (1998)

[77] Risse, M., et al., *Proc. 26th ICRC(Salt Lake City)*, **1**, 135(1999)

[78] Ryan, M.J., et al., *Phys. Rev. D*, **40**, 729(1989)

[79] Senda, D., Ogio, S. and Kakimoto, F., *Proc. 25th ICRC, Durban*, **2**, 269 (1997)

[80] Senda, D., Master thesis, Tokyo Tech. (1997)

[81] Shirasaki, Y., *Mater thesis*,Tokyo Tech.(1994)

[82] Shirasaki, Y., et al., *Astropart. Phys.*, **15**, 357(2001)

[83] Shirasaki, Y., and Kakimoto, F., *Astropart. Phys.*, **15**, 241(2001)

[84] Silberberg, R., and Tsao, C.H., *Ap. J.*, **352**, L49(1990)

[85] Sofue, Y. and Fujimoto, M., *Ann. Rev. Astron, Astrophys.*, **24**, 459 (1986)

[86] Stanev, T., *Astron. & Astrophys.*,**274**,902 (1993)

[87] Swordy, S.P., et al., *Ap. J.*, **349**, 625(1990)

[88] Swordy, S.P., and Kieda, D.B., *Astropart. Phys.*, **13**, 137(2000)

[89] Szabo, A.P., and Protheroe, R.J., *Astropart. Phys.*,**2**, 375 (1994)

[90] Tajima, T. and Shibata, K., *Plasma Astrophysics*(Addison–Wesley), (1997)

[91] Tanimori, T., et al., *Astrophys. J. Lett.*, **497**, L25-L28(1998)

[92] The Telescope Array Project Design Report (2000)

[93] Tsunesada, Y., *Doctor thesis*(Tokyo Tech.), (2002)

[94] Ulrich, H., et al., *Proc. 27th ICRC(Hamburg)*, **1**, 97(2001)

[95] Völk, H.J., and Biermann, P.L., *Ap.J.*,**333**, L65 (1988)

[96] Wang, B., *Ap. J.*, **444**, 590 (1995)

[97] Wefel, J.P., *Genesis and Propagation of Cosmic Rays Eds., M.M.Shapiro and J.P.Wefel* (NATO ASI series, Reidel), **C220**, 1 (1988)

[98] Yoshii, H., et al., *Proc. 24th ICRC(Roma)*,**2**,703(1995)

[99] Yoshii, H., et al., *Il Nuovo Cimento*,**24C**,507(2001)